SWIRLING FLUID MIXING AND COMBUSTION DYNAMICS AT SUPERCRITICAL CONDITIONS

A Dissertation
Presented to
The Academic Faculty

by

Xingjian Wang

In Partial Fulfillment
of the Requirements for the Degree
of Doctor of Philosophy in the
School of Mechanical Engineering

Georgia Institute of Technology
August 2016

SWIRLING FLUID MIXING AND COMBUSTION DYNAMICS AT SUPERCRITICAL CONDITIONS

Approved by:

Dr. Vigor Yang, co-Advisor
School of Aerospace Engineering
Georgia Institute of Technology

Dr. Devesh Ranjan
School of Mechanical Engineering
Georgia Institute of Technology

Dr. Tim Lieuwen, co-Advisor
School of Mechanical Engineering
Georgia Institute of Technology

Dr. Suresh Menon
School of Aerospace Engineering
Georgia Institute of Technology

Dr. Wenting Sun
School of Mechanical Engineering
Georgia Institute of Technology

Date Approved: March 04, 2016

To my parents for their love, encouragement, and sacrifices

ACKNOWLEDGEMENTS

I would like to thank my thesis advisors, Dr. Vigor Yang and Dr. Timothy Lieuwen for their valuable guidance and continuous support throughout the course of my PhD. I am especially grateful to Dr. Yang for his encouragement and help through extremely difficult times in my first three years of graduate study. Working with him, as one of his disciples, has been a pleasant and memorable experience.

Thanks also to Drs. Suresh Menon, Devesh Ranjan, and Wenting Sun for agreeing to serve on my thesis committee and providing helpful comments on the work.

Special thanks to Dr. Hongfa Huo for the time and energy he has spent on me for many helps in computer coding and overall guidance. I would also like to acknowledge Dr. Yanxing Wang for many enlightening discussions and invaluable help.

I would also like to thank my colleagues, Dr. Liwei Zhang, Dr. Dongjun Ma, Dr. Prashant Khare, Dr. Dilip Sundaram, Dr. Xiaodong Chen, Dr. Sharath Nagaraja, Chung-Han Wu, Jong-Chan Kim, David Ku, Yixing Li, Suo Yang, Yu-Hung Chang, Shiang-Ting Yeh, Christopher Lioi, Tim Dawson, and Murali Gopal for many discussions and wonderful times we has had together. I am very thankful to Margaret Ojala and Howard Simpson for their administrative help.

This work was sponsored by the Air Force Office of Scientific Research. The support and advice given by Dr. Mitat A. Birkan is gratefully acknowledged.

My deepest appreciation goes to my parents, Guoming Wang and Shufang Ding, for all the love they have given to me and continue to give, to my two sisters, Miaomiao Wang and Juan Wang, and to my girlfriend, Yao Jing, for their constant love and support.

TABLE OF CONTENTS

ACKNOWLEDGEMENTS ..... **iv**

LIST OF TABLES ..... **viii**

LIST OF FIGURES ..... **ix**

LIST OF SYMBOLS AND ABBREVIATIONS ..... **xvi**

SUMMARY ..... **xviii**

Chapter 1 INTRODUCTION **1**

1.1 Background and Motivation 1
1.2 Literature Review 3
1.2.1 High-Pressure Fluid Injection, Mixing, and Combustion 3
1.2.2 Counterflow Diffusion Flames of General Fluids 10
1.3 Research Objectives 14
1.4 Dissertation Outline 16

Chapter 2 Theoretical Formulation **18**

2.1 Governing Equations 18
2.2 Simplified Equations for Counterflow Configuration 21
2.3 Equation of State and Thermophysical Properties 23
2.3.1 Soave-Redlich-Kwong EOS 24
2.3.2 Thermodynamic Properties 25
2.3.3 Partial Molar and Partial Density Properties 26
2.4 Transport Properties 28
2.4.1 Dynamic Viscosity and Thermal Conductivity 28
2.4.2 Binary Mass Diffusivity 34
2.5 Turbulence Closure: Larger-Eddy-Simulation 36
2.5.1 Filtered Governing Equations 38
2.5.2 Subgrid-Scale Model 41
2.6 Turbulence/Combustion Models 45
2.6.1 Laminar Flamelet Model 46

Chapter 3 Numerical Methodology **51**

3.1 Preconditioning Scheme for Real-Fluid Mixtures 51
3.1.1 Determination of the Preconditioning Factor 56
3.2 Spatial Discretization 59
3.2.2 Finite Volume Approach 59
3.2.3 Evaluation of Inviscid Fluxes 63
3.2.4 Evaluation of Viscous and SGS Fluxes 65
3.2.5 Evaluation of Artificial Dissipation 67

3.3 Temporal Discretization 73
3.4 Boundary Conditions 75
3.4.1 Characteristic Boundary Conditions 75
3.5 Parallel Implementation 79

Chapter 4 SWIRL INJECOR FLOW DYNAMICS 81

4.1 Physical Configuration and Flow Conditions 81
4.2 Results and Discussion 82
4.2.1 Grid Independence Study 83
4.2.2 Supercritical Fluid Regions 84
4.2.3 Instantaneous Flow Field 87
4.2.4 Characteristics of Wave Propagation 91
4.2.5 Injector Flow Dynamics 94
4.2.6 Effects of Flow conditions and Geometry 102
4.3 Conclusion 108

Chapter 5 MIXING CHARACTERISTICS OF LIQUID OXYGEN/KEROSENE BI-SWIRL INJECTORS 110

5.1 Physical Configuration and Flow Conditions 110
5.2 Results and Discussion 112
5.2.1 Grid Independence Study 112
5.2.2 LOX/Kerosene Mixing and Flow Dynamics 114
5.2.3 Parametric Study 119
5.3 Conclusion 124

Chapter 6 SUPERCRITICAL COMBUSTION OF LOX/KEROSENE BI-SWIRL INJECTORS 126

6.1 Physical Configuration and Flow Conditions 126
6.2 Results and Discussion 126
6.2.1 Baseline Case 127
6.2.2 Parametric Study 135
6.3 Conclusion 142

Chapter 7 COUNTERFLOW DIFFUSION FLAMES: OXYGEN/HYDROGEN MIXTURES 143

7.1 Theoretical and Numerical Framewrk 144
7.1.1 Theoretical Formulation 144
7.1.2 Boundary conditions 144
7.1.3 Numerical Methods 145
7.2 Results and Discussions 147
7.2.1 Model Validation 148
7.2.2 S-Curve Flame Response 150
7.3 Conclusions 168

Chapter 8 COUNTERFLOW DIFFUSION FLAMES: OXYGEN/N-ALKANE HYDROCARBONS (CH_4-$C_{16}H_{34}$) 170

8.1 Problem Description 170
8.2 Results and Discussion 171
8.2.1 Oxygen/Methane System 172
8.2.2 Oxygen/n-Heptane System 189
8.2.3 Oxygen/ n-Alkane (CH_4-$C_{16}H_{34}$) Systems 194
8.3 Conclusion 197

Chapter 9 CONCLUSIONS 199

Appendix A Properties of the Favre Average 202

Appendix B Thermodynamics Relationships 203

Appendix C Derivative Expressions in SRK EOS 211

Appendix D Jacobian Matrices 213

REFERENCES 216

VITA 232

LIST OF TABLES

Table 1.1: Propellants and chamber operating conditions for selected LREs 1

Table 1.2: critical properties of typical pure substance 2

Table 2.1: Coefficients to calculate E_i in Eq. 2.90. 33

Table 2.2: Coefficients to calculate E_i in Eq.2.97. 33

Table 2.3: Diffusion volumes for selected atoms and molecules. 35

Table 4.1: Baseline geometry and operating conditions. 82

Table 4.2: Effects of injector geometry and flow conditions on LOX film thickness and spreading angle at injector exit. 103

Table 5.1: Geometric param.eters of the baseline swirl coaxial injector 111

Table 5.2: Chamber pressure and inlet conditions. 111

Table 5.3: Four levels of grid resolutions. 112

Table 5.4: The geometrical parameters of four cases. 119

Table 6.1: Geometrical parameters of four cases 127

Table 7.1: Scaling constants for renormalization of maximum flame temperature. 162

Table 8.1: Critical properties. 172

Table 8.2: Reaction Mechanisms of O_2 with H_2 and n-alkanes (CH_4~$C_{16}H_{34}$) 172

Table 8.3: Maximum flame temperature at equilibrium and extinction state for the oxygen/methane system. 182

LIST OF FIGURES

Figure 1.1: Schematic of flame-holding mechanism for oxygen-hydrogen shear-coaxial injection..... 5

Figure 1.2: Schematic diagram of a folded S-shaped flame response 12

Figure 2.1: Schematic diagram of a counterflow diffusion flame. 21

Figure 2.2: Correlation for high-pressure diffusivity using Takahashi method..... 36

Figure 3.1: Schematic of three-dimensional computational cell 60

Figure 3.2: Schematic diagram of the stencil used in evaluating inviscid flux terms in the plane. 65

Figure 3.3: Schematic diagram for a three-dimensional auxiliary cell. 66

Figure 3.4: Schematic of a two-dimensional sub-domain with ghost cells. 80

Figure 4.1: LOX/kerosene bi-swirl injector of RD-0110 engine. 82

Figure 4.2: Distribution of blocks in the whole computational domain. 83

Figure 4.3: Radial distributions of time-averaged flow properties at the axial location x/R = 8.3 for two grid systems: solid line: baseline; dashed line: finer mesh. 84

Figure 4.4: Instantaneous distribution of the density field in longitudinal and transverse views, *p*=100 atm. 85

Figure 4.5: Density (a) and density gradient (b) of oxygen as a function of temperature at various pressures. 85

Figure 4.6: Temporal evolution of density distributions at different axial locations, Δt = 0.06 ms, *p*=100 atm. 87

Figure 4.7: (a) Instantaneous distribution of density field with two iso-surfaces: ρ = 532 and 250 kg/m3; (b) iso-surface of azimuthal velocity at $u_0 = 4$ m/s; *p*=100 atm..... 88

Figure 4.8: Instantaneous snapshot of vorticity magnitude at different cross-sectional views, $p = 100$ atm. 89

Figure 4.9: Temporal evolution of spatially-averaged streamlines, $\Delta t = 0.06$ ms, $p = 100$ atm..... 90

Figure 4.10: The radial distributions of vorticity magnitude spatially averaged in the azimuthal direction at three different axial locations, $p=100$ atm. 91

Figure 4.11: Iso-surface of azimuthal velocity at $u_\theta = 22$ m/s in azimuthal phase space ($\theta = 0 \sim 2\pi$), $p=100$ atm. 92

Figure 4.12: Temporary evolution of the density iso-surface at $\rho_s = 532$ kg/m3, $p=100$ atm..... 92

Figure 4.13: Temporal evolution of density distributions at $x=10$ mm, $p=100$ atm... 94

Figure 4.14: Probe positions within the liquid film inside the injector and near the injector exit..... 95

Figure 4.15: Time histories of pressure fluctuations at four different probe locations..... 96

Figure 4.16: Power spectral densities of pressure fluctuations at four different locations (probe 1-4) in the vortex chamber. 97

Figure 4.17: Power spectral densities of pressure fluctuations at four different locations (probe 5-8) in the vortex chamber. 97

Figure 4.18: Power spectral densities of pressure fluctuations at four different locations (probe 9-12) in the nozzle. 98

Figure 4.19: Power spectral densities of pressure fluctuations at four different locations (probe 13-16) near the injector exit. 98

Figure 4.20: Speed of sound of oxygen as a function of temperature at various pressures. 99

Figure 4.21: Energy distribution of POD modes of pressure oscillations, $p=100$ atm.101

Figure 4.22: Frequency spectra of time-varying coefficient of first six POD modes of pressure oscillations, $p=100$ atm. 101

Figure 4.23: Spatial distributions of the first six POD modes of oscillatory pressure field on longitudinal ($x-r$) plane within injector, $p=100$ atm. 102

Figure 4.24: Spatial distributions of mode 1 and mode 4 of oscillatory pressure field on transverse ($r-\theta$) plane within injector. 102

Figure 4.25: Distributions of azimuthally-averaged density field for Cases 1-4. 103

Figure 4.26: Distributions of the magnitude of azimuthally-averaged density for Cases 1-4..... 104

Figure 4.27: Distributions of time-averaged density and axial velocity for Cases 2 and 5. 105

Figure 4.28: Distributions of time-averaged temperature field interpolated by streamlines. 106

Figure 4.29:Distributions of local maximum density gradient in the radial direction as a function of axial coordinate, (a) within the injector; (b) downstream of the injector. 106

Figure 5.1: Longitudinal plane view of the injector. 111

Figure 5.2: Instantaneous snapshots of the density field superimposed by a positive Q-isocontour (solid line) at 10^8 s^{-2} for increasing grid resolutions. 113

Figure 5.3: The radial distributions of time-averaged flow properties at the axial location ($x/R=10$) for increasing grid resolutions. 114

Figure 5.4: Temporal evolution of density field for the baseline (Case I). 115

Figure 5.5: Radial distributions of time-averaged density (ρ), temperature (T), axial (u_x), and azimuthal velocity (u_θ) components near the injector exit ($x/R=8.3$). 116

Figure 5.6: Close-up view of temporal evolution of density field near liquid-oxygen film for the baseline (Case I). 117

Figure 5.7: Instantaneous distributions of temperature, axial velocity, and vorticity for the baseline. 118

Figure 5.8: Close-up view of density evolution in the vicinity of injector post. 119

Figure 5.9: Instantaneous distributions of density and kerosene mass fraction for Case II. 120

Figure 5.10: Streamlines of time-averaged flowfield for four cases. 120

Figure 5.11: Time-averaged distributions of kerosene mass fraction at injector near-field for four cases. 121

Figure 5.12: Instantaneous distributions of density and kerosene mass fraction for Case III. 122

Figure 5.13: Instantaneous distributions of density and kerosene mass fraction for Case IV. 123

Figure 5.14: Temporal evolution of density field for Case IV. 123

Figure 6.1: Instantaneous flow snapshot of distributions of temperature and mass fraction of OH for Case I in a global view. 128

Figure 6.2: Instantaneous flow snapshot of distributions of temperature, density, mixture fraction, and mass fraction of H_2O for Case I. 129

Figure 6.3 Instantaneous distributions of temperature, volumetric heat release rate, and flame index at injector near-field and downstream..... 130

Figure 6.4: Radial distributions of time-averaged density, temperature, axial, and azimuthal velocity components near the injector exit (x/R=8). 131

Figure 6.5: Comparison of instantaneous distributions of the mixture fraction for (a) combustion and (b) cold-flow environments. 132

Figure 6.6: Zoom-in view of distributions of the mixture fraction for (a) combustion and (b) cold-flow environments at the injector exit..... 133

Figure 6.7: Time-averaged distributions of temperature and axial velocity interpolated by flow streamline at the injector near-field. 134

Figure 6.8: Instantaneous flow snapshot of distributions of temperature, density, mixture fraction, and mass fraction of H2O for Case II. 135

Figure 6.9: Instantaneous flow snapshot of distributions of temperature, density, mixture fraction, and mass fraction of H2O for Case III. 136

Figure 6.10: Instantaneous flow snapshot of distributions of temperature, density, mixture fraction, and mass fraction of H2O for Case IV. 138

Figure 6.11: Temporal evolution of the flame field for Case IV. 138

Figure 6.12: Time-averaged distributions of mixture fraction at the injector near-field for four cases. 139

Figure 6.13: The radial distributions of the chamber wall temperature for all cases..... 140

Figure 6.14: Time history of relative pressure oscillations in the flame zone for all cases. 141

Figure 6.15: Frequency spectra of pressure oscillations in the flame zone for all cases. 141

Figure 7.1: a) Schematic of two-point temperature-controlling continuation method, solid line: initial solution, dashed line: new solution; b) Changes of temperature distribution applying two-point temperature-controlling method, solid line: V_F = 105 cm/s, dashed line: *136* cm/s, dash-dotted line: *200* cm/s, dash-dot-dotted line: *301* cm/s..... 146

Figure 7.2: Temperature distributions at $p=1$ atm, $T_{H_2}=T_{O_2}=300$ K, and $a=500$ s-1. 148

Figure 7.3: Validation of thermodynamic and transport properties of oxygen against NIST data. p = 100 atm. Lines: the present numerical scheme; symbols: NIST data. Compressibility (Z) and density (ρ), specific heat at constant pressure (C_p), thermal conductivity (λ), and dynamic viscosity (μ). 149

Figure 7.4: Temperature distributions at $p=50$ atm, $T_{H_2}=T_{O_2}=300$ K, and $a=10004$ s-1..... 150

Figure 7.5: Maximum flame temperatures at various pressures, $T_{H_2}=T_{O_2}=300$ K. 151

Figure 7.6: Heat release rate per unit area as function of strain rate: $p=1\sim200$ atm,. 152

Figure 7.7: Scaled heat release rate q as function of normalized strain rate rate (a/a_{ext}). (a) new scale, Eq. 7.11; (b) old scale, $q=q/\sqrt{pa_{ext}}$ 155

Figure 7.8: Temperature profile at different pressures and strain rates, 1 atm $a = 101\text{s}^{-1}$ (red lines), 10 atm $a = 107.6\text{s}^{-1}$ (blue lines), and 100 atm, $a = 3000\text{s}^{-1}$ (black lines). 157

Figure 7.9: Normalized flame temperature, mass fractions, and reaction rates at different pressures and strain rates, 1 atm $a = 101\text{s}^{-1}$ (red lines), 10 atm $a = 107.6\text{s}^{-1}$ (blue lines), and 100 atm, $a = 3000\text{s}^{-1}$ (black lines)..... 157

Figure 7.10: Normalized flame thickness based on half maximum width of temperature and mass fractions of H2O, OH, and H as functions of normalized strain rate (a/a_{ext}) at different pressures. 158

Figure 7.11: Normalized maximum temperature and mass fractions of H2O, OH, and H in the flame as functions of normalized strain rate(a/a_{ext}) at different pressures. S: stable burning branch, U: unstable burning branch..... 159

Figure 7.12: Renormalized maximum mass fraction of H radical, $\hat{Y}_{H,max}$, and temperature, $\hat{T}_{max}$, in the flame zone. 161

Figure 7.13: Normalized rates of production of species as functions of normalized strain rate (a/a_{ext}) at different pressures. 163

Figure 7.14:Maximum values of flame temperature and species mass fractions as functions of pressure at chemical equilibrium conditions. 164

Figure 7.15: Maximum values of flame temperature and species mass fractions as functions of pressure at extinction strain rate. 164

Figure 7.16: Extinction strain rate, a_{ext} , and flame temperature, $T_{max,ext}$, as functions of pressure. 165

Figure 7.17: Maximum reaction rates for several different species as functions of pressure. 166

Figure 7.18: Distributions of temperature and mass fractions of major for different inlet temperatures, $p=100$ atm, $a=20004$ s-1..... 167

Figure 7.19: Maximum flame temperature for two different oxygen inlet temperatures: $p=100$ atm, $T_{H_2}=300$ K. 168

Figure 8.1: Thermodynamic and transport properties of oxygen validated against NIST data. Lines: the present scheme; symbols: NIST data. 173

Figure 8.2: Thermodynamic and transport properties of methane validated against NIST data. Lines: the present scheme; symbols: NIST data. 174

Figure 8.3: Distributions of thermophysical properties in the axial direction. Oxygen/methane system with $p=100$ atm, $T_{O_2}=120$ K, $T_{CH_4}=300$ K, and $a=90$ s^{-1}. .. 175

Figure 8.4: Distributions of temperature, species mass fractions, and heat-release rate in the mixture fraction space. Oxygen/methane system with with $p=100$ atm, $T_{CH_4}=300$ K, and $a=1000$ s^{-1}. 176

Figure 8.5: Effects of oxygen inlet temperatures on extinction properties, (a) strain rate; (b) maximum flame temperature. Oxygen/methane system with $T_{CH_4}=300$ K..... 176

Figure 8.6: Distributions of temperature and mass fractions of methane and oxygen at different pressures. Oxygen/methane system with $T_{O_2}=T_{CH_4}=300$ K, and $a=1000$ s^{-1}. 177

Figure 8.7: Distributions of temperature and species mass fractions at different pressures in the mixture-fraction space. Oxygen/methane system with $T_{O_2}=T_{CH_4}=300$ K, $a=1000$ s-1. 179

Figure 8.8: Effects of flow strain rate on maximum flame temperature at different pressures. Oxygen/methane system with $T_{O_2}=T_{CH_4}=300$ K. 180

Figure 8.9: Effects of pressure on strain rate and maximum temperature at extinction. Oxygen/methane system with $T_{O_2}=T_{CH_4}=300$ K. 180

Figure 8.10: Flame response along the S-curve for oxygen/hydrogen and oxygen/methane systems at $p=50$ atm with $T_{O_2}=T_{H_2}=T_{CH_4}=300$ K. 182

Figure 8.11: Distributions of temperature and species mass fractions at the extinction point in the pressure range of 1-150 atm. Oxygen/methane system with $T_{O_2} = T_{CH_4} = 300$ K..... 183

Figure 8.12: Distributions of global heat-release rate as a function of strain rate in the pressure range of 1-150 atm. Oxygen/methane system with $T_{O_2} = T_{CH_4} = 300$ K 185

Figure 8.13: Scaled heat-release rate q as a function of normalized strain rate (a/a_{ext}). Oxygen/methane system with $T_{O_2} = T_{CH_4} = 300$ K. (a) $q = q/\sqrt{pa_{ext}}$; (b) $q = q/p^{0.536}\sqrt{a_{ext}}$ 186

Figure 8.14: Flame thickness as a function of strain rate in the pressure range of 1-150 atm. Oxygen/methane system with $T_{O_2} = T_{CH_4} = 300$ K. 188

Figure 8.15: Scaled flame thickness $\hat{\delta} = \delta\sqrt{pa_{ext}}$ as a function of normalized strain rate (a/a_{ext}). Oxygen/methane system with $T_{O_2} = T_{CH_4} = 300$ K..... 189

Figure 8.16: Compressibility factor of n-heptane at different pressures and temperatures. 190

Figure 8.17: Distributions of temperature and mass fractions of major species. Oxygen/n-heptane system with *p*=10 atm, $T_{O_2} = T_{C_7H_{16}} = 800$ K, and *a* = 1000 s-1. 191

Figure 8.18: Effects of inlet temperature on flame maximum temperature, flame thickness, and heat-release rate at different pressures for oxygen/n-heptane system..... 192

Figure 8.19: Distributions of the heat-release rate and flame thickness as a function of strain rate in the pressure range of 1 to 200 atm. Oxygen/n-heptane system with $T_{O_2} = T_{C_7H_{16}} = 800$ K. 193

Figure 8.20: Compressibility factors of (a) $C_{12}H_{26}$ and (b) $C_{16}H_{34}$ at different pressures and temperatures. 194

Figure 8.21: Maximum flame temperature, flame thickness, and heat-release rate as a function of number of carbons in the n-alkane fuel molecule. Oxygen/hydrogen and oxygen/n-alkanes systems with *p* = 10 atm, $T_{O_2} = T_{Fuel} = 800$ K, and *a* = 1000 s-1. 196

Figure 8.22: Flame thickness parameter ($C = \delta\sqrt{pa}$) as a function of number of carbons in the n-alkane fuel molecule. Oxygen/hydrogen and oxygen/n-alkanes systems with *p* = 10 atm, $T_{O_2} = T_{Fuel} = 800$ K, and *a* = 1000 s-1..... 197

LIST OF SYMBOLS AND ABBREVIATIONS

a	flow strain rate
D	mass diffusivity
Da	Damköhler number
dip	dipole moment
E	specific total energy
e	specific internal energy
f	mixture fraction
h	specific enthalpy
k_l	reaction rate constant
m	mass flow rate
N	total number of species
p	pressure
Pr	Prandtl number
q	heat release rate
q_i	heat flux in the direction of i
R_u	universal gas constant
SGS	subgrid scale
Sc	Schmidt number
t	physical time
u	velocity component
$U_{k,j}$	diffusive velocity of species k in j direction
MW	molecular weight
x	physical coordinate

Y_k	mass fraction of species *i*
Z	compressibility factor

Greek Symbols

ρ	density
ρ_i	density of species *i*
σ	stress tensor
τ	viscous stress tensor
δ	Dirac delta
μ	molecular dynamic viscosity
ν_t	turbulent eddy visocisty
λ	thermal conductivity
$\dot{\omega}_k$	mass production rate of species *k*
χ	scalar dissipation rate

Subscripts

ign	ignition
ext	extinction
i, j, k	dummy indexes
ci	critical properties of species *i*

SUMMARY

Substantial experimental and numerical efforts on the characterization of propellant injection, mixing, and combustion processes at near- and super-critical conditions have recently led to improved understanding of the intrinsic mechanisms involved. Most existing studies, however, have been focused on shear coaxial injectors with light fluids, such as hydrogen and methane, as fuel. The situation with swirl injectors using kerosene, such as those broadly used in Russian rocket engines like the RD-0110, RD-107/108, and RD 170/180, has not been explored in detail. These engines operated at pressures much higher than the critical pressures of propellants, leading to the extreme nonlinearity and complexity of physical phenomena and therefore severe challenge to experimental diagnostics and numerical simulations.

In this dissertation, we establish a unified theoretical and numerical framework, which deals with supercritical flows and combustion over the entire range of fluid thermodynamic states of concern. Turbulent closure is achieved using the large-eddy-simulation (LES) technique. A steady laminar flamelet approach is implemented to model turbulence/chemistry interactions. Thermodynamic properties, including density, enthalpy, and specific heat at constant pressure, are evaluated according to the modified Soave-Redlich-Kwong equation of state and fundamental thermodynamic theories. Transport properties, including thermal conductivity and dynamic viscosity, are estimated according to an extended corresponding-state principle. The numerical scheme is preconditioned along with a dual-time-stepping integration using finite-volume approach. Finally, a multi-block domain decomposition technique associated with the message passing interface of parallel computing is applied to facilitate computational speed.

The ensuing framework is first applied to study the three-dimensional flow dynamics of a liquid oxygen swirl injector at supercritical pressure. The complex flow

structures are visualized and explored for the first time. A fluid transition region is defined to distinguish dense fluid from light gas at supercritical pressure according to density-temperature property diagram. This transition region becomes broader with increasing pressure but degenerates into a sharp interface at subcritical pressure. Various mechanisms dictating the flow evolution, including Kelvin-Helmholtz instability, centrifugal instability, center-recirculating flow, helical instability, and their interactions are studied using the spectral analysis and proper orthogonal decomposition technique. The longitudinal hydrodynamic instability is found to play a dominant role in the oscillatory flowfield. The helical mode is amplified and resonant with the acoustic wave at the characteristic frequency of 4.8 kHz. A parametric study is made to examine the pressure and temperature effects on the injector performance, such as film thickness and spray cone angle. The results are also compared to predictions from classical hydrodynamics theories to acquire direct insight into the flow physics involved.

Next, the mixing and combustion characteristics of liquid oxygen (LOX)/kerosene bi-swirl injectors are investigated under a supercritical condition typical of contemporary rocket engines. Emphasis is placed on the near-field flow and flame development downstream of the inner swirler. The flame is stabilized by two counter-rotating vortices in the wake region of the LOX post that is covered by the kerosene-rich mixture. Various geometric parameters, including the recess length, LOX post thickness, and kerosene annulus passage, are examined to explore their influence on mixing and combustion dynamics. The recess region advances the interaction of LOX and kerosene and thus improves the mixing efficiency. A larger post thickness results in a higher spreading angle of the LOX film and intersects the kerosene film, thereby facilitating mixing in the recess region. The width of the kerosene annulus passage significantly affects the flow evolution; a wider passage increases the spreading angle of the liquid film and advances the center-recirculating zone to an upstream location. Increasing the annulus width or post thickness might induce the initially lifted-off flame to attach to the injector post surface. This flame

attachment could increase the heat flux from hot products to the post surface. In order to achieve the optimal injector performance, future studies have to be performed to determine values of the group of recess length, post thickness, and kerosene annulus width.

Counterflow diffusion flames of general fluids are also studied using a unified framework, which is capable of capturing ignition and extinction characteristics in a wide range of pressures. An improved two-point flame-controlling continuation method is employed to solve the singularity problem at the turning points on the flame-response curve (the S-curve). Both oxygen/hydrogen and oxygen/hydrocarbon mixtures are systematically investigated over a pressure range of 0.5-200 atm. General similarities are developed in terms of flame temperature, species concentrations, flame thickness, and heat-release rate for all pressures under consideration. This suggests that the flame behaviors at high pressure can be evaluated by their counterpart at low pressure. The common features for the n-alkane family are identified. The flame properties of a given hydrocarbon fuel can be predicted from those of another hydrocarbon fuel at the same flow conditions. Tabulation of pressure-dependent flame properties can be achieved by mapping the flame solution at a given pressure, according to the correlations in the normalized strain-rate space, even if the extinction strain rate is not available beforehand. This will significantly improve computational efficiency for combustion models using tabulated chemistry, such as the flamelet, FGM, and FPI models.

CHAPTER 1

INTRODUCTION

1.1 Background and Motivation

Understanding the fundamental physicochemical mechanisms associated with mixing and combustion of cryogenic propellants in a supercritical environment, in which both the pressure and temperature exceed the thermodynamic critical states, have long been matters of serious practical concern in combustion science and technology [1, 2], mainly due to the necessity of developing high-pressure combustion devices, such as liquid-propellant rocket, gas turbine, and diesel engines. The liquid fuels and/or oxidizers are usually delivered by an injector assembly to combustion chambers at a subcritical temperature, which then undergo a sequence of processes at pressure and temperature levels well above the thermodynamic critical points of the substances as shown in Table 1.1. Here LOX represents liquid oxygen. Under these conditions, the propellants are heated and transit into the supercritical state. The mixing and combustion processes exhibit many features distinct from those under subcritical conditions, thereby rendering conventional approaches developed for the devices operating at low pressures invalid.

Table 1.1: Propellants and chamber operating conditions for selected LREs

Engines	*SSME*	*RD-170*	*Vulcain 2*
Propellants	LOX/H_2	LOX/Kerosene	LOX/H_2
Chamber Pressure (MPa)	20.6	24.5	11.7
Chamber Temperature (K)	3700	3676	3500
Thrust at sea level, (MN)	1.78	7.55	0.9
Specific Impulse (Vacuum)	453	338	431
Burning Time (seconds)	480	150	600

Table 1.1 shows three representative contemporary rocket engines, which operate at supercritical conditions. Table 1.2 lists the critical temperature and pressures of typical propellants for the reference. Successful missions require very high engine reliability, energy efficiency, and pose severe challenges to the design of the Thrust Chamber Assembly. Combustion instability has been recognized as one of the most challenging difficulties encountered in the development of liquid rocket engines [3]. In spite of extensive research on this subject, current understanding is not sufficient to support combustor design and optimization. Most of the engine developments relied on an expensive and time-consuming trial and error process. A successful design for one application may fail in another due to subtle difference in system characteristics or operating conditions.

Table 1.2: critical properties of typical pure substance

Propellants	*O_2*	*H_2*	*CH_4*	*H_2O*	*CO_2*	*He*	*N_2*	*RP-1*
T_c (K)	154.6	32.97	190.5	647	304.3	5.19	126.2	662.0
P_c (MPa)	5.04	1.29	4.60	22.1	7.38	0.23	3.39	2.17

Recent advances in modeling and simulations make it possible to examine important physicochemical processes of a candidate design and provide guidance in design optimization. With the assistance of appropriate numerical and analytical tools, substantial cost reduction in sub-scale and full-scale tests can be achieved to help develop next generation of liquid rocket engines with better performance and higher reliability. Thus, it is necessary to establish a unified theoretical and numerical framework, upon which the effects of known processes and design attributes can be studied and assessed by advanced modeling and simulation techniques.

Modeling high-pressure mixing and combustion processes numerically poses an array of challenges that include all of the classical closure problems in turbulent reacting flows and a unique set of problems caused by the introduction of thermodynamic non-

idealities and transport anomalies. The flow Reynolds number increases with pressure, and Kolmogorov scale decreases with Reynolds number according to Kolmogorov universal equilibrium theory. This scale reduction has a direct impact on flow evolution and raises the computational load to resolve key flow processes. Furthermore, near the critical point, propellant mixture properties exhibit liquid-like densities, gas-like diffusivities, and pressure-dependent solubilities. Surface tension and enthalpy of vaporization approach zero, and isothermal compressibility and specific heat increase significantly. These phenomena, coupled with extreme local property variations, have a significant impact on the evolutionary dynamics exhibited by a given system.

The complexity of the problem outlined above is numerically demanding, and a variety of uncertainties exist with regard to closure. This dissertation represents an attempt to address key issues related to modeling and understanding fluid dynamics and underlying fundamental physicochemical processes at supercritical conditions.

1.2 Literature Review

1.2.1 High-Pressure Fluid Injection, Mixing, and Combustion

Jet Injector

Researchers and scientists in Europe and the United States have conducted many studies on cryogenic fluid injection under supercritical conditions. Because the rocket engines developed in these countries primarily implement impinging jet injectors (F-1 engine for the Saturn V) or shear coaxial injectors (SSME and Vulcain engine). Extensively experimental studies were conducted to visualize the flow and flame structures using optical diagnostic techniques, including shadowgraph, excited CH, OH chemiluminescence, and planar laser induced fluorescence (PLIF) of OH. The extreme operating conditions and working environment of contemporary rocket engines pose severe challenges on experimental measurements. In spite of limitations of flow visualization and

data acquisition techniques, experimental efforts on the characteristics of propellant injection, mixing, and combustion processes at near-critical conditions have led to a better qualitative understanding of the fundamental mechanisms involved [4-8] in the last few decades.

It was found that shear-coaxial injection processes in liquid rocket engines exhibit two distinct modes of combustion. At subcritical pressures, injected liquid jets undergo the classical cascade of processes associated with atomization. Dynamic forces and surface tension promote the formation of a heterogeneous spray that evolves continuously. As a consequence, spray flames are formed and lifted away from the injector post in a manner consistent with the combustion mechanisms exhibited by local drop clusters. As the chamber pressure approaches or exceeds the critical pressure of a particular propellant, however, injected liquid jets undergo a transcritical change of state as interfacial fluid temperatures rise above the critical temperature of the local mixture. For this situation, diminished inter-molecular forces promote diffusion-dominated processes prior to atomization, and jets vaporize in the presence of exceedingly large thermophysical gradients. Well-mixed diffusion flames evolve and are anchored by small but intensive recirculation zones that exist in the shear-layers between adjacent propellant streams.

In parallel to experimental studies, attempts were made both theoretically and numerically to explore the underlying mechanisms of high-pressure fluid mixing and combustion. Oefelein and Yang [9] modeled two-dimensional mixing and combustion of oxygen and hydrogen streams at supercritical conditions using large-eddy-simulation technique and outlined the fundamental difficulties associated with modeling mixing and combustion processes at near-critical conditions. Zong et al. [10] conducted a comprehensive numerical study of nitrogen injection and mixing under supercritical conditions. The model accommodates full conservation laws and general-fluid thermodynamics and transport phenomena. All the thermophysical properties were evaluated directly from fundamental thermodynamics theories over the entire regime of

fluid states of concern. Furthermore, a unified treatment of numerical algorithms based on general fluid thermodynamics was established to improve computational accuracy and efficiency.

Oefelein [11] studied the thermal characteristics of oxygen/hydrogen shear-coaxial jet flames at supercritical pressure. Significant real-gas effects and transport anomalies occurs in colder regions of the flow, while ideal-gas thermodynamic and transport characteristics are dominant in the flame zone. The flame anchors itself in the interfacial region of high shear between the liquid oxygen core and annular hydrogen jet as shown in Fig. 1.1. The vortical expansion of low-density hydrogen stream induces strong recirculating backflow in the vicinity of the LOX-post. Inside this recirculation zone is an unsteady stagnation point that provides the flame-holding mechanism. Zong and Yang [12] later studied near-field and flame dynamics of LOX/methane shear-coaxial injectors. The LOX/methane flame is anchored between two counter-rotating wake recirculating zones, unlike LOX/hydrogen flame close to the LOX jet boundary because of high-diffusivity of hydrogen.

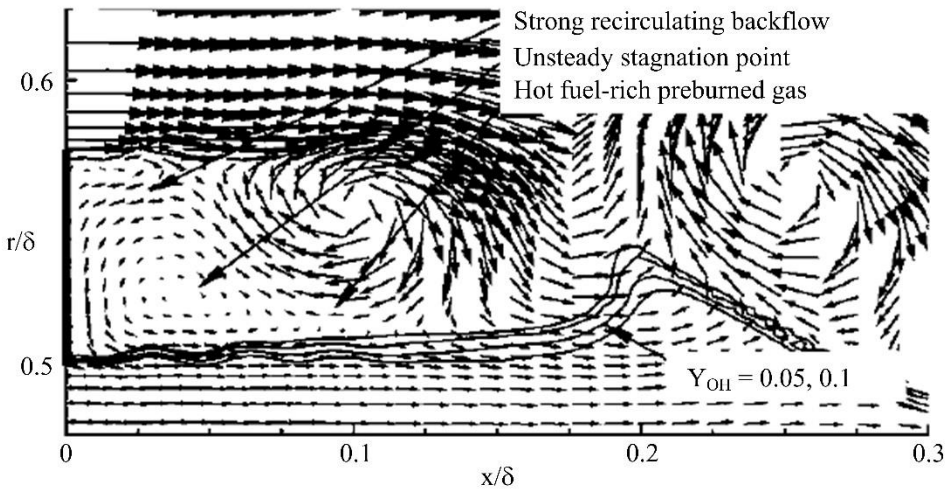

Figure 1.1: Schematic of flame-holding mechanism for oxygen-hydrogen shear-coaxial injection.

The extinction limits of the flame generated around the LOX jet boundary were studied by Juniper et al. [13] by constructing a one-dimensional counterflow diffusion flame model. The results indicated that the flame was fairly stable in the near injector region and could not easily be extinguished by the strain rate, even at a very low hydrogen stream temperature. Since the typical strain rates encountered in rocket engines were insufficient to punch a hole in the flame, the edge of this diffusion flame sheet should be stabilized behind the lip of the LOX post. Following this suggestion, a two-dimensional simulation was performed to investigate the flame stabilization mechanism behind a step over a liquid reactant surface [14]. It was reported that the most influential parameter regarding flame stabilization was the height of the step with respect to the flame thickness. If the flame was thicker than the step, it could not remain in the recirculation zone behind the step and was readily blown off.

Masquelet et al. [15] simulated the LOX/H_2 combustion in a subscale muti-injector liquid rocket engine. A sub-grid eddy break-up (EBU) model was used to limit chemical reaction rates with a mixing rate dependent on the dissipation rate of turbulent eddies. Heat flux along the chamber wall showed deviation from experiment measurements. Masquelet and Menon [16] later studied the GOX/GH_2 combustion of a single-element shear coaxial injector. Chemical reactions were calculated directly from the resolved temperature and species, without consideration of turbulence/chemistry interactions. The three-dimensional results captured the trend of heat flux profile of the experimental data, and were much better compared to their two-dimensional cases.

Swirl Injectors

Swirl injectors have recently drawn increasingly attention in the rocket community in US to achieve efficient mixing and combustion in many propulsion and power-generation systems [17, 18], especially those developed in Russia. The swirling motion can improve flame stability by producing toroidal recirculation zones and reduce combustion

length by inducing high rates of the ambient fluid entrainment and fast mixing [19, 20]. Design of injectors highly affects the occurrences of combustion instability in the combustion chamber, because all feedback couplings of combustion chamber with other engine components take place through the injection process [21, 22].

Compared to jet injectors, swirl injectors in liquid-propellant rocket engines distinguish themselves in several aspects [23]. First, the non-uniform mixing of propellants in the jet core region is avoided and the intraelement mixing is significantly improved because of the outward spreading of the liquid spray. High mixing efficiency is, thus, possible even for a large injector flowrate. Second, the large flow passage in a swirl injector renders the atomization characteristics to be less sensitive to manufacturing errors. The injector is also less susceptible to choking and cavitation. Third, the injected fluid is discharged into the chamber as a hollow spray cone. The thickness of the liquid film becomes thinner as it swirls and spreads outward. Most existing studies [24-27] on swirl injectors has focused on liquid film thickness, spray cone angle, liquid sheet breakup, and mixing efficiency under various controlling parameters such as backpressure and recess length. The fluid dynamics inside swirl injectors have been much less investigated.

Bazarov and Yang [21] applied linear theory to study the dynamics of swirl injectors and showed that the overall response function of a swirl injector can be represented by transfer characteristics of each individual element of the injector, the coupling of pressure and velocity pulsations in the tangential entries causes not only fluctuations of liquid free surface propagating at the speed of axial velocity component, but the energy disturbance in the form of fluctuations of circumferential velocity component propagating through the entire liquid layer in both the radial and axial directions. Richardson et al. [28] implemented a nonlinear model based on the boundary element method to evaluate the dynamic response of swirl injectors and compared their computational results with those of the linear theory [21]. Ismailov and Heister [29, 30] performed both analytical linear theory and nonlinear numerical computations to

investigate wave reflection and resonance inside the swirl injector using abrupt convergence resonance model and conical convergence resonance model. Injector responses at resonant conditions behave as a quarter-wave oscillator. The dimensions of vortex chamber and mass flow rates have strong effects on injector responses, while the nozzle convergence angle and nozzle length have negligible effects on injector responses.

The above studies were studied under inviscid flow conditions. The pressure and temperature of working fluids were not explicitly specified. Thermodynamic properties of injection fluids and their variations at various pressures and temperatures were also not taken into account. Liquid rocket engines normally operate at pressures much higher than critical pressures of liquid propellants, hence accurate property evaluations are critical in numerical simulations. Cho et al. [31] conducted an experimental study on surface instability of cryogenic nitrogen swirling flow at both sub- and supercritical conditions. They found the different mechanisms of flow instability between cryogenic fluids and water swirl flows. The former is dominated by precessing vortex core (PVC) in the center-recirculation zone (CTRZ) while the latter is caused by Kelvin-Helmholtz instability. For the nitrogen swirling flow, the phase change and subsequent density change differs and flow characteristics, such as the behavior of the downstream flow, spray angle, wavelength, and propagation velocity, change dramatically when the ambient pressure varies from subcritical to supercritical conditions.

Zong and Yang [32] first studied cryogenic fluid dynamics of swirl injectors at supercritical conditions. Liquid oxygen (LOX) was injected tangentially into a simplex swirl injector and mixed with gaseous oxygen in the chamber in the two-dimensional axisymmetric flow configuration. The internal flow pattern was divided into three different regimes with distinct characteristics, developing, stationary, and accelerating regimes. Hydrodynamic instabilities in the LOX, acoustic waves in the gaseous core, shear layer instabilities, and center recirculation zone induced by sudden expanding swirling film at the injector exit were identified and analyzed comprehensively. Huo et al. [33] further

extended the study by imposing external forcing to pulsate the mass flow rate at the tangential inlet. External forcing drives the flow to fluctuate at its forcing frequency and suppresses other frequencies of fluctuations generated by the original non-pulsated flow. However, these axisymmetric studies failed to provide azimuthal variations of flow properties and three-dimensional vortex-stretching mechanism. The propagation of hydrodynamic waves in azimuthal direction was thus not included. Huo et al. [34] have shown that the importance of three-dimensional flow effects in the swirl injector, which motivates the present study.

Understanding the dynamics of swirling fluid injection is a prerequisite of exploring flow physics and flame dynamics of swirl coaxial injectors, which are actually encountered more frequently in practical applications. Various injector parameters and chamber conditions have been examined to explore the injector mixing and combustion characteristics [35-40]. Sasaki et al. [35] performed a cold experiment of water/nitrogen swirl coaxial injectors at room conditions. Special attention was given to the effect of the center post recess, which tends to narrow the spreading angle and cause a deformation of the spray cone. Han et al [36] investigated the recess effects of the center element on the mixing characteristics of a swirl coaxial injector using water and kerosene. Four different recess numbers in the range of 0.71-1.37, defined as the ratio of the recess length to the post thickness, were considered. The mixing efficiency and propellant mass distribution were found to be very sensitive to the recess length. The Sauter mean diameter decreases slightly with increasing recess length and can be correlated with the empirical equations.

The aforementioned studies were conducted at low pressures without considering the effects of the elevated pressures typically encountered in operational liquid-propellant rockets engines. And most existing studies at high pressures have been focused on shear coaxial injectors using simple fluids, hydrogen and methane as fuel propellant. The investigation of swirl coaxial injectors using kerosene, which have been broadly used in

Russian rocket engines such as Rd-0110 and RD-107/108, are less-well documented in terms of experiments and numerical simulations.

Kim et al. [41] showed that as the recess length of injector post for a liquid oxygen (LOX)/kerosene bi-swirl injector increases the mechanism of propellants' mixing shifts from external mixing to internal mixing. The latter mechanism significantly improves the mixing and combustion efficiency. Ahn et al. [42, 43] conducted a set of experiments to study combustion characteristics of LOX/kerosene bi-swirl coaxial injectors at near-critical and transcritical conditions. They found that the longer injector recess promotes the interactions of propellants and improves combustion performance, and that the injector recess scarcely affects the pressure fluctuation at supercritical pressure while it might induce strong low-frequency combustion instability at subcritical pressure. The lack of flow visualization and enough data in these experimental studies restricts our understanding on detailed flame dynamics and flame-holding mechanism for swirl coaxial injectors at supercritical pressure.

1.2.2 Counterflow Diffusion Flames of General Fluids

High-pressure cryogenic propellant combustion in liquid rocket engines poses various scientific and technological difficulties, including injection optimization, ignition, flame stabilization, and combustion instabilities. The whole process is so complicated that its mechanism cannot be thoroughly understood without extensive theoretical and experimental works on simplified configurations under well-controlled conditions.

Laminar counterflow flames have been extensively studied by means of analytical, experimental, and numerical techniques, and flame behaviors and burning properties have been characterized for a wide variety of fuel and oxidizer combinations under a broad range of flow conditions[44, 45], due to their geometrical simplicity. When the flame temperature or burning rate (or any variable that characterizes the completeness of reactions, such as mass fractions of major combustion products) of a reactive system is plotted as a function

of the corresponding Damköhler number (or any variable that measures the strength of external flow stretching, such as the strain rate or scalar dissipation rate), an S-shaped relationship, commonly known as an S-curve, is obtained. This phenomenon can be attributed to the exponential dependence of the chemical reaction rate on temperature [46, 47]. Here, the Damköhler number is defined as the ratio of the flow time scale to the chemical time scale. An S-curve covers all the possible steady chemical states that a given reacting mixture can achieve. It also reflects the response of a given chemical state to changes in the local aerothermal condition in a flame zone. An S-curve can thus be used to characterize the evolution of a flame subject to continually varying flow conditions, including ignition, extinction, and instability [48, 49].

Figure 1.2 shows a schematic diagram of an S-curve. The zero Damköhler number (*Da*) condition represents the frozen limit, corresponding to pure mixing of reactants. Along the lower branch (the weakly reacting flow branch), the chemical reaction rate increases with the *Da* number. Ignition occurs at $Da = Da_{ign}$, where the heat generation exceeds the heat loss in a steady state [46]. The flame temperature increases suddenly and takes a value in the upper branch. The reaction-sheet limit is attained as the *Da* number approaches infinity. When the *Da* number is progressively decreased along the upper branch, the flame is extinguished at $Da = Da_{ext}$. Along the unstable middle branch, the flame temperature decreases with increasing *Da* number, a situation considered unphysical. The S-curve becomes monotonic, with a unique solution when the activation energy is smaller than a critical value [50]. Such a condition, however, is unlikely to occur in most practical systems, because of the large activation energies for common fuels.

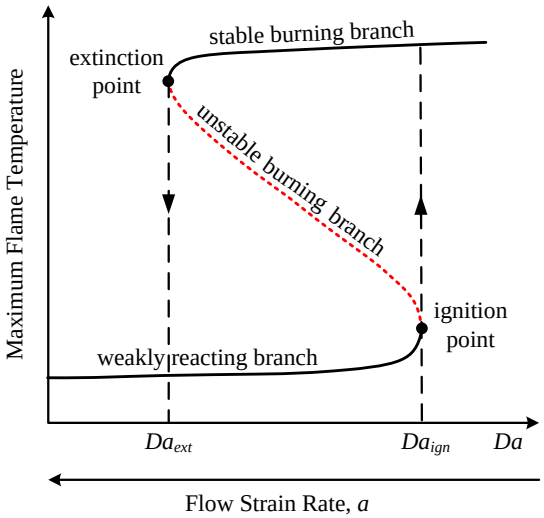

Figure 1.2: Schematic diagram of a folded S-shaped flame response

Linan [50] performed an asymptotic analysis of counterflow diffusion flames using a one-step reaction mechanism over various segments of the S-curve: the frozen ignition regime, the partial burning regime, the premixed flame regime, and the near-equilibrium regime. Numerical methods were later developed to study one-dimensional counterflow flames with detailed chemical mechanisms [51-53]. These studies, however, focused only on the upper branch of the S-curve. Giovangigli and Smooke [54] applied the arc-length continuation method of Keller [55] in flame calculations to solve the singularity problem at the extinction point, and generated a complete S-curve. An alternative method, known as the flame-controlling method, was proposed by Nishioka et al. [56] to treat the same problem. Recently, the FlameMaster code [57] and the CHEMKIN-PRO package [58], using the arc-length approach and the flame-controlling method, respectively, were developed to study the flame response throughout the entire S-curve. Those studies, however, were carried out at room conditions based on an ideal-gas assumption.

Many practical combustion devices operate at pressures well above the thermodynamic critical points of injected fuels [1]. Ribert et al. [59] incorporated general fluid properties into an existing code (DMCFs) [60] to investigate counterflow diffusion

flames of hydrogen and oxygen in the pressure range of 10-250 atm. Both subcritical and supercritical conditions for the steady-burning branch of the S-curve were considered. Phenomenological dependence of the heat release rate on pressure and strain rate was established in the form of $q \sim \sqrt{pa}$. Cryogenic inlet temperatures were also discussed for a fixed pressure and strain rate, and the pressure dependence of the extinction strain rate was explored.

Recently, Lacaze and Oefelein [61] have performed two-dimensional simulations of opposed jet flames of oxygen and hydrogen at supercritical pressures. Results were benchmarked against those in Ref. [15]. Similar observations were made of the effects of inlet temperature, pressure, and strain rate on the flame properties. Supercritical flames in the pressure range of 53-90 atm with strain rates of 5×10^4 - 5×10^6 s^{-1} were found to exhibit very limited variation in flame temperature (±3%) and major species profiles in the mixture-fraction space. A chemistry tabulation model was developed to reproduce the flame results with detailed chemistry. The studies described here ([59] and [61]) considered only the upper branch of the S-curve. The extinction point was not identified, due to numerical challenges. No flame solution beyond the extinction point was obtained, and the behavior of the unstable burning branch of the S-curve was not investigated.

Existing studies of high-pressure counterflow diffusion flames mainly focus on the oxygen/hydrogen system. Limited attention has been given to hydrocarbon fuels, which are used for a vast majority of combustion devices, including gas-turbine, liquid-rocket, and diesel engines. Pons et al. [62] studied the pressure effects of oxygen/methane flames. A fast-chemistry assumption was applied to derive scaling factors for characterizing flame properties. The analysis employed ideal-gas thermophysical properties with supercritical inlet temperatures. Pons et al. [63] later studied mass transfer and combustion in transcritical non-premixed oxygen/methane counterflows. Real-fluid properties were employed by extending the standard Chemkin package to the transcritical regime. The flame was established in the light-gas region adjacent to the sharp density gradient in the

transcritical zone. The work only considered the effect of inlet temperature on the flame structure at a pressure of 7 MPa under stable burning conditions. A more complete investigation of the flame behaviors, including extinction characteristics, is needed for a broad range of pressures and strain rates.

Heavy hydrocarbon combustion with air in a counterflow setting has been the subject of many studies. Li and Williams [64] performed both experimental and numerical investigations of diffusion and partially-premixed air/n-heptane flames. It was concluded that a reduced mechanism of 36 species and 180 reactions is insufficient for accurate prediction of intermediate species. Seiser et al. [65] explored the extinction and auto-ignition of n-heptane counterflow flames at atmospheric conditions. The effect of strain rate was found to be more influential on the low-temperature chemistry than on the reactant temperature. Efforts were also made to develop more detailed chemical mechanisms for n-heptane oxidation. Curran et al. [66] developed a comprehensive mechanism consisting of 556 species and 2540 reversible reaction steps, which was verified for pressures up to 42 atm. This mechanism was further modified and extended for C_8-C_{16} normal alkanes [67], and will be used in the present work. Most of previous studies operated at either low pressures or low strain rates for diluted fuel and air. Furthermore, reduced chemical mechanisms were often employed. A systematic investigation into the flame properties under a wide range of flow conditions is yet to be performed.

1.3 Research Objectives

The primary objective of this dissertation tends to improve the understanding of the fundamental processes of cryogenic swirling fluid injection, mixing, and combustion of LOX and kerosene under supercritical conditions using large eddy simulation. The theoretical model is based on full-conservation laws of mass, momentum, energy, and species, and accommodates real-fluid thermodynamics and transport phenomena over the

entire range of fluid states of concern. The work will be decomposed into three parts: LOX swirling flow injection, LOX/kerosene mixing, and LOX/kerosene combustion.

The complex three-dimensional flow structures and dynamics of LOX swirling flow are explored for the first time using the spectral analysis and proper orthogonal decomposition technique at supercritical conditions. LOX at a subcritical temperature is injected into a supercritical environment. Various underlying mechanisms dictating the flow evolution, including Kelvin-Helmholtz instability, centrifugal instability, center-recirculating flow, helical instability, and their interactions are studied. A parametric study is performed to examine the pressure and temperature effects on the injector design attributes, such as film thickness and spray cone angle.

The mixing and atomization characteristics of LOX/kerosene swirl coaxial injectors at supercritical conditions are investigated using the geometric prototype of RD0110 rocket engine. Both LOX and kerosene are injected at a subcritical temperature. The different behaviors of flow evolution and liquid film breakup will be recognized at supercritical conditions. Various geometric parameters, including recess region, post thickness, and kerosene annulus width, are examined to explore their influence on mixing efficiency and flow dynamics. Important information of selection criteria of injector design attributes will be provided for the optimum injector performance.

The combustion characteristics of LOX and kerosene swirl coaxial injectors are numerically investigated with operating conditions encountered in contemporary liquid-propellant rocket engines using large-eddy-simulation technique along with laminar flamelet library approach. The emphasis is placed on the region just downstream of the injector element. The flame-holding mechanism are discussed in detail. The influence of various geometric parameters, including recess region, post thickness, and kerosene annulus width, are further examined on combustion performance in terms of the capability to the thermal protection of the injector solid surface. The pressure fluctuation field is

explored in the combustion chamber near the recess region for different injector configurations.

Another objective of the current thesis is to explore the fundamental flame behaviors of general fluids in a counterflow configuration. A theoretical and numerical framework is established to study counterflow diffusion flames for general fluids over the entire thermodynamic regime. The formulation accommodates fundamental thermodynamics and transport theories, along with detailed chemical mechanisms. Both steady and unsteady burning branches of a complete flame-response curve (the S-curve) are considered. An improved two-point flame-controlling continuation method is employed to solve the singularity problem at the turning points on the S-curve. Both oxygen/hydrogen and oxygen/N-Alkane Hydrocarbons (CH_4-$C_{16}H_{34}$) flames are systematically investigated over a pressure range of 0.5 – 200 atm. The flow strain rate covers from a small value to extinction value. The general flame similarities in terms of flame temperature, flame thickness, species concentrations, reaction rates, and heat release rate, are explored in a normalized strain-rate space for the entire range of pressures under consideration.

1.4 Dissertation Outline

The dissertation is organized into 9 chapters. Chapter 2 describes the theoretical formulation of governing equations as well as auxiliary equations to close the problem. Chapter 3 presents the numerical framework, which is discretized using a preconditioned, density-based, finite-volume methodology. The overall numerical accuracy is second-order in time and fourth-order in space. Chapter 4 investigates the flow dynamics of LOX swirl injectors at supercritical pressure in a three-dimensional space, the underlying physics and flow instabilities are analyzed. Chapter 5 studies the cold-flow mixing characteristics of LOX and kerosene bi-swirl injectors with various geometries. This is followed by the study of combustion of LOX and kerosene in Chapter 6, in which the near-field flow and flame

development are discussed and the flame stabilization mechanism is identified. The suggestion is given for the selection of important injector design attributes to achieve the best performance. Chapters 7 and 8 systematically investigate counterflow diffusion flames of general fluids: oxygen/hydrogen and oxygen/n-alkanes hydrocarbon mixtures, respectively. Finally, the conclusions of this dissertation and recommendations for the future work are provided in Chapter 9.

CHAPTER 2

THEORETICAL FORMULATION

2.1 Governing Equations

The theoretical formulation is based on the full conservation equations of mass, momentum, energy, and species concentrations in Cartesian coordinate systems. In fluid mechanics, assuming continuum and negligible body forces, the differential form of Navier-Stokes equations are given by

$$\frac{\partial \rho}{\partial t} + \frac{\partial \rho u_i}{\partial x_i} = 0 , \tag{2.1}$$

$$\frac{\partial \rho u_i}{\partial t} + \frac{\partial (\rho u_i u_j)}{\partial x_j} = \frac{\partial \sigma_{ij}}{\partial x_j}, \quad (i = 1,\ 2,\ 3) \tag{2.2}$$

$$\frac{\partial \rho E}{\partial t} + \frac{\partial \left[(\rho E + p) u_i \right]}{\partial x_i} = -\frac{\partial q_i}{\partial x_i} + \frac{\partial (u_i \tau_{ij})}{\partial x_j}, \tag{2.3}$$

$$\frac{\partial \rho Y_k}{\partial t} + \frac{\partial \rho Y_k u_j}{\partial x_j} = \omega_k + \frac{\partial \left(\rho D_k \nabla_j Y_k \right)}{\partial x_j}, \qquad (k = 1,\ \ldots,\ N\text{-}1) \tag{2.4}$$

here *i*, *j*, and *k* are indexes of spatial coordinate, summation, and species. For a Newtonian fluid with Stokes' hypothesis, the viscous stress tensor, σ_{ij} in Eq. 2.2 is expressed as

$$\sigma_{ij} = -p\delta_{ij} + \tau_{ij} = -p\delta_{ij} + \mu \left(\frac{\partial u_i}{\partial x_j} + \frac{\partial u_j}{\partial x_i} \right) - \frac{2}{3} \mu \frac{\partial u_k}{\partial x_k} \delta_{ij} . \tag{2.5}$$

The Dufour effect, which is the heat flux due to concentration gradient, is generally very small and thus neglected in the current study. Then q_j in Eq. 2.3 is defined as

$$q_j = -\lambda \frac{\partial T}{\partial x_j} + \rho \sum_{k=1}^{N} \hat{h}_k Y_k U_{k,j} . \tag{2.6}$$

The specific total energy is defined as the sum of specific internal energy and kinetic energy, given by

$$E = e + \frac{u_j u_j}{2} \ , \tag{2.7}$$

where the specific internal energy is calculated from specific enthalpy, pressure, and density, given by

$$e = h - \frac{p}{\rho} \ , \tag{2.8}$$

where h is determined by the mixture concentration and partial-mass based enthalpies, $\hat{h}_k$, for which the definition will be given later.

$$h = \sum_{k=1}^{N} Y_K \hat{h}_k \ . \tag{2.9}$$

The chemical source term in Eq. 2.4 is determined from the selected chemistry kinetics. For an elementary reaction mechanism, with L-step reaction and N species,

$$\sum_{k=1}^{N} \nu'_{kl} x_k \underset{k_{bl}}{\overset{k_{fl}}{\rightleftharpoons}} \sum_{k=1}^{N} \nu''_{kl} \mathrm{x}_k, \quad l = 1, 2, \ldots, L \tag{2.10}$$

the reaction rate constants of the forward and backward reactions, k_{fl} and k_{bl}, may take the following form according to the modified Arrhenius's equation:

$$k_l(T) = A_l T^b \exp\left(-E_l / R_u T\right) \ . \tag{2.11}$$

The net production rate for each species in a multi-step mechanism is given by

$$\omega_k = MW_k \sum_{i=1}^{L} \left(\nu''_{kl} - \nu'_{kl}\right) \left[k_{fl} \prod_{k=1}^{N} [x_k]^{\nu'_{kl}} - k_{bl} \prod_{k=1}^{N} [x_k]^{\nu''_{kl}} \right], \ \mathrm{k} = 1, 2, \ldots, N. \tag{2.12}$$

In non-premixed combustion studies, mixture fraction is an important conserved variable and often used. The definition of mixture fraction is not unique. In a two-feed system, mixture fraction is simply defined as the ratio of the local mass originating from the fuel (denoted by 1) to total mass (with mass from the oxidizer stream denoted by 2),

$$Z = \frac{m_1}{m_1 + m_2} \ . \tag{2.13}$$

Although the definition based on Eq. 2.13 is straightforward, it becomes ambiguous when there are multiple inlets. In such a case, a more general definition based on elemental conservation is used. If a_{ij} denote the number of atoms of element j in a molecule of species i, then the mass of all atoms j in the system of interest is given by:

$$m_j = \sum_{k=1}^{N} \frac{a_{ij} MW_j}{MW_i} m_i \ . \tag{2.14}$$

Dividing Eq. 2.14 by the total mass, one has the mixture fraction of element j as:

$$Z_j = \frac{m_j}{m} = \sum_{k=1}^{N} \frac{a_{ij} MW_j}{MW_i} Y_i \ . \tag{2.15}$$

It is obviously that Z_j is a linear function of species, Y_i. Multiplying Eq. 2.4 by $a_{ij} MW_j / MW_i$ and summing over all the species, we have:

$$\frac{\partial \rho Z_k}{\partial t} + \frac{\partial (\rho u_j Z_k)}{\partial x_j} = \frac{\partial}{\partial x_j} \left(\rho D_k \frac{\partial Z_k}{\partial x_j} \right) . \tag{2.16}$$

The source term vanishes because of the conservation of chemical elements. If we assume that the mass diffusivity for all the species equal to D, the balance equation becomes

$$\frac{\partial \rho Z_k}{\partial t} + \frac{\partial (\rho u_j Z_k)}{\partial x_j} = \frac{\partial}{\partial x_j} \left(\rho D \frac{\partial Z_k}{\partial x_j} \right) . \tag{2.17}$$

For hydrocarbon fuels ($C_m H_n$), the coupling function can be defined as: (Burke and Schumann 1928):

$$\beta = \frac{Z_C}{m MW_C} + \frac{Z_H}{n MW_H} - 2 \frac{Z_O}{\nu'_{O_2} MW_{O_2}} \ , \tag{2.18}$$

where β is a conserved scalar. It can be normalized between 0 and 1 to obtain Bilger's (1988) definition of the mixture fraction:

$$f = \frac{Z_C / (mMW_C) + Z_H / (nMW_H) + 2(Y_{O_2,2} - Z_O) / (\nu'_{O_2} MW_{O_2})}{Z_{C,1} / (mMW_C) + Z_{H,1} / (nMW_H) + 2Y_{O_2,2} / (\nu'_{O_2} MW_{O_2})} \ . \tag{2.19}$$

From Eq. 2.17 and Eq. 2.19, one can get the transport equation for the mixture fraction:

$$\frac{\partial \rho f}{\partial t} + \frac{\partial (\rho u_j f)}{\partial x_j} = \frac{\partial}{\partial x_j}\left(\rho D \frac{\partial f}{\partial x_j}\right) . \tag{2.20}$$

2.2 Simplified Equations for Counterflow Configuration

Figure 2.1 shows the physical model of a counterflow diffusion flame produced by two opposed fluid jets issuing from two circular nozzles [59, 61]. The configuration produces an axisymmetric laminar flowfield with a stagnation plane in the middle. The theoretical formulation for this type of flames has been well established for ideal gases [54, 56]. The present study extends previous analyses by incorporating general-fluid thermodynamics and transport theories, such that a unified framework can be constructed to treat the flame response for real fluids over a complete S-curve, including both the steady- and unstable-burning branches.

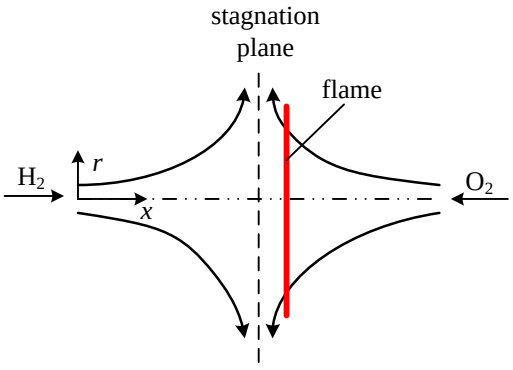

Figure 2.1: Schematic diagram of a counterflow diffusion flame.

The governing equations for steady-state axisymmetric problems in cylindrical coordinates are simplified as:

Continuity:

$$\frac{\partial}{\partial x}(r\rho u)+\frac{\partial}{\partial r}(r\rho v)=0 \tag{2.21}$$

Axial-momentum:

$$\frac{\partial}{\partial x}(r\rho uu)+\frac{\partial}{\partial r}(r\rho uv)=\frac{\partial}{\partial r}(r\tau_{rx})+r\frac{\partial \tau_{xx}}{\partial x}-r\frac{\partial p}{\partial x} \tag{2.22}$$

Radial-momentum:

$$\frac{\partial}{\partial x}(r\rho uv)+\frac{\partial}{\partial r}(r\rho vv)=\frac{\partial}{\partial r}(\tau_{rr})+r\frac{\partial \tau_{rx}}{\partial x}-r\frac{\partial p}{\partial r} \tag{2.23}$$

Energy:

$$\frac{\partial}{\partial x}(\rho uh)+\frac{1}{r}\frac{\partial}{\partial r}(r\rho vh)=-\left(\frac{\partial}{\partial x}(uq_x)+\frac{1}{r}\frac{\partial}{\partial r}(rvq_r)\right)+\phi \tag{2.24}$$

Species:

$$\frac{\partial}{\partial x}(\rho uY_k)+\frac{1}{r}\frac{\partial}{\partial r}(r\rho vY_k)+\dot{m}''_{k,diff}=MW_k\omega_k \tag{2.25}$$

A stream function, $\psi \equiv r^2F(x)$, which satisfies the continuity equation, is employed to reduce the governing equations to a set of ordinary differential equations [52].

$$\frac{\partial \psi}{\partial r}=r\rho u=2rF \tag{2.26}$$

$$\frac{\partial \psi}{\partial x}=-r\rho v=-r^2\frac{dF}{dx} \tag{2.27}$$

We further assume that the temperature and species mass fractions are only functions of x and introduce a new variable, $G \equiv dF/dx$, the system equations are further simplified as follows,

Continuity:

$$G(x)-\frac{dF(x)}{dx}=0 \tag{2.28}$$

Radial momentum:

$$H - 2\frac{d}{dx}\left(\frac{FG}{\rho}\right) + \frac{3G^2}{\rho} + \frac{d}{dx}\left[\mu\frac{d}{dx}\left(\frac{G}{\rho}\right)\right] = 0 \tag{2.29}$$

where μ is the molecular viscosity. H is defined as

$$H = \frac{1}{r}\left(\frac{\partial P}{\partial r}\right) \text{ = constant.} \tag{2.30}$$

Energy:

$$2F\sum_{k=1}^{K} Y_k \frac{\partial \hat{h}_k}{\partial x} - \frac{d}{dx}\left(\lambda\frac{dT}{dx}\right) + \rho\sum_{k=1}^{K} Y_k V_k \frac{\partial \hat{h}_k}{\partial x} + \sum_{k=1}^{K} MW_k \hat{h}_k \omega_k = 0 \tag{2.31}$$

Species:

$$2F\frac{dY_k}{dx} + \frac{d}{dx}\left(\rho Y_k V_k\right) - \omega_k = 0, \quad k = 1, \ldots, K \tag{2.32}$$

where the partial-mass enthalpy of species k, $\hat{h}_k$ is calculated based on fundamental thermodynamics theories to account for real-fluid effects [68]. At the ideal-gas limit, $d\hat{h}_k = C_{p,k}dT$, with $C_{p,k}$ being the specific heat capacity of species k. The energy equation then degenerates to the version given in Ref. [52].

2.3 Equation of State and Thermophysical Properties

In order to close the aforementioned governing equations, thermodynamic and transport properties require to be defined and an equation of state (EOS) is needed to correlate pressure, temperature, and density. Property evaluation based on ideal-gas model is not valid any more at high-pressure situations. An equation of state that can handle real-fluid properties must be selected. The thermodynamic properties have to be evaluated in a consistent manner to provide a unified treatment of real-fluid thermodynamics. In this section, the selected equation of state is first presented, and then real-fluid thermodynamics treatment, including the derivatives appearing in the preconditioning matrix are summarized.

2.3.1 Soave-Redlich-Kwong EOS

The commonly used EOS for computing real-fluid properties under high-pressure conditions includes Benedict-Webb-Rubin (BWR) [69], Peng-Robinson (PR)[70], and Soave-Redlich-Kwong (SRK) [71]. All of them can predict thermodynamic properties of vapor and liquid phases with excellent accuracy. In the present study, SRK EOS is implemented to evaluate the derivative terms in thermodynamic relations, and BWR EOS accompanied with an extended corresponding state principle is used to estimate transport properties, which will be discussed in a later section. The formula of SRK EOS is given by,

$$p = \frac{\rho R_u T}{MW - b\rho} - \frac{a\alpha}{MW}\frac{\rho^2}{MW + b\rho} \tag{2.33}$$

where a and b account for the attractive and repulsive forces between molecules. α is a modeling parameter and a function of temperature and acentric factor. For a mixture, these parameters are expresses as,

$$a\alpha = \sum_{i=1}^{N}\sum_{j=1}^{N} x_i x_j \alpha_{ij} a_{ij} \tag{2.34}$$

$$b = \sum_{i=1}^{N} x_i b_i \tag{2.35}$$

where x_i is the mole fraction of species i. The product $\alpha_{ij}a_{ij}$ in Eq. 2.34 is given by,

$$\alpha_{ij}a_{ij} = \sqrt{\alpha_i \alpha_j a_i a_j}(1 - \kappa_{ij}) \tag{2.36}$$

where κ_{ij} is the binary interaction coefficient. a_i , b_i, and other parameters are determined by critical properties and expressed as follows,

$$a_i = 0.42747\frac{R_u^2 T_{ci}^2}{p_{ci}} \tag{2.37}$$

$$b_i = 0.08664\frac{R_u T_{ci}}{p_{ci}} \tag{2.38}$$

$$\alpha_i = [1 + S_i(1 - \sqrt{T_{ri}})]^2 \tag{2.39}$$

$$T_{ri} = \frac{T}{T_{ci}} \tag{2.40}$$

$$S_i = 0.48508 + 1.5517\omega_i - 0.15613\omega_i^2 \tag{2.41}$$

Here ω_i represents the acentric factor of species *i*. For hydrogen, to account for the quantum-gas behavior, Eq. 2.30 is modified as,

$$\alpha_{H_2} = 1.202\exp(-0.30228T_r) \tag{2.42}$$

This correlation is expected to be accurate for hydrogen at temperature higher than 83K, applicable in liquid rocket.

2.3.2 Thermodynamic Properties

Thermodynamic properties can be derived directly from fundamental thermodynamic relations, which are valid for all thermodynamic states. These properties are generally taken as the sum of the low-pressure limit value using ideal-gas model and a departure function accounting for the dense-fluid corrections at high pressures. Taking advantage of the path-independence of state properties, specific internal energy, enthalpy, entropy, and specific heat capacity can be calculated as:

$$e(T,\rho) = e_0(T) + \int_{\rho_0}^{\rho}\left[\frac{p}{\rho^2} - \frac{T}{\rho^2}\left(\frac{\partial p}{\partial T}\right)_\rho\right]_T d\rho, \tag{2.43}$$

$$h(T,\rho) = h_0(T) + \int_{p_0}^{p}\left[\frac{1}{\rho} + \frac{T}{\rho^2}\left(\frac{\partial \rho}{\partial T}\right)_p\right]_T dp, \tag{2.44}$$

$$s(T,\rho) = s_0(T,\rho_0) - \int_{\rho_0}^{\rho}\left[\frac{1}{\rho^2}\left(\frac{\partial p}{\partial T}\right)_\rho\right]_T d\rho, \tag{2.45}$$

$$C_p(T,\rho) = C_{V_0}(T) - -\int_{\rho_0}^{\rho}\left[\frac{T}{\rho^2}\left(\frac{\partial^2 p}{\partial T^2}\right)_\rho\right]_T d\rho + \frac{T}{\rho^2}\left(\frac{\partial p}{\partial T}\right)_\rho^2 \Big/ \left(\frac{\partial p}{\partial \rho}\right)_T. \tag{2.46}$$

The subscript 0 refers to an ideal state at low-pressure limit and the integral terms are the departure functions. All the partial derivatives in these relations can be calculated from SRK EOS as described in the previous section, and the resultant forms are expressed as follows,

$$\left(\frac{\partial p}{\partial T}\right)_{\rho_j} = \frac{\rho R_u}{MW - b\rho} - \frac{1}{MW}\left[\frac{\partial}{\partial T}(a\alpha)\right]_{\rho, Y_i} \frac{\rho^2}{MW + b\rho}, \tag{2.47}$$

$$\left(\frac{\partial p}{\partial \rho}\right)_{T, Y_i} = \frac{MWR_uT}{(MW - b\rho)^2} - \frac{a\alpha}{MW}\frac{\rho(2MW + b\rho)}{MW + b\rho}, \tag{2.48}$$

$$\begin{aligned}\left(\frac{\partial p}{\partial \rho_i}\right)_{T,\rho_{j\neq i}} &= \frac{M_w R_u T}{M_{wi}(M_w - b\rho)^2}\left[M_w + \rho(b_i - b)\right] \\ &\quad - \frac{2\rho\sum_j x_j a_{ij}\alpha_{ij}}{M_{wi}(M_w + b\rho)} + \frac{a\alpha\rho^2 b_i}{M_{wi}(M_w + b\rho)^2}\end{aligned} \tag{2.49}$$

where the derivative $\partial(a\alpha)/\partial T$ is given in Appendix C.

2.3.3 Partial Molar and Partial Density Properties

For an ideal gas mixture, the properties are simply the sum of molar-weighted properties. However, at high-pressure conditions, the mixture properties, such as specific internal energy, specific enthalpy, and specific volume, are complex functions of temperature, pressure and chemical species. Partial molal properties for an extensive variable *X*, is defined as:

$$\bar{X}_i = \left(\frac{\partial X}{\partial n_i}\right)_{p,T,n_{j\neq i}}, \tag{2.50}$$

where *n* is the mole number. Partial molar properties are defined as:

$$\bar{\Phi}_i = \left(\frac{\partial \Phi}{\partial x_i}\right)_{p,T,x_{j\neq i}}. \tag{2.51}$$

Early works in high-pressure droplet vaporization and combustion [72, 73] indicated that partial molar properties have to be used to get reliable results. This is easily understood by taking the mixture of water and ethanol at room conditions as an example. The mixture volume (non-ideal mixture) of 1 mL water and 1 mL ethanol is less than 2 mL. In other words, the mixture property V, is not equal to the sum of molar-weighted volumes of water and ethanol. Partial molar properties have to be used to get accurate mixture properties in such situations.

However, in most CFD codes the flow properties are evaluated based on mass or density instead of mole number, making the evaluation of partial molar properties inconvenient. The concept of partial mass and density properties were introduced by Lafon et al. [74] and Meng [75] to overcome these problems.

Any partial mass property ϕ in a mixture is dependent on pressure, temperature, and species mass fractions:

$$m\phi = m\phi\left(p, T, m_i\right) . \tag{2.52}$$

Accordingly, the partial mass property is defined as

$$\hat{\phi}_i = \left(\frac{\partial m\phi}{\partial m_i}\right)_{p,T,m_{j\neq i}} . \tag{2.53}$$

Partial density property is defined in a similar manner:

$$\phi_i' = \left(\frac{\partial \rho\phi}{\partial \rho_i}\right)_{T,\rho_{j\neq i}} . \tag{2.54}$$

Here the independent variables change from pressure, species mass fractions to species densities. The relation between a partial mass and the partial density properties can be derived from fundamentals of thermodynamics [75], given by:

$$\phi_i' = \hat{\phi}_i + \rho\left(\frac{\partial\phi}{\partial p}\right)_{T,Y_j}\left(\frac{\partial p}{\partial \rho_i}\right)_{T,\rho_{j\neq i}} . \tag{2.55}$$

As an example of partial mass and partial density variable application, partial mass enthalpy is given by:

$$\hat{h}_i = e_i + \frac{T}{\rho}\frac{\left(\frac{\partial p}{\partial T}\right)_{\rho_j}}{\left(\frac{\partial p}{\partial \rho}\right)_{T,Y_j}}\left(\frac{\partial p}{\partial \rho_i}\right)_{T,\rho_{j\neq i}} . \tag{2.56}$$

2.4 Transport Properties

In addition to the modification of thermodynamic properties, transport properties are needed to be evaluated accurately by taking into account high-pressure effects. Accurate calculation of transport properties, including dynamic viscosity, thermal conductivity, and binary mass diffusivity, is very important for fluid mixing and combustion characteristics. They not only determine the flow dynamics, but also the heat and mass transfer rates [76].

As originally proposed by van der Waals in 1873, the law of corresponding states conclude that equilibrium properties can be related to the critical properties in a universal manner [77]. It expresses that the reduced *P*-*V*-*T* relationships are the same for all substances. The property of any fluid can be thus estimated by relating to its counterpart of a reference substance, whose properties can be easily obtained [78]. Chung et al.'s method [77], which also falls into the corresponding state theory category, is used in the current study for its good accuracy, relative simplicity, availability of parameters, and consistency in evaluating dynamic viscosity and thermal conductivity for high-pressure fluid mixtures. As for the binary mass diffusivity, as discussed by Poling et al. [77], there are few proposed methods to account for high-pressure effect on the diffusion coefficients, the Takahashi method is used in the current study.

2.4.1 Dynamic Viscosity and Thermal Conductivity

Dynamic viscosity and thermal conductivity of mixtures at high pressures are calculated using Chung et al.'s method, upon which the general formulations are derived from elementary kinetic theory. Extensions were made to account for various effects that are not included in the derivation. The resulting formulation provides a consistent procedure to estimate mixture dynamic viscosity and conductivity at high pressures.

According to elementary kinetic theory, the mass diffusivity *D*, dynamic viscosity μ, and thermal conductivity λ, are proportional to the average molecular speed *v* and mean free path *L*,

$$D=\frac{vL}{3}=(const)\frac{T^{3/2}}{M^{1/2}p\sigma^2}\ , \tag{2.57}$$

$$\mu=\frac{m\rho vL}{3}=(const)\frac{T^{1/2}M^{1/2}}{\sigma^2}\ , \tag{2.58}$$

$$\lambda=\frac{vLC_vn}{3}=(const)\frac{T^{1/2}}{M^{1/2}\sigma^2}\ . \tag{2.59}$$

Assuming a rigid, no interacting sphere model for molecules, the viscosity relation is given by:

$$\mu=26.69\frac{T^{1/2}M^{1/2}}{\sigma^2}\ , \tag{2.60}$$

where μ = viscosity, μP

M = molecular weight, g/mol

σ = hard-sphere diameter, Å

If the effects of molecular interaction are taken into account, viscosity can be derived as:

$$\mu=26.69\frac{T^{1/2}M^{1/2}}{\sigma^2\Omega_v}\ , \tag{2.61}$$

where Ω_v is the collision integral, which can be calculated if the potential energy of interaction is given.

A factor F_c is added to account for molecular shapes and polarities of dilute:

$$\mu = 26.69 \frac{F_c (MT)^{1/2}}{\sigma^2 \Omega_v} = 40.785 \frac{F_c (MT)^{1/2}}{V_c^{2/3} \Omega_v} \ , \tag{2.62}$$

where V_c = critical volume, cm^3/mole

$$F_c = 1 - 0.2756\omega + 0.059035\mu_r^4 + \kappa$$

$\Omega_v = A(T^*)^{-B} + Ce^{-DT^*} + Ee^{-FT^*}$, viscosity collision integral

A = 1.16145, B= 0.14874, C = 0.52487, D = 0.77320, E = 2.16178, F = 2.4378

$$T^* = 1.2593 T_r$$

ω = accentric factor

$dip_r = 131.3 \frac{dip}{(V_c T_c)^{1/2}}$, dimensionless dipole moment

κ = special correction for high highly polar substances, like alcohols and acids

For gas mixtures at low pressures, mixture properties are used to evaluate viscosity:

$$\mu_m = 26.69 \frac{F_c (MT)^{1/2}}{\sigma^2 \Omega_v} = 40.785 \frac{F_{cm} (M_m T)^{1/2}}{V_{cm}^{2/3} \Omega_{vm}} \ . \tag{2.63}$$

Mixing rules to give mixture properties used in Eq. 2.63 are given by:

$$\sigma_m^3 = \sum_i \sum_j x_i x_j \sigma_{ij}^3 \ , \tag{2.64}$$

$$T_m^* = \frac{T}{(\varepsilon / k)_m} \ , \tag{2.65}$$

$$\left(\frac{\varepsilon}{k} \right)_m = \frac{\sum_i \sum_j x_i x_j (\varepsilon_{ij} / k) \sigma_{ij}^3}{\sigma_m^3} \ , \tag{2.66}$$

$$M_m = \left[\frac{\sum_i \sum_j x_i x_j (\varepsilon_{ij} / k) \sigma_{ij}^2 M_{ij}^{1/2}}{(\varepsilon / k)_m \sigma_m^2} \right]^2 \ , \tag{2.67}$$

$$\omega_m = \frac{\sum_i \sum_j x_i x_j \omega_{ij} \sigma_{ij}^3}{\sigma_m^3} \ , \tag{2.68}$$

$$dip_m = \sigma_m^3 \sum_i \sum_j \frac{x_i x_j dip_i^2 dip_j^2}{\sigma_{ij}^3} \ , \tag{2.69}$$

$$\kappa_m = \sum_i \sum_j x_i x_j \kappa_{ij} \ . \tag{2.70}$$

The combining rules are:

$$\sigma_{ii} = \sigma_i = 0.809 V_{ci}^{1/3} \ , \tag{2.71}$$

$$\sigma_{ij} = \left(\sigma_i \sigma_j \right)^{1/2} \ , \tag{2.72}$$

$$\frac{\varepsilon_{ii}}{k} = \frac{\varepsilon_i}{k} = \frac{T_{ci}}{1.2593} \ , \tag{2.73}$$

$$\frac{\varepsilon_{ij}}{k} = \left(\frac{\varepsilon_i}{k} \frac{\varepsilon_j}{k} \right)^{1/2} \ , \tag{2.74}$$

$$\omega_{ii} = \omega_i \ , \tag{2.75}$$

$$\omega_{ij} = \frac{\omega_i + \omega_j}{2} \ , \tag{2.76}$$

$$\kappa_{ii} = \kappa_i \ , \tag{2.77}$$

$$\kappa_{ij} = \left(\kappa_i \kappa_j \right)^{1/2} \ , \tag{2.78}$$

$$M_{ij} = \frac{2 M_i M_j}{M_i + M_j} \ , \tag{2.79}$$

$$F_{cm} = 1 - 0.275 \omega_m + 0.059035 \mu_r^m + \kappa_m \ , \tag{2.80}$$

$$\mu_r^m = \frac{131.3 \mu_m}{\left(V_{cm} T_{cm} \right)^{1/2}} \ , \tag{2.81}$$

$$V_{cm} = \left(\sigma_m / 0.809\right)^3 \ , \tag{2.82}$$

$$T_{cm} = 1.2593\left(\frac{\varepsilon}{k}\right)_m \ , \tag{2.83}$$

where T_c is in K, V_c is in cm^3/mol, and dip is in debyes.

To account for high-pressure effect on the viscosity of pure gas, a correction coefficient is added to Eq. 2.51 and is given by:

$$\mu_m = \mu^* \frac{36.344\left(MT_c\right)^{1/2}}{V_c^{2/3}} \ , \tag{2.84}$$

$$\mu^* = \frac{\left(T^*\right)^{1/2}}{\Omega_v}\left\{F_c\left[\left(G_2\right)^{-1} + E_6 y\right]\right\} + \mu^{**} \ , \tag{2.85}$$

$$y = \frac{\rho V_c}{6} \ , \tag{2.86}$$

$$G_1 = \frac{1 - 0.5y}{\left(1-y\right)^3} \ , \tag{2.87}$$

$$G_2 = \frac{E_1\left\{\left[1 - e^{-E_4 y}\right]/y\right\} + E_2 G_1 e^{E_5 y} + E_3 G_1}{E_1 E_4 + E_2 + E_3} \ , \tag{2.88}$$

$$\mu^{**} = E_7 y^2 G_2 \exp\left[E_8 + E_9\left(T^*\right)^{-1} E_{10}\left(T^*\right)^{-2}\right] , \tag{2.89}$$

$$E_i = a_i + b_i\omega + c_i\mu_r^4 + d_i\kappa \ . \tag{2.90}$$

where the coefficients given by Table 2.1.

Finally, for high-pressure mixtures, mixture properties in Eqs. **2.84**-2.90 are used to calculate the mixture viscosity.

Table 2.1: Coefficients to calculate E_i in Eq. 2.90.

i	a_i	b_i	c_i	d_i
1	6.324	50.41	-51.68	1189
2	1.21×10^{-3}	-1.154×10^{-3}	-6.257×10^{-3}	0.03728
3	5.283	254.2	-168.5	3898
4	6.623	38.10	-8.464	31.42
5	19.75	7.630	-14.35	31.53
6	-1.900	-12.54	4.985	-18.15
7	24.28	3.450	-11.29	69.35
8	0.7972	1.117	0.01235	-4.117
9	-0.2382	0.06770	-0.8163	4.025
10	0.06863	0.3479	0.5926	-0.7270

Table 2.2: Coefficients to calculate E_i in Eq.2.97.

i	a_i	b_i	c_i	d_i
1	2.4166E+0	7.4824E-1	-9.1858E-1	1.2172E+2
2	-5.0924E-1	-1.5094E+0	-4.9991E+1	6.9983E+1
3	6.6107E+0	5.6207E+0	6.4760E+1	2.7039E+1
4	1.4543E+1	-8.9139E+0	-5.6379E+0	7.4344E+1
5	7.9274E-1	8.2019E-1	-6.9369E-1	6.3173E+0
6	-5.8634E+0	1.2801E+1	9.5893E+0	6.5529E+1
7	9.1089E+1	1.2811E+1	-5.4217E+1	5.2381E+2

Thermal conductivity is derived in a similar manner. The final expression for thermal conductivity is given by:

$$\lambda = \frac{31.2\lambda^{\circ}\Psi}{M'}\left(G_2^{-1} + B_6 y\right) + qB_7 y^2 T_r^{1/2} G_2 \ . \qquad (2.91)$$

With λ = thermal conductivity, W/(m·K)

λ° = low pressure gas viscosity, N·s/m

M' = molecular weight, kg/mol

$$q = 3.586\times10^{-3}(T_c M')^{1/2} / V_c^{2/3}$$

$$\Psi = 1+\alpha\left\{\left[0.215+0.28288\alpha-1.061\beta+0.26665z\right]/\left[0.6366+\beta z+1.061\alpha\beta\right]\right\}, \quad (2.92)$$

$$\alpha = \frac{C_v}{R}-\frac{3}{2}, \quad (2.93)$$

$$\beta = 0.7862-0.7109\omega+1.3168\omega^2, \quad (2.94)$$

$$z = 2.0+10.5T_r^2, \quad (2.95)$$

$$G_2 = \frac{(B_1/y)\left[1-e^{-B_4 y}\right]+B_2 G_1 e^{B_5 y}+B_3 E_1}{B_1 B_4+B_2+B_3}, \quad (2.96)$$

$$B_i = a_i+b_i\omega+c_i\mu_r^4+d_i\kappa. \quad (2.97)$$

where the coefficients listed in Table 2.2.

2.4.2 Binary Mass Diffusivity

At low pressures, the product Dp or $D\rho$ are nearly constant and independent on species composition. However, it is not the case for high-pressure mixtures. Due to lack of experimental data for binary mass diffusivity, there are only a few estimation methods. In this study, lower-pressure values of binary mass diffusivity are evaluated with Fuller et al.'s empirical correlation, recommended by Poling et al. [77]. Then a very simple method, which is also a corresponding-state method, suggested by Takahashi is adopted in the current study to account for high-pressure effect.

At low pressures, the binary mass diffusivity is given by Fuller et al. [77],

$$D_{ij} = \frac{0.00143T^{1.75}}{pM_{ij}^{1/2}\left[(\Sigma_v)_i^{1/3}+(\Sigma_v)_j^{1/3}\right]^2}, \quad (2.98)$$

where D_{ij} is binary mass diffusivity with unit of cm^2/s, Σ_v is found for each component by summing atomic diffusion volumes, which is tabulated in Poling et al. [77], Table 11-1). The data of interest are listed in Table 2.3.

Table 2.3: Diffusion volumes for selected atoms and molecules.

Atoms	Diffusion volume increments	Molecules	Diffusion volumes
C	15.9	O_2	16.3
H	2.31	Air	19.7
O	6.11	CO	18.0
N	4.54	CO_2	26.9
Aromatic Ring	-18.3	H_2O	13.1

Then high-pressure correction is evaluated based on Takahashi's correlation, which is given by:

$$\frac{D_{ij}p}{\left(D_{ij}p\right)^{+}} = f\left(T_r, p_r\right), \tag{2.99}$$

where the superscript + indicates the low-pressure values given by Eq. 2.98. The function $f\left(T_r, p_r\right)$ represents a pressure scaling factor, and is given by Fig. 2.2. The combining rules to calculate the reduced temperature and reduced pressure are given by:

$$T_c = x_i T_{c,i} + x_j T_{c,j}, \tag{2.100}$$

$$p_c = x_i p_{c,i} + x_j p_{c,j}. \tag{2.101}$$

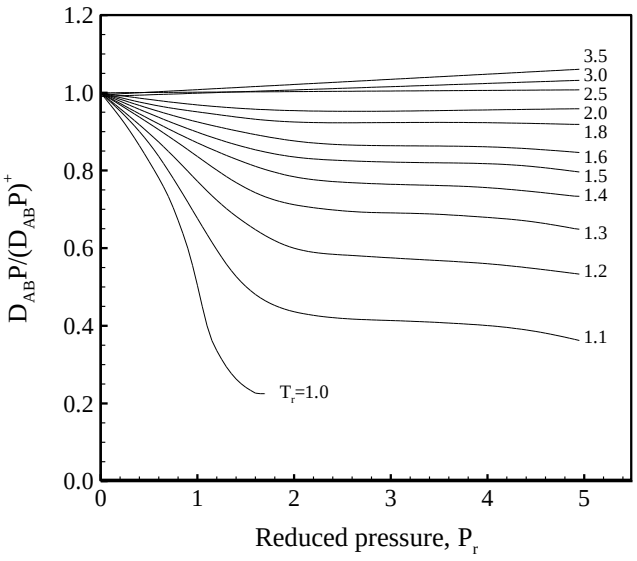

Figure 2.2: Correlation for high-pressure diffusivity using Takahashi method

2.5 Turbulence Closure: Larger-Eddy-Simulation

Although turbulence has been studied for more than ten decades after Osborne Reynolds' experiments, it is still a big challenge in fluid mechanics due to its strong nonlinear behavior [79]. Numerical simulations of turbulent motions fall into three major categories: Direct Numerical Simulation (DNS), Reynolds-Aaveraged Navier-Stokes Equation (RANS), and Large-Eddy Simulation (LES) [80].

DNS is the most straightforward method. The governing equations are discretized with enough resolution and solved numerically; it resolves the smallest scales of motion and does not require any modeling. This makes it possible to compute and visualize any quantity of interest, and it has been a very useful research tool to obtain insight on detailed kinematics and dynamics of turbulent flows [81]. DNS has been applied to supercritical mixing layers [82, 83] and combustion studies [84] to reveal physical and/or chemical processes that would not have been possible with other approaches. The database created by DNS can be used to validate existing turbulent models and turbulent/combustion models. However, the implementation of DNS requires extensively computational

resources. To resolve all scales of motion in three-dimensional space, the number of grid points are proportional to $Re_L^{9/4}$, e.g., 9 billion grid points for Re_L = 10000. Therefore, DNS is limited to small Reynolds number flows and is infeasible for industry-interested applications.

In contrast to DNS, RANS has been commonly applied method to solve turbulent flow problems, especially in engineering applications. In RANS, only statistical quantities, i.e., the ensemble or time-averaged mean quantities are predicted. The effect of all the scales of motion is modeled (except for Unsteady-RANS, in which coherent motions are partially resolved) [80]. Although RANS is inherently less expensive and has moderate success in industrial applications, it fails to account for a very wide range of scales. Based on Kolmogorov's hypothesis, at sufficiently high Reynolds number, the small-scale motions are statistically isotropic and tend to be universal to model [85]. However, the large-scale motions are strongly dependent on flow conditions and geometric boundaries, thus it is impossible for RANS to achieve a universal model that can cover a range of scales in turbulent flows [79].

As a trade-off between the accuracy and computational cost of RANS and DNS, an intermediate technique known as Large-Eddy Simulation (LES) has been developed. LES features higher accuracy than RANS, while it requires much less computational effort compared to DNS. In LES, energy-containing large-scale motions are fully resolved with the grid and filter employed, while the effect of the smallest-scale motions of turbulence is modeled [79]. Since the small-scale motions are more isotropic and universal, they can be modeled in universal manner with much less adjustments in model coefficients, as compared with the turbulent models for RANS simulations. The demanding computational cost to resolve all scales of motions explicitly and accurately in DNS is avoided.

LES seems promising to solve turbulent flow problems. However, difficulties arise near the wall region, where a series of important events occur. The production and dissipation of turbulent kinetic energy achieve peak values at less than 30 wall units [85].

The energy-containing scales depend on Reynolds number, but the growth of the small scales is prohibited by the presence of the wall, making the exchange mechanisms between large and small scales different from unconstrained flows. To capture the important energy-production events in the near-wall layer, an extremely fine grid is necessary, especially for high Reynolds number flows. Based on Chapman's estimate [86], the boundary layer is divided into outer and inner layers; the number of grid points scale with $Re^{0.4}$ for the outer layer; however, it scales with $Re^{1.8}$ for the inner layer. So for a boundary layer flow with a Reynolds number of 10^6, 99% of the grid points are required to resolve the inner layer, whose thickness is only about 10% of the boundary layer. As pointed out by Piomelli [79], the wall layer modeling is probably the most urgent challenge when it is intended to apply LES to industrially interested flows. Wall-modeled LES (WMLES) have been studied by many researchers. Cabot [87] and Balaras et. al. [88] used two-layer boundary layer equations to model the near-wall region in LES of wall bounded shear flows. Spalart [89] proposed a Detached-Eddy Simulation (DES). It used Spalart-Allmaras turbulence model or k-omega SST model for the Reynolds stress and the sub-grid stress modeling. DES has been applied to massively separated flows and seems promising for wall bounded flows. More discussion on wall layer models can be found in review papers by Piomelli [79] and Spalart [89].

In the current study, the LES technique is used to achieve turbulent closure. The small-scale motions are not resolved in LES; however, based on the energy cascade analysis, it is in this range of scales that viscous dissipations drain turbulent kinetic energy to internal energy. This part of turbulent motions has to be modeled with appropriate SGS models.

2.5.1 Filtered Governing Equations

In LES, large-scale motions, which carry most of the kinetic energy are fully resolved, while small-scale motions, which are more universal and appropriate to model,

are simulated with SGS models. To separate the large-scale motions from the small-scale ones, a low-pass filtering operation is performed explicitly or implicitly. A filtered (or resolved) variable is defined as,

$$\bar{f}(\boldsymbol{x}) = \int_{\infty} f(\boldsymbol{x}) G_f(\boldsymbol{x} - \boldsymbol{x}') d\boldsymbol{x}' , \tag{2.102}$$

where G is the filter function and satisfies $\int G(\boldsymbol{x}) d\boldsymbol{x} = 1$. The filter function determines the size and structure of the small scales. Leonard [90] indicated that if G is only a function of $\boldsymbol{x} - \boldsymbol{x}'$, the differentiation and filtering operations could commute with each other. Although for stretched grids, the commutation between filtering and differentiation is not strictly valid [91, 92], the commutation error is usually neglected for moderately stretched grids [93, 94]. The modeling error is found to be generally smaller than the discretization error [93]. One of the most commonly used filter functions, the box filter, which is also used in the current study, is defined as:

$$\bar{f}(\mathbf{x}) = \frac{1}{\Delta V} \int_{\Delta V} f(\mathbf{x}) d\mathbf{x} . \tag{2.103}$$

With the box filter, any filtered quantity is simply its average in the control volume. A detailed description of properties of various filters can be found in standard textbooks [85]. Based on the Favre-averaging [95], any instantaneous variable (f) can be expressed as the sum of a Favre-averaged filtered scale ($\tilde{f}$) and a sub-filter scale (f'')

$$f = \tilde{f} + f'' , \tag{2.104}$$

where

$$\tilde{f} = \frac{\overline{\rho f}}{\bar{\rho}} . \tag{2.105}$$

Since $\overline{f'} \neq 0$ and $f'' \neq 0$, the filtering operation in LES is different from the conventional Reynolds averaging in time domain. The filtered Favre-averaged mass, momentum,

energy, mixture fraction, and progress variable transport equations in conservative form can be written as

$$\frac{\partial \bar{\rho}}{\partial t}+\frac{\partial \bar{\rho}\tilde{u}_i}{\partial x_i}=0\,, \tag{2.106}$$

$$\frac{\partial \bar{\rho}\tilde{u}_i}{\partial t}+\frac{\partial(\bar{\rho}\tilde{u}_i\tilde{u}_j)}{\partial x_j}=-\frac{\partial \bar{p}}{\partial x_i}+\frac{\partial(\tau_{ij}-\tau_{ij}^{SGS})}{\partial x_j}\ ,\ i=1,2,3, \tag{2.107}$$

$$\frac{\partial \bar{\rho}\tilde{E}}{\partial t}+\frac{\partial\left[(\bar{\rho}\tilde{E}+\bar{p})\tilde{u}_i\right]}{\partial x_i}=\frac{\partial}{\partial x_i}\left(\bar{q}_i+\tilde{u}_j\tau_{ij}-Q_i^{SGS}-H_i^{SGS}+\sigma_i^{SGS}\right), \tag{2.108}$$

$$\frac{\partial \bar{\rho}\tilde{f}}{\partial t}+\frac{\partial(\bar{\rho}\tilde{u}_j\tilde{f})}{\partial x_j}=\frac{\partial}{\partial x_j}\left(\bar{\rho}D\frac{\partial \tilde{f}}{\partial x_j}-\Phi_j^{SGS}\right), \tag{2.109}$$

$$\frac{\partial \bar{\rho}\tilde{C}}{\partial t}+\frac{\partial(\bar{\rho}\tilde{u}_j\tilde{C})}{\partial x_j}=\frac{\partial}{\partial x_j}\left(\bar{\rho}D\frac{\partial \tilde{C}}{\partial x_j}-\Psi_j^{SGS}\right)+\overline{\omega_C}\,, \tag{2.110}$$

where the SGS terms are defined as:

$$\tau_{ij}^{SGS}=\overline{\rho u_i u_j}-\bar{\rho}\tilde{u}_i\tilde{u}_j\ , \tag{2.111}$$

$$Q_i^{sgs}=(\bar{q}_i-q_i)\,, \tag{2.112}$$

$$H_i^{SGS}=\left(\overline{\rho E u_i}-\bar{\rho}\tilde{E}\tilde{u}_i\right)+\left(\overline{pu_i}-\bar{p}\tilde{u}_i\right), \tag{2.113}$$

$$\sigma_{ij}^{SGS}=\left(\overline{u_j\tau_{ij}}-\tilde{u}_j\tau_{ij}\right), \tag{2.114}$$

$$\Phi_j^{SGS}=\left(\overline{\rho u_j f}-\bar{\rho}\tilde{u}_j\tilde{f}\right), \tag{2.115}$$

$$\Psi_j^{SGS}=\left(\overline{\rho u_j C}-\bar{\rho}\tilde{u}_j\tilde{C}\right). \tag{2.116}$$

The SGS stress term τ_{ij}^{SGS}, SGS energy flux term H_i^{SGS}, and SGS scalar flux terms Φ_j^{SGS}, and Ψ_j^{SGS}, result from filtering the corresponding convective terms. The SGS viscous work term σ_{ij}^{SGS}, comes from correlations of the velocity field with the viscous

stress tensor. The resolved-scale progress variable production rate $\overline{\omega_C}$, is also unclosed. The modeling of these SGS terms is discussed in detail in the following subsections.

In addition to the conservation equations, the equation of state must also be filtered. By introducing the compressibility factor, *Z*, the alternative form of EOS can be written as

$$p = \frac{Z\rho R_u T}{MW} = \rho R_u Z T \sum_{k=1}^{N} \frac{Y_k}{MW_k} \tag{2.117}$$

Filtering Eq. 2.117 gives us

$$\bar{p} = \bar{\rho} R_u \sum_{k=1}^{N} \frac{\overline{ZTY_k}}{MW_k} + \bar{\rho} R_u \sum_{k=1}^{N} \frac{\overline{ZTY_k} - \overline{ZTY_k}}{MW_k} \tag{2.118}$$

For ideal gas without heat release, the correlations (second term in the right hand side) in the filtered equation of state can be neglected [96]. This may not be true for high-pressure, real-fluid mixtures. However, due to the difficulty and uncertainty in modeling those correlations, they are neglected without justification.

The filtered total energy, E can be approximated as

$$E = \tilde{h} - \frac{p}{\bar{\rho}} + \frac{u_k^2}{2} + k^{SGS} = \psi + \int_{p_0}^{p} \left[\frac{1}{\rho} + \frac{T}{\rho^2} \left(\frac{\partial \rho}{\partial T} \right)_p \right] dp - \frac{p}{\bar{\rho}} + \frac{u_k^2}{2} + k^{SGS} \ , \tag{2.119}$$

where $\psi = \sum_{k=1}^{N} Y_k h_k^0$ and $k^{sgs} = \frac{\tau_{kk}^{SGS}}{2\bar{\rho}} = \frac{1}{2}\left(\frac{\overline{\rho u_k u_k}}{\bar{\rho}} - u_k^{\ 2} \right)$.

2.5.2 Subgrid-Scale Model

In LES, the unresolved motions of sub-grid scales have to be represented by an appropriate SGS model. Most of SGS models use the concept of eddy viscosity, ν_t, which is similar to dynamic viscosity but generally with much higher value. Using eddy viscosity, the subgrid viscous shear stress can be written as,

$$\tau_{ij}^{SGS} - \frac{\delta_{ij}}{3} \tau_{kk}^{SGS} = -2\nu_t S_{ij} \ , \tag{2.120}$$

where S_{ij} is the symmetric part of velocity gradient tensor, $S_{ij} = \frac{1}{2}\left(\partial u_i / \partial x_j + \partial u_j / \partial x_i\right)$. In the following section, two commonly used SGS models are introduced.

2.5.2.1 Algebraic Smagorinsky Model

The Smagorinsky SGS model [97] has been widely used because of its simplicity and good accuracy. The eddy viscosity is obtained algebraically to avoid solving additional equations. The model uses the equilibrium hypothesis, which claims that the small-scale motions with much short time scales can rapidly adjust to the flow perturbations and recover equilibrium nearly instantaneously. A balance equation between turbulent kinetic energy production and viscous dissipation thus exists: $-\tau_{ij} S_{ij} = \varepsilon_v$. Followed by this assumption, the Smagorinsky model is written as,

$$\nu_t = \left(C_S \bar{\Delta}\right)^2 |S| \,, \tag{2.121}$$

$$|S| = \sqrt{2 S_{ij} S_{ij}} \,, \tag{2.122}$$

$$\bar{\Delta} = \sqrt[3]{\Delta_1 \Delta_2 \Delta_3} \,, \tag{2.123}$$

where $\bar{\Delta}$ is the filter width, which is usually proportional to the grid size. The coefficient C_s can be determined from a priori test on decaying isotropic turbulence [98] with C_s=0.16. Erlebacher et al. [99] extended the above model to compressible flows,

$$\tau_{ij}^{SGS} = -2\bar{\rho}\nu_t \left(S_{ij} - \frac{\delta_{ij}}{3} S_{kk} \right) + \frac{2}{3} \bar{\rho} k^{SGS} \delta_{ij} \,, \tag{2.124}$$

$$\nu_t = \left(C_R \Delta D\right)^2 |S| \,, \tag{2.125}$$

$$k^{SGS} = C_I (\Delta D)^2 S_{ij} S_{ij}, \tag{2.126}$$

where the dimensionless quantities C_R and C_I represent the compressible Smagorinsky constants. The Van-Driest damping function (D) is used to take into account the inhomogeneities near the wall [100], and is expressed as

$$D=1-\exp\left(-\left(y^+/25\right)^2\right), \tag{2.127}$$

where $y^+ = yu_\tau/\nu$ and u_τ is friction velocity.

The subgrid energy flux term H_j^{sgs} is modeled based on the gradient transport assumption

$$H_i^{SGS} = -\bar{\rho}\frac{\nu_t}{Pr_t}\frac{\partial H}{\partial x_i} = -\bar{\rho}\frac{\nu_t}{Pr_t}\left(\frac{\partial \tilde{h}}{\partial x_i} + \tilde{u}_j\frac{\partial \tilde{u}_j}{\partial x_i} + \frac{1}{2}\frac{\partial k^{SGS}}{\partial x_i}\right) \tag{2.128}$$

where Pr_t represents the turbulent Prandtl number, and a standard value 1.0 is used. The SGS viscous work term, σ_{ij}^{sgs}, is neglected due to its small contribution to the total energy equation [79, 101].

The convective mixture fraction flux term is usually approximated as

$$\Phi_j^{sgs} = -\bar{\rho}\frac{\nu_t}{Sc_t}\frac{\partial \tilde{f}}{\partial x_j} \tag{2.129}$$

where Sc_t is the turbulent Schmidt number. However, the use of the gradient transport assumption for reactive species is questionable.

The algebraic Smagorinsky model described above is the most widely used model in LES. However, as pointed out by Germano et al. [102], it has several limitations. First, the optimal model constant must be changed for a different class of flows. The model does not have the accurate limiting behavior near the wall [103]. The SGS stress does not vanish in laminar flow and the model is found to be very dissipative in the laminar/transition region. In addition, the model does not account for the backscatter of energy from small to large scale, which has been shown to be of importance in the transition region.

2.5.2.2 Dynamic Smagorinsky Model

The dynamic model introduced by Germano et al. [102] improves some of the aforementioned deficiencies in algebraic models. The dynamic model uses the assumption of scale invariance by applying the coefficient measured from the resolved scales to the

SGS range. It calculates the model coefficients dynamically from the information already contained in the resolved velocity field during the simulation. Apply the test-filter $\tilde{G}$, with characteristic $\tilde{\Delta}>\bar{\Delta}$ (typically, $\tilde{\Delta}=2\bar{\Delta}$), to the equations of motion, one obtains filtered governing equations similar to Eqns. 2.106-2.110, but replacing $\tilde{f}=\overline{\rho f}/\bar{\rho}$ with $\tilde{\tilde{f}}=\overline{\rho f}/\tilde{\rho}$, yields the sub-testscale stress T_{ij}, defined as:

$$T_{ij}=\overline{\rho u_i u_j}-\bar{\rho}\tilde{u}_i\tilde{u}_j \ . \tag{2.130}$$

Formally, the dynamical procedure is based on the Germano identity [104]

$$L_{ij}=T_{ij}-\tau_{ij}^{SGS}=\bar{\rho}\tilde{u}_i\tilde{u}_j-\overline{\rho u_i u_j} \ . \tag{2.131}$$

The following expressions can be derived for the dynamic evaluation of C_R and C_I using the least square minimization approach of Lilly [105] for the momentum SGS stress tensor.

$$C_R=\frac{\langle L_{ij}M_{ij}\rangle}{\langle M_{kl}M_{kl}\rangle}-\frac{1}{3}\frac{\langle M_{mn}M_{mn}\rangle}{\langle M_{kl}M_{kl}\rangle} \tag{2.132}$$

$$C_I=\frac{\langle L_{kk}\rangle}{\langle\beta-\langle\alpha\rangle\rangle} \tag{2.133}$$

The forms of M_{ij}, β and α are given as follows

$$M_{ij}=\beta_{ij}-\langle\alpha_{ij}\rangle \tag{2.134}$$

$$\beta_{ij}=-2\hat{\Delta}^2\langle\bar{\rho}\rangle\left|\bar{S}\right|\left(\bar{S}_{ij}-\frac{\delta_{ij}}{3}\bar{S}_{kk}\right) \tag{2.135}$$

$$\alpha_{ij}=-2\Delta^2\bar{\rho}\left|S\right|\left(S_{ij}-\frac{\delta_{ij}}{3}S_{kk}\right) \tag{2.136}$$

$$\alpha=2\bar{\rho}\Delta^2\left|S\right|^2 \tag{2.137}$$

$$\beta=2\hat{\Delta}^2\langle\bar{\rho}\rangle\left|\bar{S}\right|^2 \tag{2.138}$$

The same idea can be applied to model SGS turbulent stress to dynamically calculate the turbulent Prandtl number and Schmidt number in Eq. 2.128 and Eq. 2.129.

2.6 Turbulence/Combustion Models

In LES, although the energy-carrying eddy motions are resolved with sufficient grid resolution, motions of small scales, such as the Kolmogorov scale, are not resolved, which plays a crucial role in reactant mixing at molecular levels. The chemical reaction rate is a very strong nonlinear function of local species concentration and temperature at the molecular level, which are highly dependent on the turbulent mixing. Chemical reactions release heat and alter species concentration and temperature gradients of the smallest turbulent eddies, which in turn change the turbulent mixing process. Chemical reaction occurring at different time scales may interact with turbulence eddies of different length/time scales, which further complicates the picture. The interaction of these two processes occurs at length scales from the smallest turbulent scales to much larger inertial sub-range scales, which cannot be completely resolved in LES studies. The physical processes associated with these interactions are modeled with turbulent combustion models.

There are several combustion models for the LES of non-premixed turbulent combustion. The most straightforward way is to evaluate the filtered reaction rate from the filtered quantities, without consideration of the sub-grid interactions of turbulence and chemistry. This method has been used by several researchers due to the simplicity [9, 106].

Conditioned Momentum Closure (CMC) was developed by Klimenko [107] and Bilger [108] independently for non-premixed turbulent combustion. Variables of interest are conditioned with mixture fraction before the Favre averaging to obtain conditional moment equations. CMC has been used in homogenous and boundary layer flows. With those applications, CMC can be related to flamelet equations [47]. However, this method solves conditional species equations for all species; the computational cost increases with the number of species, which may become prohibitively costly when detailed chemical mechanism is used.

The Linear-Eddy Model (LEM) was developed by Kerstein [109, 110] has been used by the author, Menon and colleagues [111, 112]. The one-dimensional laminar reactive scalar field is combined with stochastically independent rearrangement events to mimic turbulence/chemistry interactions. However, this model suffers from prohibitive computational costs in applications. The Monte Carlo method for PDF transport equations was developed by Pope and extensively tested in RANS and LES [47]. However, the formulation is very complicated, and the computation cost is considerably high for even a moderate number of species. Dynamically thickened flame was developed by Légier et al. [113] for both premixed- and non-premixed combustion. This model can account for unsteady combustion such as extinction, re-ignition etc. However, it has similar difficulties when detailed chemistry is used. Flamelet concept proposed by Peters [47] has been extensively studied. The steady flamelet model is chosen in the current study to account for turbulence/chemistry interactions and identify the flame stabilization mechanism for supercritical combustion.

2.6.1 Laminar Flamelet Model

The basic assumption of the laminar flamelet model is that the chemical time scales are shorter than that of the smallest turbulent eddies: Kolmogorov scales. Consequently, a turbulent flame can be envisioned as a synthesis of thin reaction zones (i.e., flamelets) embedded in an otherwise inert turbulent flow field. The inner structure of the flame can be handled separately from turbulent flow simulations. Instead of directly treating the reactive scalar (i.e., species concentration), the focus is placed on the identification of the flame surface in the flow-field, which can be obtained by solving the conservation equation of the mixture fraction together with the mass, momentum, and energy equations.

The flame thickness is smaller than the grid size employed in LES and is not actually resolved. Therefore, the filtered species mass fraction of the i^{th} species, $\tilde{Y}_i(x,t)$, in each computational cell should be evaluated by convoluting the state relationships,

$Y_i(f,\chi_{st})$, with the *SGS* Filtered Density Function (*FDF*) of mixture fraction, $P(f)$, and the *SGS FDF* of scalar dissipation rate, $P(\chi_{st})$, as shown below:

$$\tilde{Y}_i(x,t)=\int_0^1\int_0^\infty Y_i(f,\chi_{st})P(\chi_{st})P(f)d\chi_{st}df. \tag{2.139}$$

It should be noted that a statistical independence is intrinsically assumed in Eq. 2.139 between the *SGS* variations of mixture fraction and scalar dissipation. The unresolved *SGS* fluctuation of the mixture fraction is commonly represented by a presumed β-shaped Probability Density Function (PDF) parameterized by the filtered mixture fraction and its *SGS* variance, which takes the following form,

$$P(f;\tilde{f},f''^2)=\frac{f^{\alpha-1}(1-f)^{\beta-1}}{\Gamma(\alpha)\Gamma(\beta)}\Gamma(\alpha+\beta), \tag{2.140}$$

where Γ is the γ-function. The parameters α and β are defined as

$$\alpha=\tilde{f}\left(\frac{\tilde{f}(1-\tilde{f})}{f''^2}-1\right), \tag{2.141}$$

$$\beta=(1-\tilde{f})\left(\frac{\tilde{f}(1-\tilde{f})}{f''^2}-1\right). \tag{2.142}$$

The *SGS* variance of mixture fraction, f''^2, is modeled based on the scale similarity assumption [114],

$$f''^2=K_b\overline{\bar{\rho}(\tilde{f}-\tilde{\tilde{f}})^2}/\bar{\bar{\rho}}, \tag{2.143}$$

where K_b is a model constant chosen as 3. It has been validated by many researchers that the β-function *PDF* provides an excellent estimation of the *SGS* mixture fraction distribution for non-premixed reacting turbulent flows [115]. For simplicity, the *SGS* FDF of the scalar dissipation rate, $P(\chi_{st})$, which is typically assumed to be a lognormal, is considered as a Dirac peak at the filtered scalar dissipation rate. Further investigation is

required to validate this assumption. The filtered rate of scalar dissipation, $\tilde{\chi}$, is modeled based on the eddy viscosity approach as suggested by Girimaji and Zhou [116]

$$\tilde{\chi} = 2\left(\frac{\nu}{Sc} + \frac{\nu_t}{Sc_t}\right)\left(\frac{\partial f}{\partial x_j}\frac{\partial f}{\partial x_j}\right). \tag{2.144}$$

The thermo-chemistry state relation is established through a steady-state flamelet approach. Taking advantage of the fact that the flamelet library only needs to be calculated once for every specified case, chemistry kinetics with any number of species and reaction steps can be used for the establishment of the flamelet library. The flamelet library should cover a broad range of strain rates, from near chemistry equilibrium to near-extinction limit. For all the calculations, the pressure is fixed at the same as the application; and the inlet temperatures of the fuel and oxidizer take the corresponding inlet temperature of the application cases. Consistent with the flamelet assumption, the corresponding scalar dissipation rate, χ, for each solution is evaluated as a function of filtered mixture fraction. The solutions are then integrated based on Eq. 2.139 and tabulated as functions of $\tilde{\chi}$, $\tilde{f}$, and f''^2. The calculated filtered mixture fraction, mixture fraction variance, and the scalar dissipation rate from LES simulation are used to determine the appropriate entry in the table.

2.6.1.1 Steady vs Unsteady Flamelets

In the present study, the flamelet library is generated from steady-state laminar counterflow diffusion flames. Thus, the species profile does not include the history effect of the chemical reactions, i.e. the time taken to achieve the steady state flame profile. In a real turbulent flame, slow chemistry reactions, such as CO oxidation, take a much longer time compared to other reactions. Following Peters' argument, if the scalar dissipation rate is changing slowly enough so that the change of chemical reactions can follow the pace of the local flow variations, the steady flamelet is a valid assumption [47]. Otherwise, the

unsteady effect may become important. According to Pitsch et al. [117], it is valid to apply a steady flamelet within the range of 30 nozzle diameter from the fuel nozzle exit. Extreme caution must be taken in the further downstream, where the scalar dissipation rate becomes small and the chemistry may not be fast enough to follow the flow variations. In the current study, the focus is on the near field of the injector faceplate and the unsteady effect is not expected to be significant.

2.6.1.2 Differential Diffusion Effect

Unit Lewis number is assumed to achieve the mixture fraction equation [47]. It is interesting to know how much accuracy of numerical solution is sacrificed by this assumption. The effect of differential diffusion has been examined by Pitsch and Peters [118]. They found that the existence of a laminar region in the near field of the jet exit causes the differential diffusion effect, which is only important within a 10-diameter distance from the jet exit. However, the temperature and the species concentration distributions are influenced by the differential diffusion effect farther downstream. This is not assessed in the current study for several reasons. First, hydrocarbon fuels feature a Lewis number closer to unity, compared to hydrogen, which will make the differential diffusion less important than that in hydrogen flames. Second, the differential diffusion effect itself is still an open research issue. There are model and numerical uncertainties associated with the evaluation of this effect; a simple inclusion of this model does not guarantee a better prediction. For simplicity and ease of discussion of the model validity and its performance in supercritical applications, this effect is not addressed in the current study. Finally, in the process of building the flamelet library, the differential diffusion effect is considered within the model used herein [119]. However, in the LES study, the unit Lewis number is assumed.

2.6.1.3 Scalar Dissipation

As pointed out by Poinsot and Veynante [120], the effect of external mixing (turbulent flow) is lumped into the scalar dissipation rate, while chemistry is decoupled from the flow and retrieved from the lookup table. Consequently, the scalar dissipation rate accounts for the effect of turbulent mixing as an external parameter on the laminar flamelet structures. The procedure to estimate this variable directly affects the chemical species distribution, the flame structure, and the combustion dynamics. Instead of assuming a pre-assumed shape of scalar dissipation as proposed by Peters, the scalar dissipation as a function of the mixture fraction is calculated from the laminar counterflow flamelets, which are generated in physical space using a one-dimensional code [121, 122]. This is different from Pitsch's methods, which are conducted in the mixture fraction space, and the dependence of scalar dissipation is modeled by an exponential function of the mixture fraction.

Although the laminar flamelet method is easy to implement and fairly inexpensive, it has several drawbacks. Firstly, the mixture fraction essentially does not carry information about the chemical reaction state. The flamelet method uses the scalar dissipation rate as an additional parameter to account for the flame stretching and quenching effect. However, the scalar dissipation rate does not provide a unique mapping from the mixture fraction to the corresponding chemical state. A pure mixing of fuel and oxidizer cannot be accounted for in the flamelet method if the local scalar dissipation is smaller than the quenching limit. This drawback is due to the lack of information regarding the local chemical state in the flow field. The Flamelet/Progress-Variable (FPV) method is able to overcome the limitations of the flamelet method by incorporating an additional transport equation for tracking a scalar in the form of a progress variable. This method has been developed to account for extinction, ignition, and unsteady mixing effect [123]. It will be interesting to examine the performance of these two methods in the future work.

CHAPTER 3

NUMERICAL METHODOLOGY

Numerical simulations of supercritical injection, mixing, and combustion bear a series of difficulties. This chapter outlines the intrinsic challenges and the corresponding methodologies to handle these problems. The numerical scheme, with a unified treatment of real-fluid thermodynamic properties, is capable of solving the three dimensional governing equations in a general curvilinear coordinate system. The solver uses finite volume approach with structured grid system. To obtain time-accurate solutions, the preconditioned dual-time-stepping technique, with a Runge-Kutta integration in pseudo-time iterations, is used to resolve the numerical difficulties associated with low-Mach number flows. The resulting numerical scheme is TVD-assured, fourth order accurate in space and second order accurate in time. MPI-parallelization is used to expedite the calculation and reduce the turnaround time.

3.1 Preconditioning Scheme for Real-Fluid Mixtures

The three-dimensional, unsteady, Favre-filtered governing equations listed in Chapter 2 can be re-written in a vector form:

$$\frac{\partial \mathbf{Q}}{\partial t}+\frac{\partial\left(\mathbf{E}-\mathbf{E}_{\mathbf{v}}\right)}{\partial x}+\frac{\partial\left(\mathbf{F}-\mathbf{F}_{\mathbf{v}}\right)}{\partial y}+\frac{\partial\left(\mathbf{G}-\mathbf{G}_{\mathbf{n}}\right)}{\partial z}=\mathbf{H}, \tag{3.1}$$

where the vectors $\mathbf{Q}, \mathbf{E}, \mathbf{F}, \mathbf{G}, \mathbf{E}_{\mathbf{n}}, \mathbf{F}_{\mathbf{v}}, \mathbf{G}_{\mathbf{n}},$ and $\mathbf{H}$ are defined as:

$$\mathbf{Q}=\left(\bar{\rho}, \bar{\rho} \tilde{u}, \bar{\rho} \tilde{v}, \bar{\rho} \tilde{w}, \bar{\rho} \tilde{E}, \bar{\rho} \tilde{f}\right)^{T}, \tag{3.2}$$

$$\mathbf{E}=\left(\bar{\rho} \tilde{u}, \bar{\rho} \tilde{u}^{2}+\bar{p}, \bar{\rho} \tilde{u} \tilde{v}, \bar{\rho} \tilde{u} \tilde{w},\left(\bar{\rho} \tilde{E}+\bar{p}\right) \tilde{u}, \bar{\rho} \tilde{u} \tilde{f}\right)^{T}, \tag{3.3}$$

$$\mathbf{F}=\left(\bar{\rho} \tilde{v}, \bar{\rho} \tilde{u} \tilde{v}, \bar{\rho} \tilde{v}^{2}+\bar{p}, \bar{\rho} \tilde{v} \tilde{w},\left(\bar{\rho} \tilde{E}+\bar{p}\right) \tilde{v}, \bar{\rho} \tilde{v} \tilde{f}\right)^{T}, \tag{3.4}$$

$$\mathbf{G}=\left(\bar{\rho}w,\bar{\rho}uw,\bar{\rho}vw,\bar{\rho}w^2+\bar{p},\left(\bar{\rho}E+\bar{p}\right)w,\bar{\rho}w\tilde{f}\right)^T , \tag{3.5}$$

$$\mathbf{E}_v=\begin{pmatrix}0,\bar{\tau}_{xx}-\tau_{xx}^{sgs},\bar{\tau}_{xy}-\tau_{xy}^{sgs},\bar{\tau}_{xz}-\tau_{xz}^{sgs},u\bar{\tau}_{xx}+v\bar{\tau}_{xy}+w\bar{\tau}_{xz}+\bar{q}_x-H_x^{sgs}+\sigma_x^{sgs},\\ \bar{\rho}D\tilde{f}_x+\bar{\rho}\dfrac{\nu_t}{Sc_t}\tilde{f}_x\end{pmatrix}^T , \tag{3.6}$$

$$\mathbf{F}_v=\begin{pmatrix}0,\bar{\tau}_{xy}-\tau_{xy}^{sgs},\bar{\tau}_{yy}-\tau_{yy}^{sgs},\bar{\tau}_{yz}-\tau_{yz}^{sgs},u\bar{\tau}_{xy}+v\bar{\tau}_{yy}+w\bar{\tau}_{yz}+\bar{q}_y-H_y^{sgs}+\sigma_y^{sgs},\\ \bar{\rho}D\tilde{f}_y+\bar{\rho}\dfrac{\nu_t}{Sc_t}\tilde{f}_y\end{pmatrix}^T , \tag{3.7}$$

$$\mathbf{G}_v=\begin{pmatrix}0,\bar{\tau}_{xz}-\tau_{xz}^{sgs},\bar{\tau}_{yz}-\tau_{yz}^{sgs},\bar{\tau}_{zz}-\tau_{zz}^{sgs},u\bar{\tau}_{xz}+v\bar{\tau}_{yz}+w\bar{\tau}_{zz}+\bar{q}_z-H_z^{sgs}+\sigma_z^{sgs},\\ \bar{\rho}D\tilde{f}_z+\bar{\rho}\dfrac{\nu_t}{Sc_t}\tilde{f}_z\end{pmatrix}^T , \tag{3.8}$$

$$\mathbf{H}=\left(0,0,0,0,0,0\right)^T , \tag{3.9}$$

where the superscript T stands for the transpose of the vector.

There are two severe numerical challenges in solving these equations for high-pressure mixing and combustion. First, thermodynamic non-idealities and transport anomalies take place as the fluid transits from subcritical to supercritical conditions. Treating these abnormal changes in a manner consistent with the intrinsic characteristics of the numerical algorithm presents a major obstacle. Second, the rapid variation of the fluid state and wide range of characteristic time and length scales pose the well-known stiffness problem. The stiffness of the system results from: 1) ill-conditioned eigenvalues; 2) competing convective and diffusion processes; and 3) pressure singularities in the momentum equation.

The Mach number in present simulations is relatively small, and thus the dynamic pressure is negligibly smaller than the static pressure (high-pressure situations). This could cause the computer round-off error override the dynamic pressure in the momentum equation, i.e., the pressure singularity problem. To overcome this difficulty, the static pressure is decomposed into a constant reference pressure and a gauge pressure [124, 125],

$$p = p_0 + p_g \ . \tag{3.10}$$

Here the averaged pressure in the flowfield is generally selected as the reference pressure, while the gauge pressure is the fluctuating part induced by unstable flow motions. With this decomposition, p is replaced with p_g in the momentum equations. To solve the ill-conditioned eigenvalue problem, let us look at the following equations:

$$\frac{\partial \mathbf{Q}}{\partial t} + \mathbf{A}\frac{\partial \mathbf{Q}}{\partial x} + \mathbf{B}\frac{\partial \mathbf{Q}}{\partial y} + \mathbf{C}\frac{\partial \mathbf{Q}}{\partial z} = 0 , \tag{3.11}$$

where $\boldsymbol{A} = \partial \boldsymbol{E} / \partial \boldsymbol{Q}$, $\boldsymbol{B} = \partial \boldsymbol{F} / \partial \boldsymbol{Q}$, and $\boldsymbol{C} = \partial \boldsymbol{G} / \partial \boldsymbol{Q}$ are the Jacobian matrices. Analysis shows that the eigenvalues of matrix **A** is:

$$\lambda_1 = u + c, \lambda_2 = u - c, \lambda_{3,4,5,6} = u \ . \tag{3.12}$$

In low Mach number flows, $M \ll 1$, the ratio of the largest eigenvalue to the smallest one is close to inverse of Mach number, indicating that the eigenvalues are order of magnitude different. For a given CFL number, the maximum local time step determined by the largest eigenvalue hence is extremely small, resulting in a very slow convergence. It becomes unacceptable for even lower-Mach number or time accurate simulations.

To cure the eigenvalue disparity problem in low Mach number flows, the time-derivative preconditioning method [124-127] are implemented associated with the methodologies developed by Meng and Yang [68] for handling general fluid thermodynamics, to take full account of the thermodynamic non-idealities and transport anomalies in the whole fluid state of concern. Zong and Yang [128] made further improvement by changing primitive variable *h* to *T*, getting rid of the cost intensive computation associated with iterative calculations to get temperature from enthalpy. A unified treatment of thermodynamic properties and associated preconditioning matrix makes the numerical scheme accurate, robust, and efficient.

The basic idea of the preconditioning method is to add a pseudo time differential term in Eq. 3.1, with multiplication factor of a preconditioning matrix:

$$\Gamma\frac{\partial \mathbf{Z}}{\partial t}+\frac{\partial \mathbf{Q}}{\partial t}+\frac{\partial\left(\mathbf{E}-\mathbf{E}_{\mathbf{v}}\right)}{\partial x}+\frac{\partial\left(\mathbf{F}-\mathbf{F}_{\mathbf{v}}\right)}{\partial y}+\frac{\partial\left(\mathbf{G}-\mathbf{G}_{\mathbf{n}}\right)}{\partial z}=\mathbf{H}, \tag{3.13}$$

$$\mathbf{Z}=\left(\bar{\mathbf{p}}_{\mathbf{g}}, u, v, w, T, f\right)^{T} . \tag{3.14}$$

If Γ is chosen carefully so that the eigenvalues of these matrixes are of the same order of magnitude, the resulting equations have well-conditioned eigenvalues and converge efficiently in all Mach number flows. When pseudo time approaches infinity, (steady state solutions are achieved with respect to pseudo time), the original governing equations are recovered. It can be seen that the efficiency of preconditioning method is largely determined by the selection of the preconditioning matrix.

Following Zong [129], the transfer matrix is derived (see Appendix B) as:

$$T=\frac{\partial \mathbf{Q}}{\partial \mathbf{Z}} . \tag{3.15}$$

In this matrix, a common term $\left(\partial \rho / \partial p\right)_{T, Y_i}$ can be related to speed of sound and specific heat capacity ratio:

$$\left(\frac{\partial \rho}{\partial p}\right)_{T, Y_i}=\frac{C_p}{C_v}\left(\frac{\partial \rho}{\partial p}\right)_{s, Y_i}=\frac{\gamma}{a^2} . \tag{3.16}$$

a^2 is replaced with β to define the preconditioning matrix,

$$\Gamma=\begin{pmatrix} \frac{\gamma}{\beta} & 0 & 0 & 0 & \rho_T & \rho_f \\ \frac{\gamma}{\beta}u & \bar{\rho} & 0 & 0 & u\rho_T & u\rho_f \\ \frac{\gamma}{\beta}v & 0 & \bar{\rho} & 0 & v\rho_T & v\rho_f \\ \frac{\gamma}{\beta}w & 0 & 0 & \bar{\rho} & w\rho_T & w\rho_f \\ \frac{\gamma}{\beta}\tilde{h}_t+\frac{T}{\bar{\rho}}\rho_T & \bar{\rho}u & \bar{\rho}v & \bar{\rho}w & \bar{\rho}c_p+h_t\rho_T & \rho_f E+\bar{\rho}E_f \\ \frac{\gamma}{\beta}f & 0 & 0 & 0 & \rho_T f & \bar{\rho}+f\rho_f \end{pmatrix}, \tag{3.17}$$

where $\tilde{h}_t$ is the total specific enthalpy, $\rho_T=\left(\partial\rho/\partial T\right)_{p,y_i}$, $\rho_f=\partial\rho/\partial f$, and $E_f=\partial E/\partial f$. β is defined as

$$\beta=\frac{\gamma\varepsilon a^2}{1+(\gamma-1)\varepsilon}, \tag{3.18}$$

where ε ($0<\varepsilon\le 1$) is the preconditioning factor. Unlike the definition of preconditioning matrix by other researchers, all of the off-diagonal terms in Eq. 3.17 have been retained. By keeping these terms, the unaltered system is identically restored as $\varepsilon\to 1$;

$$\lim_{\varepsilon\to 1}\Gamma=T. \tag{3.19}$$

The conditioned governing equations in the pseudo-time space are characterized by the new Jacobian matrices, $\Gamma^{-1}A_v$, $\Gamma^{-1}B_v$, and $\Gamma^{-1}C_v$, the eigenvalues of which are given by:

$$\begin{aligned} \lambda_1&=\frac{1}{2}[U(\varepsilon+1)+\sqrt{U^2(1-\varepsilon)^2+4\varepsilon a^2}], \\ \lambda_2&=\frac{1}{2}[U(\varepsilon+1)-\sqrt{U^2(1-\varepsilon)^2+4\varepsilon a^2}], \\ \lambda_{3,4,5,6}&=U, \end{aligned} \tag{3.20}$$

where U represents u, v, and w in x-, y- and z-direction, respectively. If ε is small enough, the first two eigenvalues can be of the same order of magnitude as others. Note that no

assumption is made to the form of the equation of state, it can be applied to any fluid state without loss of accuracy.

3.1.1 Determination of the Preconditioning Factor

From the definition of the preconditioning matrix, and the resulting system eigenvalues, it is clear that the effectiveness of the preconditioning method is totally determined by the choice of the preconditioning factor, ε. The value of ε in each computational cell is crucial to get well-conditioned eigenvalues and thus the fast convergence of the numerical scheme.

Various time scales are associated with each computational cell in each direction, due to local flow convection, acoustic propagation, momentum, and thermal and mass diffusion processes. These processes have to be taken into account when choosing the preconditioning factor. The non-dimensional numbers characterizing the time scales associated with these physical processes are CFL number, Mach number, von Neumann number, cell Reynolds number, Prandtl number, and Schmidt number.

The CFL number, which characterizes the local convective propagation rates in the three coordinate directions are defined as:

$$CFL_x = \frac{\rho(\lambda_x)\Delta\tau}{\Delta x},\ CFL_y = \frac{\rho(\lambda_y)\Delta\tau}{\Delta y},\ CFL_z = \frac{\rho(\lambda_z)\Delta\tau}{\Delta z}, \tag{3.21}$$

where $\rho(\lambda_x),\ \rho(\lambda_y),\ \rho(\lambda_z)$ are the maximum eigenvalues in each direction, respectively.

The von Neumann number, which characterizes the diffusion propagation rates, is defined as:

$$VNN_x = \frac{\nu\Delta\tau}{\Delta x^2},\ VNN_y = \frac{\nu\Delta\tau}{\Delta y^2},\ VNN_z = \frac{\nu\Delta\tau}{\Delta z^2}, \tag{3.22}$$

The cell Reynolds number, which indicates the ratio of local velocities to momentum diffusion velocity, is defined as:

$$\mathrm{Re}_x = \frac{u\Delta x}{\nu},\ \mathrm{Re}_y = \frac{v\Delta y}{\nu},\ \mathrm{Re}_z = \frac{w\Delta z}{\nu}, \tag{3.23}$$

If the respective quantities *Re, RePr,* and *ReSc* exceed unity in one of directions, the convection velocity is larger than the corresponding velocity scale, thus convective effects dominant and the conservation equations exhibit a hyperbolic character. For this situation an inviscid criterion must be employed. If *Re, RePr*,or *ReSc* are less than or equal to unity, diffusive effects dominate, a parabolic character is exhibited and a viscous criteria must be employed.

The final preconditioning factor is selected based on the methodology developed by Choi and Merkel [124], Buelow et al. [130], and Venkateswaran and Merkel [131]. Optimal values are specified locally as:

$$\varepsilon = \min[1, \max(\varepsilon_{inv}, \varepsilon_{vis})]. \tag{3.24}$$

The subscripts refer to the inviscid and viscous preconditioning factors, respectively. The criteria employed to evaluate these terms are discussed below.

3.1.1.1 Inviscid Preconditioning Factor

In the limit of infinitely large Reynolds numbers, or inviscid flows, following Choi and Merkle [124], ε is assigned a value proportional to the local Mach number to ensure that the pseudo acoustic speed and flow velocity are of the same order of magnitude. To achieve correct limiting behavior, as Mach number approaches zero (e.g. in the stagnant region), a minimum value (typically 10^{-5}) is used. The resulting preconditioning factor is defined as:

$$\varepsilon_{inv} = \begin{cases} \varepsilon^2, & M < \varepsilon; \\ 2M^2, & \varepsilon < M < 1; \\ 1, & M \geq 1. \end{cases} \tag{3.25}$$

In inviscid flows, Eq. 3.25 gives minimal disparity in system eigenvalues and optimal damping rates. The convergence rate is primarily dependent on the local pseudo CFL number, which is determined by the stability criterion.

3.1.1.2 Viscous Preconditioning Factor

In regions where diffusion processes are important, the effect of diffusion on the preconditioning factor has to be considered. Buelow et al. [130, 132] have conducted a variety of studies to determine an optimal viscous preconditioning factor for the Navier-Stokes equations. Results from stability analysis indicate that three different requirements must be addressed in order to specify a generalized criterion. For high cell Reynolds numbers ($\mathrm{Re} \gg 1$) the acoustic wave speeds should be scaled to the same order of magnitude as the particle speeds, as is accomplished by the inviscid preconditioning factor defined above. For low cell Reynolds numbers ($\mathrm{Re} \ll 1$) and high acoustic cell Reynolds numbers ($\mathrm{Re}/M \gg 1$) the diffusion rates should be scaled to the same order of magnitude as the acoustic speeds. For low cell Reynolds numbers and low acoustic cell Reynolds numbers, the diffusion rates should be scaled to the particle speeds. The only way to satisfy these conditions simultaneously is to define a viscous preconditioning factor that is dependent on the Fourier wavenumber. Such a definition is not appropriate for implementation in a CFD code. To overcome the difficulties outlined above, a preconditioning factor based on local length scales which is tuned to damp the low wavenumber modes has been developed. This definition requires a priori assumption of the orientation of dominating convective and diffusion processes within a given grid configuration and the choice of ε_{vis} is somewhat more involved. In three dimensions, there are three possible CFL numbers, and two possible VNN numbers, and six possible values of ε_{vis}. The most restrictive of the CFL and VNN numbers are usually chosen for stability

reasons and these values are the most likely candidates for determining ε_{vis}. Some freedom does exist, however, in how ε_{vis} is evaluated.

In practice, the grid system is stretched near the wall, so that predominating diffusion processes, which is in a direction normal to the predominating convective processes, are resolved. Under these conditions, the rate limiting diffusion processes typically coincide with the maximum von Neumann number in a given cell. To retain the benefits of the time step given by Eq. 3.21, this quantity must be optimized with respect to the minimum CFL number. In three-dimensions, this is achieved by: 1) equating Eq. 3.21 with Eq. 3.22; 2) solving for respective values of ε; and 3) choosing the largest of the three values obtained. Performing this operation yields an expression of the form

$$\varepsilon_{vis} = \max\left[\frac{\tilde{u}^2 \delta_x (\delta_x - 1)}{\tilde{u}^2 \delta_x^2 + a^2}, \ \frac{\tilde{v}^2 \delta_y (\delta_y - 1)}{\tilde{v}^2 \delta_y^2 + a^2}, \ \frac{\tilde{w}^2 \delta_z (\delta_z - 1)}{\tilde{w}^2 \delta_z^2 + a^2} \right], \tag{3.26}$$

where

$$\begin{aligned} \delta_x &= \max\left(\nu, \ \frac{\nu}{\mathrm{Pr}}, \ \frac{\nu}{Sc_i}\right) \frac{1}{\tilde{u}} \frac{CFL}{VNN}, \\ \delta_y &= \max\left(\nu, \ \frac{\nu}{\mathrm{Pr}}, \ \frac{\nu}{Sc_i}\right) \frac{1}{\tilde{v}} \frac{CFL}{VNN}, \\ \delta_z &= \max\left(\nu, \ \frac{\nu}{\mathrm{Pr}}, \ \frac{\nu}{Sc_i}\right) \frac{1}{\tilde{w}} \frac{CFL}{VNN}. \end{aligned} \tag{3.27}$$

This equation takes into account the effects of momentum, energy, and mass diffusion processes on the overall convergence rate.

3.2 Spatial Discretization

3.2.2 Finite Volume Approach

The conservation laws of fluid motion presented in Chapter 2 can be expressed in differential or integral form. The former can be solved by finite differencing approach, but it has inherent difficulties associated with irregular gird system [133]. Integral methods,

including finite volume and finite element methods, can ensure the conservation of properties in each computational cell. In the current study, finite volume approach is thus implemented.

To utilize the finite-volume approach, the governing equations are integrated over the control volume V enclosed by the surface S in the physical domain as

$$\iiint_V \left(\mathbf{\Gamma} \frac{\partial \mathbf{Z}}{\partial \tau} + \frac{\partial \mathbf{Q}}{\partial t} + \frac{\partial (\mathbf{E} - \mathbf{E}_v)}{\partial x} + \frac{\partial (\mathbf{F} - \mathbf{F}_v)}{\partial y} + \frac{\partial (\mathbf{G} - \mathbf{G}_v)}{\partial z} - \mathbf{H} \right) dV = 0. \qquad (3.28)$$

The generalized control volume in a structured grid system is a hexahedron formed by eight nodes as shown in Fig. 3.1. where $\vec{n}_\xi$, $\vec{n}_\eta$, and $\vec{n}_\zeta$ are area unit vectors normal to the surfaces in the ξ-, η-, and ζ-directions, respectively. In order to enhance numerical efficiency and minimize the complexity arising from the irregular shape of the computational mesh, a grid transformation is made to convert a curvilinear coordinate system in the physical space into a uniform grid system in the computational space.

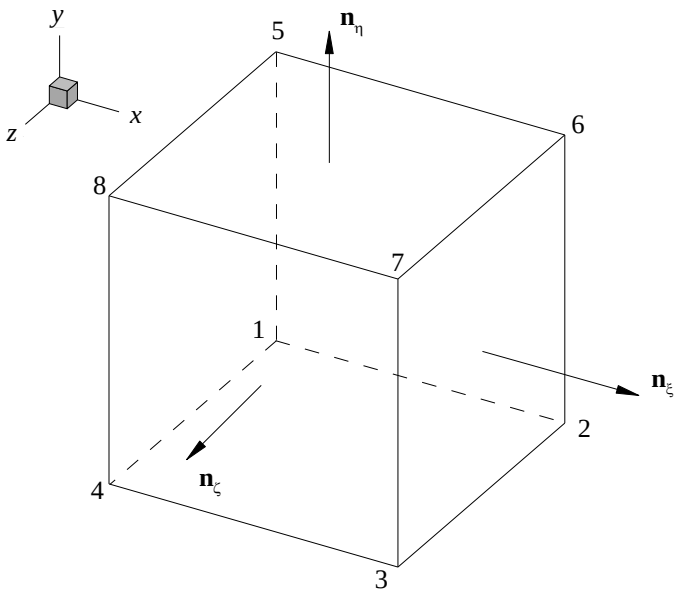

Figure 3.1: Schematic of three-dimensional computational cell

Upon applying the Gauss' divergence theorem over a hexahedral cell as shown in Fig. 3.1, Eq. 3.28 can be re-written as:

$$\iiint_V (\mathbf{\Gamma}\frac{\partial \mathbf{Z}}{\partial \tau}+\frac{\partial \mathbf{Q}}{\partial t})dV+\int_{S_\xi}\mathbf{W}\bullet\mathbf{n}_\xi dS_\xi+\int_{S_\eta}\mathbf{W}\bullet\mathbf{n}_\eta dS_\eta+\int_{S_\zeta}\mathbf{W}\bullet\mathbf{n}_\zeta dS_\zeta=\iiint_V \mathbf{H}dV\,, \qquad (3.29)$$

where

$$\mathbf{W}=\left(\mathbf{E}-\mathbf{E}_v\right)\mathbf{i}+\left(\mathbf{F}-\mathbf{F}_v\right)\mathbf{j}+\left(\mathbf{G}-\mathbf{G}_v\right)\mathbf{k}\,. \qquad (3.30)$$

S_ξ, S_η, and S_ζ are the surface areas that are perpendicular to the surface vectors $\vec{n}_\xi$, $\vec{n}_\eta$ and $\vec{n}_\zeta$, respectively. These areas can be combined with the area unit vectors $\vec{n}_\xi$, $\vec{n}_\eta$ and $\vec{n}_\zeta$ into a vector form given by:

$$\begin{aligned}
\vec{S}_\xi &= S_\xi \vec{n}_\xi = S_{\xi x}\vec{i}+S_{\xi y}\vec{j}+S_{\xi z}\vec{k}\,,\\
\vec{S}_\eta &= S_\eta \vec{n}_\eta = S_{\eta x}\vec{i}+S_{\eta y}\vec{j}+S_{\eta z}\vec{k}\,,\\
\vec{S}_\zeta &= S_\zeta \vec{n}_\zeta = S_{\zeta x}\vec{i}+S_{\zeta y}\vec{j}+S_{\zeta z}\vec{k}\,.
\end{aligned} \qquad (3.31)$$

And the unit area vectors are related to cell surface areas as

$$\begin{aligned}
\vec{n}_\xi &= \left(S_{\xi x}\vec{i}+S_{\xi y}\vec{j}+S_{\xi z}\vec{k}\right)/\left|\vec{S}_\xi\right|\,,\\
\vec{n}_\eta &= \left(S_{\eta x}\vec{i}+S_{\eta y}\vec{j}+S_{\eta z}\vec{k}\right)/\left|\vec{S}_\eta\right|\,,\\
\vec{n}_\zeta &= \left(S_{\zeta x}\vec{i}+S_{\zeta y}\vec{j}+S_{\zeta z}\vec{k}\right)/\left|\vec{S}_\zeta\right|\,.
\end{aligned} \qquad (3.32)$$

The surface vectors and the cell volume can be calculated directly from the grid points [134]:

$$\begin{aligned}
\vec{S}_\xi &= \frac{1}{2}\left(\vec{r}_{72}\times\vec{r}_{36}\right)=\frac{1}{2}\begin{vmatrix}\vec{i} & \vec{j} & \vec{k}\\ x_2-x_7 & y_2-y_7 & z_2-z_7\\ x_6-x_3 & y_6-y_3 & z_6-z_3\end{vmatrix}\,,\\
\vec{S}_\eta &= \frac{1}{2}\left(\vec{r}_{86}\times\vec{r}_{75}\right)=\frac{1}{2}\begin{vmatrix}\vec{i} & \vec{j} & \vec{k}\\ x_6-x_8 & y_6-y_8 & z_6-z_8\\ x_5-x_7 & y_5-y_7 & z_5-z_7\end{vmatrix}\,,
\end{aligned} \qquad (3.33)$$

$$S_\zeta = \frac{1}{2}\left(r_{74} \times r_{83}\right) = \frac{1}{2}\begin{vmatrix} \dot{i} & \dot{j} & \dot{k} \\ x_4 - x_7 & y_4 - y_7 & z_4 - z_7 \\ x_3 - x_8 & y_3 - y_8 & z_3 - z_8 \end{vmatrix},$$

$$\Delta V = \frac{1}{3} r_{17} \left(S_\xi + S_\eta + S_\zeta \right).$$

Assuming that the increments $\Delta\xi=\Delta\eta=\Delta\zeta=1$ in the body-fitted coordinate system and substituting Eq. 3.30 and Eq. 3.32 into Eq. 3.29 yields the following governing equation in the general coordinates

$$\left\{\mathbf{\Gamma}\frac{\partial \mathbf{Z}}{\partial \tau} + \frac{\partial \mathbf{Q}}{\partial t}\right\} + \left(\mathbf{E}_\xi - \mathbf{E}_{\xi\nu}\right)\Big|_{i-1/2,j,k}^{i+1/2,j,k} + \left(\mathbf{F}_\eta - \mathbf{F}_{\eta\nu}\right)\Big|_{i,j-1/2,k}^{i,j+1/2,k} + \left(\mathbf{G}_\zeta - \mathbf{G}_{\zeta\nu}\right)\Big|_{i,j,k-1/2}^{i,j,k+1/2} = \mathbf{H}, \quad (3.34)$$

where the vectors $\mathrm{E}_\xi, \mathrm{F}_\eta, \mathrm{G}_\zeta, \mathrm{E}_{\xi\nu}, \mathrm{F}_{\eta\nu}$, and $\mathrm{G}_{\zeta\nu}$ are defined as

$$\begin{aligned}
\mathbf{E}_\xi &= \left(S_{\xi x}\mathbf{E} + S_{\xi y}\mathbf{F} + S_{\xi z}\mathbf{G}\right), \quad & \mathbf{E}_{\xi\nu} &= \left(S_{\xi x}\mathbf{E}_\nu + S_{\xi y}\mathbf{F}_\nu + S_{\xi z}\mathbf{G}_\nu\right), \\
\mathbf{F}_\eta &= \left(S_{\eta x}\mathbf{E} + S_{\eta y}\mathbf{F} + S_{\eta z}\mathbf{G}\right), \quad & \mathbf{F}_{\eta\nu} &= \left(S_{\eta x}\mathbf{E}_\nu + S_{\eta y}\mathbf{F}_\nu + S_{\eta z}\mathbf{G}_\nu\right), \\
\mathbf{G}_\zeta &= \left(S_{\zeta x}\mathbf{E} + S_{\zeta y}\mathbf{F} + S_{\zeta z}\mathbf{G}\right), \quad & \mathbf{G}_{\zeta\nu} &= \left(S_{\zeta x}\mathbf{E}_\nu + S_{\zeta y}\mathbf{F}_\nu + S_{\zeta z}\mathbf{G}_\nu\right),
\end{aligned} \quad (3.35)$$

The quantities $\mathbf{E}_{\xi,i\pm1/2,j,k}, \mathbf{E}_{\xi\nu,i\pm1/2,j,k}, \mathbf{F}_{\eta,i,j\pm1/2,k}, \mathbf{F}_{\eta\nu,i,j\pm1/2,j,k}, \mathbf{G}_{\zeta,i,j,k\pm1/2}$, and $\mathbf{G}_{\zeta\nu,i,j,k\pm1/2}$ represent the numerical fluxes associated with each cell interface. $\tilde{S}$ represents cell surface areas per cell volume. In fact, the above analysis describes the transformation of a quadrilateral cell with a volume ΔV in x-y-z coordinates to a cubic cell with unit volume in the general coordinate (i.e., ξ-η-ζ coordinates).

To accelerate convergence, the pseudo-time integration is based on the local time step in the computational domain. The maximum pseudo-time increment $\Delta\tau$ of each cell can be evaluated by

$$\Delta\tau = \frac{\Delta\tau_\xi \;\; \Delta\tau_\eta \;\; \Delta\tau_\zeta}{\Delta\tau_\xi \;\; \Delta\tau_\eta + \Delta\tau_\eta \;\; \Delta\tau_\zeta + \Delta\tau_\zeta \;\; \Delta\tau_\xi}, \quad (3.36)$$

where

$$\Delta\tau_\xi = \frac{CFL\cdot\ \Delta V}{\left|\rho(\lambda_x)S_{\xi x}+\rho(\lambda_y)S_{\xi y}+\rho(\lambda_z)S_{\xi z}\right|/\left|S_\xi\right|}\ ,$$
$$\Delta\tau_\eta = \frac{CFL\ \cdot\Delta V}{\left|\rho(\lambda_x)S_{\eta x}+\rho(\lambda_y)S_{\eta y}+\rho(\lambda_z)S_{\eta z}\right|/\left|S_\eta\right|}\ , \qquad (3.37)$$
$$\Delta\tau_\zeta = \frac{CFL\ \cdot\Delta V}{\left|\rho(\lambda_x)S_{\zeta x}+\rho(\lambda_y)S_{\zeta y}+\rho(\lambda_z)S_{\zeta z}\right|/\left|S_\zeta\right|}\ .$$

3.2.3 Evaluation of Inviscid Fluxes

Different approaches in evaluating the numerical fluxes lead to disparate numerical characteristics. In the central difference scheme, the convective flux at a cell face in the ξ-direction can be written as

$$\hat{\mathbf{E}}_{\xi,i+1/2,j} = \frac{1}{2}\left[\mathbf{E}_\xi(\mathrm{Z}^L)+\mathbf{E}_\xi(\mathrm{Z}^R)\right], \qquad (3.38)$$

The above equation corresponds to the stencil illustrated in Fig. 3.2. The superscripts *L* and *R* represent the left and right cells, respectively. Depending on how these terms are evaluated, a wide variety of central and upwind schemes can be obtained. According to Rai and Chakravarthy [135], the numerical flux in Eq. 3.34 is computed as

$$E_{\xi,i+1/2,j,k} = E_{\xi,i+1/2,j,k} - \phi^{(4)}_{i+1/2,j,k}\left(\frac{E_{\xi,i+3/2,j,k}-2E_{\xi,i+1/2,j,k}+E_{\xi,i-1/2,j,k}}{24}\right), \qquad (3.39)$$

where $\phi^{(4)}$ is the flux limiter. This term switches the truncation error associated with the flux-difference from fourth-order accuracy when $\phi^{(4)}=1$, to second-order accuracy when $\phi^{(4)}=0$. To evaluate Eq. 3.38 for this desired accuracy, the left and right state terms (Z^L, Z^R) in Eq. 3.39 must be computed using the same or higher order accuracy. For uniform grid system, these terms are written as follows to facilitate easy switching and make the scheme TVD (total-variation-diminishing).

$$Z^{L}_{i+1/2,j,k} = Z_{i,j,k} + \phi^{(2)}_{i+1/,j,k}\left(\frac{3\nabla Z_{i+1,j,k} + \nabla Z_{i,j,k}}{8}\right) + \phi^{(4)}_{i+1/2,j,k}\left(\frac{-5\nabla Z_{i+2,j,k} + 7\nabla Z_{i+1,j,k} + \nabla Z_{i,j,k} - 3\nabla Z_{i-1,j,k}}{128}\right), \tag{3.40}$$

$$Z^{R}_{i+1/2,j,k} = Z_{i,j,k} - \phi^{(2)}_{i+1/,j,k}\left(\frac{\nabla Z_{i+2,j,k} + 3\nabla Z_{i+1,j,k}}{8}\right) + \phi^{(4)}_{i+1/2,j,k}\left(\frac{3\nabla Z_{i+3,j,k} - \nabla Z_{i+2,j,k} - 7\nabla Z_{i+1,j,k} + 5\nabla Z_{i,j,k}}{128}\right), \tag{3.41}$$

$$\nabla Z_{i,j} = Z_{i,j} - Z_{i-1,j} \ . \tag{3.42}$$

These stencils are fifth-order accuracy ($\phi^{(4)}=1,\phi^{(2)}=1$), third-order accuracy ($\phi^{(4)}=0,\phi^{(2)}=1$), and first-order accuracy ($\phi^{(4)}=0,\phi^{(2)}=0$), respectively. The present work utilizes second-order overall accuracy for spatial discretization with the exception of first order accuracy close to the physical boundaries. The third-order accurate evaluation of the left and right states is thus employed. The fluxes in η-, and ζ-directions can be computed in a similar fashion as above.

In practical applications, non-uniform grids are generally used. If the same procedure is used to evaluate the left and right state terms, Taylor series expansion shows that there is a truncation error of first order. This will significantly reduce the overall order of accuracy of the numerical scheme. Extremely refined grids are used to diminish such side effect.

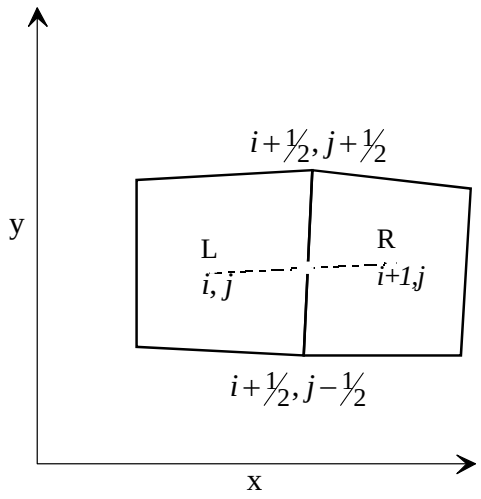

Figure 3.2: Schematic diagram of the stencil used in evaluating inviscid flux terms in the plane.

Fosso et al. [136] proposed higher-order accurate compact interpolation for curvilinear finite volume schemes to take into account the effect of grid non-uniformity. The values of interest at cell surfaces can be estimated from the cell average values in its neighborhood, by applying Taylor series expansion and solving the linear equations. Appropriate boundary treatment procedures have been developed for multi-block applications. However, this method is more expensive due to extra calculations of the surface values in each iteration. The current study compromises by mimicking the so-called Cartesian-like scheme using curvilinear abscissa scheme in the cited work. Instead of implicit equations, explicit equations are obtained to improve the numerical accuracy of spatial differencing for convective flux evaluation.

3.2.4 Evaluation of Viscous and SGS Fluxes

A three-dimensional auxiliary cell is shown schematically by the dash-dotted lines in Fig. 3.3. The viscous fluxes need to be evaluated at the center of the cell faces, i.e., $i+1/2, j, k$ for the viscous flux in the axial direction. Using divergence theorem and applying it to a small control volume ΔV, the viscous fluxes can be approximated as

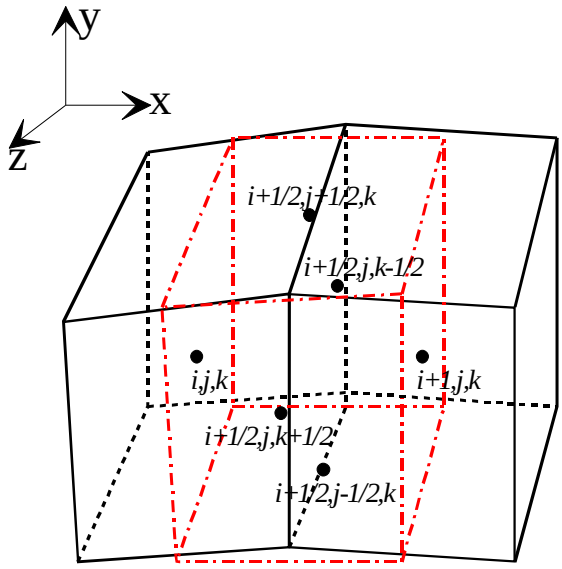

Figure 3.3: Schematic diagram for a three-dimensional auxiliary cell.

$$\nabla \cdot \vec{f} = \frac{1}{\Delta V} \oint_S \vec{f} \cdot \vec{n} dS \,. \tag{3.43}$$

Applying the above formulation to the auxiliary cell at $(i+1/2, j, k)$ gives

$$\left(\frac{\partial f}{\partial x}\right)_{i+1/2,j,k} = \frac{1}{\Delta V_{i+1/2,j,k}} \Big[f \;\; S_{\xi x_x}\big|_{i+1,j,k} - f \;\; S_{\xi x}\big|_{i,j,k} + f \;\; S_{\eta x}\big|_{i+1/2,j+1/2,k} - f \;\; S_{\eta x}\big|_{i+1/2,j-1/2,k} + f \;\; S_{\zeta x}\big|_{i+1/2,j,k+1/2} - f \;\; S_{\zeta x}\big|_{i+1/2,j,k-1/2} \Big] . \tag{3.44}$$

Similarly

$$\left(\frac{\partial f}{\partial y}\right)_{i+1/2,j,k} = \frac{1}{\Delta V_{i+1/2,j,k}} \Big[f \;\; S_{\xi y}\big|_{i+1,j,k} - f \;\; S_{\xi y}\big|_{i,j,k} + f \;\; S_{\eta y}\big|_{i+1/2,j+1/2,k} - f \;\; S_{\eta y}\big|_{i+1/2,j-1/2,k} + f \;\; S_{\zeta y}\big|_{i+1/2,j,k+1/2} - f \;\; S_{\zeta y}\big|_{i+1/2,j,k-1/2} \Big] , \tag{3.45}$$

$$\left(\frac{\partial f}{\partial z}\right)_{i+1/2,j,k} = \frac{1}{\Delta V_{i+1/2,j,k}} \Big[f \;\; S_{\xi z}\big|_{i+1,j,k} - f \;\; S_{\xi z}\big|_{i,j,k} + f \;\; S_{\eta z}\big|_{i+1/2,j+1/2,k} - f \;\; S_{\eta z}\big|_{i+1/2,j-1/2,k} + f \;\; S_{\zeta z}\big|_{i+1/2,j,k+1/2} - f \;\; S_{\zeta z}\big|_{i+1/2,j,k-1/2} \Big] . \tag{3.46}$$

Note that f in the above equations are elements of the viscous flux vectors, $\mathbf{E}_{\xi v}$, $\mathbf{F}_{\eta v}$, or $\mathbf{G}_{\zeta v}$. Physical variables with one-half indices need to be interpolated from the quantities at the neighboring cell centers and are given by

$$
\begin{aligned}
f_{i+1/2,j\pm1/2,k} &= \frac{1}{4}\left(f_{i,j,k} + f_{i+1,j,k} + f_{i+1,j\pm1,k} + f_{i,j\pm1,k}\right), \\
f_{i+1/2,j,k\pm1/2} &= \frac{1}{4}\left(f_{i,j,k} + f_{i+1,j,k} + f_{i+1,j,k\pm1} + f_{i,j,k\pm1}\right).
\end{aligned}
\tag{3.47}
$$

The evaluation of SGS fluxes follows a similar procedure as for the viscous and diffusive fluxes.

The viscous term evaluation procedure outlined above results in lower order of accuracy for non-uniform grids for reasons similar to the convective flux terms. However, in large Reynolds number flows, convection is dominant, and the effect of grid uniformity is neglected in the current study. Further study is warranted to consistently improve the numerical accuracy.

3.2.5 Evaluation of Artificial Dissipation

Artificial dissipation plays a crucial role in the stability of a numerical scheme. The form of dissipation terms must be higher order of accuracy that that of the numerical scheme to keep their magnitude minimal. For the present case, the numerical differentiation of the flux vectors is fourth-order accurate in the core region of the computational domain. Accordingly, the artificial dissipation is fourth-order accurate. The accuracy order of the numerical scheme decreases near the physical boundary, and the artificial dissipation also goes to a lower order. The form of numerical dissipation is quite often a blending of second- and fourth-order dissipation terms. The second-order terms are used near shock waves and flame zones to prevent spurious oscillations, while the fourth-order terms are important for stability and convergence. The standard dissipation model can be written as

$$\begin{aligned} \mathrm{AD} &= \textit{artificial dissipation} \\ &= \mathbf{d}_{i+1/2,j,k} - \mathbf{d}_{i-1/2,j,k} \ , \end{aligned} \tag{3.48}$$

where

$$\mathrm{d}_{i\pm1/2,j,k} = \frac{\varepsilon_2}{8}\frac{1}{\Delta t}\frac{\partial Z}{\partial \xi}\bigg|_{i\pm1/2,j,k} - \frac{\varepsilon_4}{8}\frac{1}{\Delta t}\frac{\partial^3 Z}{\partial \xi^3}\bigg|_{i\pm1/2,j,k} + \frac{\varepsilon_6}{8}\frac{1}{\Delta t}\frac{\partial^5 Z}{\partial \xi^5}\bigg|_{i\pm1/2,j,k} \ , \tag{3.49}$$

ε_2, ε_4, and ε_6 correspond to the coefficients of the second-, fourth- and sixth-order accurate artificial dissipation terms and in the present formulation, $\Delta\xi = 1$.

Even though the standard dissipation model has been proven to be reasonably effective in many cases, there are strong motivations for reducing the numerical dissipation being produced. The standard model also has difficulties in hypersonic flows and in density stratified supercritical fluids with steep discontinuities as it occurs in the present case. A scalar dissipation model was constructed by Swanson and Turkel [137] and by Jorgenson and Turkel [138] to overcome the above difficulties. In their model

$$\mathbf{d}_{i+1/2,j,k} = \varepsilon^{(2)}_{i+1/2,j,k} \ \ \rho_{i+1/2,j,k}(\lambda) \ \ \frac{\partial Z}{\partial \xi}\bigg|_{i+1/2,j,k} - \ \ \varepsilon^{(4)}_{i+1/2,j,k}\rho_{i+1/2,j,k}(\lambda) \ \ \frac{\partial^3 Z}{\partial \xi^3}\bigg|_{i+1/2,j,k} \ . \tag{3.50}$$

The modified eigenvalues are given by

$$\tilde{\lambda}_1 = \tilde{\lambda}_2 = \tilde{\lambda}_3 = \tilde{\lambda}_4 = \tilde{\lambda}_5 = \tilde{\lambda}_6 = \rho(\lambda) \ , \tag{3.51}$$

where $\rho(\lambda)$ is the spectral radius of the flux Jacobian matrix $\Gamma^{-1}\mathrm{A}$.

$$\varepsilon^{(2)}_{i+1/2,j,k} = \kappa^{(2)} \max(\nu_{i-1,j,k}, \ \nu_{i,j,k}, \ \nu_{i+1,j,k}, \ \nu_{i+2,j,k}) \ , \tag{3.52}$$

$$\nu_{i,j,k} = \left| \frac{p_{i-1,j,k} - 2p_{i,j,k} + p_{i+2,j,k}}{p_{i-1,j,k} + 2p_{i,j,k} + p_{i+1,j,k}} \right| \ , \tag{3.53}$$

$$\varepsilon^{(4)}_{i+1/2,j,k} = \max\left(0, \ (\kappa^{(4)} - \varepsilon^{(2)}_{i+1/2,j,k}\right) \ , \tag{3.54}$$

$$\kappa^{(2)} = \frac{1}{4} \sim \frac{1}{2}, \quad \kappa^{(4)} = \frac{1}{64} \sim \frac{1}{32} \ . \tag{3.55}$$

The first term on RHS given in Eq. 3.50 is nonlinear. Its purpose is to introduce an entropy-like condition and to suppress oscillations in the neighborhood of shock discontinuities. This term is small in the smooth portion of the flow field. The switch $\nu_{i,j,k}$ is important near discontinuities, in which large pressure gradients exist. For high-pressure fluid mixing and combustion, however, this switch is tuned to include temperature or density gradients other than pressure gradients, as pressure may still be uniform across the boundary between different fluid layers. The fourth-order term is basically linear and is included to damp high-frequency modes and allow the scheme to approach a steady state. Only this term affects the linear stability of the scheme and is reduced to zero near the discontinuity.

Although effective, the scalar dissipation model results in much dissipation and probably contaminates the accuracy of the simulation. Because the scalar dissipation model uses the same artificial dissipation coefficient for all the equations regardless of the actual wave speeds, resulting in excessive smearing. This situation deteriorates in locations where the local preconditioning factor is not optimized such that the eigenvalues of the Jacobian matrix are in different orders of magnitude. Furthermore, the scalar dissipation is not conservative, and leads to mass conservation problem in practice.

To overcome the difficulties with the scalar dissipation model, matrix dissipation formulations are derived for real-fluid mixture systems following Swanson and Turkel [137] and by Jorgenson and Turkel [138]. To demonstrate the procedure of adding matrix artificial dissipation, backward differencing in time is applied to the governing equations, giving:

$$\left\{\mathbf{\Gamma}+a\frac{\Delta\tau}{\Delta t}\mathbf{T}\right\}\frac{\partial\mathbf{Z}}{\partial\tau}+\frac{\partial\mathbf{E}}{\partial x}+\frac{\partial\mathbf{F}}{\partial y}+\frac{\partial\mathbf{G}}{\partial x}=-\frac{1}{\Delta t}\left(a\mathbf{Q}^{m}-\phi\right), \tag{3.56}$$

or equivalently:

$$\frac{\partial}{\partial x}\left(\rho uY_k\right)+\frac{1}{r}\frac{\partial}{\partial r}\left(r\rho vY_k\right)+\dot{m}''_{k,diff}=MW_k\omega_k \tag{3.57}$$

where $a = 3/2$, $\phi = \left(2\mathbf{Q}^n - \mathbf{Q}^{n-1}\right)/2$, and $\mathbf{A}_v, \mathbf{B}_v,$ and $\mathbf{C}_v$ are Jacobian matrices defined as $\mathbf{A}_v = \partial\mathbf{E}/\partial\mathbf{Z}$, $\mathbf{B}_v = \partial\mathbf{F}/\partial\mathbf{Z}$, $\mathbf{C}_v = \partial\mathbf{G}/\partial\mathbf{Z}$. They are derived as following:

$$\begin{pmatrix} U\rho_p & \rho l_x & \rho l_y & \rho l_z & U\rho_T & U\rho_f \\ l_x + uU\rho_p & \rho(U + ul_x) & \rho ul_y & \rho ul_z & uU\rho_T & uU\rho_f \\ l_y + vU\rho_p & \rho vl_x & \rho(U + vl_y) & \rho vl_z & vU\rho_T & vU\rho_f \\ l_z + wU\rho_p & \rho wl_x & \rho wl_y & \rho(U + wl_z) & wU\rho_T & wU\rho_f \\ (\rho_p h_t + \rho h_p)U & \rho(h_t l_x + uU) & \rho(h_t l_y + vU) & \rho(h_t l_z + wU) & (\rho_T h_t + \rho h_T)U & (\rho_f h_t + \rho h_f)U \\ fU\rho_p & \rho fl_x & \rho fl_y & \rho fl_z & fU\rho_T & (f\rho_f + \rho)U \end{pmatrix}. \quad (3.58)$$

If we replace *l* with $\xi, \eta,$ and ζ we can get $\mathbf{A}_v, \mathbf{B}_v,$ and $\mathbf{C}_v$, respectively.

At this point, the eigenvalues and eigenvectors of the preconditioned system can be derived. Let

$$\mathbf{S} = \mathbf{\Gamma} + a\frac{\Delta\tau}{\Delta t}\mathbf{T}$$
$$= \left(1 + \frac{3}{2}\frac{\Delta\tau}{\Delta t}\right)\begin{pmatrix} \rho_p'' & 0 & 0 & 0 & \rho_T & \rho_f \\ \rho_p'' u & \rho & 0 & 0 & u\rho_T & u\rho_f \\ \rho_p'' v & 0 & \rho & 0 & v\rho_T & v\rho_f \\ \rho_p'' w & 0 & 0 & \rho & w\rho_T & w\rho_f \\ \rho_p'' h_t + \dfrac{T}{\rho}\rho_T & \rho u & \rho v & \rho w & \rho c_p + h_t\rho_T & \rho_f E + \rho E_f \\ \rho_p'' f & 0 & 0 & 0 & \rho_T f & \rho + f\rho_f \end{pmatrix}, \quad (3.59)$$

where $\rho_p'' = \left(\dfrac{\gamma}{\beta} + \dfrac{3}{2}\dfrac{\Delta\tau}{\Delta t}\left(\dfrac{\partial\rho}{\partial p}\right)_{T,Y_i}\right) \Big/ \left(1 + \dfrac{3}{2}\dfrac{\Delta\tau}{\Delta t}\right)$. Then $\mathbf{S}^{-1}$ can be derived as:

$$\mathbf{S}^{-1}=\frac{1}{1+\frac{3}{2}\frac{\Delta\tau}{\Delta t}}\begin{pmatrix} g_{11} & \frac{u\rho_T}{d} & \frac{v\rho_T}{d} & \frac{w\rho_T}{d} & -\frac{\rho_T}{d} & g_{16} \\ -\frac{u}{\rho} & \frac{1}{\rho} & 0 & 0 & 0 & 0 \\ -\frac{v}{\rho} & 0 & \frac{1}{\rho} & 0 & 0 & 0 \\ -\frac{w}{\rho} & 0 & 0 & \frac{1}{\rho} & 0 & 0 \\ g_{51} & -\frac{u\rho_p''}{d} & -\frac{u\rho_p''}{d} & -\frac{u\rho_p''}{d} & \frac{\rho_p''}{d} & g_{56} \\ -\frac{f}{\rho} & 0 & 0 & 0 & 0 & \frac{1}{\rho} \end{pmatrix}, \tag{3.60}$$

where

$$g_{11}=\frac{1}{d}\left\{\rho c_p+\rho_T\left[h-\frac{1}{2}\left(u^2+v^2+w^2\right)\right]+\left(\rho_f c_p-f\rho_T h_f\right)\right\},$$

$$g_{16}=\frac{1}{d}\left(\rho_T h_f-c_p\rho_f\right),$$

$$g_{51}=\frac{1}{d}\left\{\begin{matrix}\left[-\frac{T}{\rho}\rho_T+\rho_p''\left[h-\frac{1}{2}\left(u^2+v^2+w^2\right)\right]\right] \\ +\left(f\rho'' h_f-\frac{T}{\rho^2}\rho_f\rho_T f\right)\end{matrix}\right\}\left(\rho_T h_f-c_p\rho_f\right), \tag{3.61}$$

$$g_{16}=\frac{1}{d}\left(\frac{T}{\rho^2}\rho_f\rho_T-\rho_p'' h_f\right)$$

$$\mathbf{S}^{-1}\mathbf{A}_v=\frac{1}{1+\frac{3}{2}\frac{\Delta\tau}{\Delta t}}\begin{pmatrix} U\varepsilon' & \frac{\rho^2 c_p}{d}l_x & \frac{\rho^2 c_p}{d}l_y & \frac{\rho^2 c_p}{d}l_z & 0 & 0 \\ \frac{l_x}{\rho} & U & 0 & 0 & 0 & 0 \\ \frac{l_y}{\rho} & 0 & U & 0 & 0 & 0 \\ \frac{l_z}{\rho} & 0 & 0 & U & 0 & 0 \\ \frac{U}{d}\left(-\frac{T}{\rho}\rho_T\right)\left(\rho_p-\rho_p''\right) & -\frac{T\rho_T}{d}l_x & -\frac{T\rho_T}{d}l_y & -\frac{T\rho_T}{d}l_z & U & 0 \\ 0 & 0 & 0 & 0 & 0 & U \end{pmatrix}. \tag{3.62}$$

The eigenvalues are:

$$\lambda_{1,2,3,6} = Ub$$
$$\lambda_{4,5} = \frac{b}{2}\left[U\left(1+\varepsilon'\right) \pm \sqrt{U^2\left(1-\varepsilon'\right)^2 + 4\frac{\rho c_p}{d}|\nabla l|^2} \right] \tag{3.63}$$
$$b = 1\Big/\left(1+\frac{3}{2}\frac{\Delta\tau}{\Delta t}\right).$$

The left and right eigenvectors, which correspond to each of the eigenvalues are given by:

$$\mathbf{M} = \begin{pmatrix} 0 & 0 & 0 & \frac{\lambda_5 - \varepsilon' Ub}{\lambda_5 - \lambda_4} & \frac{\lambda_5 - \varepsilon' Ub}{\lambda_4 - \lambda_5} & 0 \\ 0 & m_1/\rho & n_1/\rho & \frac{l_x b}{\rho(\lambda_4 - \lambda_5)} & \frac{l_x b}{\rho(\lambda_5 - \lambda_4)} & 0 \\ 0 & m_2/\rho & n_2/\rho & \frac{l_y b}{\rho(\lambda_4 - \lambda_5)} & \frac{l_y b}{\rho(\lambda_5 - \lambda_4)} & 0 \\ 0 & m_3/\rho & n_3/\rho & \frac{l_z b}{\rho(\lambda_4 - \lambda_5)} & \frac{l_z b}{\rho(\lambda_5 - \lambda_4)} & 0 \\ \frac{T\rho_T}{\rho^2 c_p} & 0 & 0 & B_1 & B_2 & 0 \\ 0 & 0 & 0 & 0 & 0 & 1 \end{pmatrix}, \tag{3.64}$$

$$\mathbf{M}^{-1} = \begin{pmatrix} 1 & 0 & 0 & 0 & \frac{\rho^2 c_p}{T\rho_T} & 0 \\ 0 & \rho m_1 & \rho m_2 & \rho m_3 & 0 & 0 \\ 0 & \rho n_1 & \rho n_2 & \rho n_3 & 0 & 0 \\ 1 & \rho(\lambda_4/b - \varepsilon' U) l_x & \rho(\lambda_4/b - \varepsilon' U) l_y & \rho(\lambda_4/b - \varepsilon' U) l_z & 0 & 0 \\ 1 & \rho(\lambda_5/b - \varepsilon' U) l_x & \rho(\lambda_5/b - \varepsilon' U) l_y & \rho(\lambda_5/b - \varepsilon' U) l_z & 0 & 0 \\ 0 & 0 & 0 & 0 & 0 & 1 \end{pmatrix}, \tag{3.65}$$

where $B_1 = -\frac{T\rho_T}{\rho^2 c_p}\frac{\lambda_5 - \varepsilon' Ub}{\lambda_5 - \lambda_4}$, and $B_2 = -\frac{T\rho_T}{\rho^2 c_p}\frac{\lambda_4 - \varepsilon' Ub}{\lambda_4 - \lambda_5}$.

Following Swanson and Turkel [137], the matrix dissipation term in ξ direction is given by:

$$\mathbf{AD}_i = \mathbf{d}_{i+1/2} - \mathbf{d}_{i-1/2} \,, \tag{3.66}$$

$$\mathbf{d}_{i+1/2} = \mathbf{\Gamma}_{i+1/2} |\mathbf{A}|_{i+1/2} \left(\varepsilon^{(2)}_{i+1/2} \left. \frac{\partial \mathbf{Z}}{\partial \xi} \right|_{i+1/2} - \varepsilon^{(4)}_{i+1/2} \left. \frac{\partial^3 \mathbf{Z}}{\partial \xi^3} \right|_{i+1/2} \right), \tag{3.67}$$

$$|\mathbf{A}|_{i+1/2} = \mathbf{M}_{i+1/2} |\mathbf{\Lambda}|_{i+1/2} \mathbf{M}^{-1}{}_{i+1/2} \,, \tag{3.68}$$

where $\mathbf{\Lambda} = diag(\lambda_1, \lambda_2, \lambda_3, \lambda_4, \lambda_5, \lambda_6)$. The half point values are evaluated using Roe averaging technique. To avoid numerical difficulties caused by zero artificial viscosity at stagnation points or sonic regions, the eigenvalues are limited by:

$$|\lambda_i| = \max\left(|\lambda_i|, V_n \rho(\mathbf{A})\right), \text{ with } \rho(\mathbf{A}) = \max(\lambda_i), i = 1,6 \,. \tag{3.69}$$

The higher-order term is not helpful to TVD or upwinding property, but is intended to eliminate high frequencies and accelerate numerical convergence.

The artificial dissipation coefficient $\varepsilon^{(2)}$ is based on the following switch:

$$\begin{aligned}
&\varepsilon^{(2)}_{i+1/2} = \kappa^{(2)} \max(\nu_i, \nu_{i+1}) \,, \\
&\nu_i = \max \left(\begin{array}{c} \dfrac{(p_{i+1} - 2p_i + p_{i-1})}{\left[(1-\omega)\left(|p_{i+1} - p_i| + |p_i - p_{i-1}| \right) + \omega (p_{i+1} - 2p_i + p_{i-1}) \right]}, \\ \dfrac{(T_{i+1} - 2T_i + T_{i-1})}{\left[(1-\omega)\left(|T_{i+1} - T_i| + |T_i - T_{i-1}| \right) + \omega (T_{i+1} - 2T_i + T_{i-1}) \right]}, \\ \dfrac{(\rho_{i+1} - 2\rho_i + \rho_{i-1})}{\left[(1-\omega)\left(|\rho_{i+1} - \rho_i| + |\rho_i - \rho_{i-1}| \right) + \omega (\rho_{i+1} - 2\rho_i + \rho_{i-1}) \right]} \end{array} \right), \\
&\varepsilon^{(4)}_{i+1/2} = \max\left[0, \left(\kappa^{(4)} - \varepsilon^{(2)}_{i+1/2} \right) \right] \,,
\end{aligned} \tag{3.70}$$

where $\frac{1}{4} \le \kappa^{(2)} \le \frac{1}{2}$, $\frac{1}{64} \le \kappa^{(4)} \le \frac{1}{32}$, $0.05 \le \omega \le 0.5$. The resulting scheme is TVD given the switches above.

3.3 Temporal Discretization

The physical time derivatives in Eq. 3.34 are evaluated by backward differencing

$$\frac{\partial Q}{\partial t} = \frac{1}{\Delta t}[a_1 Q^{n+1} - \phi(Q^n, Q^{n-1}, \ldots)] . \tag{3.71}$$

The coefficient a_1 and function ϕ in Eq. 3.71 can be specified to any level of temporal accuracy desired. In the current work, a three-point backward difference with second-order accuracy is employed. For this situation

$$a_1 = \frac{3}{2}, \ \phi = \frac{1}{2}(4Q^n - Q^{n-1}) . \tag{3.72}$$

The superscripts m and n denote iterations within the pseudo-time domain (inner-loop) and physical time domain (outer-loop), respectively. The physical time term Q^{n+1} can be linearized as

$$Q^{m+1} = Q^m + T\Delta Z^{m+1} . \tag{3.73}$$

Substituting Eq. 3.71 and Eq. 3.73 into Eq. 3.34 yields the following discretized system

$$\begin{aligned} &\left\{\Gamma + a\frac{\Delta\tau}{\Delta t}T\right\}\Delta Z + \frac{\Delta\tau}{\Delta V}\left(\left(\mathrm{E}_\xi - \mathrm{E}_{\xi v}\right)\Big|_{i-1/2,j,k}^{i+1/2,j,k} + \left(\mathrm{F}_\eta - \mathrm{F}_{\eta v}\right)\Big|_{i,j-1/2,k}^{i,j+1/2,k} + \right. \\ &\left.\left(\mathrm{G}_\zeta - \mathrm{G}_{\zeta v}\right)\Big|_{i,j,k-1/2}^{i,j,k+1/2}\right) = \mathrm{H}^{m+1}\Delta\tau - \frac{\Delta\tau}{\Delta t}(a_1 Q^m - \phi) . \end{aligned} \tag{3.74}$$

A fourth-order Runge-Kutta (RK-4) scheme is used to solve the governing equation 3.74 in the pseudo-time space due to its higher temporal accuracy and relatively larger CFL number requirement (i.e., $2\sqrt{2}$ for an Euler calculation using RK-4). A thorough investigation of the stability characteristics of the RK-4 method, based on convection of the turbulence energy-spectrum, has been performed by Apt and Yang [139] to establish its creditability and accuracy. Using the four-step Runge-Kutta scheme, each pseudo-time integration is completed through four consecutive intermediate steps, as given below

$$\begin{aligned} Z_0 &= Z^m , \\ Z_1 &= Z^m + \Delta Z_1, \ (\Gamma + \frac{\Delta\tau}{\Delta t}T - \Delta\tau D)\Delta Z_1 = \alpha_1 \Delta\tau \cdot \mathrm{R}(Z_0) , \end{aligned} \tag{3.75}$$

$$Z_2 = Z^m + \Delta Z_2,\ (\Gamma + \frac{\Delta\tau}{\Delta t}T - \Delta\tau D)\Delta Z_2 = \alpha_2 \Delta\tau \cdot \mathrm{R}(Z_1)\,,$$

$$Z_3 = Z^m + \Delta Z_3,\ (\Gamma + \frac{\Delta\tau}{\Delta t}T - \Delta\tau D)\Delta Z_3 = \alpha_3 \Delta\tau \cdot \mathrm{R}(Z_2)\,,$$

$$Z^{m+1} = Z^m + \Delta Z^{m+1},\ (\Gamma + \frac{\Delta\tau}{\Delta t}T - \Delta\tau D)\Delta Z^{m+1} = \Delta\tau \cdot \mathrm{R}(Z_3)\,,$$

where

$$\begin{aligned} R(z) = \mathrm{H}^{\mathrm{m}} - \frac{1}{\Delta t}(a_1 Q^m - \phi) - [&\left(\mathrm{E}_{\xi} - \mathrm{E}_{\xi v}\right)\Big|_{i-1/2,j,k}^{i+1/2,j,k} \\ &+ \left(\mathrm{F}_{\eta} - \mathrm{F}_{\eta v}\right)\Big|_{i,j-1/2,k}^{i,j+1/2,k} + \left(\mathrm{G}_{\zeta} - \mathrm{G}_{\zeta v}\right)\Big|_{i,j,k-1/2}^{i,j,k+1/2}]\,. \end{aligned} \tag{3.76}$$

Superscripts 'm' and '$m+1$' stand for the solution at the 'm^{th}' and '$(m+1)^{\mathrm{th}}$' pseudo-time steps, respectively. The coefficients α_1, α_2, and α_3 can be varied to obtain a variety of schemes with different stability properties. The standard four-step scheme has the following values (Jameson, 1983)

$$\alpha_1 = \frac{1}{4}\ ,\quad \alpha_2 = \frac{1}{3}\ ,\quad \alpha_3 = \frac{1}{2}\ . \tag{3.77}$$

The iteration begins from pseudo-time steps (inner-loop). At convergence in pseudo-time step, the solution proceeds one physical time step (outer-loop).

3.4 Boundary Conditions

In all cases considered, second-order accurate boundary conditions are implemented. The inlet and exit conditions are specified using the method-of-characteristics (MOC). Adiabatic and noslip conditions are imposed at the solid wall. Elsewhere conditions are specified using second-order extrapolated values. These conditions produce zero normal gradients with respect to pressure, velocity, temperature, and species mass fraction.

3.4.1 Characteristic Boundary Conditions

At the inlet and outlet boundary, care must be taken when specifying the numerical boundary conditions. One has to ensure that the unphysical spurious wave reflections are avoided at the boundary and the flow is capable of relaxing to ambient conditions in the prescribed ways, which can be satisfied using the MOC proposed by Poinsot and Lelef [140]. In the absence of a significant diffusion processes, the MOC method provides correct number of conditions that must be specified, as well as conditioned information from the interior domain.

Implementation of the MOC procedure involves diagonalizing the governing system to a quasi-one-dimensional characteristic form

$$[S+LM^{-1}\Gamma^{-1}(\Gamma+\frac{\Delta\tau}{\Delta t}T-\Delta\tau D)]\Delta Z=-LM^{-1}\Gamma^{-1}$$
$$\left\{(\frac{\partial E}{\partial x}+\frac{\partial F}{\partial y}+\frac{\partial G}{\partial z})+\Omega+\frac{\Delta\tau}{\Delta t}(a_1Q^n-\phi)-H\right\}. \quad (3.78)$$

All of the terms in Eq. 3.78 are evaluated at cell centroids using the finite difference methodology. The term Ω is the vector of specified boundary conditions. The term L is a selection matrix that singles out the desired characteristics at respective boundaries. The Jabobian matrix S is defined as $S=\partial\Omega/\partial Z$.

In the absence of significant diffusion processes, the MOC procedure dictates the correct number of conditions that must be specified at each boundary and provides well-conditioned information from the interior domain. In this study, the conditions imposed at the inlet and exit planes remain subsonic. At the inlet, there is one outgoing characteristic and N+3 conditions must be specified. Here the temperature, velocity, and species concentrations are employed assuming fully-developed turbulent channel flow. These conditions are given by

$$\Omega_{inlet} = \Delta V \begin{pmatrix} 0 \\ u - u_{ref} \\ v - v_{ref} \\ w - w_{ref} \\ T - T_{ref} \\ Y_1 - Y_{1_{ref}} \\ \vdots \\ Y_N - Y_{N-1_{ref}} \end{pmatrix}, \; L_{inlet} = \begin{pmatrix} 1 & 0 & 0 & 0 & 0 & 0 & \dots & 0 \\ 0 & 0 & 0 & 0 & 0 & 0 & \dots & 0 \\ 0 & 0 & 0 & 0 & 0 & 0 & \dots & 0 \\ 0 & 0 & 0 & 0 & 0 & 0 & \dots & 0 \\ 0 & 0 & 0 & 0 & 0 & 0 & \dots & 0 \\ 0 & 0 & 0 & 0 & 0 & 0 & \dots & 0 \\ \vdots & \vdots & \vdots & \vdots & \vdots & \vdots & \ddots & \vdots \\ 0 & 0 & 0 & 0 & 0 & 0 & \dots & 0 \end{pmatrix}. \tag{3.79}$$

where u_{ref}, v_{ref}, w_{ref}, and T_{ref}, $Y_{1_{ref}}$, …, $Y_{N-1_{ref}}$ represent the specified values of velocity components, temperature, and species mass fraction, respectively. At the exit, there are N+3 outgoing characteristics and one condition must be specified. Here a far-field pressure condition is simulated using the methodologies proposed by Rudy and Strikwerda [141], Poinsot and Lele [140], and Baum et al. [142].

To simulate the far-field boundary the incoming characteristic given by Eq. 3.78 is modified to provide a nonreflecting outflow condition. The equation of interest is given by the selection matrix

$$L = \begin{pmatrix} 1 & 0 & 0 & 0 & 0 & 0 & \dots & 0 \\ 0 & 0 & 0 & 0 & 0 & 0 & \dots & 0 \\ 0 & 0 & 0 & 0 & 0 & 0 & \dots & 0 \\ 0 & 0 & 0 & 0 & 0 & 0 & \dots & 0 \\ 0 & 0 & 0 & 0 & 0 & 0 & \dots & 0 \\ 0 & 0 & 0 & 0 & 0 & 0 & \dots & 0 \\ \vdots & \vdots & \vdots & \vdots & \vdots & \vdots & \ddots & \vdots \\ 0 & 0 & 0 & 0 & 0 & 0 & \dots & 0 \end{pmatrix}. \tag{3.80}$$

Associated with this equation is the term

$$\Pi_2 = \lambda_2 \left[\frac{1}{\varepsilon} \frac{u - \lambda_2}{a} \frac{\partial p}{\partial x} - \rho a \frac{\partial u}{\partial x} \right], \tag{3.81}$$

which characterizes the time variation of the normal component of acoustic waves that propagate from an infinitely distant downstream source into the computational domain.

The term λ_2 is the acoustic eigenvalue given by Eq. 3.20. Conceptually, a perfectly non-reflecting subsonic outflow condition can be obtained if this term is set equal to zero. Specifying such a condition, however, eliminates the information provided by the acoustic waves and leads to an ill-posed problem. To simulate this information Rudy and Strikwerda [141], Poinsot and Lele [140], and Baum et al. [142] proposed that Eq. 3.81 be replaced with the term

$$\Pi_2^k = k(p - p_\infty), \tag{3.82}$$

where k is a constant that determines the speed with which the average pressure in the computational domain relaxes towards the imposed pressure at infinity p_∞. This condition introduces small amplitude acoustic waves using scaling arguments that are based on known quantities at the exit. Rudy and Strikwerda [141] proposed that optimal values of k are given by

$$k = 2\frac{\sigma}{x_c}\frac{\varepsilon a^2(1-\bar{M}^2)}{\sqrt{u(1-\varepsilon)^2 + 4\varepsilon a^2}}. \tag{3.83}$$

The factor presented here has been modified from that given by Rudy and Strikwerda [141] to accommodate the dual-time preconditioned system. Here $\bar{M}^2$ represents the maximum Mach number in the computational domain, x_c is the characteristic axial length of the domain, ε is the local preconditioning factor, and a is the local speed of sound. The term σ is a scaling factor used for optimization. Poinsot and Lele [140], and Baum et al. [142] have shown that values ranging from 0.25 to 0.5 provide the best results. When lower values are specified, solutions tend to drift away from the reference pressure. When larger values are specified, flow oscillations are introduced.

To implement the MOC methodology with the far field pressure condition described above, the $N+3$ outgoing characteristics are selected and the incoming characteristic is modified by replacing the incoming wave amplitude given by Eq. 3.81. These conditions are given by

$$\Omega_{outlet} = \Delta V \begin{pmatrix} p - p_{ref} \\ 0 \\ 0 \\ 0 \\ 0 \\ 0 \\ \vdots \\ 0 \end{pmatrix}, \; L_{outlet} = \begin{pmatrix} 0 & 0 & 0 & 0 & 0 & 0 & \cdots & 0 \\ 0 & 1 & 0 & 0 & 0 & 0 & \cdots & 0 \\ 0 & 0 & 1 & 0 & 0 & 0 & \cdots & 0 \\ 0 & 0 & 0 & 1 & 0 & 0 & \cdots & 0 \\ 0 & 0 & 0 & 0 & 1 & 0 & \cdots & 0 \\ 0 & 0 & 0 & 0 & 0 & 1 & \cdots & 0 \\ \vdots & \vdots & \vdots & \vdots & \vdots & \vdots & \ddots & \vdots \\ 0 & 0 & 0 & 0 & 0 & 0 & \cdots & 1 \end{pmatrix}. \tag{3.84}$$

The far-field pressure condition has been shown to be effective in reducing reflections at the subsonic exit boundary and is relatively accurate and stable.

3.5 Parallel Implementation

Since the explicit time-stepping numerical scheme is applied in the current study, only the data from neighboring cells instead of the whole computational domain were required during the calculation of variables in each cell. Since the data dependence is weak, the domain decomposition technique is best suited for this kind of application. It is also commonly implemented in distributed-memory parallel computer systems. In the field of computational fluid dynamics (CFD), it is generally referred to as mesh partitioning, based on the geometric substructure of the computational domain. In the domain-decomposition technique, the physical domain is divided into several sub-domains. Variables in each cell are updated to the next time step simultaneously. In order to calculate the spatial derivatives at the sub-domain boundaries, ghost cells or halo data around the computing cells are introduced. Figure 3.4 shows an example of a two-dimensional sub-domain with ghost cells. Because the variables in the ghost cell are updated in another sub-domain, message passing is required to synchronize data between different sub-domains. The communication overhead is directly proportional to the volume-to-surface ratio of the grid system in that sub-domain. Maximizing the computation-to-communication ratio leads to higher parallel execution efficiency.

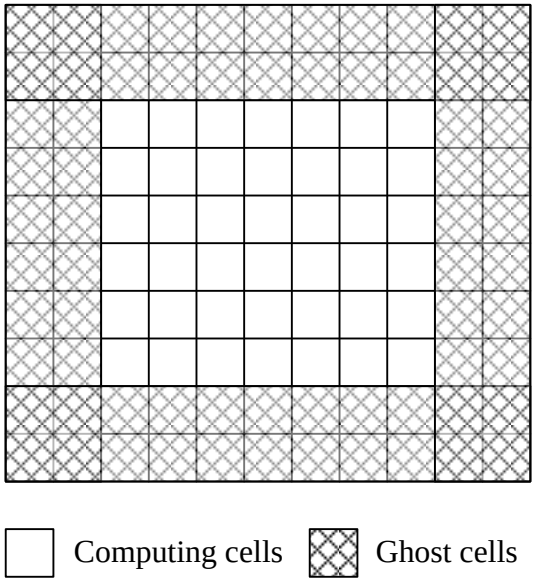

Figure 3.4: Schematic of a two-dimensional sub-domain with ghost cells.

High Performance Computing (HPC) clusters used to conduct the large-scale computations required in the current studies. The in-house program is highly paralleled, and each decomposed sub-domain is computed by one CPU core. Communication at the domain boundary is made through a message passing interface (MPI).

CHAPTER 4

SWIRL INJECOR FLOW DYNAMICS

Swirl injectors have been broadly used in contemporary liquid-propellant rocket engines to achieve efficient mixing and combustion, but the understanding of injector flow physics and dynamics at supercritical conditions is still very limited. This chapter intends to improve such understanding by carrying out a systematic three-dimensional numerical study of simplex swirl injector under supercritical condition using LOX as the oxidizer. We are going to characterize the three-dimensional flow structures and underlying physics for the first time and explore various instability mechanisms dictating fluctuations of flow properties.

4.1 Physical Configuration and Flow Conditions

Figure 1a shows the prototype of the liquid-liquid bi-swirl injector of concern originating from the RD-0110 engine, which powered the third stage of the Soyuz space vehicle. LOX and kerosene are injected tangentially through six cylindrical inlets, respectively. In this chapter, we only consider the inner swirler, i.e., the pure LOX injection, and remove outer swirler in the coaxial annulus. Figure 1b shows the major components of the inner swirler: tangential inlets, a vortex chamber, and a discharge nozzle. The baseline geometry and operating conditions are listed in Table 4.1, where R_v and R represent the radii of the vortex chamber and discharge nozzle, respectively, and L the injector length. T_{in}, T_0, p_0, and $\dot{m}$ denote the inlet temperature, ambient temperature, ambient pressure, and mass flow rate, respectively.

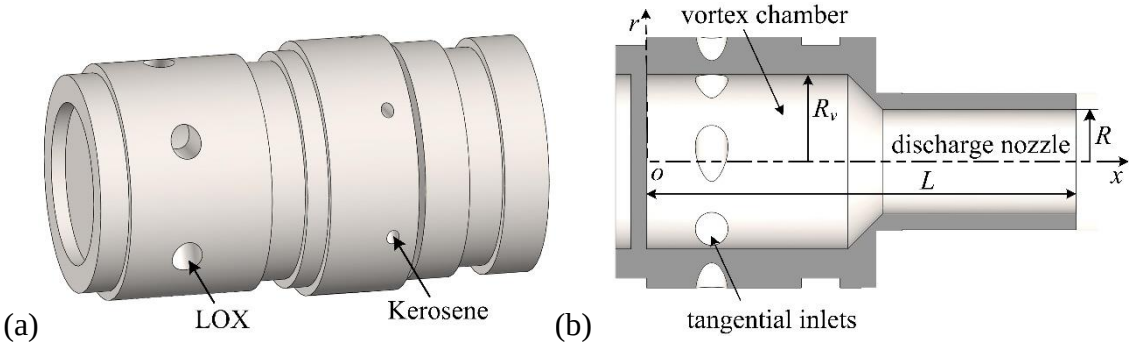

Figure 4.1: LOX/kerosene bi-swirl injector of RD-0110 engine.

Table 4.1: Baseline geometry and operating conditions.

R_v (mm)	R (mm)	L (mm)	T_{in} (K)	T_0 (K)	p_0 (atm)	$\dot{m}$ (kg/s)
4.5	2.7	22.7	120	300	100	0.15

The computational domain includes the injector interior (8.4R in the axial direction) and a downstream region (25R with 7.4R in the axial and radial directions, respectively). The noslip and adiabatic boundary conditions are applied at the injector solid surface. At the inlets, the azimuthal and radial velocities are determined from the given mass flow rate and swirl strength. The pressure is automatically obtained from radial momentum equation. A broadband noise with a Gaussian distribution is superimposed onto the inlet velocity components to provide the turbulence at an early stage. The disturbances are produced by the Gaussian random-number generator with an intensity of 5% of the mean quantities, which is sufficient to trigger the instability inherent in the flowfield. At the downstream boundary, the non-reflecting boundary conditions based on characteristic equations proposed by Poinsot and Lelef [143] are applied to avoid undesirable wave reflection by extrapolation of primitive variables from the interior region. A reference pressure is applied to preserve the average pressure in the computational domain.

4.2 Results and Discussion

4.2.1 Grid Independence Study

The baseline mesh system has 5 million cells, of which 1.7 million cells locate within the injector. The meshes are clustered near the wall, mixing layer, and immediately downstream of the injector to resolve steep gradients in these regions. The smallest grid size in the radial direction is 5 μm, compared to the Taylor scale of 8.4 μm at the injector exit. The computational domain is divided into 636 blocks with each computed on a single processor. Figure 4.2 shows the distribution of blocks. The physical time step is 10^{-6} ms and the Courant-Friedrichs-Lewy (CFL) number is 0.4.

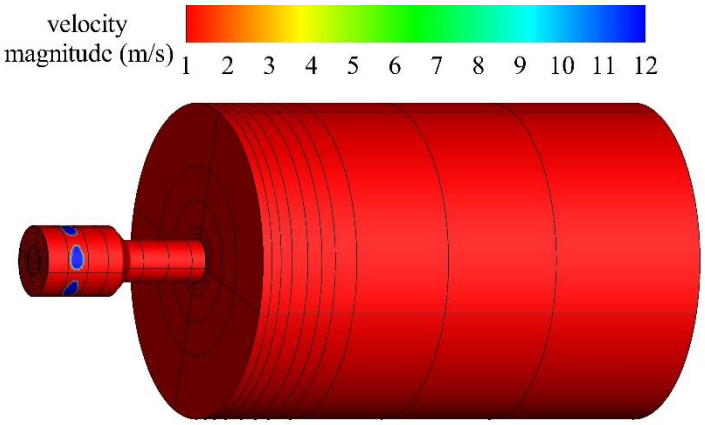

Figure 4.2: Distribution of blocks in the whole computational domain.

In order to ensure the appropriate accuracy of underlying flow physics with the aforementioned grid resolution, a grid independence study is performed as the validation procedure. Since enormous computation cost is required for a finer three-dimensional grid system, an axisymmetric study is conducted with the identical grid resolution in radial and axial directions. Periodic boundary conditions are specified in the azimuthal direction. A finer mesh, which doubles the number of cells in both axial and radial directions, is studied as the comparable case.

Figure 4.3 shows the radial distributions of mean density (ρ), temperature (T), and velocity components (u_x and u_θ) for two grid systems near the injector exit. The maximum derivation of all flow properties is less than 5%. In addition, it is found that the relative errors of spreading angle and liquid film thickness are lower than 3%, and that the frequency spectrum of the pressure field indicates an identical dynamic behaviors. Therefore, the current grid system is believed to capture the main characteristics of the LOX injection and mixing process.

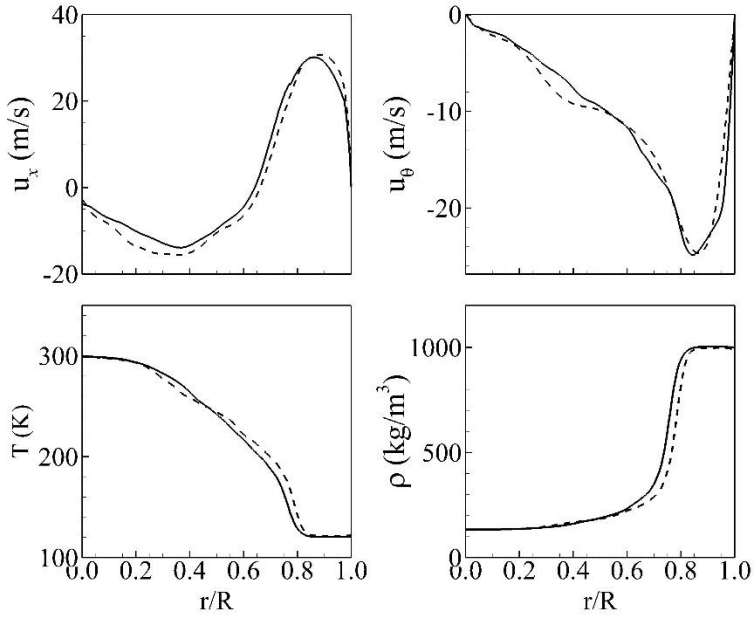

Figure 4.3: Radial distributions of time-averaged flow properties at the axial location x/R = 8.3 for two grid systems: solid line: baseline; dashed line: finer mesh.

4.2.2 Supercritical Fluid Regions

Figure 4.4 shows the instantaneous distribution of the oxygen density field in both longitudinal and transverse views. LOX is tangentially introduced at a subcritical temperature (120 K) into the vortex chamber, which is initially occupied by gaseous oxygen (300 K). The swirl-induced centrifugal force produces a large pressure gradient in

the radial direction, leading to the LOX film flowing along the injector wall. A low-density gaseous core forms in the center region due to the conservation of mass and angular momentum. The density varies smoothly from liquid-like dense fluid near the wall to gas-like dense fluid near the centerline along the radial direction. A natural question is how to distinguish the fluid states of liquid-like and gas-like.

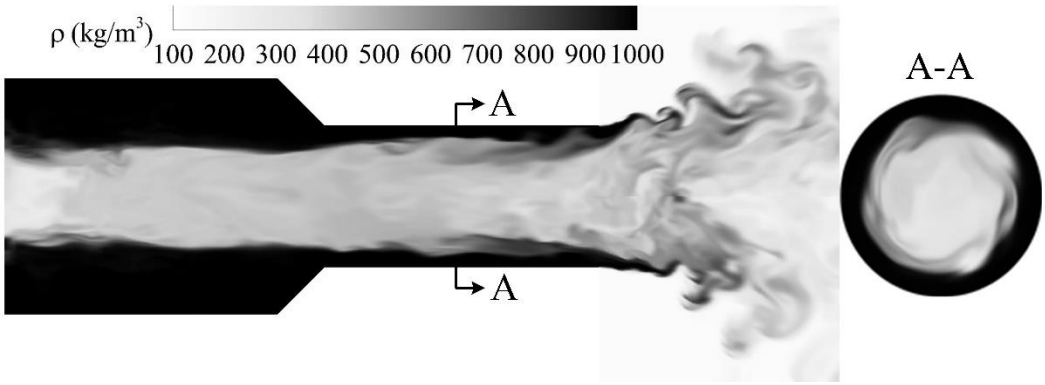

Figure 4.4: Instantaneous distribution of the density field in longitudinal and transverse views, *p*=100 atm.

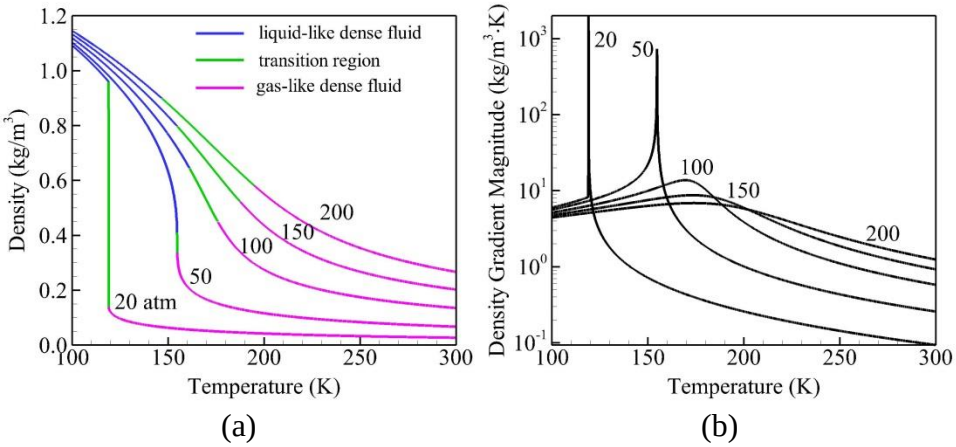

(a) (b)

Figure 4.5: Density (a) and density gradient (b) of oxygen as a function of temperature at various pressures.

The idea can be conceived from the density-temperature property diagram as shown in Fig. 4.5. At subcritical pressures, a distinctive interface separates the dense-liquid phase

from the light-gas phase when the temperature increases (e.g., p = 20 atm). Such interface corresponds to the infinite value of the density gradient with respect to temperature in Fig. 4.5b. At supercritical pressures, however, a finite value of the maximum density gradient exists, and it represents the sharpest change of fluid density. A fluid transition region is thus defined as the regime where the density gradient is not less than the 90% of its maximum magnitude. As indicated in Fig.4.5a, the transition region (green lines) connects the fluid in a liquid state (blue lines) with the fluid in a gaseous state (pink lines). It becomes wider with the increasing pressure, but degenerates into a sharp interface as the pressure decreases to subcritical values.

For p = 100 atm, the upper and lower bound of density values for the transition region are 645 and 450 kg/m^3, respectively. Figure 4.6 shows the temporal evolution of density distributions at different axial locations. The area enclosed by the two solid curves represents the transition region. It becomes larger as the LOX film convects downstream.

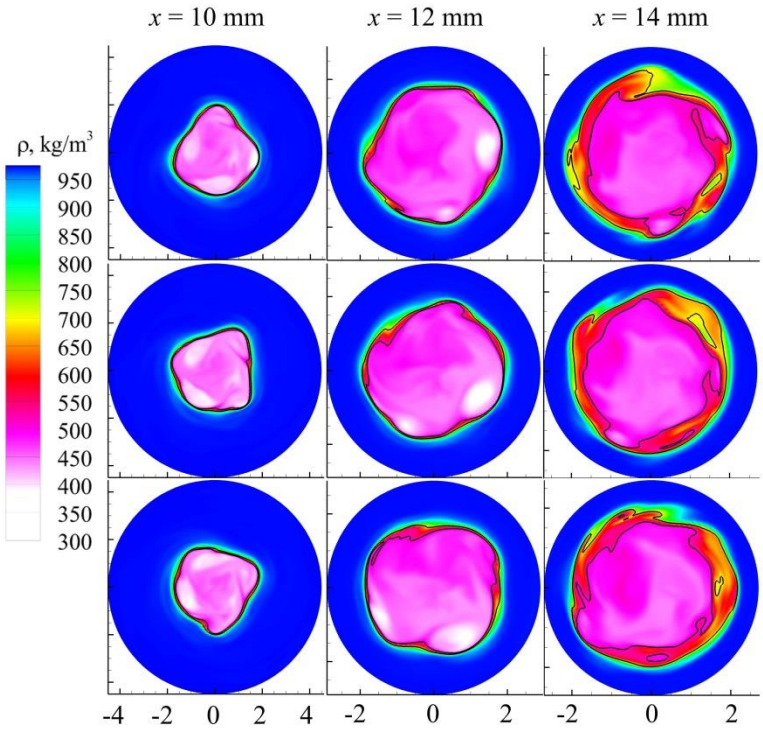

Figure 4.6: Temporal evolution of density distributions at different axial locations, Δt = 0.06 ms, *p*=100 atm.

4.2.3 Instantaneous Flow Field

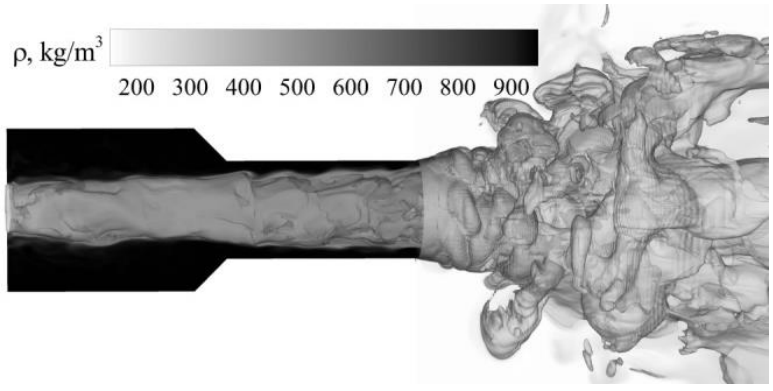

(a)

(b)

Figure 4.7: (a) Instantaneous distribution of density field with two iso-surfaces: ρ = 532 and 250 kg/m3; (b) iso-surface of azimuthal velocity at $u_\theta = 4$ m/s; *p*=100 atm

Figure 4.7a shows the instantaneous distribution of density field interpolated with two density iso-surfaces (ρ = 532 and 250 kg/m^3). The strong swirling motion and its associated centrifugal force produce large pressure gradients in the radial direction and a low-pressure core near the centerline, leading to the LOX film flowing along the wall. The low-density gaseous core in the center forms because of the conservation of mass and angular momentum. The axial velocity increases significantly through the converging nozzle. As a consequence, the thickness of the LOX film in the vortex chamber is larger than that in the discharge nozzle due to mass conservation. The density iso-surfaces are corrugated by various flow instabilities in the injector, leading to the wavy structures of the liquid film. Figure 4.7b shows the iso-surface of the azimuthal velocity at 4 m/s. The central gaseous core is highly wrinkled due to the interaction of hydrodynamic and acoustic instabilities. Helical instability is observed near the injector exit and disappears further downstream due to the decay of swirling motion.

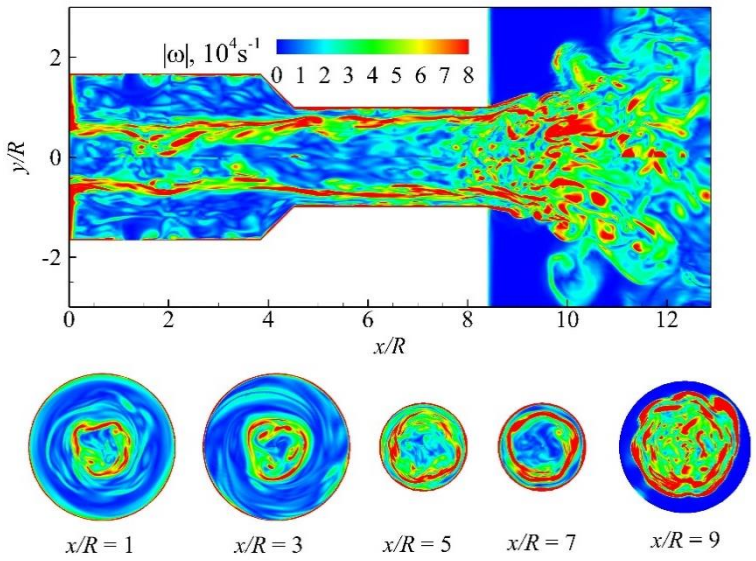

Figure 4.8: Instantaneous snapshot of vorticity magnitude at different cross-sectional views, $p = 100$ atm.

Figure 4.8 shows the snapshot of the vorticity magnitude at different cross-sectional views. The flow evolution exhibits several distinct features. The flowfield is essentially irrotational in the LOX film and central gaseous core due to the small velocity difference in these regions. Strong vorticity zones concentrate in the wall boundary layer and in the mixing layer between dense liquid and light gas. The flow expands at the injector exit and the swirling motion decays rapidly along the axial distance. According to the radial momentum balance,

$$\frac{\partial p}{\partial r} \sim f_c \sim \frac{\rho u_0^2}{r} \tag{4.1}$$

where f_c represents the centrifugal force and u_0 the azimuthal velocity. The decrease of azimuthal velocity renders pressure to recover in the downstream region, and the resultant positive pressure gradient tends to decreases axial velocity and eventually generates the center-recirculating flow, a phenomenon commonly called vortex breakdown. This causes dynamic distribution of vorticity at the injector near-field. The vorticity layer, generated by the flow detachment from the injector rim, subsequently rolls, tilts, stretches, and breaks

up into small eddies. These eddies interact and merge with the surrounding flow and finally dissipate further downstream. The temporal evolution of the flowfield permits insight into the vortex breakdown phenomenon. Figure 4.9 shows the instantaneous streamlines on a longitudinal plane, spatially averaged in the azimuthal direction, during a typical flow period. As the small bubble separates from its parent, it travels downstream and eventually coalesces with the large vortex bubble in the downstream.

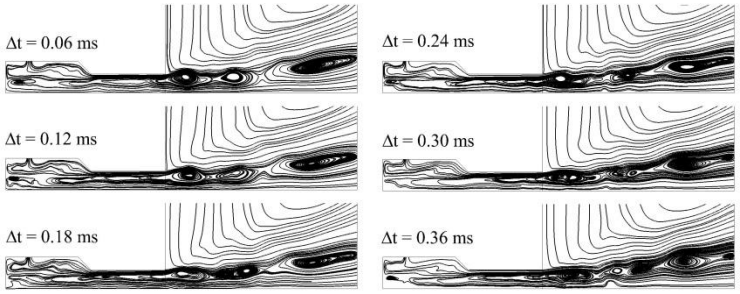

Figure 4.9: Temporal evolution of spatially-averaged streamlines, $\Delta t = 0.06$ ms, $p = 100$ atm.

Vorticity dynamics plays an essential role in the description of turbulent flows. To identify the major mechanisms responsible for vorticity production/destruction under supercritical conditions, the budget of vorticity magnitude is examined to quantify the overall vorticity variation. The transport equation for vorticity magnitude follows the form

$$\frac{Dw \cdot w}{Dt} = 2w \cdot (w \cdot \nabla)u - 2w \cdot w(\nabla \cdot u) - 2w \cdot \nabla\left(\frac{1}{\rho}\right) \times \nabla(p) + 2w \cdot \nabla \times \left(\frac{\nabla \cdot \tau}{\rho}\right) \qquad (4.2)$$

where w is the vorticity and τ the viscous stress tensor. The four terms on the right-hand side represent the effects of vortex stretching/tilting, volume dilatation, baroclinic torque, and viscous dissipation, respectively. For a cryogenic fluid under supercritical conditions, severe property variations occur when the swirling liquid is heated by the ambient gas. Both the volume dilatation and baroclinic torque become significant in determining vorticity transport. Figure 4.10 shows the radial distributions of azimuthally-averaged

vorticity budget normalized by the bulk velocity and momentum thickness at three different axial locations. Vortex stretching/tilting is dominant for the shear-layer vorticity production in the vortex chamber ($x/R_n=1$) and discharge nozzle ($x/R_n=5$). In the injector near-field ($x/R_n=9$), however, both of volume dilatation and baroclinic torque are significant in the outer shear-layer, where the LOX film mixing with ambient gaseous oxygen.

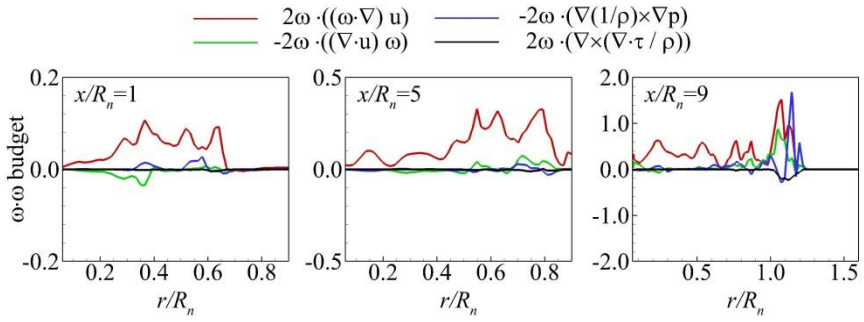

Figure 4.10: The radial distributions of vorticity magnitude spatially averaged in the azimuthal direction at three different axial locations, $p=100$ atm.

4.2.4 Characteristics of Wave Propagation

For a liquid swirler, a disturbance at the inlet causes the fluctuation of the liquid free surface, which then propagates downstream both longitudinally and azimuthally. Figure 4.11 shows the the iso-surface of the azimuthal velocity at 22 m/s in the phase space, in which the physical domain is unwrapped in the azimuthal direction. Generally, a flow variable can be expressed by a Fourier series in the cylindrical coordinate system (x, r, θ),

$$G(x,r,\theta,t)=\sum_{m=-\infty}^{\infty} g_m(x,r,t)e^{im\theta} \tag{4.3}$$

where g_m is the Fourier coefficient and m the azimuthal wave number. $m=0$ represents the axisymmetric mode, and the others ($m\neq 0$) the helical modes. In the vortex chamber (x <= 10.4 mm), three helical waves coupled with small-scale structures are observed,

indicating that the helical mode $m=-3$ dominates the flowfield. The later section will demonstrate that this specific helical mode is triggered by the excited acoustic wave with the same frequency. In the discharge nozzle, the higher axial velocity accelerates the spiral structure, leading to the bend-over of the wave shape. The helical waves are distorted by the strong axial shear-layer because of the large velocity difference between the LOX film and gaseous core.

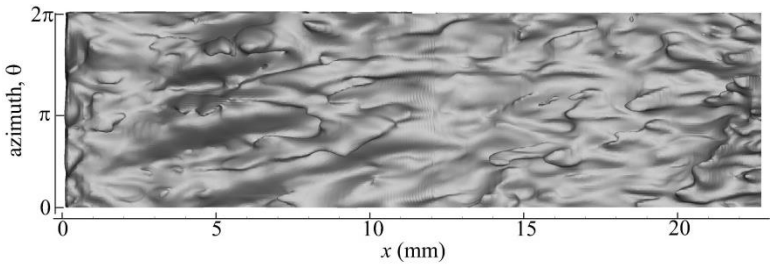

Figure 4.11: Iso-surface of azimuthal velocity at $u_\theta = 22$ m/s in azimuthal phase space ($\theta = 0 \sim 2\pi$), $p = 100$ atm.

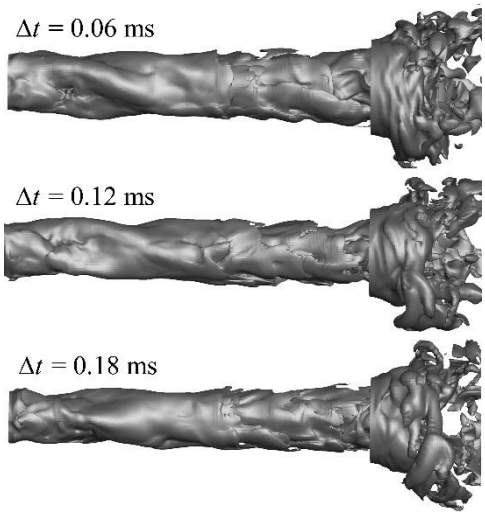

Figure 4.12: Temporary evolution of the density iso-surface at $\rho_s = 532$ kg/m3, $p = 100$ atm.

To understand the propagation mechanisms, hydrodynamic waves in longitudinal and azimuthal directions are analyzed separately. Figure 4.12 shows the temporal evolution

of the density iso-surface at $\rho = 532$ kg/m^3. The spiral shape forms in the vortex chamber, while the cone-shaped surface is produced with ligaments in the discharge nozzle. This difference might be related to the Kelvin-Helmholtz (KH) shear-layer instability in the fluid transition region. The flow motion is swirl-dominated with a small axial momentum in the vortex chamber, and hence the axial KH instability is relatively weak and induces a smooth iso-surface. The axial velocity of the LOX film significantly increases through the converging nozzle, leading to the strong KH instability in the discharge nozzle. In addition, the baroclinic effect resulting from the misalignment of the density gradient and pressure gradient can induce the flow instability. The significance of these effects can be determined from the vorticity transport budget as described in the previous section. The calculated propagation speed for the longitudinal wave is approximately 30 m/s. For an inviscid, incompressible flow with the neglect of the radial velocity and assumption of an infinitesimal film thickness compared to the wavelength, the form of the wave speed bears a close resemblance to that for shallow-water wave propagation [21] and can be expressed explicitly as,

$$a_x = \sqrt{\left(\frac{u_{in}^2 R_{in}^2}{r_m^3}\right)\left(\frac{R^2 - r_m^2}{2r_m}\right)} \tag{4.4}$$

here u_{in}, R_{in}, and r_m represent the inlet velocity, swirling arm, and radius of the liquid film surface, sespectively. The computed wave speed by Eq. 4.4 is 37 m/s, which overweighs the current simulation result. This can be explained by the neglect of fluid compressibility and viscous effects in Eq. 4.4.

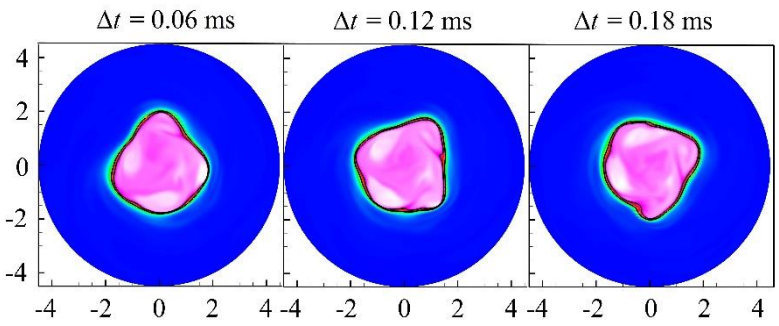

Figure 4.13: Temporal evolution of density distributions at $x=10$ mm, $p=100$ atm.

Figure 4.13 shows the temporal evolution of density distributions at $x=10$mm in the transverse direction. The azimuthal wave speed in the transition region is 27.4 m/s. According to the inviscid theory, the azimuthal wave speed can be approximated as,

$$a_\theta = \sqrt{\left(\frac{u_{in}^2 R_{in}^2}{r_m^3}\right)\left(R_n - r_m\right)} \tag{4.5}$$

It gives the azimuthal wave at a speed of 33 m/s, which is slightly larger than the current value. The characteristic frequency of the helical mode $m=-1$ is found to be 1.6 kHz if one traces the fluid particle in a period. Given the frequency of the helical mode $m=-1$, the frequencies of all helical modes can thus be obtained by,

$$f_m = \frac{1}{0.62}\times|m| \text{ kHz},\ m=\pm1,\ \pm2,\ \pm3,\ldots \tag{4.6}$$

Therefore, the frequency of the dominant helical mode $m=-3$ is 4.8 kHz according to Eq. 4.6.

4.2.5 Injector Flow Dynamics

The injector dynamics involve intricated flow processes covering a wide range of time and length scales. Quantitative information can be obtained using spectral analysis. Figure 4.14 shows the selected probe positions in the LOX film that are used for spectral analysis. These positions are well-distributed in the vortex chamber, discharge nozzle, and immediately downstream of injector. To ensure the probed data statistically meaningful,

the time histories of pressure fluctuations at probes 1, 8, 10, and 11 along the flow passage are presented in Fig. 4.15. It is observed that the pressure at these locations oscillates periodically and that the data are reasonable for spectral analysis. The time period of hydrodynamic wave in the longitudinal direction is estimated at 1.1 ms, corresponding to the frequency of 0.9 kHz.

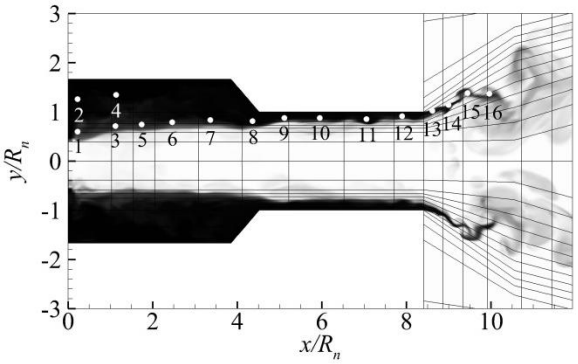

Figure 4.14: Probe positions within the liquid film inside the injector and near the injector exit.

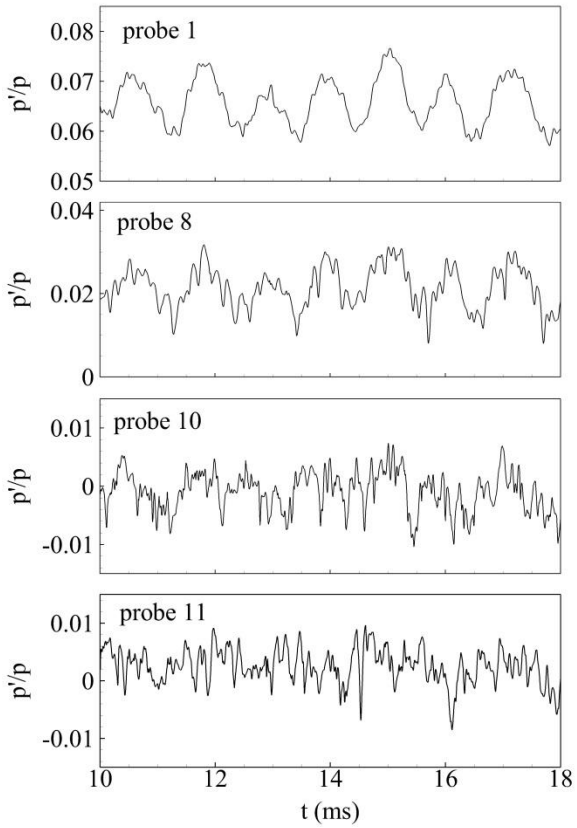

Figure 4.15: Time histories of pressure fluctuations at four different probe locations.

Figures 4.16-19 show the power spectral densities of pressure oscillations at different locations along the injector. Flow instabilities are quantitified and decomposed into various modes. The high-frequency modes with small wavelengths are confined in the vortex chamber because of wave reflection between the headend and conical convergent section, while low-frequency modes with long wavlengths are able to transmit to the discharge nozzle. Most of flow disturbances thus remain in the vortex chamber, leading to the relatively small amplitude pressure fluctuations in the discharge nozzle as shown in Fig. 4.19. Two dominant modes at the frequency of 0.9 kHz and 0.6 kHz are observed at all probe positions inside the injector. The former is closely related to the longitudinal hydrodynamic wave, while the latter may be related to the radial wave induced by centrifugal instability.

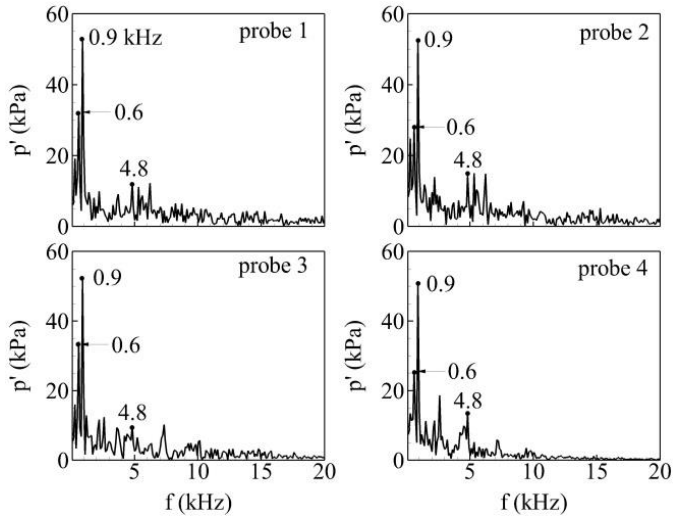

Figure 4.16: Power spectral densities of pressure fluctuations at four different locations (probe 1-4) in the vortex chamber.

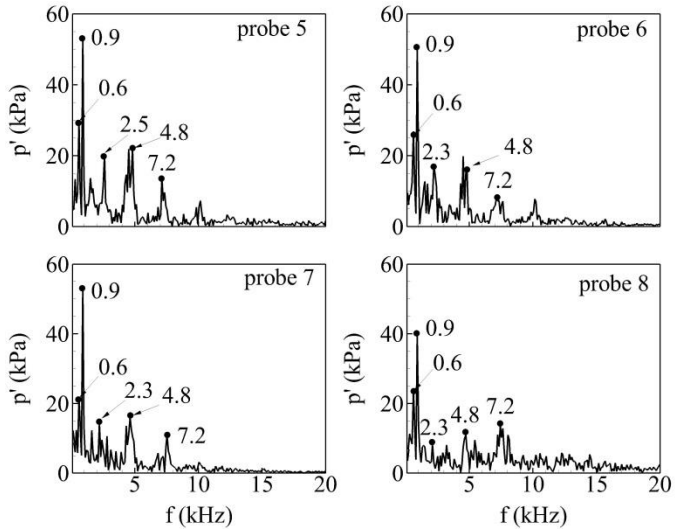

Figure 4.17: Power spectral densities of pressure fluctuations at four different locations (probe 5-8) in the vortex chamber.

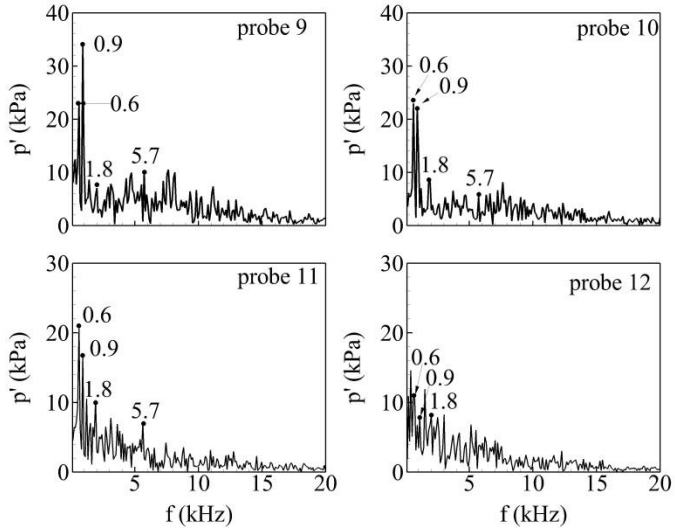

Figure 4.18: Power spectral densities of pressure fluctuations at four different locations (probe 9-12) in the nozzle.

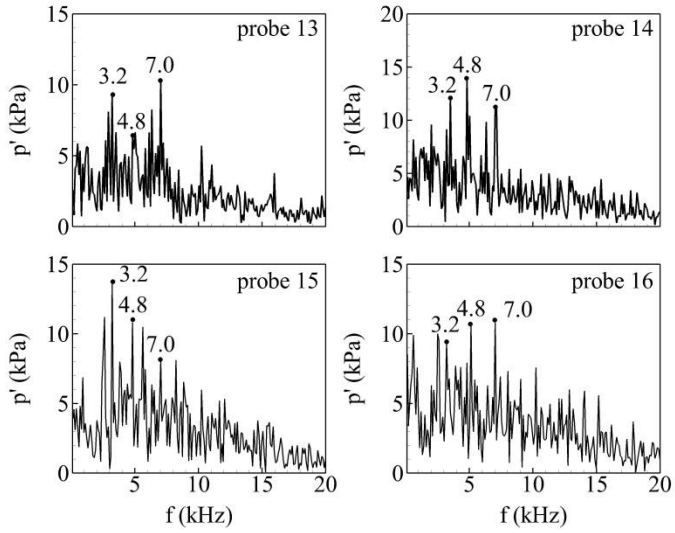

Figure 4.19: Power spectral densities of pressure fluctuations at four different locations (probe 13-16) near the injector exit.

The injector configuration can be acoustically treated as a quarter-wave resonator and characterized by a formula of the natural frequency,

$$f = c/4(L+\Delta l) \qquad (4.7)$$

where L is the injector length, c is the speed of sound, and Δl is the correction factor and is taken as $0.6R$. In the present study, the temperature of oxygen varies from subcritical to

supercritical along the radial direction. The speed of sound changes accordingly. Figure 4.20 shows the oxygen sound speed as a function of temperature at various pressures. It first decreases and then increases with the increasing temperature. The average speed of sound, estimated as 470 m/s, is used to compute the acoustic frequency, which turns out to be 4.8 kHz. The acoustic wave drives the specific helical mode $m=-3$ with the same frequency (4.8 kHz) in the vortex chamber. The flow motion becomes broadband and no dominant oscillation can be found due to the strong interactions of the outer shear layer and the center recirculation zone near the exit of injector. Shear-layer and centrifugal instabilities are coupled with acoustic instability, incurring that the spectral contents become very rich and are characterized by several different frequencies in various regions.

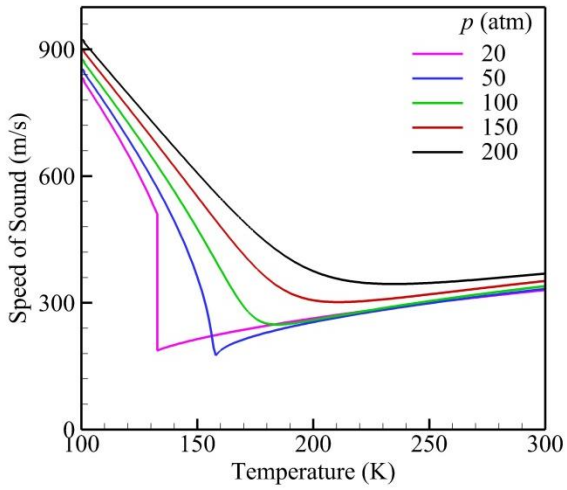

Figure 4.20: Speed of sound of oxygen as a function of temperature at various pressures.

The injector flow dynamics are further explored using the proper orthogonal decomposition (POD) technique, which is an empirical mathematical technique capable of extracting dynamically significant structures from the flowfield of concern. For a given flow property, $f(\boldsymbol{x},t)$, the POD analysis can determine a set of orthogonal functions, $\varphi_j(\boldsymbol{x})$, $j=1, 2, ...$, such that the projection of $f(\boldsymbol{x},t)$ onto the first n functions,

$$\hat{f}(\boldsymbol{x},t)=\bar{f}(\boldsymbol{x})+\sum_{j=1}^{n}a_j(t)\varphi_j(\boldsymbol{x}) \tag{4.8}$$

has the smallest error, defined as $E\left(\| f-\hat{f} \|\right)$. Here $\boldsymbol{x}$ is the spatial coordinate in the three-dimensional space and $a_j(t)$ represents the temporal variation of the jth mode. $E(\cdot)$ and $\|\cdot\|$ denote the time average and L^2-norm in the space, respectively. The scalar function f can be extended to a vector F by introducing an appropriate inner product. A more complete discussion of this subject can be found in Refs. [144] and [145]. This chapter mainly focuses on the pressure-fluctuation field, p'. In order to capture all possible characteristic modes related to pressure oscillations, the POD analysis was conducted for p' with the full-scale three-dimensional database containing 333 snapshots of the flowfield within the injector. The time interval between snapshots is 30 μs, compared to the iterative time step of 1 μs employed in the numerical simulations. The size of the database is around 300 GB, so extensive computer storage space is required for the POD analysis.

Figure 4.21 shows the energy distribution of POD modes according to the pressure-fluctuation field. Mode 1 occupies 74% of total energy and the first six modes capture more than 80% of the total energy of the oscillatory field. Figure 4.22 shows the frequency spectra of the time-varying coefficients $a_j(t)$ of these modes. The first three modes are closely related to hydrodynamic instability waves with two dominant frequencies, 0.6 and 0.9 kHz, whereas the other three modes share the dominant frequency of 4.8 kHz.

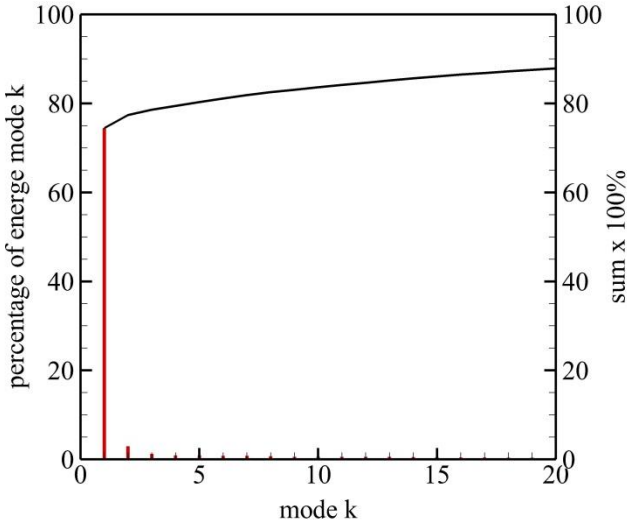

Figure 4.21: Energy distribution of POD modes of pressure oscillations, $p = 100$ atm.

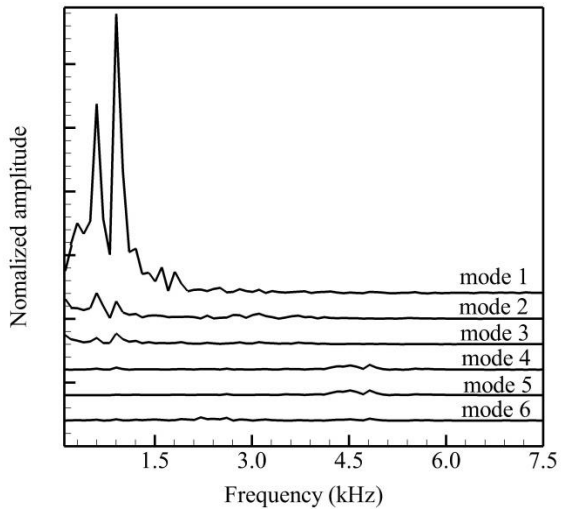

Figure 4.22: Frequency spectra of time-varying coefficient of first six POD modes of pressure oscillations, $p = 100$ atm.

Figure 4.23 shows the spatial distribution of the first six POD modes of oscillatory pressure field on a longitudinal plane. The first mode shape exhibits a descending trend along the axial direction with a maximum at the headend. The second and third modes show the similar pattern to the first mode but with much weaker strength and different phase angle. The fourth, fifth, and sixth modes also have the similar shape with different phase angle, and are closely related to the acoustic and helical waves as illustrated

previously with the characteristic frequency of 4.8 kHz. Figure 4.24 shows the spatial distributions of modes 1 and 4 on the transverse plane. A uniform pressure distribution of mode 1 in the circumferential direction (axisymmetric mode, m=0) implies that the disturbance propagates mainly in the longitudinal direction. The pressure difference in the radial direction caused by the swirl-induced centrifugal instability represents the radial wave. The well-organized wave shape for mode 4 with three periods in a circle further confirms the appearance of helical mode $m=-3$.

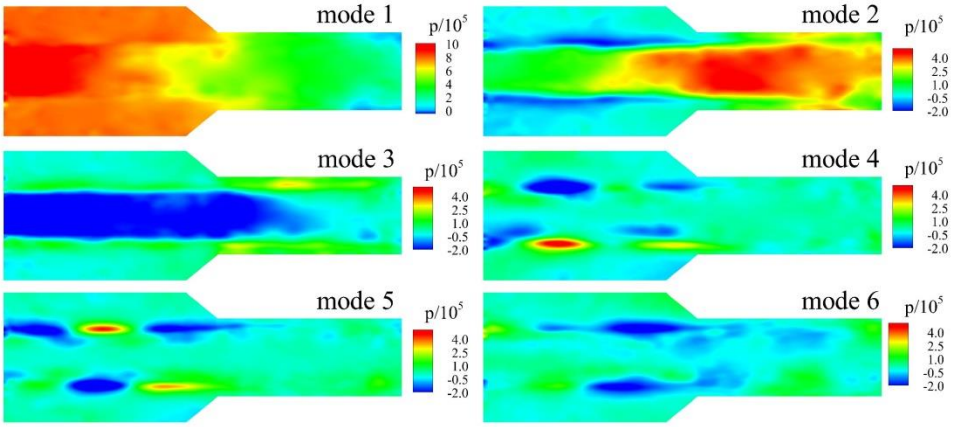

Figure 4.23: Spatial distributions of the first six POD modes of oscillatory pressure field on longitudinal ($x-r$) plane within injector, $p=100$ atm.

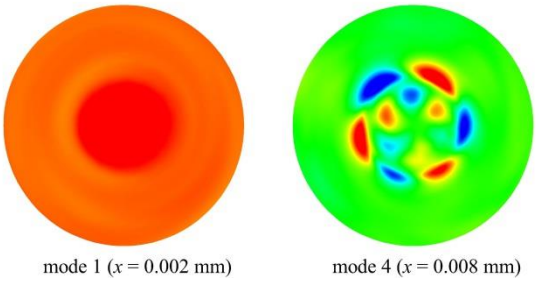

Figure 4.24: Spatial distributions of mode 1 and mode 4 of oscillatory pressure field on transverse ($r-\theta$) plane within injector.

4.2.6 Effects of Flow conditions and Geometry

The effects of chamber pressure and temperature on the injector dynamics are studied in this subsection. Table 4.2 lists the detailed information for five cases of concern. Cases 1-4 operates at different conditions with the same three-dimensional (3D) geometry, while Case 5 has the same operating conditions as Case 2 but with an axisymmetric configuration.

Table 4.2: Effects of injector geometry and flow conditions on LOX film thickness and spreading angle at injector exit.

Case	Geometry	p (atm)	T (K)	h_T (mm)	h_p (mm)	2α (deg)
1	3D	69	300	0.809	0.446	107.1
2	3D	100	300	0.612	0.419	104.0
3	3D	200	300	0.532	0.392	102.1
4	3D	100	600	0.514	0.500	103.1
5	Axisymmetric	100	300	0.392	0.324	97.9
	Inviscid Theory			0.431		96.5

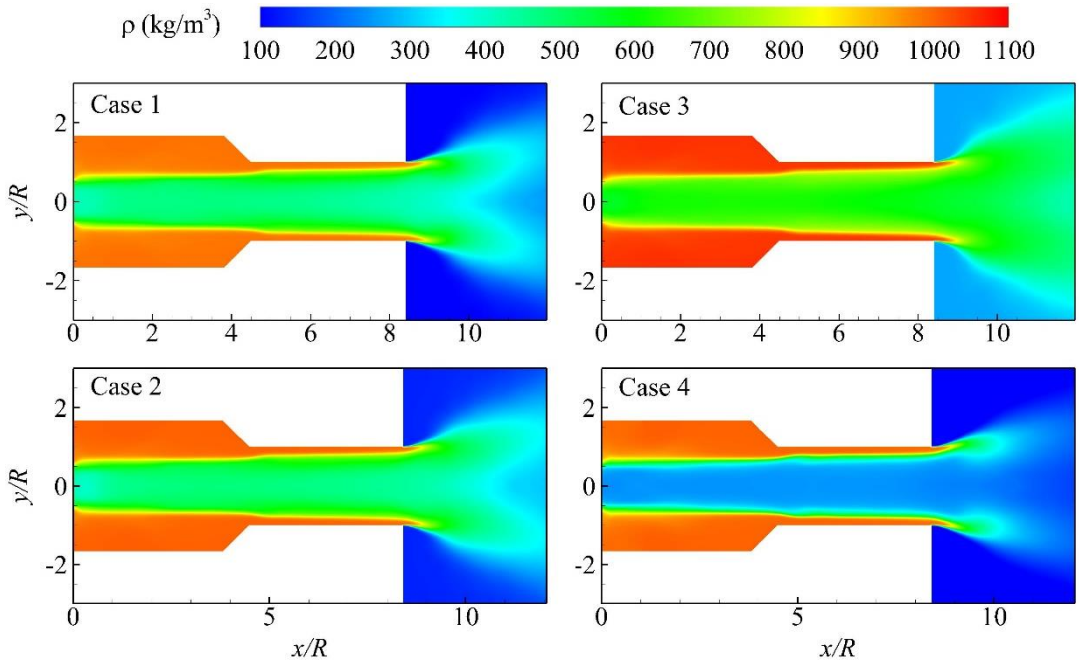

Figure 4.25: Distributions of azimuthally-averaged density field for Cases 1-4.

Figure 4.25 shows the distributions of the azimuthally-averaged mean density for Cases 1-4. The density in the gaseous core increases with pressure, whereas it decreases significantly as the temperature varies from 300 to 600 K. At p = 200 atm, the minimum density of oxygen in the chamber exceeds 260 kg/m^3. Figure 4.26 shows the distributions of the magnitude of azimuthally-averaged density gradient for Cases 1-4. The density gradient in the central gaseous core is close to zero. The radius of the gaseous core decreases with increasing pressure. The steep density gradient zone is extended into a broader area downstream of the injector as the pressure increases. As the chamber temperature changes from 300 to 600 K, the steep density gradient zone decays drastically but the central gaseous core grows remarkably.

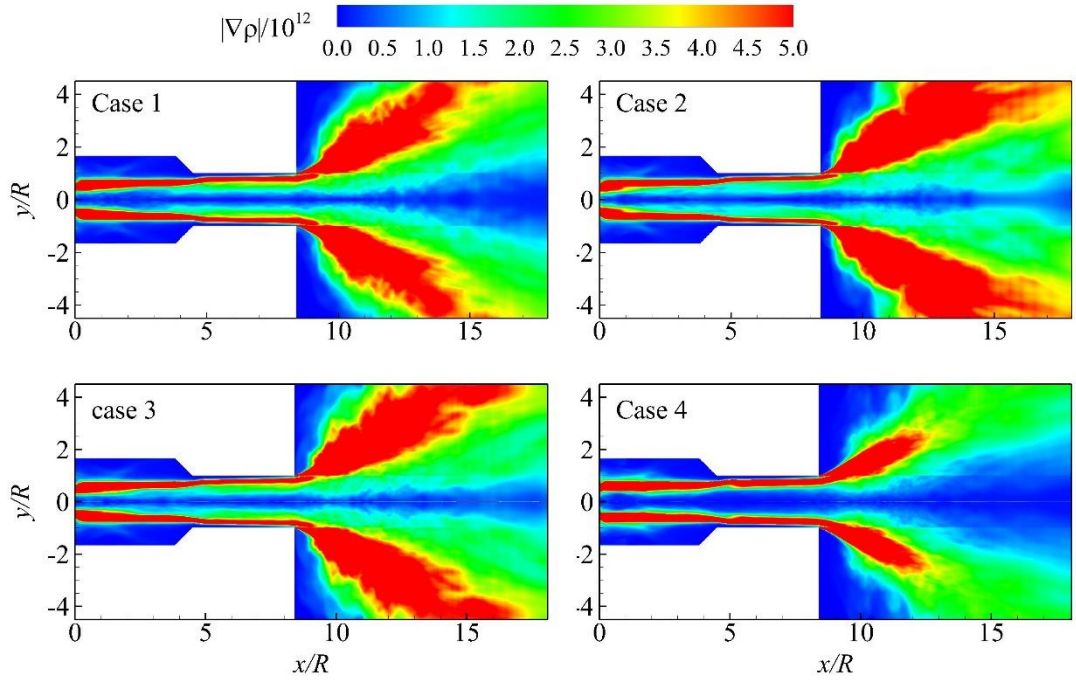

Figure 4.26: Distributions of the magnitude of azimuthally-averaged density for Cases 1-4.

Figure 4.27 shows the mean flow properties of density and axial velocity for Cases 2 and 5 to study the effect of geometry. The results of Case 2 are spatially-averaged in the

azimuthal direction. It can be observed that the axisymmetric case has a larger spreading angle than the 3D case. One reason may lie in that the axisymmetric simplification restrains the LOX film to develop in the radial and axial directions, while the vortex stretching and tilting mechanism occurring only in the 3D case enables the vigorous flow dynamics in the azimuthal direction other than radial and axial directions. The liquid film spreads outwardly farther in the radial direction for the axisymmetric case and hence induces the larger spreading angle. It is noted that the density of the gaseous core is higher for the 3D case. This is contributes to the smaller spreading angle for the 3D case. As shown in Fig. 4.28, the recirculating zone is closer to the center line for the 3D case, and carries more dense-liquid off the main stream, which flows back into the injector and cools down the gaseous core. In addition, the axisymmetric study predicts slightly larger axial velocity of the LOX film due to the lack of significant viscous dissipation when the flow goes along the spiral wall passage as in the 3D case. The liquid film thickness is therefore thinner in the axisymmetric case according to the conservation of mass.

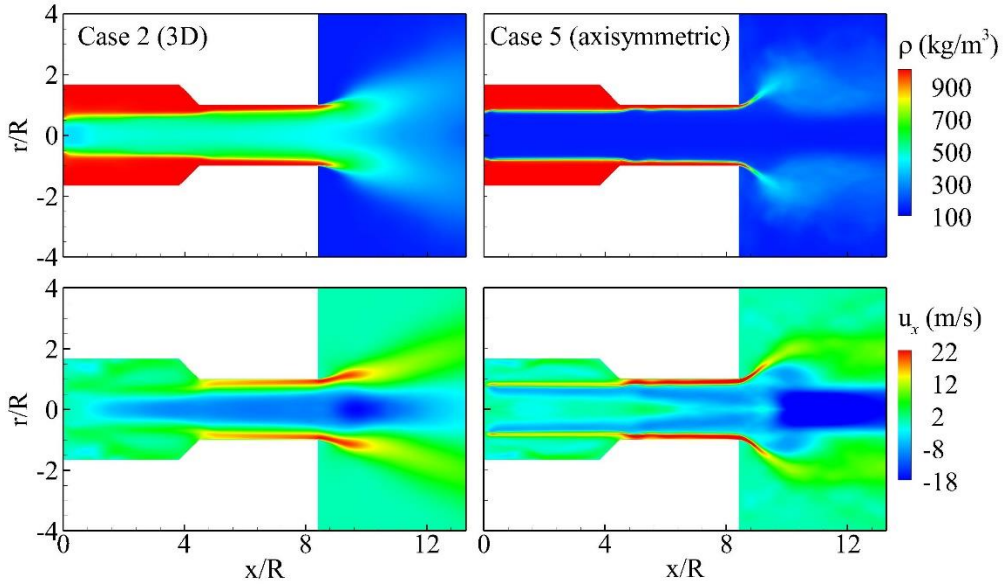

Figure 4.27: Distributions of time-averaged density and axial velocity for Cases 2 and 5.

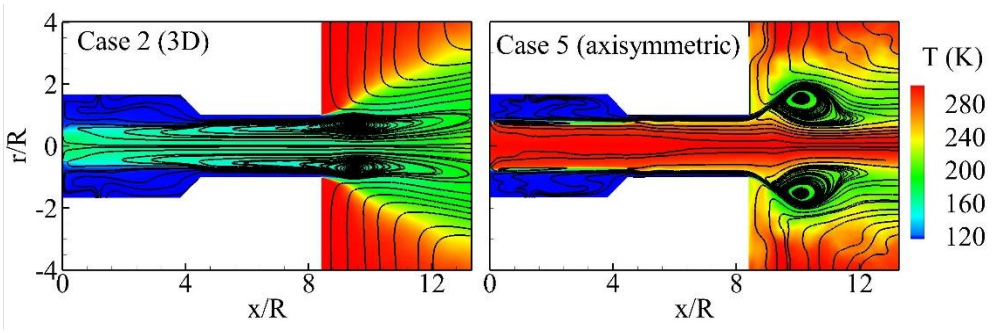

Figure 4.28: Distributions of time-averaged temperature field interpolated by streamlines.

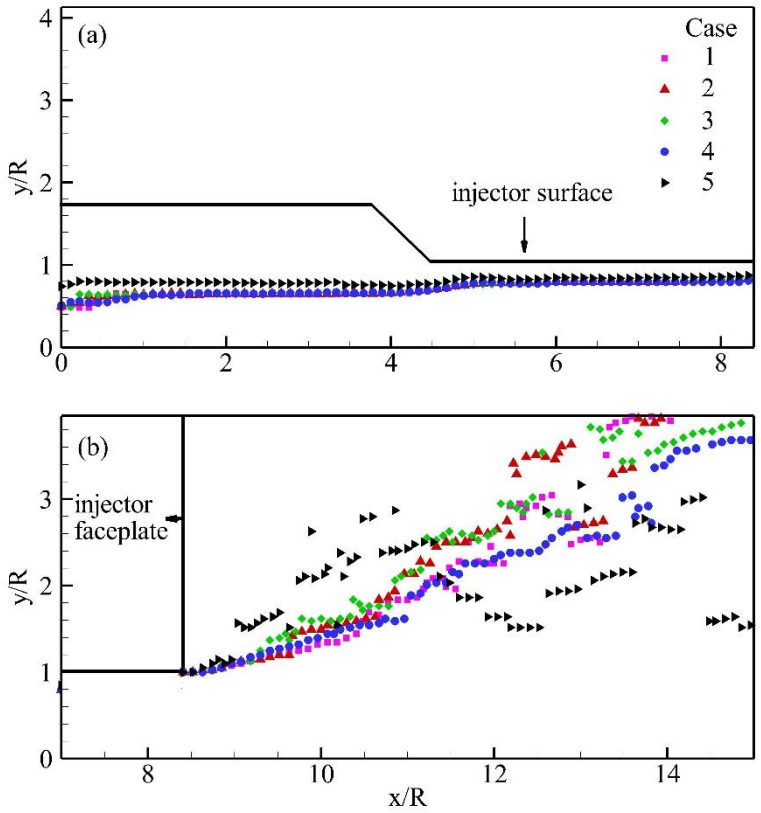

Figure 4.29:Distributions of local maximum density gradient in the radial direction as a function of axial coordinate, (a) within the injector; (b) downstream of the injector.

As discussed previously, the distinct interface between liquid and gas phases occurring at subcritical pressures is replaced by a continuous transition region at supercritical pressures. The liquid-film thickness must thus be defined in a different way

at supercritical pressures. Huo et al. [33] introduced two ways to identify the film thickness for a given axial location. One is defined as the distance between the surface of maximum density gradient and the injector wall along the radial direction. The other is the distance between the surface of critical temperature and the injector wall. Figure 4.29 extracts the location of the maximum density gradient in the radial direction as a function of axial coordinate. The liquid film thickness at the injector exit is listed in Table 4.2 for all cases. The film thickness increases slightly with the increasing pressure for 3D cases. The film thickness for axisymmetric case (Case 5) is thinner than that for the 3D case (Case 2). The absence of swirling structures in the azimuthal direction for the axisymmetric study induces the less momentum loss at the injector wall and hence higher axial velocity of the liquid film, leading to a thinner film because of the conservation of mass. The film thickness based on the critical temperature is also included in Table 4.2. Although the method of the critical temperature predicts a higher flame thickness than that of the maximum density gradient, the trend of variation of film thickness with pressure is similar for both of methods. The estimation from classical inviscid theory is also provided for comparison, which assumes the injector characteristics are solely determined by a geometric constant, *K*, regardless of the operating conditions. This assumption turns out to be relatively rough since the film thickness show the distinction among different operating conditions.

Figure 4.29b also includes the information of the spray cone angle, which determines the efficiency of atomization and mixing. Here the spray cone angle is defined as twice of the angle between the dotted curve and the axial axis in the chamber. It is seen that the chamber pressure has the negligible influence on the cone angle, while the higher chamber temperature (Case 4) renders a slightly smaller cone angle. It is noteworthy that the axisymmetric study (Case 5) yields a much higher cone angle than the 3D studies (Cases 1-4). The reason for this has been explained in the previous section. Table 4.2 also provides the spreading angle calculated by velocity components at the injector exit, $\alpha = tan(u_0 / u_x)$. The angles for the 3D studies are larger than those for both axisymmetric

study and inviscid theory. This is not physically meaningful, indicating that the angle computed by velocity components might not provide a proper presentation of film spreading. Instead, the angle visualized by the curves of maximum density gradient exhibits the consistent behavior of spreading and is useful to explore the influences of various parameters.

4.3 Conclusion

A systematic investigation of swirling flow dynamics has been conducted at supercritical conditions. Various fundamental instability mechanisms determining the flow dynamics have been examined by implementing the spectral analysis and proper orthogonal decomposition technique. The interface, representing the phase change from dense liquid to light gas at subcritical conditions, disappears at supercritical pressures and is replaced by a transition region in which density varies smoothly and continuously with temperature. The hydrodynamic instability in the longitudinal direction is dominant across the injector, and the azimuthal wave at mode 3 resonates with acoustic wave at 4.8 kHz and amplifies itself significantly compared to other modes. The converging section reflects the waves back into the vortex chamber and only allows part of waves with long wavelengths to transmit to the discharge nozzle.

A parametric study is made to examine the pressure and temperature effects on the injector design. The gaseous core decreases with the increasing pressure. The liquid film thickness increases slightly with pressure and is consistent with the prediction by the inviscid theory. The axisymmetric study estimates a much smaller film thickness and larger spreading angle than the 3D studies due to the lack of flow dynamics in the azimuthal direction. The spreading angle defined by the maximum density gradient provides more physical interpretation of liquid spreading than the traditional definition by the ratio of axial and tangential velocity component. The spreading angle is nearly independent of the

pressure. The current study will provide the important information for the future research on the mixing and combustion of swirling injection flows at supercritical conditions.

CHAPTER 5

MIXING CHARACTERISTICS OF LIQUID OXYGEN/KEROSENE BI-SWIRL INJECTORS

In Chapter 4, we investigated the dynamics of the swirling injection of pure LOX, which basically represents the behaviors of mono-propellant injectors. In practice, we deal with bi-propellant injector configuration more frequently, such as injectors used in RD-0110 and RD-170 engines. Most existing experiments and numerical simulations have been focused on shear coaxial injectors with simple propellants, such as H_2/O_2 and CH_4/O_2. Very limited information is available on the mixing and combustion dynamics of bi-propellant swirl injectors in rocket operating conditions, which is typically at pressures much higher than the critical pressures of the propellants, leading to the extreme nonlinearity and complexity of physical phenomena and therefore severe challenge to experiments. In this chapter, a numerical study is carried out to investigate the mixing and atomization characteristics of liquid oxygen/kerosene bi-swirl injectors at supercritical conditions. This is followed by the study of combustion dynamics in Chapter 6. The theoretical and numerical framework have been described in detail in Chapter 2. Various geometric parameters, including recess region, post thickness, and kerosene annulus width, are examined to explore their influence on mixing efficiency and flow dynamics.

5.1 Physical Configuration and Flow Conditions

The prototype of the bi-swirl injector has been introduced in Chapter 4. Instead of considering the inner swirler only, we recover the original injector by adding the outer swirler, in which kerosene is injected tangentially through a coaxial annulus.. Figure 5.1 exhibits the longitudinal plane view of the injector, providing the major components: tangential inlets, a discharge nozzle, a vortex chamber, and a coaxial annulus. The baseline geometrical parameters are summarized in Table 5.1, where R_v, R, $R_{in,\,1}$, and $R_{in,\,2}$, denote

the radii of vortex chamber, discharge nozzle, LOX, and kerosene tangential inlets, respectively. Δr, l, h, and L represent the lengths of coaxial annulus, recess region, post thickness, and injector in the axial direction, respectively. The injector operating conditions including chamber pressure (p_0) and inlet properties are listed in Table 5.2.

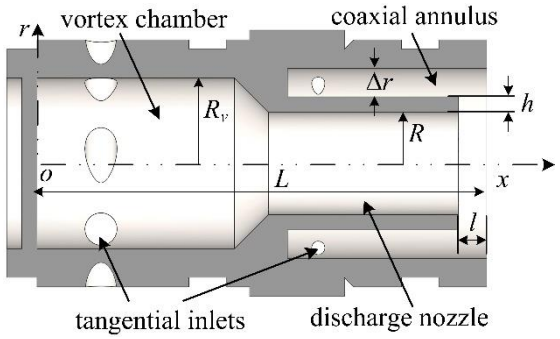

Figure 5.1: Longitudinal plane view of the injector.

Table 5.1: Geometric param.eters of the baseline swirl coaxial injector

R_v (mm)	R (mm)	$R_{in,1}$, (mm)	$R_{in,2}$ (mm)	Δr (mm)	l (mm)	h (mm)	L (mm)
4.5	2.7	0.85	0.35	0.5	1.5	0.8	24.2

Table 5.2: Chamber pressure and inlet conditions.

p_0 (MPa)	$T_{in,1}$ (K)	$T_{in,2}$ (K)	$\dot{m}_1$ (kg/s)	$\dot{m}_2$ (kg/s)
10	120	300	0.15	0.065

The computational domain includes injector interior ($8.4R$ in the axial direction) and a downstream region ($25R$ and $8R$ in axial and radial directions, respectively). Because of the enormous computational effort required for calculating the flow evolution in the entire regime, only a cylindrical sector with periodic boundary conditions specified in the azimuthal direction is treated. The noslip and adiabatic boundary conditions are applied at the injector solid surface. At the inlets, the azimuthal and radial velocities are determined from the given mass flow rate and swirl strength. The pressure is automatically obtained from radial momentum equation. At the downstream boundary, the non-reflecting boundary conditions based on characteristic equations proposed by Poinsot and Lelef [143]

are applied to avoid undesirable wave reflection by extrapolation of primitive variables from the interior region. A reference pressure is applied to preserve the average pressure in the computational domain through small-amplitude acoustic waves originating from a virtual boundary.

5.2 Results and Discussion

Kerosene is a complex mixture of alkanes, aromatics, and cycloalkanes, widely used in aircraft engines. The average chemical formula for kerosene differs from one source to another. The three-component surrogate model [146, 147], n-decane/n-propylbezene/n-propyl-cyclohexane (74%/15%/11% by volume), was shown to yield the best agreement with the jet-stirred reactor data and is implemented in the present study.

5.2.1 Grid Independence Study

Table 5.3: Four levels of grid resolutions.

Grid Level	Smallest Gird Size (μm)	Grid Points (million)	Blocks
1	8	0.1	93
2	4	0.4	372
3	2	1.6	372
4	1	6.4	1488

In order to guarantee the appropriate numerical resolution and accurate flow physics, a grid independence study is undertaken to determine the required spatial resolution. Four different levels of mesh resolutions are examined and the detailed information is listed in Table 5.3. The grid size reduces into half as the grid level elevates by one. Since the grid size decreases exponentially, the iterative time step must decrease accordingly to ensure the convergence. The total number of grid points increase from 0.1 (level 1) to 6.4 million (level 4). The whole computational domain is divided into blocks, and each block is computed by one CPU core. For Grid Level 4, the resolution is close to

direct numerical simulation because the grid size is nearly equivalent to the Kolmogorov scale.

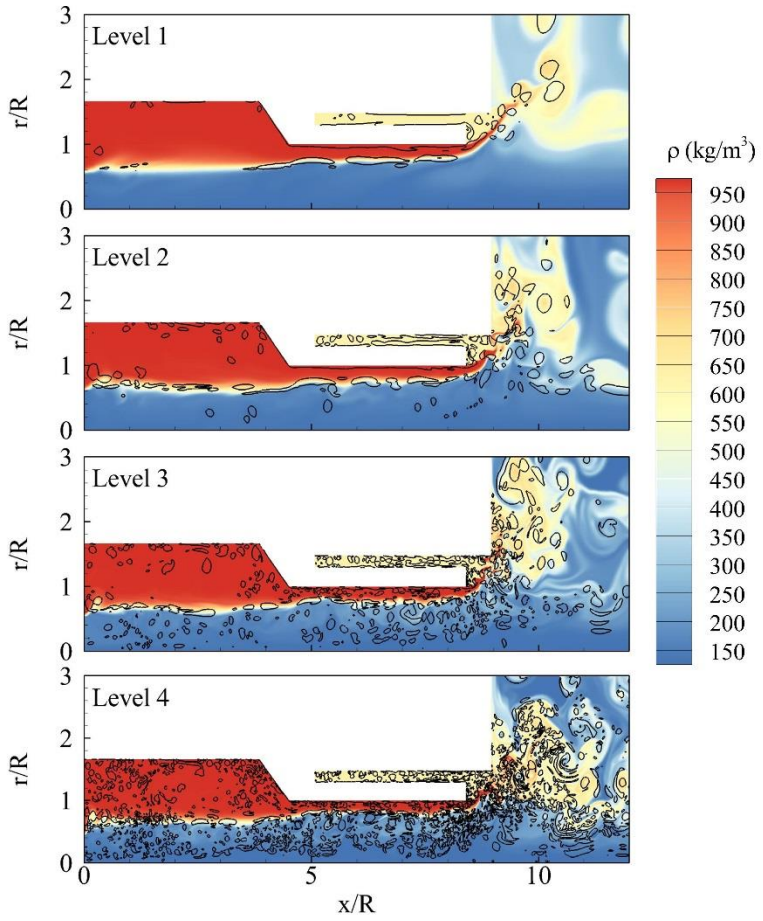

Figure 5.2: Instantaneous snapshots of the density field superimposed by a positive Q-isocontour (solid line) at 10^8 s^{-2} for increasing grid resolutions.

Figure 5.2 shows the instantaneous snapshots of the density field superimposed by the second invariant of the velocity gradient tensor [148], Q, defined as $Q=\left(|\Omega|^2-|S|^2\right)/2$ to identify the vortical structures in the flow field. Here Ω and S represent the antisymmetric and symmetric components of the velocity gradient tensor. Similarities in terms of flow patterns, LOX film thickness, and spreading angle, are observed among the four grid levels. The small vortical structures can be captured even from the coarsest grid (Level 1). With the increasing grid resolution, the finer vortical

motions representing smaller turbulent eddies are recognized in the center gaseous core and the LOX/kerosene mixing zone in the injector near-field.

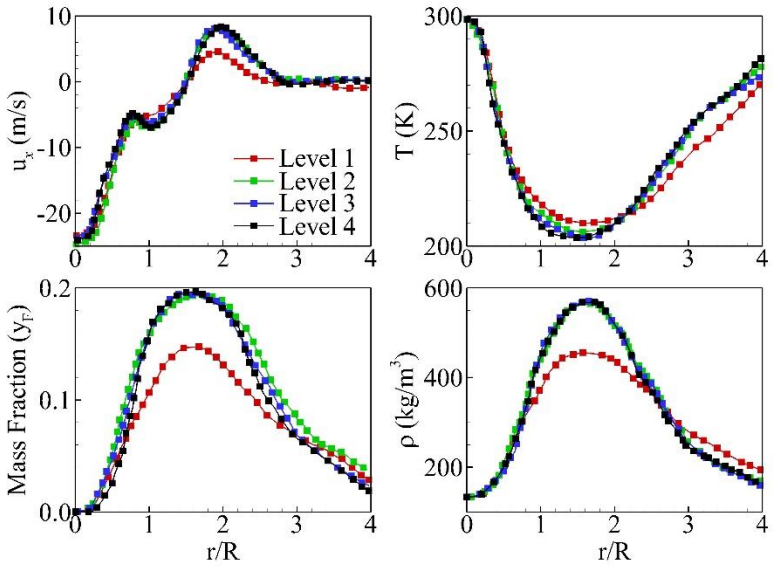

Figure 5.3: The radial distributions of time-averaged flow properties at the axial location ($x/R=10$) for increasing grid resolutions.

In order to show the sensitivity of flow statistics to the grid resolution, the radial distributions of representative time-averaged flow properties, including axial velocity (u_x), temperature (T), kerosene mass fraction (y_F), and density (ρ) at $x/R=10$, were compared for different grid resolutions as shown in Fig. 5.3. The coarse grid Level 1 shows the significant difference from other grid levels. Although the slight distinction occurs for Level 2, the averaged properties are nearly insensitive to the grid resolution starting from Level 2. To ensure the flow information captured accurately in the following study, the grid system of Level 3 is selected as a tradeoff between computational accuracy and burden.

5.2.2 LOX/Kerosene Mixing and Flow Dynamics

The swirling flow dynamics for injectors without a coaxial flow have been investigated rigorously in Chapter 4, in which the flow evolution of the LOX film is similar to the flow pattern of the inner swirler as shown in Fig. 5.4. The strong swirling motion and its associated centrifugal force produce large pressure gradients in the radial direction and induce a low-pressure core around the centerline, leading to the LOX film flowing along the injector wall. The low-density gaseous core in the center forms because of the conservation of mass and angular momentum. As the LOX stream exits from the central injector, a spreading conical liquid sheet forms and impinges with the kerosene stream. Consequently, LOX and kerosene mix efficiently and transport downstream.

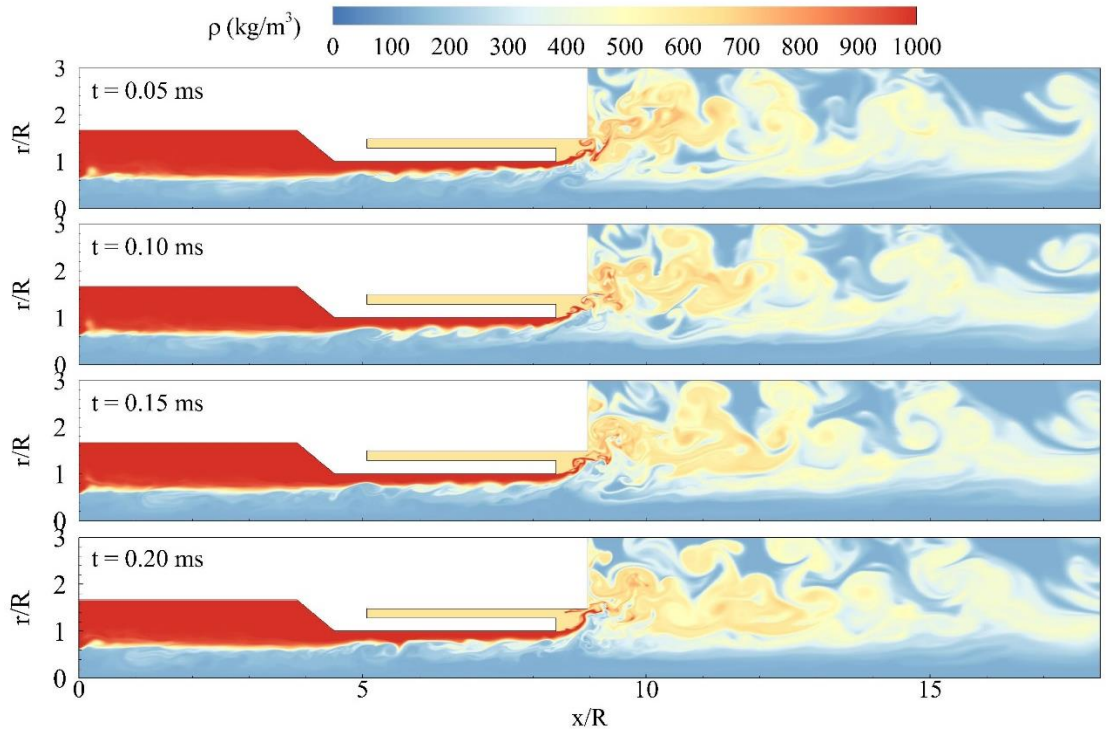

Figure 5.4: Temporal evolution of density field for the baseline (Case I).

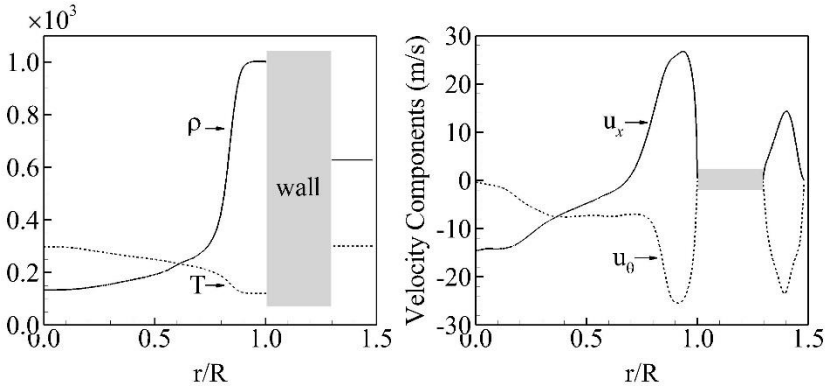

Figure 5.5: Radial distributions of time-averaged density (ρ), temperature (T), axial (u_x), and azimuthal velocity (u_θ) components near the injector exit ($x/R=8.3$).

Figure 5.5 presents the time-averaged density, temperature, and axial and tangential velocity components near the injector exit. The temperature changes gradually from a subcritical state at the wall ($T=120\,\mathrm{K}, r/R=1$) to a supercritical state in the center ($T=300\,\mathrm{K}, r/R=0$). A fluid transition region exists, unlike a sharp interface between a liquid and a gas occurring at subcritical pressures. Followed by this transcritical change of fluid state, the density varies smoothly from a large value in the LOX film to a small value in the gaseous core. On the contrary to the LOX film, the kerosene stream fully occupies the annulus passage due to the confinement of upper and lower walls. The flow in the kerosene passage ($r/R \geq 1.3$) appears to be fully developed. The distributions of density and temperature are nearly uniform and the maximum of axial and azimuthal velocities locate at the annulus centerline. In the LOX passage, however, the velocity maximizes in the LOX film, followed by the shear-layer between the LOX and center gaseous core. The flow then reverses its direction near the centerline because of the center-recirculating flow.

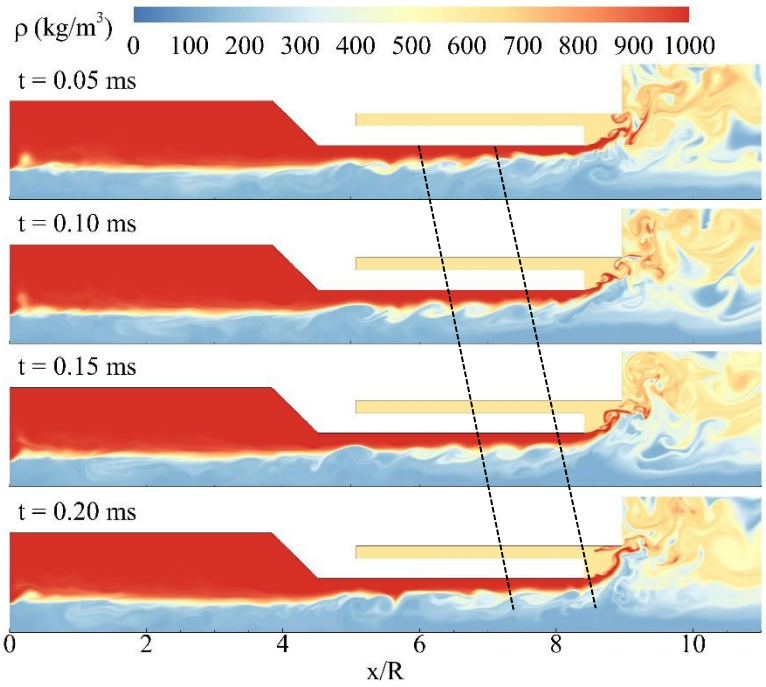

Figure 5.6: Close-up view of temporal evolution of density field near liquid-oxygen film for the baseline (Case I).

The LOX film in the center injector is intrinsically unstable and characterizes three-dimensional hydrodynamic instabilities, leading to the film oscillations longitudinally and circumferentially. The circumferential mode, however, cannot be obtained in the present axisymmetric simulation. Figure 5.6 shows a close-up view of the density evolution near the LOX film for the baseline case, implying the presence of the longitudinal mode. The wave develops and convects downstream. The calculated wave speed is approximately 23 m/s in the discharge nozzle ($4.5 \leq x/R \leq 8.4$), where the time-averaged thickness of the LOX film is nearly a constant.

Figure 5.7 shows the instantaneous distributions of axial velocity, tangential velocity, and vorticity magnitude. The axial velocity of the LOX film in the vortex chamber starts with a low value near the injector headend and increases substantially through the converging nozzle, indicating significant transfer from angular momentum to axial momentum. This explains that the thickness of the LOX film in the vortex chamber is much

bigger than that in the discharge nozzle because of mass conservation. Large vortical structures occur at various locations, including the injector solid surface, shear-layer, and LOX/kerosene mixing regions. The shear-layer region coincides with the fluid transition region, in which the volume dilatational and baroclinic effects are considerable in vorticity production other than vortex the stretching and tilting effect as shown in Chapter 4.

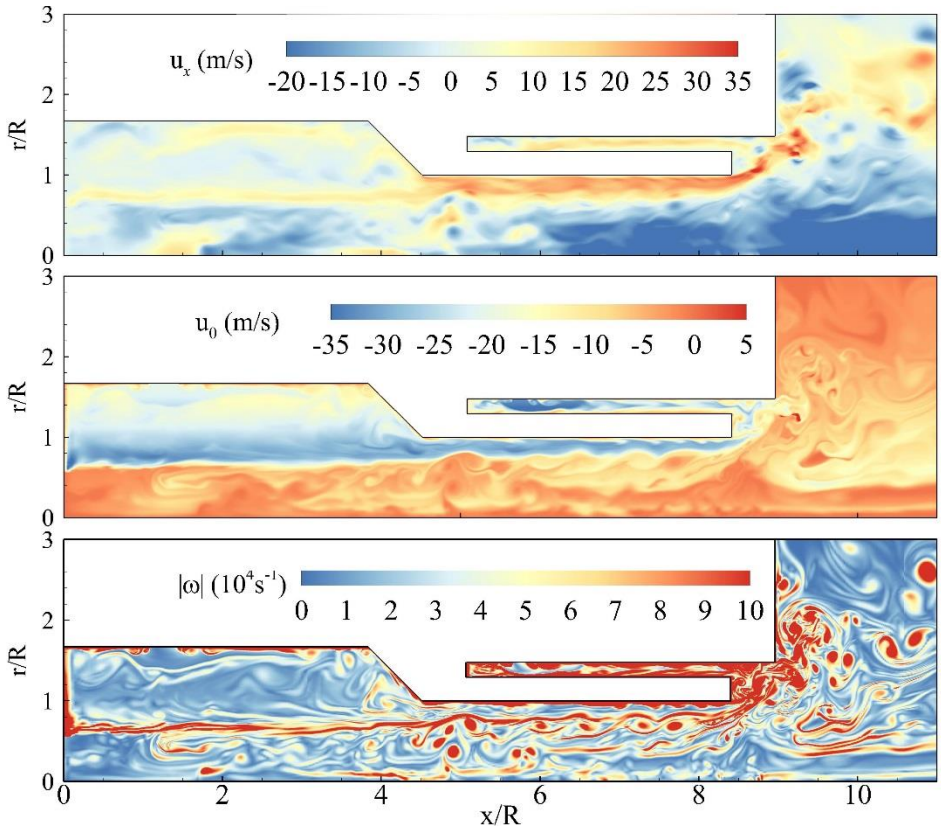

Figure 5.7: Instantaneous distributions of temperature, axial velocity, and vorticity for the baseline.

Figure 5.8 shows a close-up view of density evolution in the vicinity of the injector post. The LOX and kerosene streams emanating from the injector interact dynamically in the recess region. The kerosene stream occupies the majority of the recess region and cover the LOX post, while the LOX stream spreads upwards to form a strong mixing layer, in which the film surface is highly wrinkled by the shear-layer-induced flow instability. The

traditional liquid breakup process at supercritical conditions does not occur and is replaced by large-scale turbulent mixing, along with which the LOX and kerosene mix fairly efficiently by coherent structures and propagate downstream.

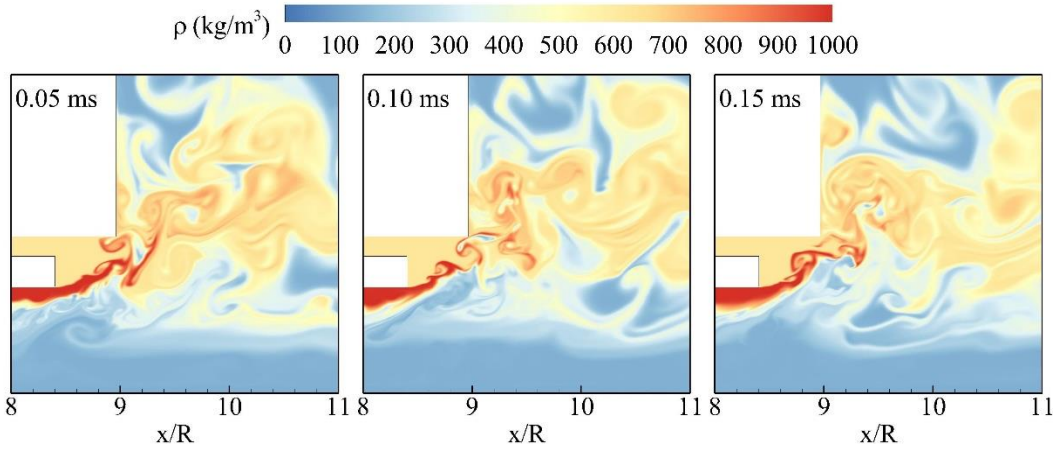

Figure 5.8: Close-up view of density evolution in the vicinity of injector post.

5.2.3 Parametric Study

Table 5.4: The geometrical parameters of four cases.

Case Number	Annulus Length (Δr, mm)	Post Thickness (h, mm)	Recess Length (l, mm)
I (Baseline)	0.5	0.8	1.5
II	0.5	0.8	**0.0**
III	0.5	**1.3**	1.5
IV	**1.0**	0.8	1.5

As shown in Fig. 5.8, LOX and kerosene mix together in the recess region, where the cone-shaped LOX film is formed and intercepts the incoming kerosene film to achieve efficient mixing. The geometry of injector may impact the mixing characteristics. Parametric studies are conducted in this section to explore the influence of recess region, post thickness, and kerosene annulus width on the mixing characteristics. Table 5.4 lists

the controlling parameters of four cases. Case I, considered as the baseline case, is compared with other cases. The recess region is removed in Case II, while the post thickness is larger in Case III and the kerosene annulus wider in Case IV.

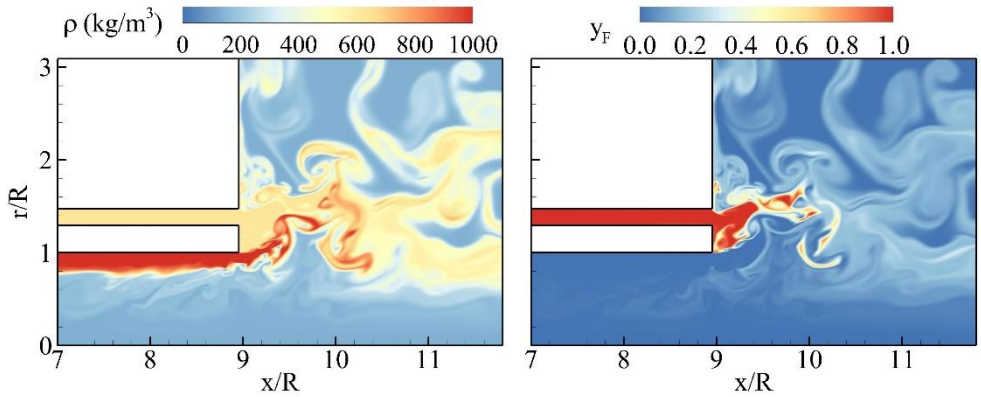

Figure 5.9: Instantaneous distributions of density and kerosene mass fraction for Case II.

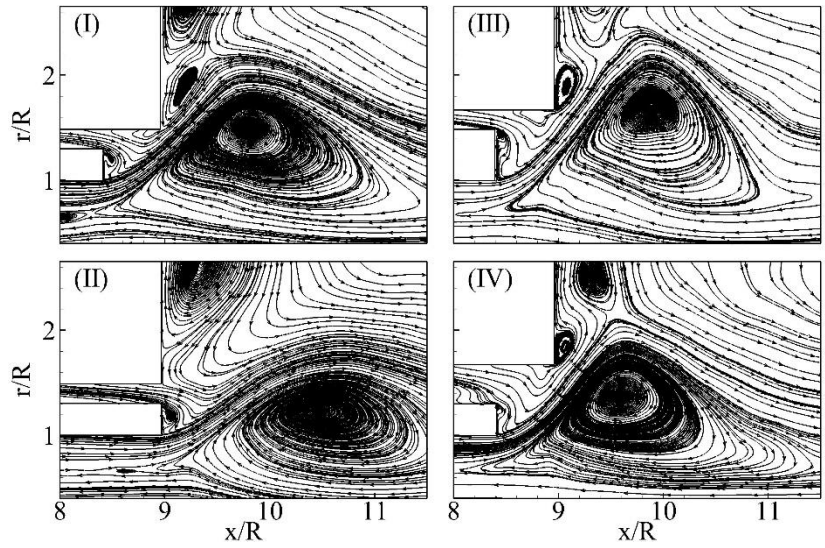

Figure 5.10: Streamlines of time-averaged flowfield for four cases.

Figure 5.9 shows the instantaneous snapshots of density and kerosene mass fraction for Case II. The significant difference from the baseline (Case I) can be recognized. The absence of recess region clearly delays the mixing and elongates the mixing area in the

further downstream, therefore diminishing the mixing efficiency. The spreading angle of LOX stream becomes smaller. This can be observed clearly from the time-averaged flow streamline in Fig. 5.10, where the center-recirculating bubble for Case I is steeper and closer to the injector exit than that for Case II. The advance mixing process in the recess region reduces the size of recirculation zone in the vicinity of injector post and produces two separate recirculating zones near the upper-left wall of the chamber rather than one bulk bubble in Case II.

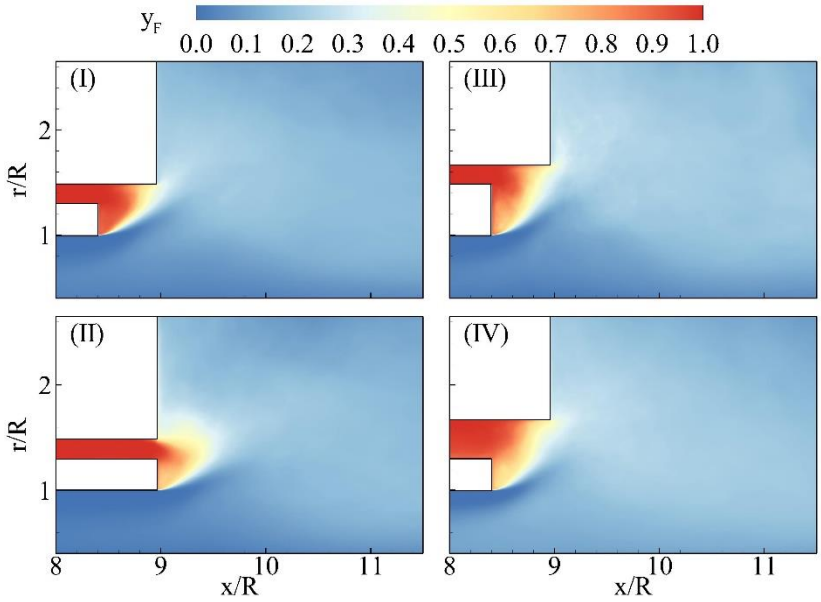

Figure 5.11: Time-averaged distributions of kerosene mass fraction at injector near-field for four cases.

Figure 5.11 shows the time-averaged distributions of kerosene mass fraction for four cases in the vicinity of the injector post. It is seen that the kerosene film covers the LOX post only in Case I. The spreading conical LOX sheet blocks the incoming kerosene stream, which has to adjust its direction. The restriction of upper surface of the annulus imposes the kerosene stream to only turn downwards in the recess region before its expansion in the injector downstream in Case I. However, because of the absence of the recess region in case II, the kerosene stream spreads both upwards and downwards in the downstream, leaving insufficient amount of kerosene near the LOX post. The recess region

enhances the interaction of propellants and enriches the dynamics of the injector near-field, therefore improving the mixing efficiency.

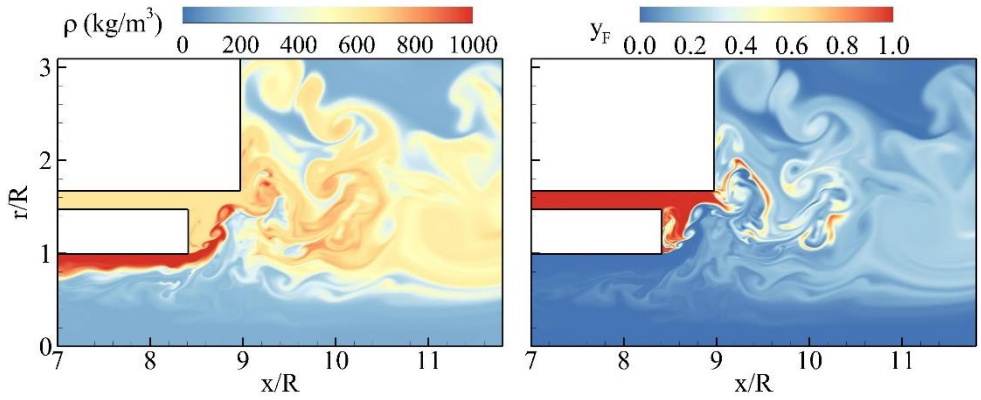

Figure 5.12: Instantaneous distributions of density and kerosene mass fraction for Case III.

Figure 5.12 shows the instantaneous snapshots of density and kerosene mass fraction for Case III. For the larger post thickness in Case III, the spreading angle is higher and the stagnation point in the center-recirculating zone shifts to a higher radial position as shown in Fig.5.10. This larger angle in turn imposes the LOX film to intercept the kerosene film more efficiently in a broader area. The main stream of kerosene is divided into two branches, one flows along with the LOX stream while the other flows along the chamber wall. The detached bubble in Case I is pushed by the kerosene stream to the chamber wall in Case III.

A shown in Fig. 5.11, a considerable layer of the kerosene film in Case I conceals the LOX post and can potentially protect it from overheat in case of combustion. For the thicker post, however, the propellants mixture near the lower portion of the injector post is close to be stoichiometric. The strong heat flux generated from combustion could possibly damage the injector post surface. Interesting research can be done to determine an optimum thickness of the injector post to achieve the balance of both efficient mixing and post protection.

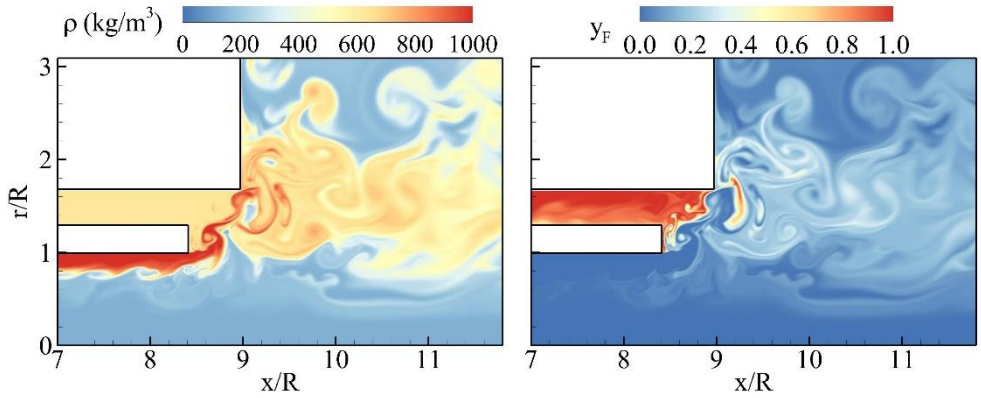

Figure 5.13: Instantaneous distributions of density and kerosene mass fraction for Case IV.

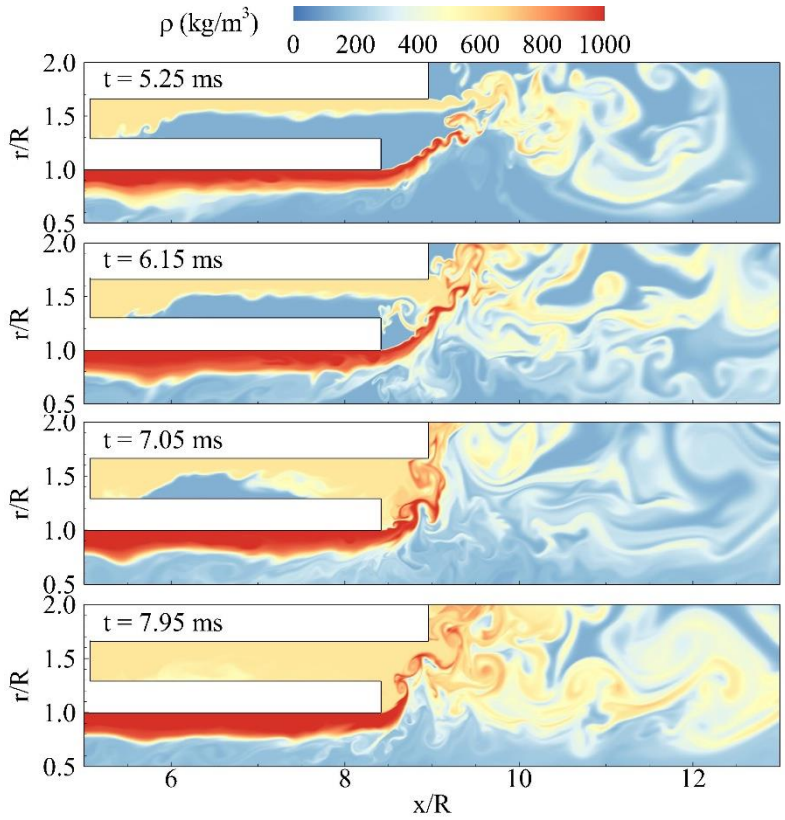

Figure 5.14: Temporal evolution of density field for Case IV.

The effects of the kerosene annulus width is also explored. Figure 5.13 shows the instantaneous distributions of density and kerosene mass fraction for Case IV. The spreading angle increases with the annulus width, and the center-recirculating bubble

slightly shifts upstream accordingly, which leads to significant amount of the mixture downstream recirculating into the central injector. Similar to Case III, the kerosene stream is divided into two branches and does not cover the LOX post as it does in Case I. Figure 5.14 shows the temporal evolution of density field for Case IV. It can be seen that much longer time is required for the kerosene film to reach the fully-developed state in the annulus. At the initial stage of flow evolution, the thickness of the kerosene stream is smaller than the annulus width, leading to a gaseous core next to the lower annulus surface. The kerosene stream is then intercepted by the cone-shaped LOX spreading sheet and turns its flow direction. After the enough accumulation in the recess region, kerosene flows back into the annulus and eventually occupies the whole annulus in a fully-developed state at t = 7.95 ms, compared to t=5.82 ms for Case I. The complex flow structures in Case IV introduce additional shear-layer in the annulus and increase the momentum loss.

5.3 Conclusion

The injection and mixing characteristics of the LOX/kerosene bi-swirl injectors have been numerically investigated at supercritical conditions. The theoretical formulation incorporates real-fluid thermophysical properties into the conservation laws to render a unified treatment for a fluid at any state. The accuracy of numerical resolution was tested through the grid independence study. The flow similarities were observed for different levels of grid resolution. The finer vortical structures were obtained as the grid size decreases. The mixing characteristics and flow dynamics were discussed in depth. The recess region significantly improves the mixing efficiency by advancing the interaction of propellants. The spreading angle of the LOX film increases, as either the post thickness or the annulus width increases. The larger spreading angle enables the LOX film to intercept the kerosene film in a more effective way, therefore facilitating the mixing. But the thicker post may face a significant amount of heat flux from the hot products in the combusting condition due to the lack of coverage of the kerosene film. Although the wider annulus

requires a longer time to reach a fully-developed state in the annulus, it shifts the recirculation bubble upstream and recirculates the propellant mixture into the center injector, which could stabilize the combustion in the reacting flows. In the process of industrial design, these parameters must be selected carefully to achieve the desired injector performance.

CHAPTER 6

SUPERCRITICAL COMBUSTION OF LOX/KEROSENE BI-SWIRL INJECTORS

In Chapter 5, the injection and mixing characteristics of LOX and kerosene mixture were investigated with various geometries. Further study is required to examine if these geometries affect the combustion efficiency in a similar way. Existing experimental studies could only provide limited qualitative information of properties due to the extreme conditions in case of combustion, which motivates the present study. This chapter is the continuing research of previous chapters by studying the combustion characteristics of LOX and kerosene using the same configuration. The emphasis is placed on the region just downstream of a bi-swirl injector element. The flame stabilization mechanism will be studied for the first time for the various liquid swirl coaxial injectors at supercritical conditions. The flow and flame structures at injector near-filed will be explored extensively. The pressure fluctuation field characterizing the flame dynamics will also be discussed in detail.

6.1 Physical Configuration and Flow Conditions

The configuration implemented in this chapter is identical to that described in Chapter 5. The schematic and relevant operating conditions were shown in Fig. 5.1 and Table 5.1, respectively. Four cases with different geometries listed in Table 5.3 are conducted. The setup of boundary conditions is similar to the mixing case. Please refer to Sec. 5.1 for more details.

6.2 Results and Discussion

The detailed information of the theoretical and numerical framework have been described in Chapters 2 and 3. Turbulence /chemistry interactions are treated by the laminar

flamelet model. Combustion process of aviation fuels, such as kerosene, is very intricate due to the complex hydrocarbon mixtures. It is generally necessary to apply the much less complex surrogate mixtures to model the kerosene combustion. A three-component surrogate fuel [149], n-decane/n-propylbenzene/n-propylcyclohexane (74%/15%/11% mol), was shown to be the most appropriate for simulating the experiments. The laminar flamelet library is established through the tabulation of solutions of counterflow diffusion flames. A skeletal mechanism with 106 species and 382 reactions developed by Wang et al. [150] is implemented because of its high accuracy in predicting global combustion characteristics.

Table 6.1 summarizes these four cases with the same operation conditions. Case I, regarded as the baseline case, is compared with other cases. The recess region is removed in Case II, while the post thickness is larger in Case III and the kerosene annulus wider in Case IV. The following sections will discuss the flow and flame structures for the baseline first and then analyze the geometric effects on the combustion characteristics through the comparisons of four cases. Suggestion will be given on the future injector design for the optimal mixing and combustion performance.

Table 6.1: Geometrical parameters of four cases

Case Number	Annulus Width (Δr, mm)	Post Thickness (h, mm)	Recess Length (l, mm)
I	0.5	0.8	1.5
II	0.5	0.8	0.0
III	0.5	1.3	1.5
IV	1.0	0.8	1.5

6.2.1 Baseline Case

Figure 6.1 provides a global view of temperature and OH mass fraction distributions for the baseline case (Case I). It can be seen that liquid propellants emanating from the inlets meet and ignite in the recess region. The flame is highly wrinkled by various

turbulent eddies in the combustion chamber. Hot products from combustion reverse the flow direction near the centerline and flow back into the center injector, potentially preheating the LOX stream.

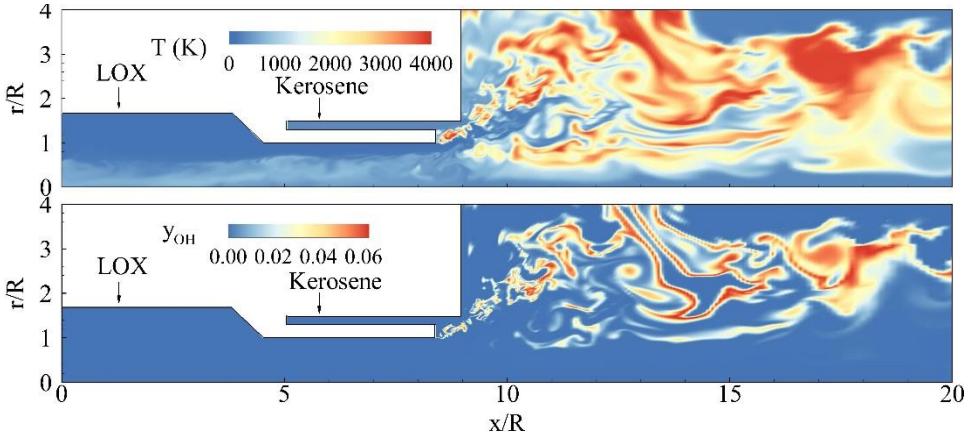

Figure 6.1: Instantaneous flow snapshot of distributions of temperature and mass fraction of OH for Case I in a global view.

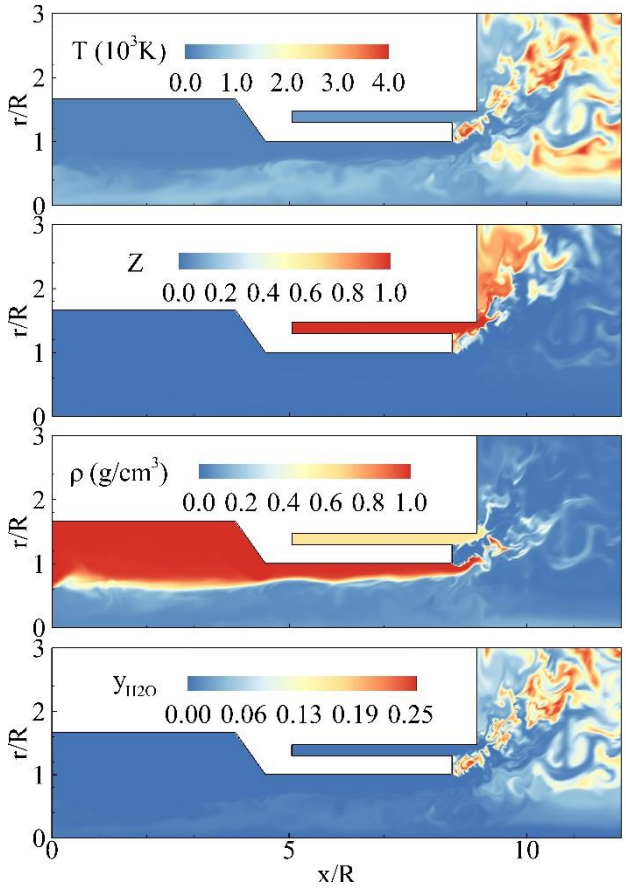

Figure 6.2: Instantaneous flow snapshot of distributions of temperature, density, mixture fraction, and mass fraction of H_2O for Case I.

Figure 6.2 shows the instantaneous snapshot of flow properties, including temperature (T), mixture fraction (Z), density (ρ), and mass fraction of H_2O (y_{H2O}) for the baseline case in a close view of injector inside and near-field. The flow evolution of liquid film in the central and coaxial injectors is very similar to that occurring in the cold-flow environment. The LOX stream flows along the viscous wall due to the swirl-induced centrifugal force, leading to the formation of a thin LOX film and a central gaseous core. The thickness of the LOX film can be determined by the mass conservation. The surface of the LOX stream oscillates in a small amplitude due to hydrodynamic instabilities. Contrary to the LOX stream, the kerosene stream fills up the whole annulus and becomes fully-developed before leaving the annulus.

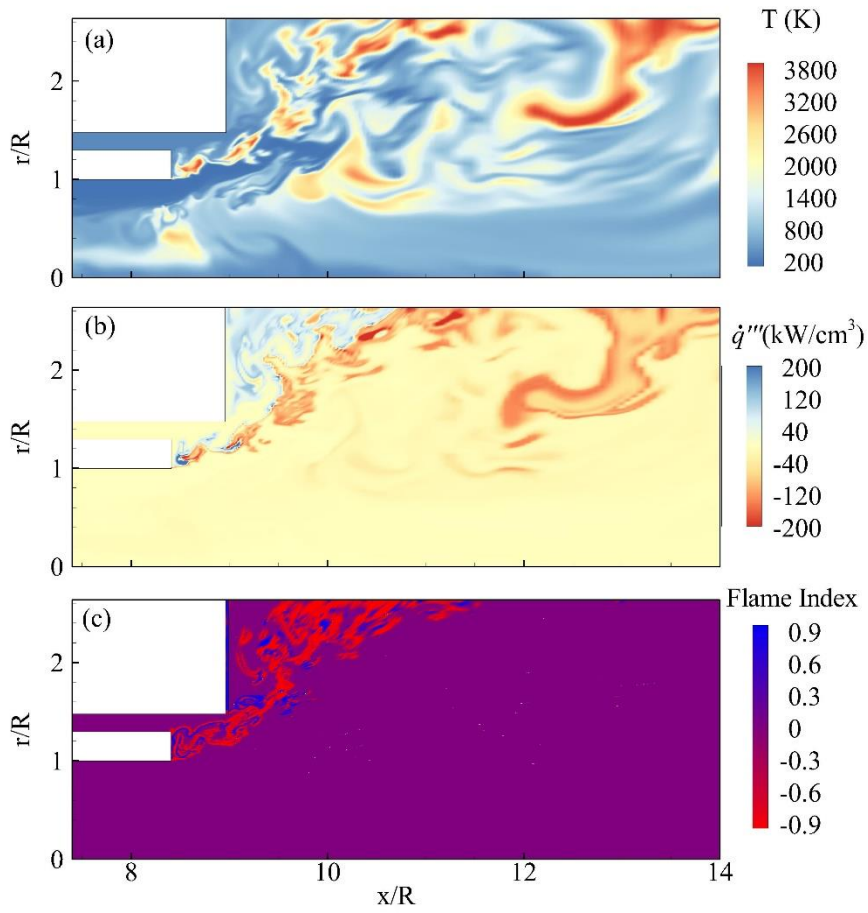

Figure 6.3 Instantaneous distributions of temperature, volumetric heat release rate, and flame index at injector near-field and downstream

Figure 6.3 shows the instantaneous distributions of temperature, volumetric heat release rate, and flame index at injector near-field and downstream. Here the flame index is defined as: $Z_{FO} = (\nabla Y_F \nabla Y_O)/(|\nabla Y_F \| \nabla Y_O|)$, which is used to distinguish premixed flames from diffusion flames according to Takeno *et al* [151]. Positive values of Z_{FO} represent premixed flames while negative values represent diffusion flames. As shown in Fig. 6.3c, the overall flame field is diffusion-dominated and separates kerosene and oxygen. The negative heat release rate represents a large amount of energy taken out from combustion. It is noted that a significant area exists for positive heat release near the post surface and injector faceplate. The positive value represents endothermic reactions of kerosene

decomposition process, where small hydrocarbons are generated and quickly oxidized in the further downstream. The overall integrated heat release rate is about -3.0 x 10^5 kW/kg. The further analysis on correlation between heat release and other flow parameters are undergoing and the corresponding combustion response function will be determined.

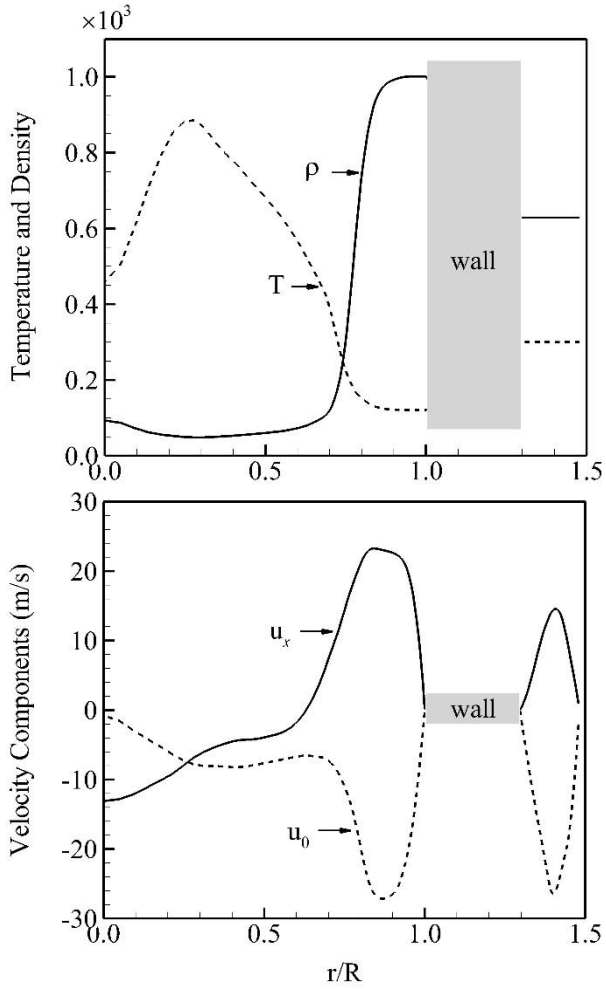

Figure 6.4: Radial distributions of time-averaged density, temperature, axial, and azimuthal velocity components near the injector exit (x/R=8).

Figure 6.4 shows the radial distributions of time-averaged density, temperature, and velocity components at the injector exit. It is found that the distributions of temperature and density in the annulus are uniform and that the distributions of axial and azimuthal velocity components are nearly symmetric, corresponding to the fully-developed flow as

shown in Fig. 6.2, which is potentially beneficial to the thermal protection of the annulus wall. In the central injector, however, non-uniform property distributions are observed. The axial velocity becomes negative as $r/R < 0.63$. The gaseous core initially with a temperature of 300 K is heated up to 900 K by this reversal flow of the hot products from the downstream chamber. The oxygen temperature gradually increases from a subcritical temperature (120 K) at the wall to a supercritical temperature (900 K) in the gaseous core, indicating a transcritical change of state. In the meantime, the oxygen density varies smoothly from a liquid-like state to gas-like state as the distance from the wall increases.

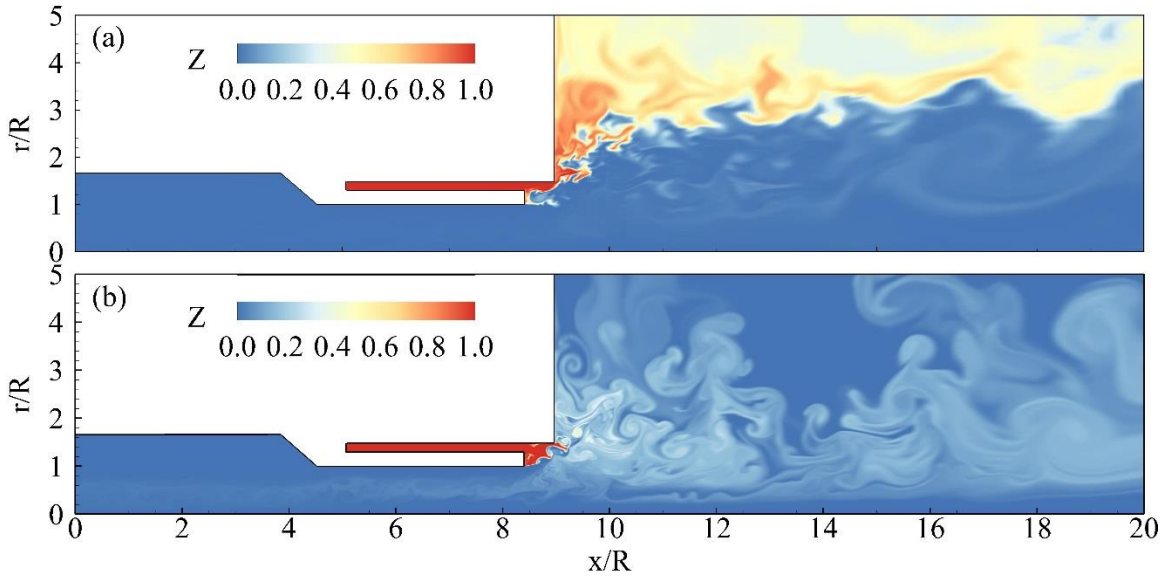

Figure 6.5: Comparison of instantaneous distributions of the mixture fraction for (a) combustion and (b) cold-flow environments.

The temperature distribution in Fig. 6.2 reveals that a diffusion-dominated flame emanates from the recess region and propagates downstream along the surface of LOX stream. A wake region consisting of hot combustion products separates LOX from kerosene streams. Figure 6.5 shows the comparison of instantaneous distributions of the mixture fraction for combustion and cold-flow cases. Significant differences are observed in the recess region and chamber. Figure 6.6 exhibits the zoom-in view of mixture fraction

field in the vicinity of the injector post. The kerosene stream expands downwards and occupies the major part of the recess region for the cold-flow case. However, the downward movement of the kerosene stream is inhibited by the expansion of hot products in the flame zone for the combustion case, so that the kerosene-rich mixture only cover the injector post wall and upper part of the recess region. The large-scale vortices, taking place at the interfacial surface of LOX and kerosene in the cold-flow case, are pushed by hot products to the kerosene annulus and significantly enhance the mixing of the kerosene and hot products. In the chamber, the hot products further drives the kerosene stream flowing along the chamber wall, unlike the cold-flow case that develops a well-distributed mixture propagating downstream.

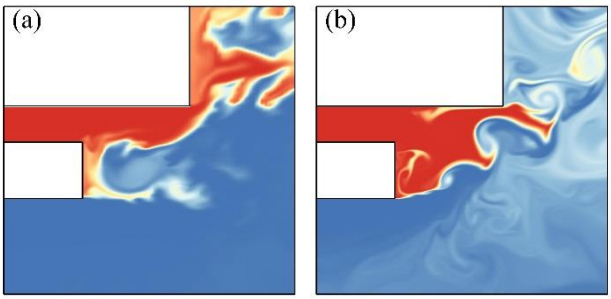

Figure 6.6: Zoom-in view of distributions of the mixture fraction for (a) combustion and (b) cold-flow environments at the injector exit.

Flame stabilization is a critical issue in the combustor design. Figure 6.7 shows the time-averaged distributions of temperature and axial velocity interpolated by flow streamline. The study [9, 152] has shown that the flame is stabilized by the recirculation flow downstream of the LOX post for a shear coaxial injector with cryogenic propellants. This recirculating flow acts as a hot-product pool providing energy to ignite incoming propellants. Similar phenomenon is observed for a swirl coaxial injector in the present study. The flame initiates and anchors in the recess region close to the injector post, where two counter-rotating recirculation zones are formed as shown in Fig. 6.7. The flame is

herein stabilized in this low-velocity and high-temperature region. The recirculating flows are also generated at the left wall of the chamber and near the centerline and play an important role in stabilizing combustion by preheating incoming kerosene and LOX, respectively. The center-recirculating flow, closely related to vortex breakdown as shown in Chapter 4, carries significant amount of heat flux back to the central injector to enhance the preheat effect. This explains the tremendous increase of temperature in the gaseous core as shown in Fig. 6.4.

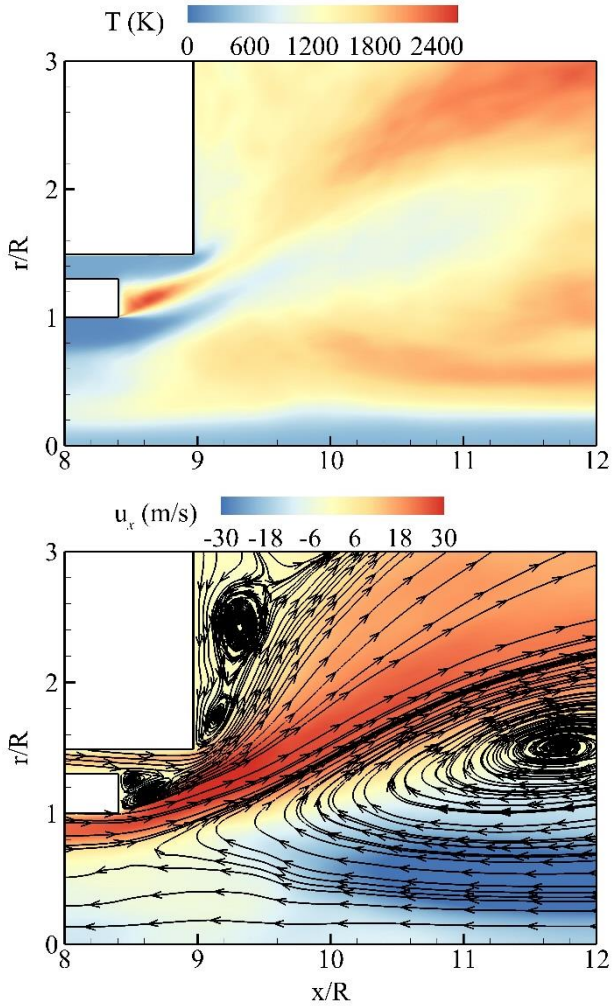

Figure 6.7: Time-averaged distributions of temperature and axial velocity interpolated by flow streamline at the injector near-field.

6.2.2 Parametric Study

This session will investigate various geometric parameters that might influence the performance of mixing and combustion. Emphasis is given on recess region, post thickness, and kerosene annulus width, which were regarded as the important factors for the injector mixing characteristics in the previous cold flow studies.

6.2.2.1 Effect of Recess Region

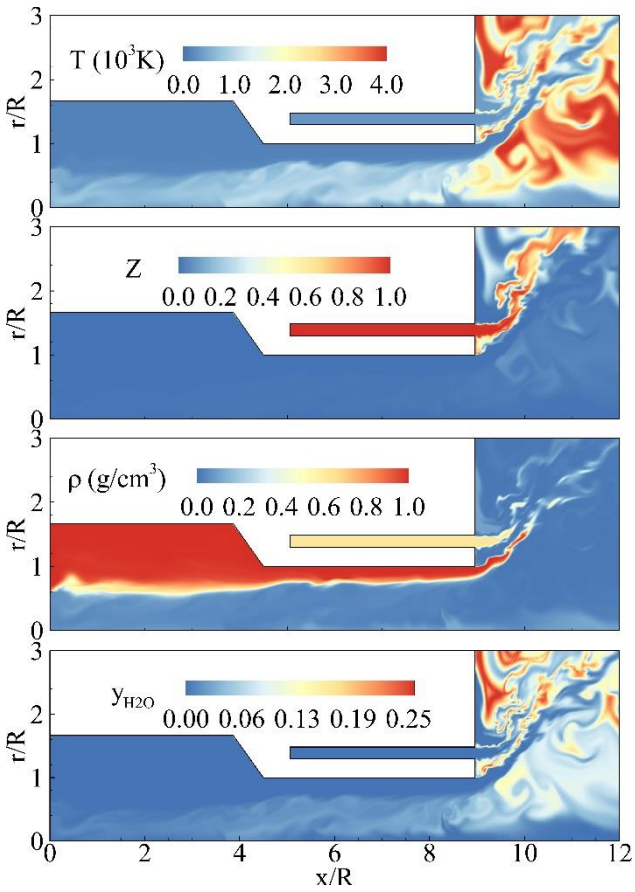

Figure 6.8: Instantaneous flow snapshot of distributions of temperature, density, mixture fraction, and mass fraction of H2O for Case II.

In Fig. 6.8, the influence of recess region on flame characteristics is examined. The kerosene film penetrates further downstream in the chamber in Case II, compared to Case I with a recess region. The mixing of kerosene and LOX thus occurs externally in Case II,

while it starts internally in the recess region in Case I. This justified the previous finding that the presence of recess region advances the propellants' mixing and improves the combustion efficiency [41] remarkably. The recess region behaves like an undisturbed combustion chamber, which keeps propellants well-mixed and ignited in an area close to the injector and flame insensitive to the disturbances in the chamber. Furthermore, the outward spreading angle of kerosene film is much smaller in the absence of recess region in Case II, and this is disadvantageous to the thermal protection of the left wall of the chamber, as will be discussed in the later session.

6.2.2.2 Effect of Post Thickness

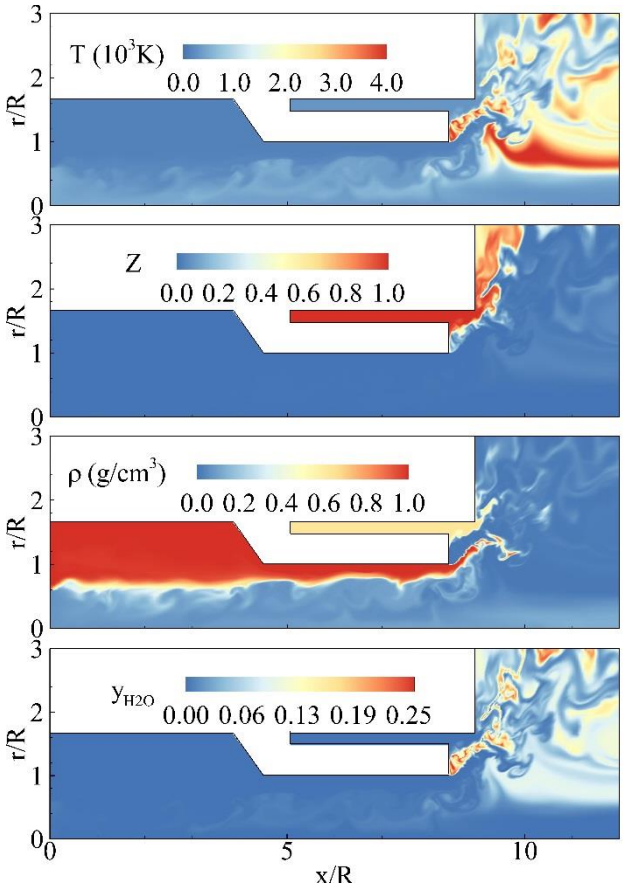

Figure 6.9: Instantaneous flow snapshot of distributions of temperature, density, mixture fraction, and mass fraction of H2O for Case III.

Figure 6.9 shows the instantaneous distributions of flame properties at a larger post thickness for Case III. Similar to results of cold-flow studies, the spreading angle in Case III is larger, which improves the mixing of LOX and kerosene and leads to a steeper flame shape than in Case I. The left wall of the chamber is covered by the cold kerosene stream, which can avoid overheating of the corner-recirculation of hot products. However, the kerosene film fails to cover the whole injector post as it does in Case I, and the bottom portion of the post has a mixture ratio close to stoichiometry. The flame is thus closely attached to the lower tip of the injector post, which is exposed to a considerable amount of heat release from combustion and is easy to be destroyed. This thickened injector might be regarded as an improper design for the consideration of thermal protection. Nevertheless, it is promising that a critical injector post thickness between Cases I and III can be found to achieve an optimum performance with larger spreading angle and full coverage of injector post by kerosene film.

6.2.2.3 Effect of Kerosene Annulus Width

Figure 6.10 shows the instantaneous distributions of flame properties for Case IV with a larger annulus width. It was found that much longer time is required for the kerosene film to reach a full-developed state in the annulus in Chapter 5. The flame is fully attached to the injector post and tends to fluctuate with the motions of eddies. As shown in Fig. 6.11 on the temporal evolution of the flame field, the flame is, initially anchored to the post, accumulated in the recess region, then carried into the annulus by swirling eddies, and eventually extinguished by incoming cold kerosene stream. This unstable flame behavior might generate and modify the flow oscillations in the injector. Similar to Case III, the exposure of injector post to the hot products is potentially destructive to the injector assembly if the cooling process is not sufficient for a real combustor system.

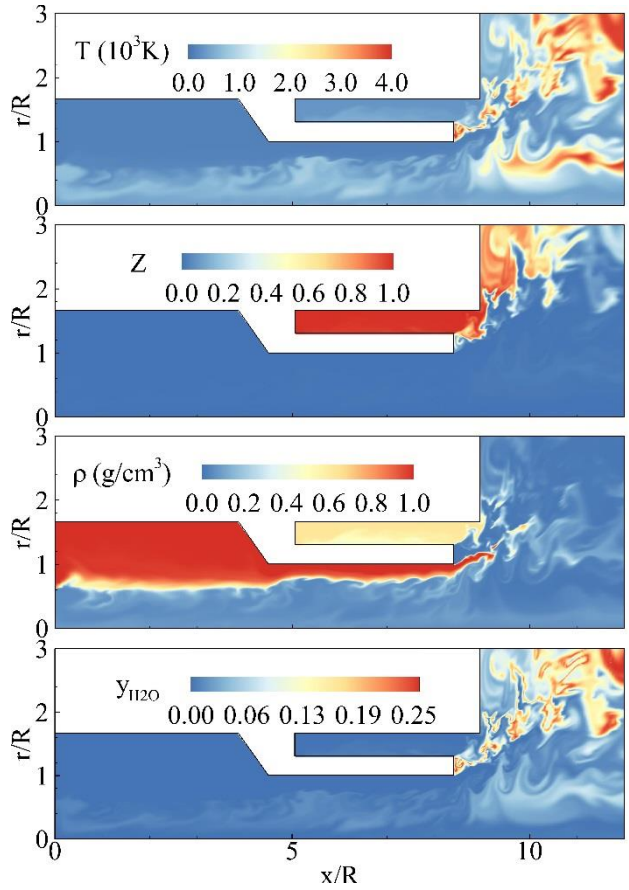

Figure 6.10: Instantaneous flow snapshot of distributions of temperature, density, mixture fraction, and mass fraction of H2O for Case IV.

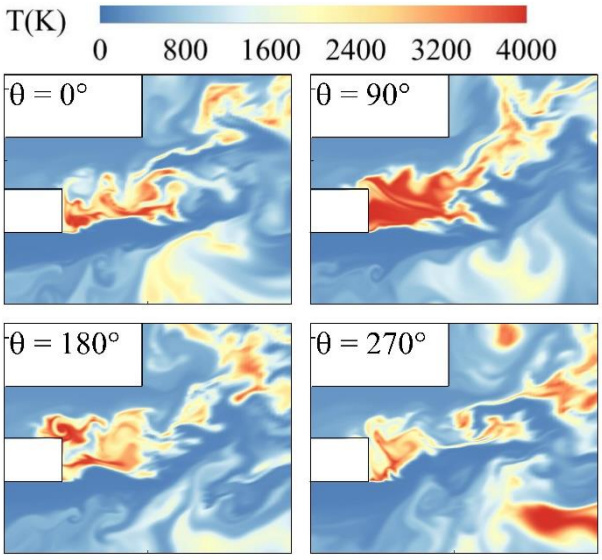

Figure 6.11: Temporal evolution of the flame field for Case IV.

Figure 6.12 shows the time-averaged distributions of mixture fraction at the injector near-field for four cases. It is clearly seen that the spreading angle for Case II is the smallest, while the kerosene film for other cases tend to flow along the chamber wall, which protects the wall from overheating by the recirculation of hot products. The temperature profile at the chamber wall in the radial direction in Fig. 6.13 yields that the wall heat load for Case II is much higher than other cases. This indicates that the existence of recess region significantly reduces the heat flux from combustion to the chamber wall and therefore alleviates the load of cooling channels.

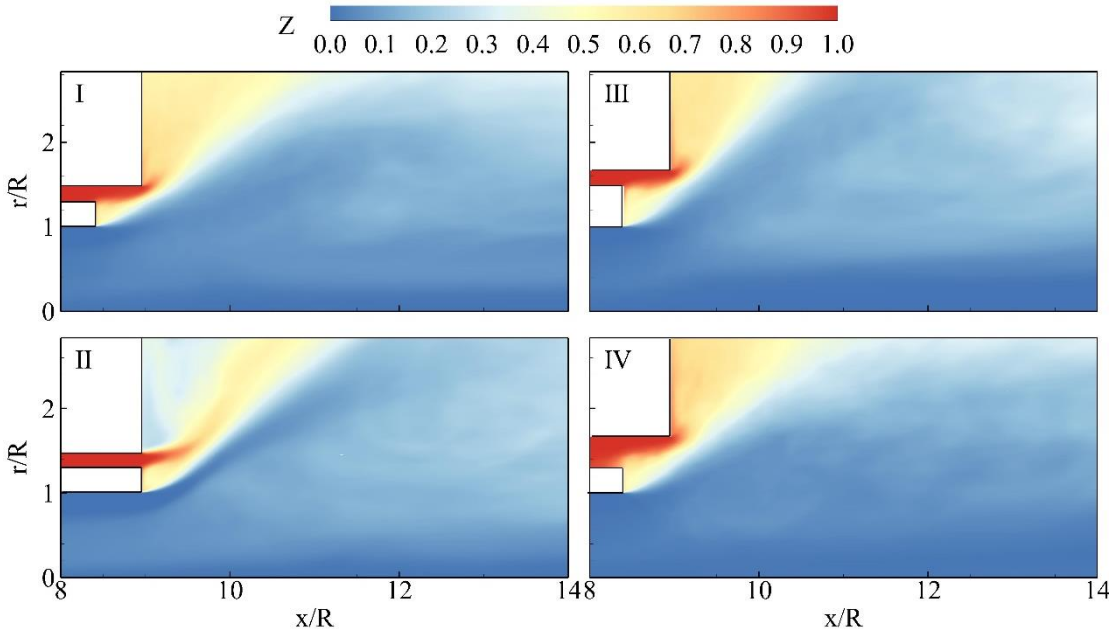

Figure 6.12: Time-averaged distributions of mixture fraction at the injector near-field for four cases.

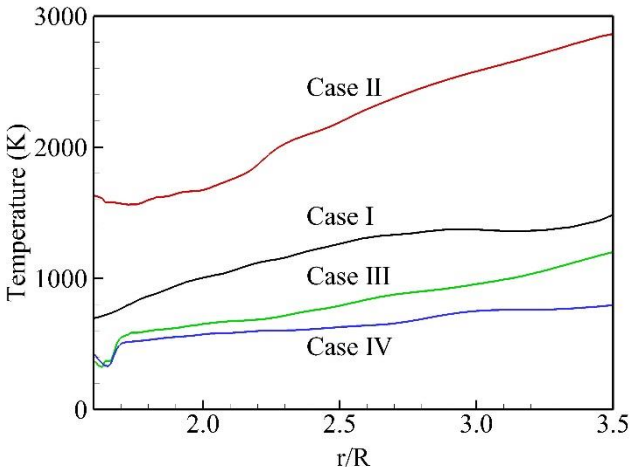

Figure 6.13: The radial distributions of the chamber wall temperature for all cases.

6.2.2.4 Near-field Flame Dynamics

The oscillatory flowfield was carefully investigated to gain insight into the driving mechanism for acoustic oscillations. A number of probes were placed at various locations to record the flow motions. Figures 6.14 and 6.15 show the pressure fluctuations (p') downstream of the LOX post, denoted by the black dot in the time and frequency space, respectively. The pressure oscillates periodically due to the strong interactions of vortices and their coupling effects with the flame. The maximum amplitude of the relative pressure, defined as p'/p_0, is less than 10% for all cases, but the amplitude in Cases II and IV is considerably higher. The power spectral density reveals the same dominant frequency (6.47 kHz) for Cases I, III, and IV, corresponding to the vortex shedding frequency. This can be explained by the similar velocity profiles of these cases with the recess region emanating from the inner swirler, which induce similar inner shear layers between the LOX stream and the hot products. The absence of the recess region seems to shift the dominant motion to the high-frequency regime. The variation of the kerosene annulus width has a negligible effect on the dominant vortex-shedding frequency, but it determines the amplitude of fluctuation. Further analysis on heat-release-rate oscillations induced by acoustic and

vortical perturbations will be represented in subsequent work to study underlying flame responses.

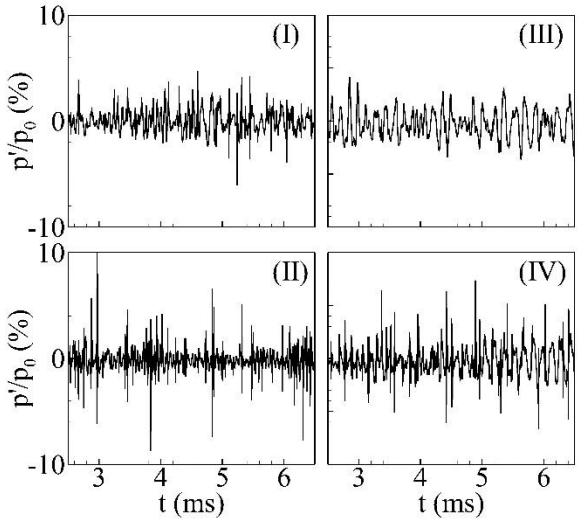

Figure 6.14: Time history of relative pressure oscillations in the flame zone for all cases.

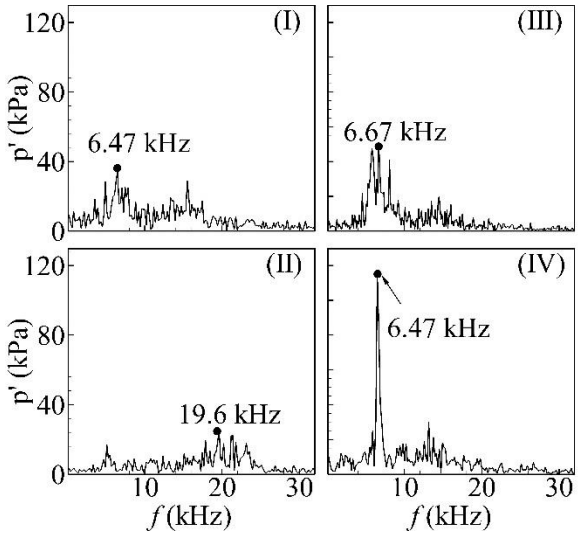

Figure 6.15: Frequency spectra of pressure oscillations in the flame zone for all cases.

6.3 Conclusion

This chapter provides a systematic investigation of flow evolution and flame dynamics under various injector geometries. The flame is stabilized by two counter-rotating recirculation flows containing hot combustion products in the recess region, which plays a significant role in not only accomplishing efficient mixing and combustion but providing thermal protection of the injector faceplate. Decreasing the annulus width or post thickness might induce the initially attached flame to detach from the injector post surface. Consistent with results of cold-flow studies, the spreading angle increases as either the post thickness or the kerosene annulus width increases. But neither of them can sustain a completely thermal protection of the injector post surface. The larger annulus width produces the largest amplitude of pressure oscillations and introduces flame in the lower surface of the annulus, potentially leading to unstable combustion. In order to achieve the optimal combustion performance, further parametric studies have to be performed to determine values of the group of recess length, post thickness, and kerosene annulus width.

CHAPTER 7

COUNTERFLOW DIFFUSION FLAMES: OXYGEN/HYDROGEN MIXTURES

Laminar counterflow flames have been extensively studied under different flow and boundary conditions, due to their geometrical simplicity, fundamental flame behaviors and burning properties. For a reactive system with large activation energy, the flame response displays an S-shaped curve with respect to Damköhler number. This curve can be used to characterize the evolution of a flame subject to continually varying flow conditions, including ignition, extinction, and instability. Existing studies on counterflow diffusion flames of general fluids only considered the steady burning branch of S-shaped curve and failed to capture the extinction and ignition characteristics. Although the FlameMaster [57] and CHEMKIN-PRO package [58], using the arc-length approach and the flame-controlling method, respectively, were developed to study the flame response throughout the entire S-curve, they are limited to ideal gases.

This chapter is going to investigate the responses of oxygen/hydrogen flames based on the theoretical framework established in Chapter 2. Within this general framework, the flame solution for real fluids would be obtained over a complete S-curve with detailed chemical mechanisms. Results will shed light on flame behaviors over the entire fluid thermodynamic regime, from compressed liquid to ideal gas through the transcritical state. Results can also be implemented to generate chemistry tables for supercritical combustion models using tabulated chemistry, such as the flamelet approach in Ref. [12].

The operating pressure ranges from 0.5 to 200 atm. The inlet temperatures of oxygen and hydrogen considered here are between 120-300 K and 20-300 K, respectively. Detailed information about the flame structures and heat release characteristics is obtained for strain rates of 10^2-10^8 s^{-1}. The major contributions of the present study include: (1) flame solutions for real fluids are extended to the entire S-curve; (2) a theoretical analysis

is derived from the conservation equations to quantify the dependence of the heat release rate on pressure and strain rate, as well as the effect of pressure on the extinction strain rate; and (3) general flame similarities are established in a normalized strain-rate space for the flame temperature, flame thickness, species concentrations, reaction rates, and heat release rate.

7.1 Theoretical and Numerical Framewrk

7.1.1 Theoretical Formulation

The present study extends previous analyses by incorporating general-fluid thermodynamics and transport theories, such that a unified framework can be constructed to treat the flame response for real fluids over a complete S-curve, including both the steady- and unstable-burning branches. The governing equations were discussed in Chapter 2. It is noted that enthalpy is used instead of temperature in the energy equation, given that the enthalpy is a sole function of temperature for general fluids. SRK EOS introduced previously is implemented to close the formulation.

Full account is taken of general-fluid thermodynamics and transport over the entire temperature and pressure regimes of concern. The thermodynamic properties, such as enthalpy, Gibbs energy, and specific heat capacity, are derived directly from fundamental thermodynamic theories. They are expressed as the sum of an ideal-gas property at the same temperature and a thermodynamic departure function accounting for dense-fluid correction [1]. Transport properties, such as viscosity and thermal conductivity, are estimated using the method of Chung et al. [153]. The binary mass diffusivity is obtained by the Takahashi method calibrated for high pressure conditions [154]. The implementation and validation of the property evaluation schemes are outlined in Refs. [1] and [155].

7.1.2 Boundary conditions

Boundary conditions must be specified properly. Two types of boundary conditions are typically applied. Dixon-Lewis et al. [51] assumed a stagnation-point potential flow at the boundaries by linearly correlating the radial and axial velocities with a constant strain rate. Kee et al. [52] considered a uniform (plug) flow at the nozzle exit by specifying zero radial velocity. Chelliah et al. [53] showed that the plug-flow boundary condition is more suitable for counterflow burners. It is thus employed in the present study.

At the fuel inlet,

$$F=\frac{\rho_F u_F}{2}, G=0, T=T_F, \rho u Y_k+\rho Y_k V_k=\left(\rho u Y_k\right)_F \tag{7.1}$$

At the oxidizer inlet,

$$F=\frac{\rho_O u_O}{2}, G=0, T=T_O, \rho u Y_k+\rho Y_k V_k=\left(\rho u Y_k\right)_O \tag{7.2}$$

where the subscripts *F* and *O* denote the fuel and oxidizer streams, respectively. The distance between the two inlets is fixed to L = 2 cm, with the fuel inlet at $x = 0$ and the oxidizer inlet at $x = L$. It is worth noting that the velocity boundary condition in [15] and [18] is specified in such a manner that its gradient corresponds to the strain rate of concern. The strain rate in the current work, however, is treated as an eigenvalue of the numerical system, not an input parameter.

7.1.3 Numerical Methods

The governing equations can be written in the following vector form,

$$L(\phi)=0 \tag{7.3}$$

where $\phi=\phi\left(F_{J=1}, G_{J=1}, H_{J=1}, T_{J=1}, Y_{k,J=1}, \ldots, F_{J=N}, G_{J=N}, H_{J=N}, T_{J=N}, Y_{k,J=N}\right)$ includes all primary variables at the grid points and *L* is a differential operator. The subscript *J* is the grid index and N is the number of grid points. For a given chemical mechanism involving *K* species, the total number of differential equations is $N(K+3)$. A modified Newton iteration method is implemented to solve these equations.

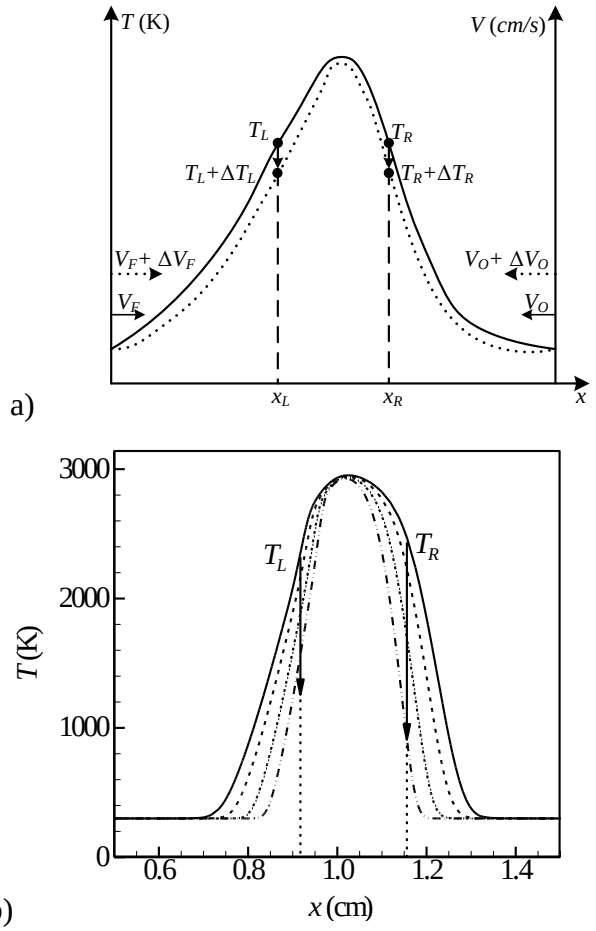

Figure 7.1: a) Schematic of two-point temperature-controlling continuation method, solid line: initial solution, dashed line: new solution; b) Changes of temperature distribution applying two-point temperature-controlling method, solid line: V_F = 105 cm/s, dashed line: *136* cm/s, dash-dotted line: *200* cm/s, dash-dot-dotted line: *301* cm/s.

Equation 7.3 represents a well-posed two-point boundary-value problem. The flame solution along the steady branch of the S-curve has been previously obtained for ideal gases [54, 56] and real fluids [59, 63]. When the strain rate reaches its extinction limit, a numerical singularity appears, leading to a serious difficulty in convergence. A two-point flame-controlling continuation method [56] is employed to overcome this challenge, as illustrated in Fig. 7.1. Given an initial solution denoted by the solid line in Fig. 7.1a, two control points (X_L, X_R) are selected on both sides of the peak temperature, with known temperature values (T_L, T_R). Applying a temperature change at the two control points gives

rise to a new flame solution denoted by the dashed line. The temperature changes are negative in Fig. 7.1a, that is, $\Delta T_L < 0$ and $\Delta T_R < 0$. As a result, the maximum flame temperature decreases while the fuel inlet velocity and strain rate increase. Figure 7.1b shows typical numerical results. The maximum flame temperature continues to decrease and finally reaches a critical point where extinction occurs, corresponding to Da_{ext} as shown in Fig. 2.1. Near the extinction point, further decreases in the temperatures at the two controlling points result in a monotonic decrease in the maximum flame temperature. The flame solution then moves smoothly from the upper branch to the middle branch.

Since two internal boundary conditions have been applied at the controlling points, two boundary conditions must be released to render the governing equations well posed. In the present work, dummy equations are added for H and u_F at every grid point except the two controlling points. The mathematical formulation follows.

At controlling point X_L,

$$\frac{dH}{dx} = 0, J \neq J_{R,\,fix}; T[J] = T_R, J = J_{R,\,fix} \tag{7.4}$$

At controlling point X_R,

$$\frac{du_F}{dx} = 0, J \neq J_{L,\,fix}; T[J] = T_L, J = J_{L,\,fix} \tag{7.5}$$

where the subscripts R and L denote the control points on the right and left hand sides of the flame, respectively. The subscript *fix* denotes a fixed point in the flowfield.

7.2 Results and Discussions

The theoretical and numerical framework outlined above is used to study the S-curve response of hydrogen-oxygen counterflow diffusion flames over a broad range of pressures and strain rates. The chemical kinetic mechanism developed by Li et al. [156] is employed; it consists of 8 species $(H_2, H, O, O_2, OH, HO_2, H_2O, H_2O_2)$ and 19 reversible elementary reactions. This mechanism has been validated against experimental data for shock tubes,

flow reactors and laminar premixed flames over a temperature range of 298-3000 K, a pressure range of 0.3-87 atm, and an equivalence ratio range of 0.25-5.0. It should be noted that the present study covers pressures up to 200 atm, and flame temperatures over 3000 K. An improved kinetics scheme is warranted for higher pressures and temperatures. For reference, the critical pressures and temperatures for oxygen and hydrogen are listed in Table 1.2.

7.2.1 Model Validation

As part of model validation, a hydrogen-oxygen counterflow diffusion flame at 1 atm is first considered. The strain rate, defined based on the maximum velocity gradient on the fuel side [53], is a = 500 s^{-1}. The inlet temperatures are fixed at 300 K. Four different approaches are employed. The baseline case is an ideal-gas approach modeled using the CHEMKIN package. Case II employs the SRK EOS with ideal-gas property evaluation. Case III incorporates the SRK EOS and real-fluid thermodynamics. Case IV accommodates a full treatment of real fluids, including the SRK EOS, thermodynamic, and transport properties.

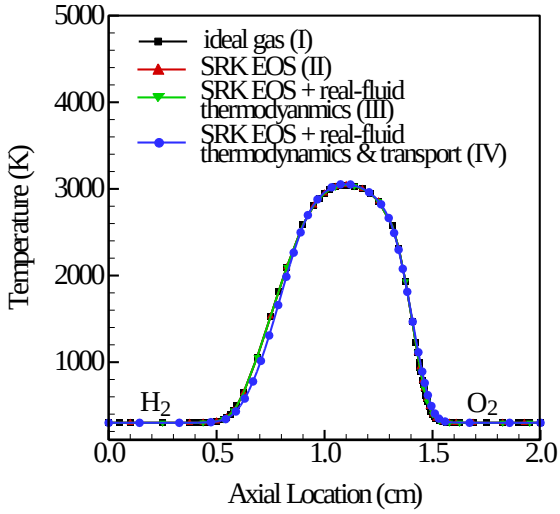

Figure 7.2: Temperature distributions at $p=1$ atm, $T_{H_2}=T_{O_2}=300$ K, and $a=500$ s^{-1}.

Figure 7.2 shows the temperature profiles obtained from the four different approaches. They are nearly identical for the first three cases with a maximum flame temperature of 3022 K. For Case IV, the flame shape is slightly different in the fuel-rich region, and the maximum flame temperature is 11 K higher. The difference appears to be negligible. Results indicate that the SRK EOS and real-fluid property evaluation schemes are implemented properly. The fluid behavior at the ideal-gas limit is recovered accurately. Although not shown here, flame structure results from the present numerical scheme and the CHEMKIN code are almost identical in terms of species and heat release distributions. Such close agreement validates the present analysis.

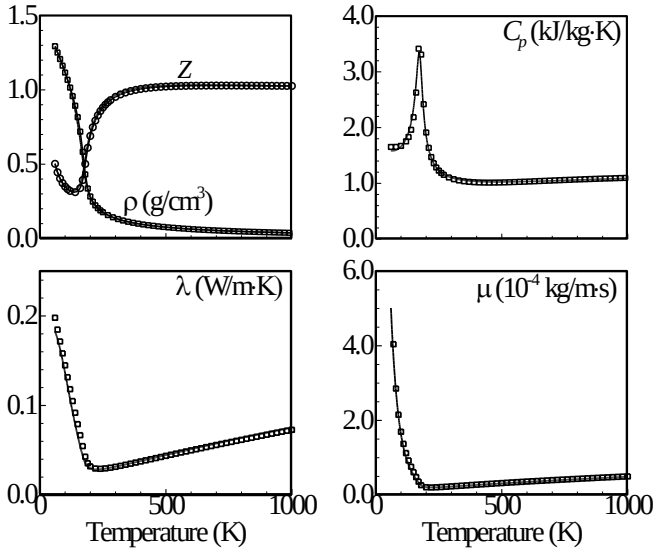

Figure 7.3: Validation of thermodynamic and transport properties of oxygen against NIST data. *p* = 100 atm. Lines: the present numerical scheme; symbols: NIST data. Compressibility (*Z*) and density (ρ), specific heat at constant pressure (C_p), thermal conductivity (λ), and dynamic viscosity (μ).

The property evaluation scheme must be examined carefully. Fluids often experience thermodynamic and transport anomalies when they are injected from a compressed-liquid state into an environment where the temperature and pressure exceed their critical values, especially at pressures close to the critical point [14]. Figure 7.3 plots

thermophysical properties showing good agreement with the NIST database for oxygen at 100 atm, over a temperature range covering both the subcritical and supercritical regimes. The compressibility factor is significantly smaller than unity at low temperatures, which is not the case for the ideal gas condition.

7.2.2 S-Curve Flame Response

The flame response to the variation of the flow strain rate is investigated over a broad pressure range of 0.5-200 atm. The inlet temperatures of oxygen and hydrogen vary from 120-300 K and 20-300 K, respectively. The flame characteristics over the entire fluid thermodynamic regime, from compressed liquids to ideal gases, are examined systematically. As an example, Fig. 7.4 shows the temperature profiles at 50 atm with a strain rate of 10004 s^{-1}. Significant differences between the results of the ideal-gas (I) and real-fluid (IV) approaches are observed.

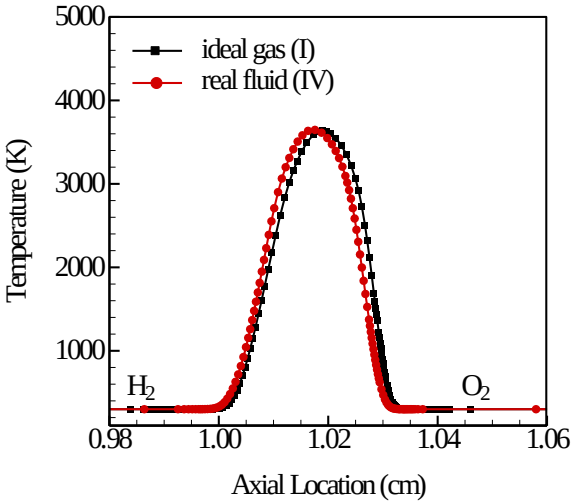

Figure 7.4: Temperature distributions at $p=50$ atm, $T_{H_2}=T_{O_2}=300$ K, and $a=10004$ s-1.

7.2.2.1 Effect of Pressure and Strain Rate

Figure 7.5 shows the maximum flame temperature as a function of strain rate at various pressures. The solid and dashed lines are real-fluid and ideal-gas (CHEMKIN) results, respectively. They match closely. The weakly reacting (lower) branch shown schematically in Fig. 1 is not present here, due to the low inlet temperature of 300 K, which is well below the ignition point. A complete S-curve response can be obtained with a higher inlet temperature [56]. The maximum flame temperature remains almost constant at low strain rates, and starts to decrease progressively until the extinction point is reached. At low strain rates, the *Da* number is large. Chemical reactions have sufficient time to release thermal energy to balance heat loss. Further increase in the strain rate renders the flow residence time comparable to the chemical reaction time. The resultant incomplete combustion results in a lower flame temperature. The heat generation eventually reaches a point that cannot overcome the heat loss; the flame comes to a sharp extinction. For a given strain rate, the maximum flame temperature always increases with increasing pressure.

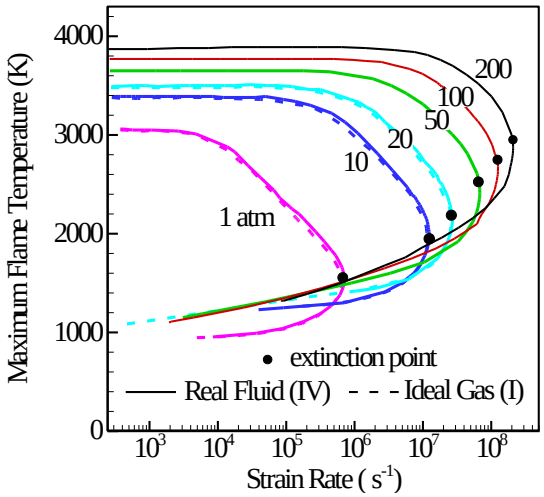

Figure 7.5: Maximum flame temperatures at various pressures, $T_{H_2} = T_{O_2} = 300$ K.

Figure 7.6 shows the effect of strain rate at various pressures on the total heat release rate per unit area, defined as

$$q = \int_0^L \left(\sum_{k=1}^{K} \hat{h}_k MW_k \omega_k \right) dx \tag{7.6}$$

A linear relationship is observed on log-log scales. Along the stable burning (upper) branch, the heat release rate first increases linearly with the strain rate, then reaches a maximum (indicated with dots in Fig. 7.6), and finally decreases, before the flame is extinguished. At the extinction point, the variation of the heat-release rate with respect to the strain rate becomes infinite, producing a mathematical singularity. Further decrease of the strain rate beyond this point reduces the heat release rate. The unstable burning (lower) branch shows an inverse behavior as compared to the upper branch. This result appears to be the first of its kind obtained beyond the extinction limit for high-pressure conditions using a real-fluid approach.

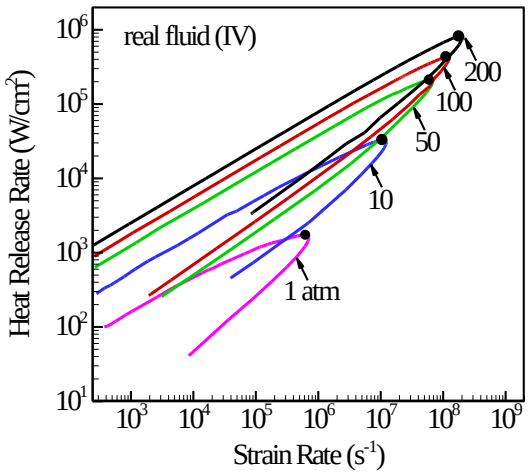

Figure 7.6: Heat release rate per unit area as function of strain rate: $p = 1 \sim 200$ atm,

The heat-release rate profiles indicate a strong similarity for different pressures. Careful data analysis shows that the heat-release rate in the upper (stable burning) branch of the S-curve can be correlated with pressure and strain rate a as $q \sim \sqrt{pa}$. The same

relationship was previously obtained by Ribert et al. [59] and Lacaze and Oefelein [61], but the physical meaning of the relationship has not yet been clearly explained. In addition, the pressure effects on the maximum flame temperature and species concentrations are yet to be addressed. A theoretical analysis is thus developed in the present study by means of the energy and species conservation, in order to provide direct insight into observed phenomena.

When the strain rate is significantly smaller than the extinction value, a_{ext} (that is, the flow time is much greater than its chemical counterpart and the *Da* number is large), the flame is diffusion-controlled. An order of magnitude analysis of the energy conservation in Eq. 2.24 shows that the heat flux is primarily driven by conduction rather than mass diffusion. Furthermore, these two terms are greater than the convection term by at least two orders of magnitude. Both findings are corroborated by the present numerical results. With the neglect of higher-order terms, the energy balance between heat production and heat loss by conduction becomes

$$\frac{d}{dx}\left(\lambda\frac{dT}{dx}\right)-\sum_{k=1}^{K}MW_k\hat{h}_k\omega_k\approx 0 \tag{7.7}$$

Integrating Eq. 7.7 throughout the flame zone, we have

$$q=\int_0^L\sum_{k=1}^{K}MW_k\hat{h}_k\,\omega_k\,dx\cong\bar{\lambda}\frac{\bar{T}}{\delta^2}\delta \tag{7.8}$$

where $\bar{\lambda}$ is the average thermal conductivity, $\bar{T}$ the mean temperature in the flame zone, and δ the flame thickness. The left-hand side of Eq. 7.8 represents the rate of chemical energy release per unit flame area. In a diffusion-controlled flame, $MW_k\omega_k$ in the species equation, Eq. 2.25, is determined by the molecular diffusion process represented by $d\left(\rho Y_k V_k\right)/dx$, with the convection term $\rho u dY_k/dx$ being an order of magnitude smaller. A dimensional analysis suggests that $d\left(\rho Y_k V_k\right)/dx\sim\rho D/\delta^2$. Assuming a Lewis number of unity, the thermal diffusivity, $\alpha=\lambda/\rho c_p$, becomes identical to the mass diffusivity *D*.

In the flame zone, $\hat{h}_k \sim c_p \bar{T}$ Substitution of these terms into the left hand side of Eq. 7.8 gives $q \sim \bar{\lambda}\bar{T}/\delta$, which is the same as the right hand side of Eq. 7.8. The thermal conductivity varies with temperature as $\bar{\lambda} \sim \sqrt{\bar{T}/MW_{mix}}$. The right hand side of Eq. 7.8 becomes $\bar{T}^{1.5}/\left(\delta\sqrt{MW_{mix}}\right)$. The flame thickness can be correlated with the mass diffusivity and strain rate as $\delta \sim \sqrt{D/a}$ [2], where the mass diffusivity *D* depends on temperature and pressure in the form of $D \sim \bar{T}^{1.5}/\left(p\sqrt{MW_{mix}}\right)$, according to gas kinetics theories [157]. Incorporation of the above expressions into Eq. 7.8 leads to

$$q \sim \frac{\bar{T}^{0.75}}{MW_{mix}^{0.25}}\sqrt{pa} \tag{7.9}$$

This relationship was previously derived by Poinsot and Veynante [120] based on assumptions of infinitely fast chemistry and constant density. The present study addresses this issue from a different perspective. For a given reactive system, the flame temperature and mixture molecular weight are relatively insensitive to pressure. Equation 7.9 reduces to $q \sim \sqrt{pa}$ and recovers the phenomenological correlation introduced by Ribert et al. [59]. The present work provides a theoretical basis for the heat-release relationship with pressure and strain rate.

As indicated by Fig. 7.5, the maximum flame temperature at low strain rates depends weakly on pressure as $\bar{T} \sim p^{0.045}$. The mixture molecular weight changes slightly with the strain rate and pressure, with the maximum deviation being less than 20% over the conditions of concern. It is thus assumed to remain constant to first approximation. Equation 7.9 becomes

$$\frac{q}{p^{0.534}} \sim \sqrt{a} \tag{7.10}$$

Normalization of the strain rate by its extinction value, a_{ext}, gives

$$\frac{q}{p^{0.534}a_{ext}^{0.5}} \sim \sqrt{\frac{a}{a_{ext}}} \tag{7.11}$$

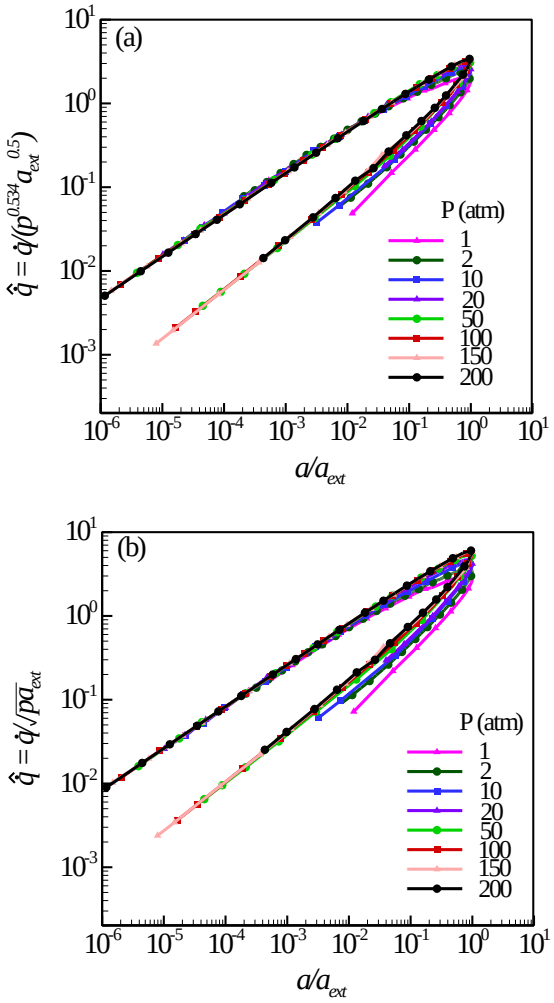

Figure 7.7: Scaled heat release rate q as function of normalized strain rate rate (a/a_{ext}). (a) new scale, Eq. 7.11; (b) old scale, $q = q/\sqrt{pa_{ext}}$.

Figure 7.7a shows the scaled heat release rate, $q \equiv q/\left(p^{0.534}a_{ext}^{0.5}\right)$, as a function of the reduced strain rate, a/a_{ext}. All the curves collapse to a single profile. The correlation works well even near the extinction point, especially for pressures greater than 2 atm. The

same information with a simplified version of the scaled heat release, $q \equiv q / \sqrt{p a_{ext}}$, is given in Fig. 7.7b. The difference between the two scaled heat releases appears to be quite modest, although Eq. 7.11 offers slightly improved agreement. The importance of the present analysis is twofold: (1) the physical basis for the heat-release dependence on pressure and strain rate is established directly from the conservation laws, and (2) a general correlation for the heat-release rate is obtained.

The general correlation for heat release in Eq. 7.11 suggests that the flame behaviors at high pressures can be predicted based on those at low pressures. To further clarify the existence of such a flame similarity, results for the flame thickness, temperature, species concentrations, and reaction rates are examined over a broad range of strain rates and pressures. Figure 7.8 shows the temperature distributions at three different pressures and strain rates. Although the flame thickness and maximum flame temperature for the three cases are quite different, due to the combined effect of pressure and strain rate, they bear intrinsic similarities. To this end, we first align the flames by shifting the location of the maximum flame temperature to x = 0, normalize the x-coordinate by $\bar{T}^{0.75} / \sqrt{pa}$, and then normalize the flame property of interest with respect to its maximum value for a given flame. The results are given in Fig. 7.9. The normalized profiles of temperature, mass fractions of H_2O, OH, and H, and reaction rates of H_2O and OH are almost identical for different pressures and strain rates. A strong similarity in the flame profiles exists, especially for pressures greater than 10 atm.

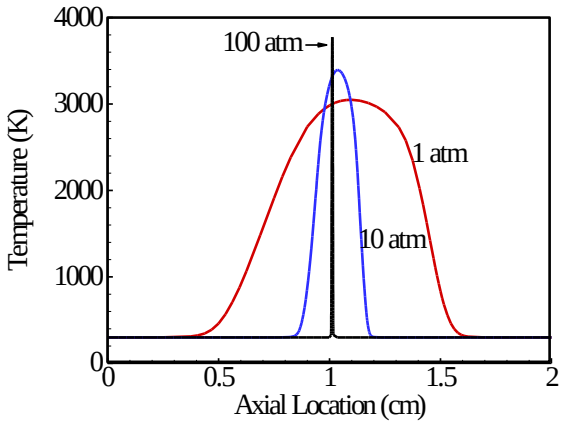

Figure 7.8: Temperature profile at different pressures and strain rates, 1 atm $a = 101\text{s}^{-1}$ (red lines), 10 atm $a = 107.6\text{s}^{-1}$ (blue lines), and 100 atm, $a = 3000\text{s}^{-1}$ (black lines).

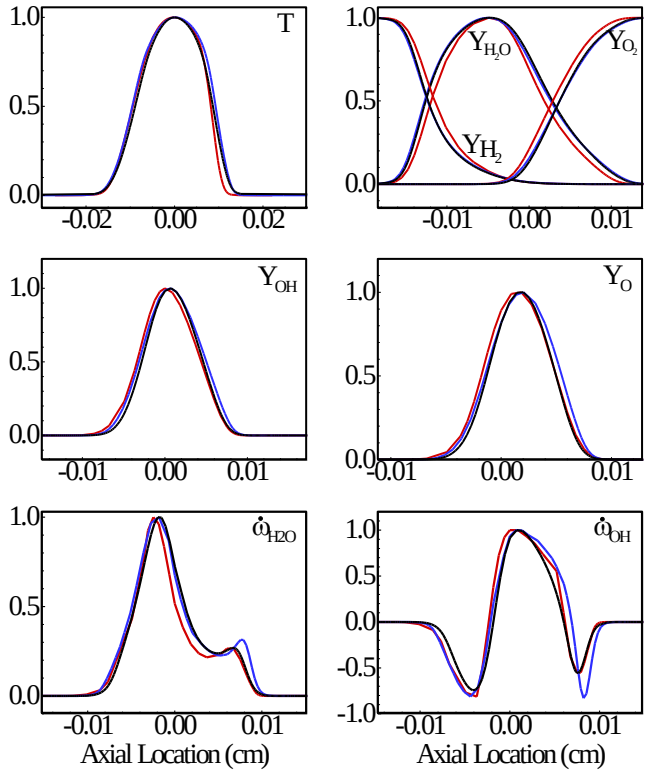

Figure 7.9: Normalized flame temperature, mass fractions, and reaction rates at different pressures and strain rates, 1 atm $a = 101\text{s}^{-1}$ (red lines), 10 atm $a = 107.6$ s^{-1} (blue lines), and 100 atm, $a = 3000\text{s}^{-1}$ (black lines).

Figures 7.8 and 7.9 show the results of only three selected strain rates and pressures. It is desirable, however, to confirm the similarities of flame structures over a wide range

of flow conditions. Figure 7.10 presents four different types of flame thickness, δ, defined based on the half maximum width of the temperature and mass fractions of H_2O, OH and H, respectively, as functions of the normalized strain rate a/a_{ext}. The pressure covers a range of 1-200 atm, and the flame thickness is scaled by $1/\sqrt{pa_{ext}}$. Identical profiles for the flame thickness are obtained over the entire S-curve.

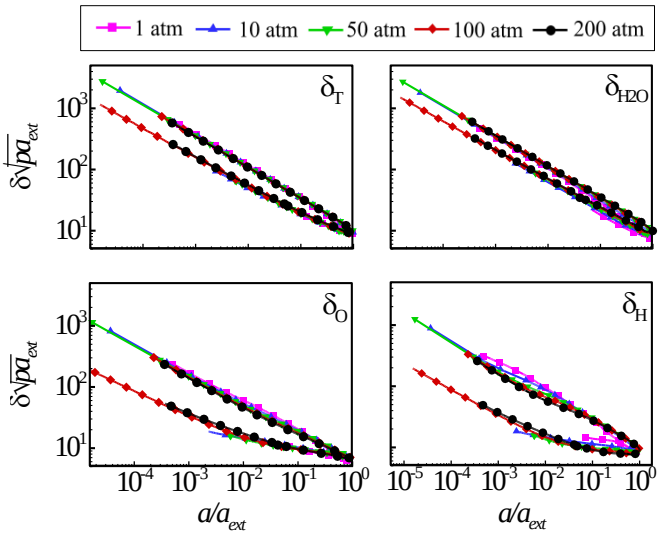

Figure 7.10: Normalized flame thickness based on half maximum width of temperature and mass fractions of H2O, OH, and H as functions of normalized strain rate (a/a_{ext}) at different pressures.

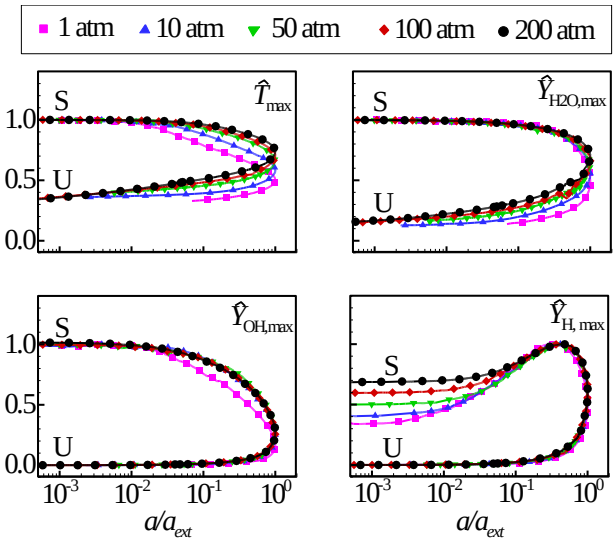

Figure 7.11: Normalized maximum temperature and mass fractions of H2O, OH, and H in the flame as functions of normalized strain rate(a/a_{ext}) at different pressures. S: stable burning branch, U: unstable burning branch.

The flame structures feature a similar trend for temperature and species. Figure 7.11 shows the maximum temperature and mass fractions of combustion products in the flame zone as functions of the normalized strain rate a/a_{ext}. All the flame quantities are normalized with respect to their largest values over the entire S-curve. For example, the maximum flame temperature is normalized by its highest value at the limit of zero strain rate. The normalized maximum flame temperatures for various pressures fall onto a single profile at low strain rates, but start to deviate at larger strain rates ($0.1a_{ext}$ for high pressures and $0.01a_{ext}$ for 1 atm). The H_2O and OH mass fractions exhibit strong similarities for the stable burning branch of the S-curve, except for the 1 atm case. The situation with the H radical, however, is quite different. The largest value of the maximum H mass fraction in a flame ($Y_{H,max}$) occurs at a high strain rate, and the normalized profiles collapse for a/a_{ext} >0.1. For low strain rates (a/a_{ext} <0.01), $Y_{H,max}$ profiles are flat at all pressures. A careful examination of $Y_{H,max}$ profiles suggests a different scaling strategy. For each pressure,

$Y_{H,\max}$ can be renormalized in terms of two extreme values over the stable burning branch, $\left(Y_{H,\max}\right)_S$ and $\left(Y_{H,\max}\right)_L$ as follows:

$$\hat{Y}_{H,max} = \frac{Y_{H,max} - \left(Y_{H,max}\right)_S}{\left(Y_{H,max}\right)_L - \left(Y_{H,max}\right)_S} \tag{7.12}$$

where the subscripts *S* and *L* outside the parentheses denote the smallest and largest values on the upper branch of the s-curve, respectively. The scaled $\hat{Y}_{H,max}(p)$ at different pressures have different profiles, but all the profiles can be expressed as the sum of the profile at 1 atm and a Gaussian distribution as follows:

$$\hat{Y}_{H,max}(p) = \hat{Y}_{H,max}\big|_{1\,atm} + G(p) \tag{7.13}$$

where

$$G(p) = \frac{C}{\sqrt{2\pi}\sigma} exp\left\{-\frac{\left[log\left(a/a_{ext}\right) - \mu\right]^2}{2\sigma^2}\right\} \tag{7.14}$$

The mean and standard deviation are $\mu = -1.4$ and $\sigma = 0.8$, respectively. The coefficient C is a function of pressure,

$$C = 0.46 - 0.636 log\left(p/p_0\right) \text{ with } p_0 = 1\,\text{atm}. \tag{7.15}$$

Figure 7.12 shows $\hat{Y}_{H,max}(p)$ and $\hat{Y}_{H,max}(p) - G(p)$. The scaling given by Eq. 7.13 collapses the results at various pressures and strain rates perfectly.

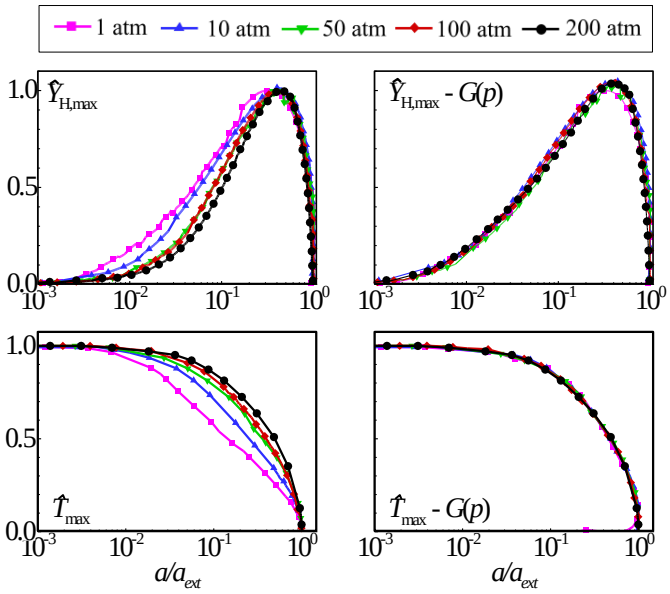

Figure 7.12: Renormalized maximum mass fraction of H radical, $\hat{Y}_{H,max}$, and temperature, $\hat{T}_{max}$, in the flame zone.

Similarly, the maximum flame temperature can be scaled as

$$\hat{T}_{max} = \frac{T_{max} - (T_{max})_S}{(T_{max})_L - (T_{max})_S} \tag{7.16}$$

where $(T_{max})_S$ and $(T_{max})_L$ represent the smallest and largest maximum flame temperature on the upper branch of the s-curve. $\hat{T}_{max}(p)$ can be correlated with the profile at 200 atm and a Gaussian distribution in the following form

$$\hat{T}_{max}(p) = \hat{T}_{max}\big|_{200\ atm} + G(p) \tag{7.17}$$

where the standard deviation σ remains 0.8 for all pressure conditions, but the mean μ and the coefficient C are pressure-dependent, as listed in Table 7.2. $\hat{T}_{max}(p)$ and $\hat{T}_{max}(p) - G(p)$ are also shown in Fig. 7.12. The maximum temperature profiles at different pressures thus become identical. Consequently, correlations for flame solutions at different pressures can be established for all species concentrations, as well as the flame temperature. Results for a given pressure can thus be mapped from those at another pressure.

Table 7.1: Scaling constants for renormalization of maximum flame temperature.

p, atm	$C/\sqrt{2\pi}$	μ
1	-0.5	0.8
10	-0.3	0.65
50	-0.15	0.6
100	-0.05	0.15

Figure 7.13 shows the maximum reaction rates for different species, normalized by their respective highest values over the entire S-curve, as a function of normalized strain rate. Almost all the curves collapse, except for slight deviations at low pressures for the unstable burning branch.

Detailed flame information at a given pressure can be mapped to another through the scaling relationships discussed above. With this general flame similarity, the database size for chemistry tabulation can be significantly reduced, provided the reference quantities (either at the equilibrium states with low-strain rates, or close to the extinction points) are available for normalizations. Figure 7.14 shows the maximum flame temperature and mass fractions of H_2O, OH, O, H, HO_2, and H_2O_2 at the chemical equilibrium state (zero strain rate) as a function of pressure. Linear relationships are obtained for all variables on either a semi-log or a log-log scale. The increase of the flame temperature with pressure may be attributed to the suppression of dissociation reactions at high pressures. The maximum mass fraction of OH remains almost independent of pressure. Figure 7.15 shows the maximum values of flame properties at extinction strain rates. Results bear close similarity to those at the equilibrium state (see Fig. 7.14).

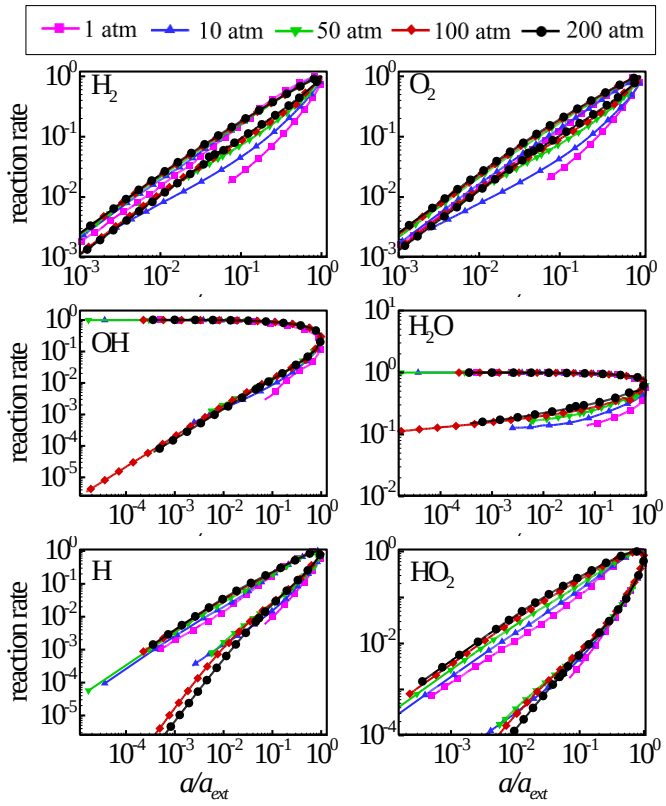

Figure 7.13: Normalized rates of production of species as functions of normalized strain rate (a/a_{ext}) at different pressures.

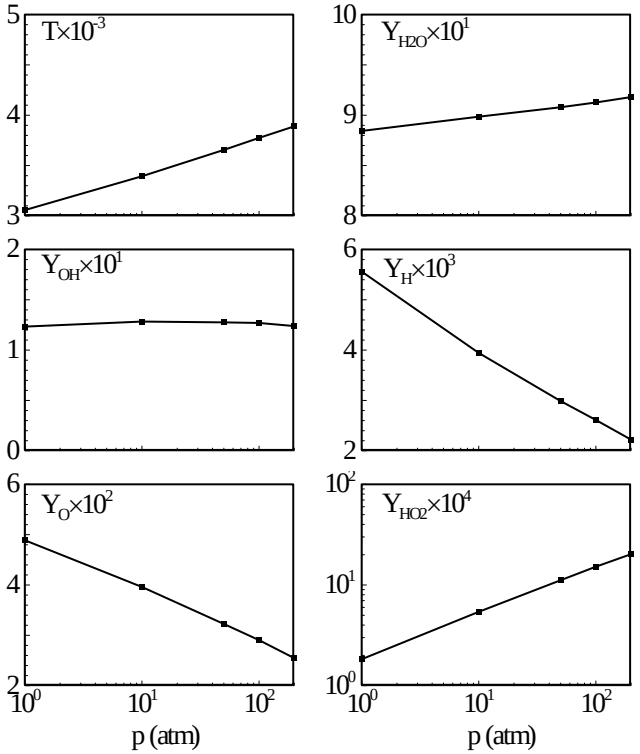

Figure 7.14:Maximum values of flame temperature and species mass fractions as functions of pressure at chemical equilibrium conditions.

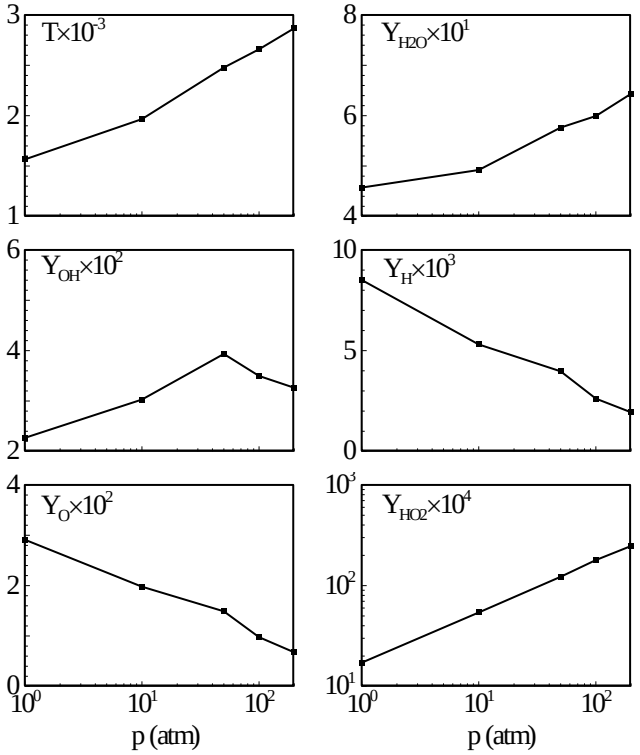

Figure 7.15: Maximum values of flame temperature and species mass fractions as functions of pressure at extinction strain rate.

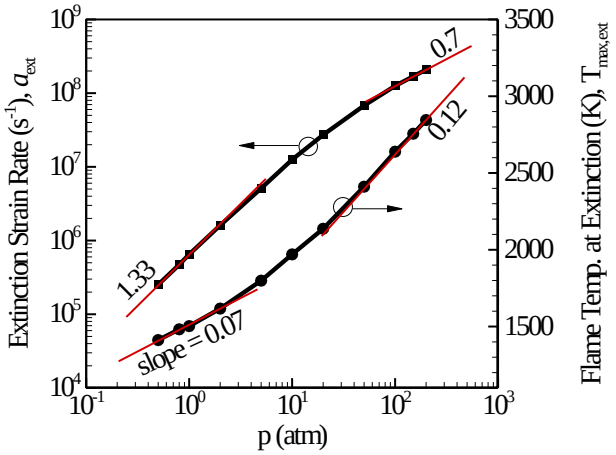

Figure 7.16: Extinction strain rate, a_{ext} , and flame temperature, $T_{max,ext}$, as functions of pressure.

Figure 7.16 shows the strain rates and flame temperatures at the extinction points over a pressure range of 0.5-200 atm. The extinction strain rate increases almost linearly with pressure on a log-log scale $a_{ext} \sim p^{1.33}$, for p ≤ 10 atm. The relationship becomes less pressure dependent at high pressures with $a_{ext} \sim p^{0.7}$. The extinction flame temperature can be approximately scaled with pressure in the form $T_{f,ext} \sim p^{0.07}$ for p ≤ 2 atm, and $T_{f,ext} \sim p^{0.12}$ for higher pressures.

At the extinction point, the chemical and flow time scales are of the same order of magnitude, and the flame is kinetics-controlled. The present analysis shows that the dependence of the reaction order, *n,* on pressure has a value of 2.2 for $p \le 5 atm$. It decreases to 1.7 at high pressures. If we assume that the molecular weight of reaction products MW_{mix} is independent of pressure, and $\bar{h}$ is linearly proportional to T , with some straightforward manipulations, Eq. (14) becomes:

$$a_{ext} \sim \frac{\bar{\omega}}{\bar{\rho}} \sim Tp^{n-1} \qquad (7.18)$$

Substitution of the pressure dependence of the flame temperature leads to $a_{ext} \sim p^{1.3}$ at 0.5 atm and $a_{ext} \sim p^{0.8}$ at 200 atm. The correlation shown in Fig. 16 is thus derived analytically. The extinction strain rate a_{ext} at a given pressure can be estimated based on the value at 1 atm, in accordance with Eq. 7.18. For hydrogen and oxygen flames, approximately, $a_{ext} \sim p$ over the entire pressure range considered in the present study.

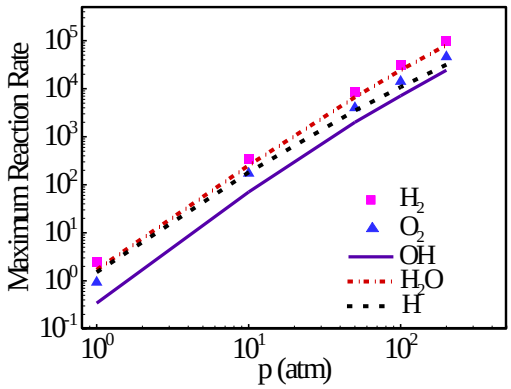

Figure 7.17: Maximum reaction rates for several different species as functions of pressure.

Figure 7.17 shows the maximum reaction rates for selected species over the entire s-curve in the pressure range of 1-200 atm. The information is used to normalize the reaction rates in Fig. 13. The slopes for O_2, H_2, H_2O and OH are almost the same, with an approximate value of 2.0. The increase of reaction rate renders the flame increasingly resistant to flow strain at high pressures. The decreased slope for H with increasing pressure may be attributed to the suppressed dissociation reactions at high pressures.

7.2.2.2 Effect of Inlet Condition

Figure 7.18a shows the flame structures at 100 atm with different inlet temperatures in both the subcritical and supercritical regimes. The difference in the flame location results from the variation of the inlet velocity for a given strain rate of a = 20000 s^{-1}. To facilitate comparison, the flames are aligned by shifting the location of the maximum flame

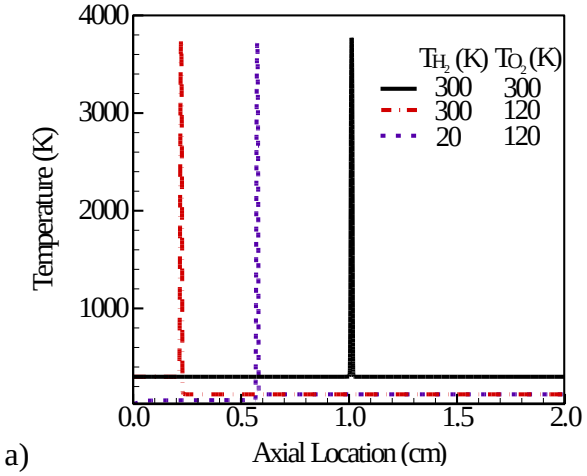

a)

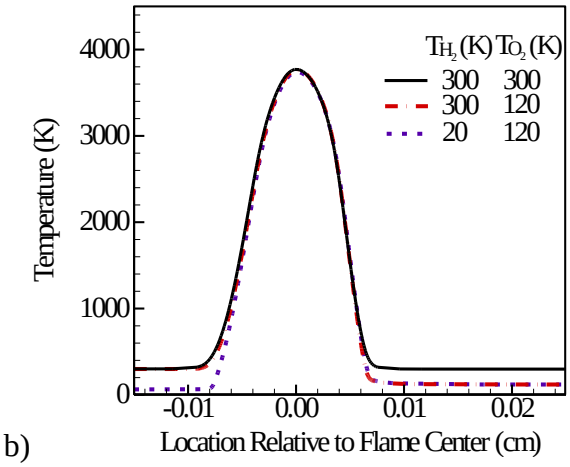

b)

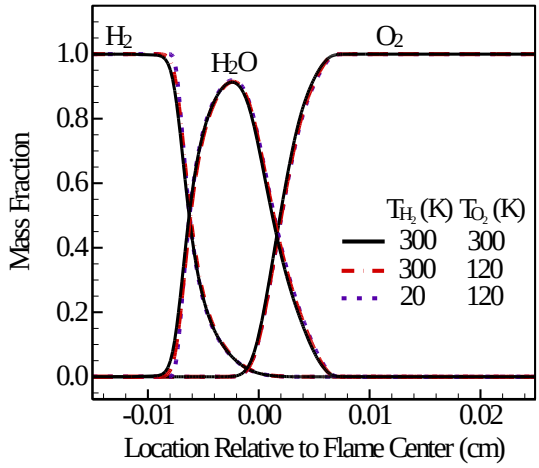

c)

Figure 7.18 continued: Distributions of temperature and mass fractions of major species for different inlet temperatures, $p = 100$ atm, $a = 20004$ s-1.

temperature to x =0. The result is shown in Fig. 7.18b and Fig. 7.18c for the temperature and species mass fraction distributions, respectively. The difference in maximum flame temperature among the three cases appears to be very small. The first case ($T_{H_2} = T_{O_2} = 300K$) features a slightly wider flame and a higher maximum flame temperature (3771 K), while the third case ($T_{H_2} = 20K, T_{O_2} = 120K$) has the smallest flame thickness and lowest maximum flame temperature (3740 K). The second case ($T_{H_2} = 300K, T_{O_2} = 120K$) has a maximum flame temperature of 3764 K.

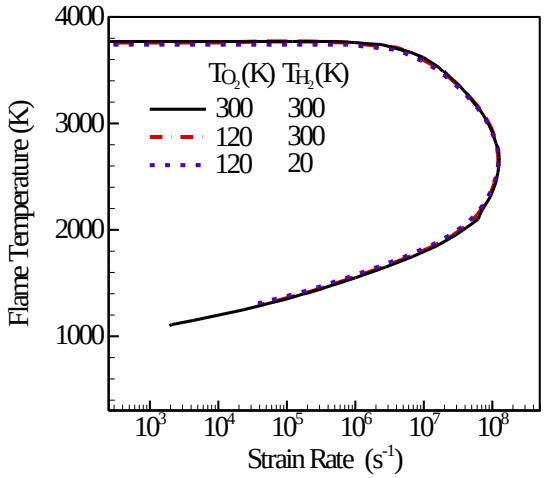

Figure 7.19: Maximum flame temperature for two different oxygen inlet temperatures: $p = 100$ atm, $T_{H_2} = 300$ K.

Figure 7.19 shows the effect of the strain rate on the flame temperature at *p* = 100 atm. The decrease of the oxygen inlet temperature from 300 to 120 K has only a small effect on the flame temperature (less than 10 K), over the entire S-curve.

7.3 Conclusions

A general study has been performed to explore the effect of strain rate on counterflow diffusion flames for real fluids over the entire thermodynamic regime. The work covers all three burning branches of an S-curve. The formulation accommodates fundamental thermodynamics and transport theories, along with detailed chemical

mechanisms. As a specific example, oxygen/hydrogen flames were systematically investigated for pressures in the range of 0.5-200 atm and strain rates of 10^2-10^8 s^{-1}. The major conclusions are as follows.

1. An analytical model was developed to corroborate and refine a previously observed relationship between the heat-release rate and pressure and strain rate in the form of $q \sim p^{0.534}\sqrt{a}$. The heat release rate, when normalized with respect to $p^{0.534}\sqrt{a_{ext}}$, correlates well with the normalized strain rate (a/a_{ext}).

2. As suggested by the heat-release relationship, intrinsic flame similarities are demonstrated for such properties as flame temperature, flame thickness, species concentrations, reaction rates, and heat release rate at different pressures. These properties, when normalized properly, collapse to single profiles in the normalized strain-rate space (a/a_{ext}).

3. The extinction strain rate, a major reference parameter in the flame similarity analysis, is clearly identified. It exhibits a quasi-linear relationship with pressure, a phenomenon which can also be explained analytically. Tabulation of pressure-dependent flame properties can be achieved by mapping the flame solution at a given pressure, according to the correlations in the normalized strain-rate space, even if the extinction strain rate is not available beforehand. This will significantly improve computational efficiency for combustion models using tabulated chemistry, such as the flamelet, FGM, and FPI models.

4. Cryogenic inlet temperature appears to affect only the flame location, and has a negligible effect on the flame structure over the entire S-curve. Consequently, the ideal-gas flame solutions can be used for fluids at supercritical conditions.

CHAPTER 8

COUNTERFLOW DIFFUSION FLAMES: OXYGEN/N-ALKANE HYDROCARBONS (CH_4-$C_{16}H_{34}$)

Existing studies of high-pressure counterflow diffusion flames mainly focus on the oxygen/hydrogen system. Limited attention has been given to hydrocarbon fuels, which are used for a vast majority of combustion devices, including gas-turbine, liquid-rocket, and diesel engines. The purpose of chapter is to explore the characteristics of counterflow diffusion flames of oxygen and hydrocarbon fuels. A wide range of n-alkanes (CH_4-$C_{16}H_{34}$) will be treated under both subcritical and supercritical conditions. In this chapter, we are going to extend the general framework using in oxygen/hydrogen mixtures in Chapter 7 and accommodates detailed chemical kinetics and fluid properties of hydrocarbon fuels. Emphasis will be given to the effects of pressure, inlet temperature, and strain rate on the flame structures and burning behaviors, including extinction, heat-release rate, and flame temperature, as well as the temperature and species distributions. The flame response over the entire S-curve will be obtained, and general correlations will be developed systematically.

8.1 Problem Description

The physical model of concern is a counterflow diffusion flame generated by two opposing fluid jets issuing from two circular nozzles, as shown in Fig.1.2. This axisymmetric geometry significantly simplifies the governing equations to a quasi-one-dimensional framework[158]. The theoretical framework was introduced in detail in Chapter 2, and applied to study the oxygen/hydrogen system over a wide range of thermodynamic fluid states and flow conditions in Chapter 7. The formulation accommodates the conservation equations of mass, momentum, species, and energy, and

takes full account of general-fluid thermodynamics and transport phenomena. Thermodynamic properties, including enthalpy, specific heats, and internal energy, are derived from fundamental thermodynamic theories. They are expressed as the sum of an ideal-gas property at the given temperature and a departure function accounting for dense-fluid corrections. The latter requires a robust equation of state that correlates density and temperature with pressure. A modified Soave-Redlich-Kong (SRK) equation of state [71] is employed because of its easy implementation and validity over a broad range of fluid states. Transport properties are determined by means of the corresponding-state principles.

The integrated theoretical model and numerical method is capable of treating the flame responses for general fluids over the entire S-curve, including both the stable and unstable branches [121][121][121][121][121][121]. The singularity problem at the turning points (extinction and ignition) is circumvented using an improved two-point flame-controlling continuation method. The flame solution can transit smoothly across these turning points. The setup of boundary conditions was described in Chapter 7. The flow strain rate is defined as the absolute maximum velocity gradient in the flowfield, which generally occurs in the mixing zone on the fuel side.

8.2 Results and Discussion

Counterflow diffusion flames of oxygen and n-alkane hydrocarbon fuels (CH_4-$C_{16}H_{34}$) are investigated systematically. Emphasis is focused on the effects of inlet temperature, pressure, and strain rate on the flame characteristics. As benchmarks, detailed behaviors of oxygen/methane and oxygen/n-heptane systems are analyzed at both subcritical and supercritical conditions. A general correlation is then obtained to identify the common features of the n-alkane family (CH_4-$C_{16}H_{34}$). Table 8.1 lists the critical properties of oxygen, hydrogen, and selected n-alkane fuels (Linstrom and Mallard, 2014).

Table 8.1: Critical properties.

Reactants	T_{cr}, K	p_{cr}, atm	V_{cr}, cm^3/mol
O_2	154.6	49.8	73.4
H_2	33.2	12.8	65.0
CH_4	190.6	45.6	98.6
C_7H_{16}	540.0	27.0	428.0
$C_{12}H_{26}$	658.2	17.9	754.0
$C_{16}H_{34}$	722.0	13.8	1034.0

8.2.1 Oxygen/Methane System

Table 8.2 provides the chemical kinetic mechanisms employed in the present study for oxygen and n-alkane fuels. The oxygen/methane chemical scheme developed by Petersen et al. [159] consists of 38 species and 190 reaction steps. It was validated against shock-tube experiments at pressures up to 260 atm, temperatures as low as 1040 K, and equivalence ratios up to 6. The mechanisms for C_2H_6-$C_{16}H_{34}$ were validated with pressures up to 80 atm and temperatures in the range of 650-1600 K.

Table 8.2: Reaction Mechanisms of O_2 with H_2 and n-alkanes (CH_4~$C_{16}H_{34}$)

Fuels	Number of Species	Number of Reactions	Reference
H_2	9	21	Ó Conaire et al. [160]
CH_4	38	190	Petersen et al. [159]
C_2H_6	155	689	Marinov et al. [161]
C_3H_8	155	689	Marinov et al. [161]
C_4H_{10}	155	689	Marinov et al. [161]
C_5H_{12}	560	2538	Curran et al. [66]
C_6H_{14}	560	2538	Curran et al. [66]
C_7H_{16}	560	2538	Curran et al. [66]
C_8H_{18}	691	2992	Westbrook et al. [67]
$C_{10}H_{22}$	952	3899	Westbrook et al. [67]
$C_{12}H_{26}$	1078	5056	Westbrook et al. [67]
$C_{14}H_{30}$	1666	6476	Westbrook et al. [67]
$C_{16}H_{34}$	2115	8157	Westbrook et al. [67]

As a validation procedure, the property evaluation scheme is examined carefully. Figures 8.1 and 8.2 show the calculated compressibility factor (Z), density (ρ), specific heat at constant pressure (C_p), and thermal conductivity (λ) for oxygen and methane, respectively. They match closely with the NIST data [162]. The temperature range covers both the subcritical and supercritical regimes. The property anomalies in the vicinity of the critical point [1] are clearly observed. The abrupt variations at the subcritical pressure (20 atm) arise from the phase change from dense liquid to light gas. This phenomenon disappears, however, at supercritical pressures, rendering smooth and continuous transitions with the temperature.

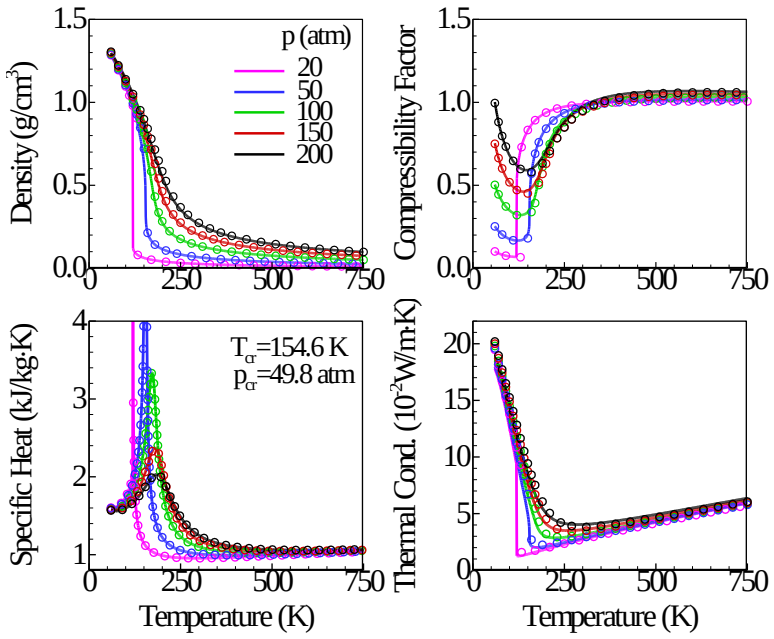

Figure 8.1: Thermodynamic and transport properties of oxygen validated against NIST data. Lines: the present scheme; symbols: NIST data.

Figure 8.3 shows the distributions of thermophysical properties in the flame zone with oxygen and methane inlet temperatures of 120 and 300 K, respectively. The pressure is 100 atm and the flow strain rate is 90 s^{-1}. The compressibility factor varies rapidly from 0.3 to 1.0 in a thin region on the oxygen side when the local temperature increases across

the critical point of 154.6 K. The corresponding density drops sharply from 1.0 to 10^{-4} g/cm^3. Similar phenomena occur for other thermodynamic and transport properties. In spite of such steep changes of fluid properties in the low-temperature region on the oxygen side, the oxygen stream heats up rapidly and behaves like a perfect gas before entering the flame zone.

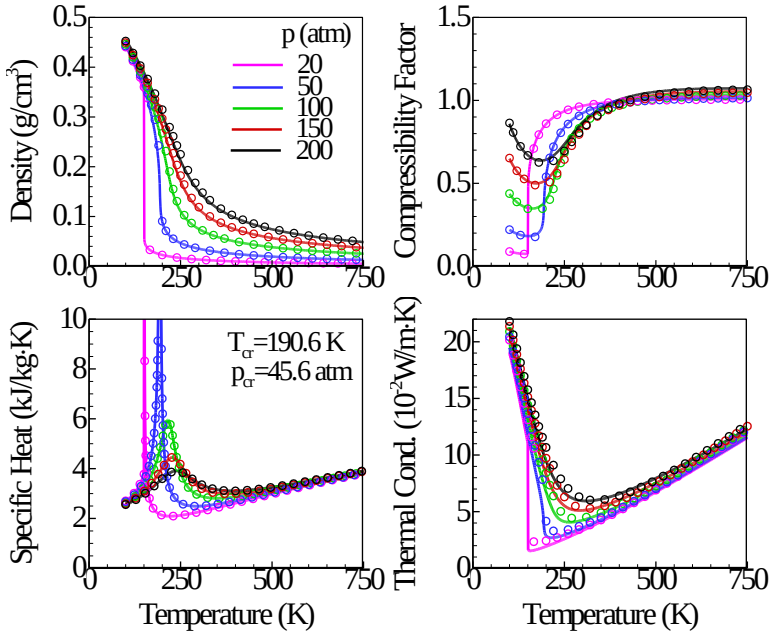

Figure 8.2: Thermodynamic and transport properties of methane validated against NIST data. Lines: the present scheme; symbols: NIST data.

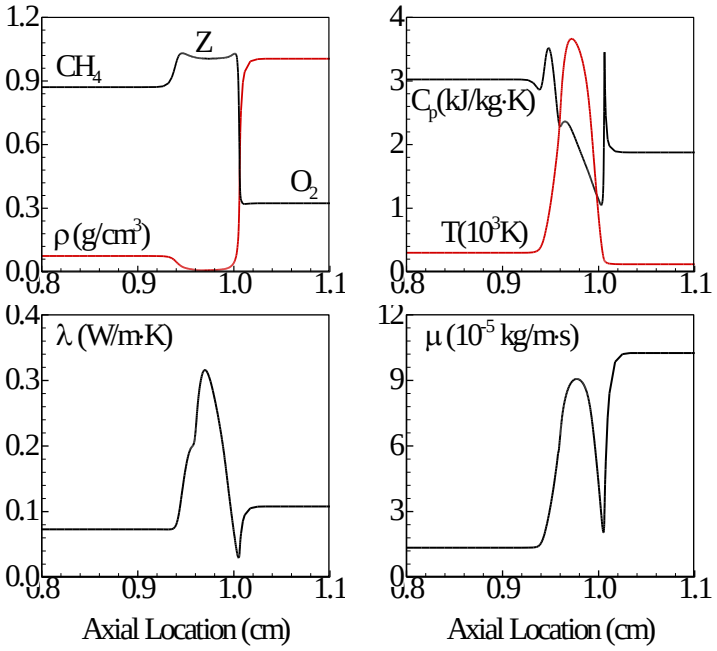

Figure 8.3: Distributions of thermophysical properties in the axial direction. Oxygen/methane system with $p = 100$ atm, $T_{O_2} = 120$ K, $T_{CH_4} = 300$ K, and $a = 90\ \text{s}^{-1}$.

Figure 8.4 shows the flame structures at 100 atm with three different oxygen inlet temperatures of 120, 300, and 500 K, covering both the subcritical and supercritical regimes. The methane inlet temperature remains fixed at 300 K and the strain rate is $a = 1000\ \text{s}^{-1}$. In spite of the distinct distributions of flow properties with different oxygen inlet temperatures in the physical space, the property distributions in the mixture-fraction space collapse into single profiles, especially in the flame zone. The case with $T_{O_2} = 500$ K features a slightly wider flame. The distribution of heat-release rate exhibits two peaks and one valley. The latter is caused by dominant effects of pyrolysis-type reactions that occur endothermically on the fuel side. Figure 8.5 shows the effect of the oxygen inlet temperature on the flame extinction at two different pressures. The extinction strain rate moderately increases almost linearly with increasing T_{O_2}, whereas the maximum flame temperature at extinction remains nearly constant. Overall, the oxygen inlet temperature has a negligible effect on the flame structure, as can be predicted using an ideal-gas assumption. If the inlet temperature falls in the cryogenic fluid range (e.g., $T_{O_2} = 120$ K),

real-fluid effects must be taken into account to accurately capture the local flow development.

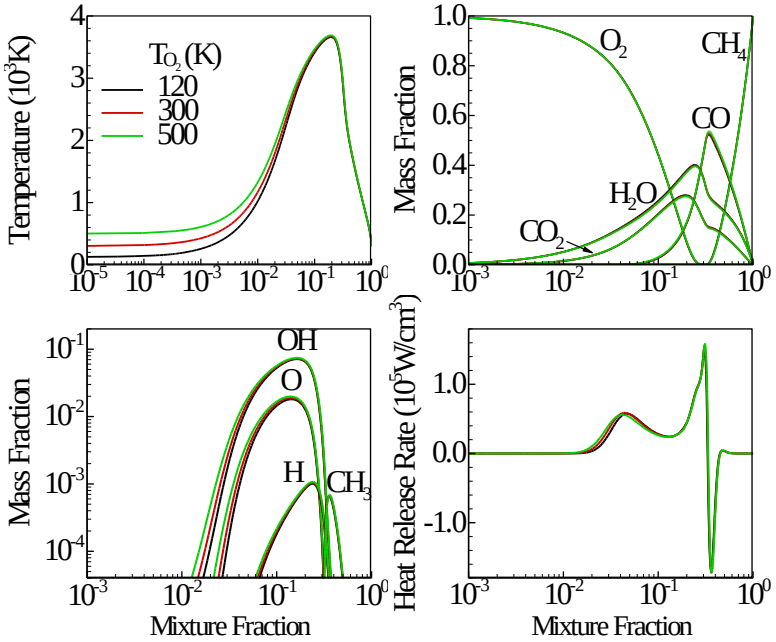

Figure 8.4: Distributions of temperature, species mass fractions, and heat-release rate in the mixture fraction space. Oxygen/methane system with with $p = 100$ atm, $T_{CH_4} = 300$ K, and $a = 1000\ \text{s}^{-1}$.

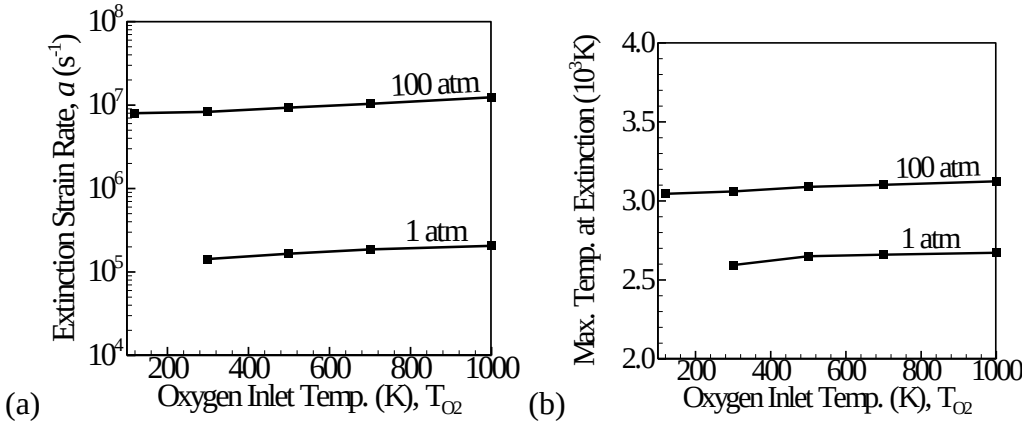

Figure 8.5: Effects of oxygen inlet temperatures on extinction properties, (a) strain rate; (b) maximum flame temperature. Oxygen/methane system with $T_{CH_4} = 300$ K.

Figure 8.6 shows the distributions of the temperature and mass fractions of oxygen and methane throughout the flowfield at pressures of 1-150 atm. The inlet temperature is set to 300K for both reactants, and the flow strain rate is fixed at 1000 s^{-1}. The peak flame temperature increases progressively with pressure, while the flame thickness decreases significantly with increasing pressure. Methane and oxygen are consumed completely in the flame region, a situation referred to as intensively stable burning. Because of the variation of the flame thickness with pressure, the temperature and species fields exhibit distinct profiles in the physical space.

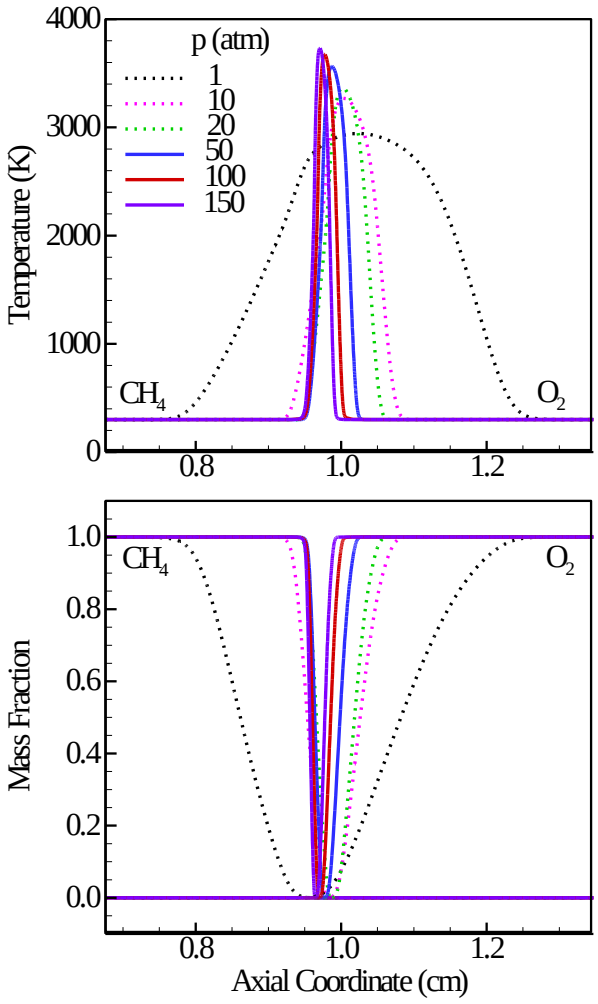

Figure 8.6: Distributions of temperature and mass fractions of methane and oxygen at different pressures. Oxygen/methane system with $T_{O_2} = T_{CH_4} = 300$ K, and $a = 1000$ s^{-1}.

The situation in the mixture-fraction space shown in Fig. 8.7, however, becomes fundamentally different with all the data collapsed to a single distribution, regardless of the pressure. Seshadri and Peters [163] divided a methane-air diffusion flame into three distinct zones: the fuel-consumption zone, the water-gas shift, and the H_2-CO oxidation zones. In the present study, the fuel-consumption zone on the methane side is clearly displayed in Fig. 8.7a. The mass fractions of H_2 and CO reach their maxima where the methane concentration diminishes. The H_2-CO oxidation layer is located on the oxygen side, where the maxima of H_2O and CO_2 concentrations occur. The mass fractions of the intermediate species shown in Fig. 8.7c reveal different behaviors with respect to pressure. While the O and H concentrations decrease with increasing pressure as radical recombination reactions are strengthened, the OH concentration does not indicate such a monotonic trend, because of the competition of chain-branching and radical-recombination reactions at high pressure. As a result, in the mixture fraction space, the major species exhibit similar behaviors, while those of the intermediate species are distinctly distributed with pressure. The latter play a crucial role in determining heat-release properties through radical reactions.

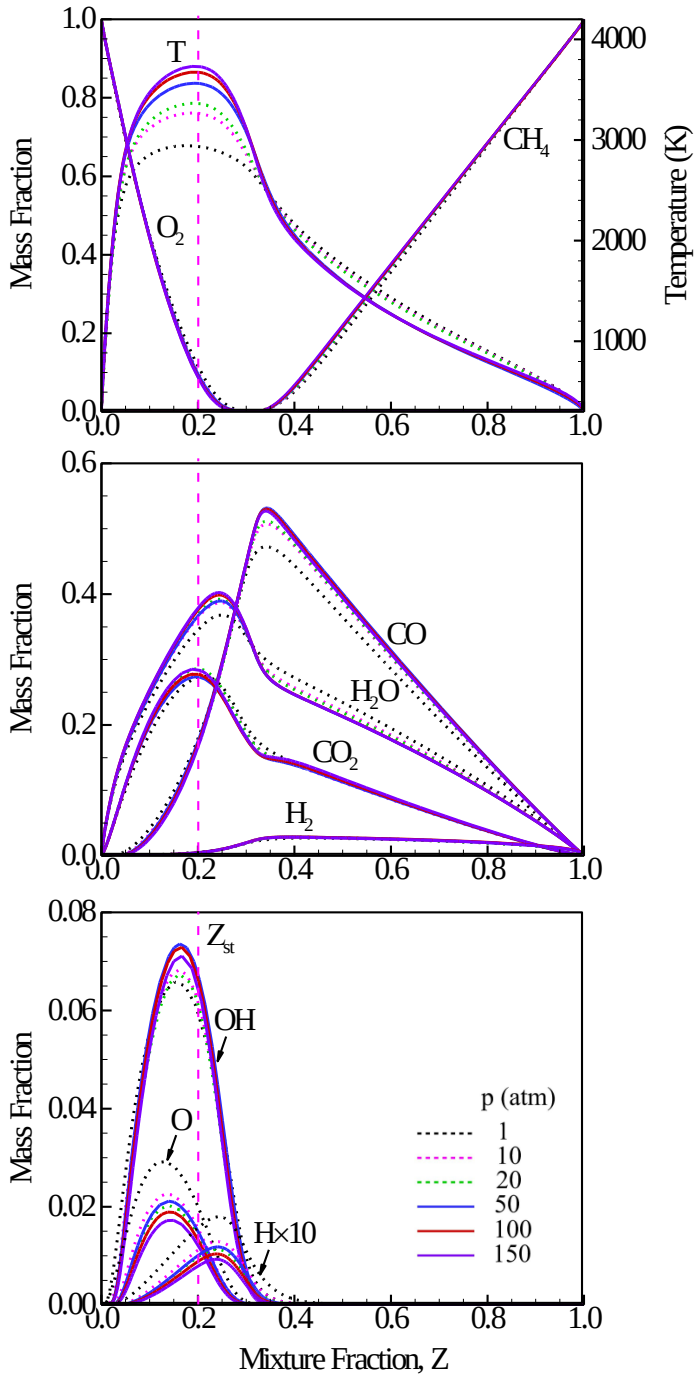

Figure 8.7: Distributions of temperature and species mass fractions at different pressures in the mixture-fraction space. Oxygen/methane system with $T_{O_2} = T_{CH_4} = 300$ K, $a = 1000$ s-1.

Figure 8.8 shows the maximum flame temperature as a function of strain rate at various pressures. The inlet temperatures for both methane and oxygen are fixed at 300 K,

and the momentum fluxes at the two boundaries are set to be equal, in order to place the stagnation plane at the center for all cases. The stable (upper) and unstable (middle) burning branches of the S-curve are obtained. The weakly reacting (lower) branch is not present here because the inlet temperature of 300 K is well below the ignition point.

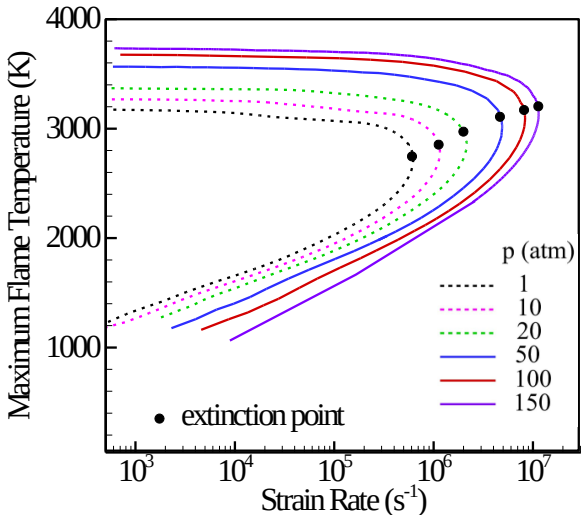

Figure 8.8: Effects of flow strain rate on maximum flame temperature at different pressures. Oxygen/methane system with $T_{O_2} = T_{CH_4} = 300$ K.

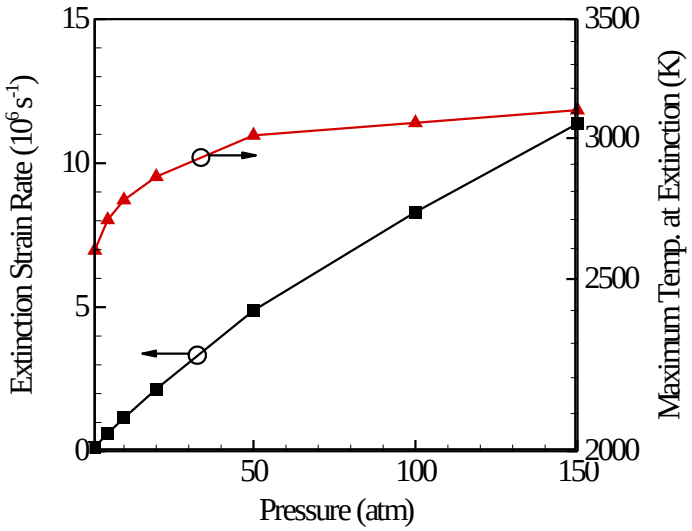

Figure 8.9: Effects of pressure on strain rate and maximum temperature at extinction. Oxygen/methane system with $T_{O_2} = T_{CH_4} = 300$ K.

The flame behaviors bear close similarity to those of the oxygen/hydrogen system discussed in Chapter 7, in which detailed physical explanations are provided. For a given strain rate, the maximum flame temperature increases with pressure as a result of the reduced dissociation associated with endothermic reactions. The maximum flame temperature remains almost constant at low strain rates, and starts to decrease progressively until the extinction point is reached. At low strain rates, the chemical time scale is much smaller than the flow time scale. Thermal energy released by chemical reactions overrides heat loss. A further increase in the strain rate, however, renders the flow time scale comparable to its chemical counterpart. The ensuing heat loss leads to a lower flame temperature and eventually to flame extinction.

Figure 8.9 shows the effects of pressure on the peak flame temperature and flow strain rate at the extinction point. The extinction strain rate is almost linearly proportional to pressure, up to 50 atm. Its rate of increase then drops slightly after this point. At low pressures (p < 50atm), the extinction is dominated by second-order chain-branching reactions. The chemical time scale is inversely proportional to pressure; a linear relationship thus exists between the extinction strain rate and pressure [164]. At high pressures (p >50atm), the crossover temperature characterizing radical-recombination reactions increases faster than the peak temperature for chain-branching reactions. Radical-recombination reactions consequently play a more influential role and cause the bend-over of the curve. The peak flame temperature at extinction T_{ext} increases with increasing pressure in a manner similar to that for the equilibrium flame temperature T_{eq}, as listed in Table 8.3. Power-law relationships can be established between the peak flame temperature and pressure: $T_{eq} \sim p^{0.0474}$ in equilibrium, $T_{ext} \sim p^{0.0383}$ at extinction. This information will be employed in the scaling analysis of the heat-release rate. Figure 8.10 shows the flame response along the S-curve for the oxygen/hydrogen and oxygen/methane systems at 50 atm. The extinction strain rate for hydrogen (~10^7 s^{-1}) is an order of magnitude larger than

that for methane (~10^6 s^{-1}). The oxygen/hydrogen flame is significantly more resistant to the flow straining than its oxygen/methane counterpart. This may be attributed to the greater thermal and mass diffusivities and faster kinetics of hydrogen.

Table 8.3: Maximum flame temperature at equilibrium and extinction state for the oxygen/methane system.

Pressure (atm)	1	5	10	20	50	100	150
T_{eq} (K)	2953	3174	3268	3370	3566	3650	3741
T_{ext} (K)	2594	2699	2769	2854	3011	3060	3111

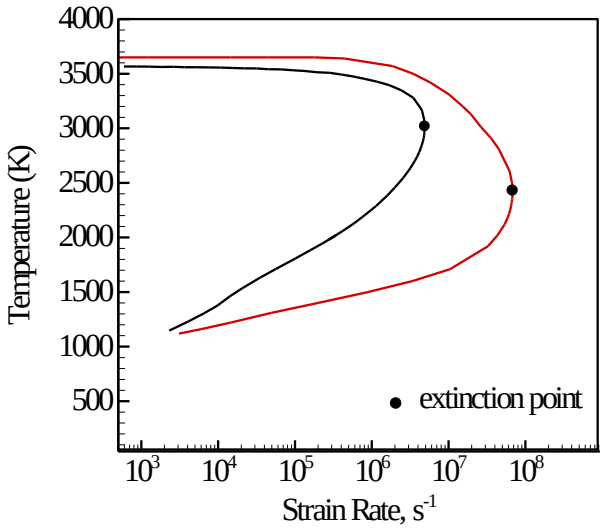

Figure 8.10: Flame response along the S-curve for oxygen/hydrogen and oxygen/methane systems at $p=50$ atm with $T_{O_2}=T_{H_2}=T_{CH_4}=300$ K.

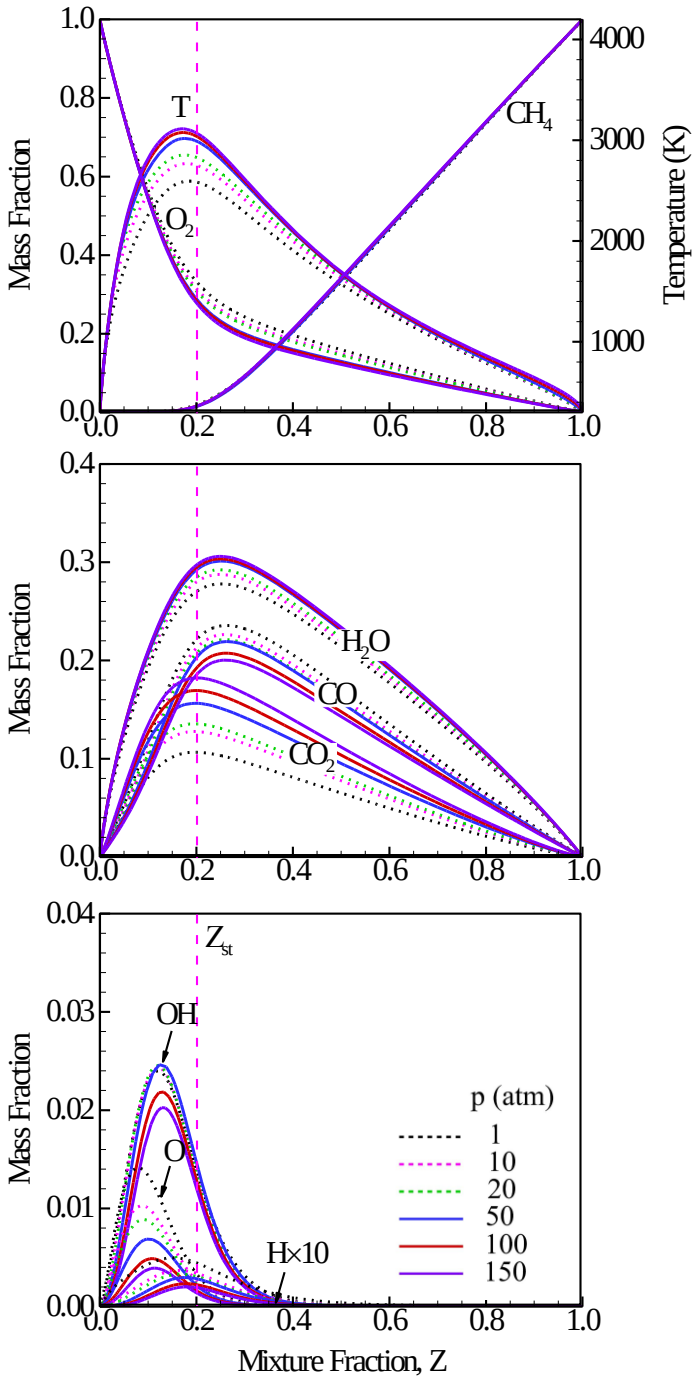

Figure 8.11: Distributions of temperature and species mass fractions at the extinction point in the pressure range of 1-150 atm. Oxygen/methane system with $T_{O_2} = T_{CH_4} = 300$ K.

In order to extract more information about extinction characteristics at different pressures, the distributions of temperature and species concentrations at the extinction

point are plotted in the mixture-fraction space, as shown in Fig. 8.11. The inlet temperatures are $T_{O_2} = T_{CH_4} = 300$ K. The extinction flame temperature increases with increasing pressure. Figure 8.11a indicates that unburned oxygen penetrates into the methane stream at extinction, and the methane reacts completely in the flame zone. The oxygen penetration declines at higher pressures, which explains the increase in peak temperature with increasing pressure. Figures 8.11b and 8.11c present the mass-fraction distributions of major and minor species at extinction. The production of H_2O and CO_2 increases with pressure, whereas production of other species, such as CO, O, OH, and H, decreases. High flame temperature tends to facilitate the decomposition of oxygen, which outweighs the reduction of oxygen dissociation at high pressure and consequently results in decreased presence of oxygen across the flame. The H_2-CO oxidation is intensified at high pressure, leading to increased H_2O and CO_2 concentrations and lower concentrations of other species, as evidenced in Figs. 8.11b and 8.11c.

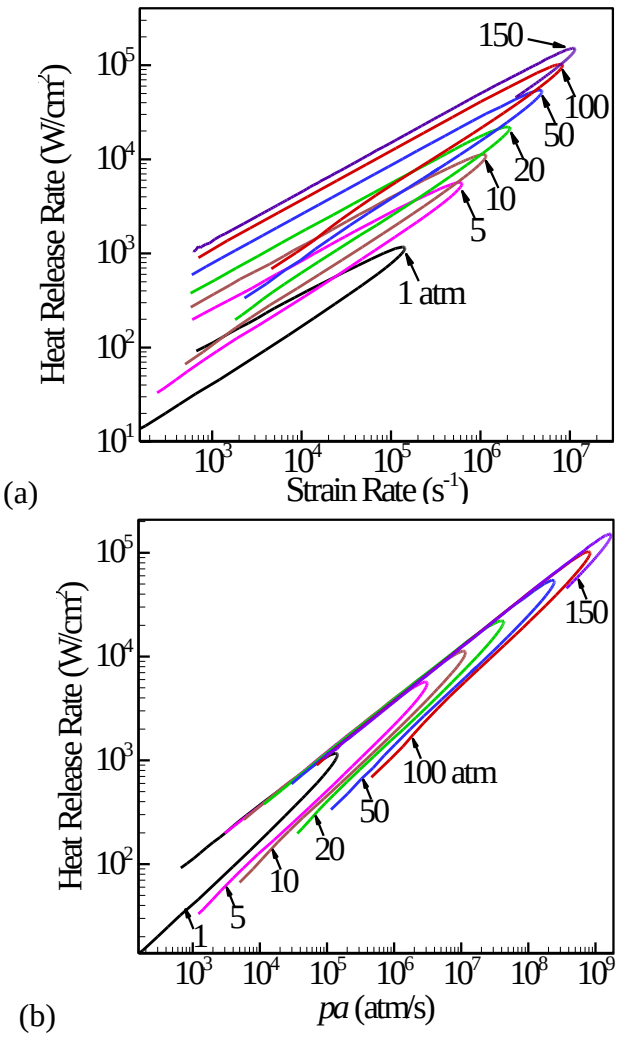

Figure 8.12 continued: Distributions of global heat-release rate as a function of strain rate in the pressure range of 1-150 atm. Oxygen/methane system with $T_{O_2} = T_{CH_4} = 300$ K

Figure 8.12a shows the global heat-release rate q as a function of the strain rate over a pressure range of 1-150 atm. The result is obtained by integrating the local heat-release rate over the entire flame zone. In the stable-burning (upper) branch of the S-curve at a given pressure, the heat-release rate increases linearly with the strain rate because of the increased mass flow rate. It reaches a maximum and then decreases toward the extinction point. The behaviors near the extinction point are well captured. The heat-release rate in the unstable-burning (lower) branch is also obtained for the first time for the

oxygen/methane system using a real-fluid approach. The results in Fig. 8.12b confirms the previous finding of Pons et al. [62] that $q \sim \sqrt{pa}$ in the stable-burning branch except for the region in the vicinity of the extinction point. A similar trend for the oxygen/hydrogen system was observed by Ribert et al. [59] and Huo et al. [121].

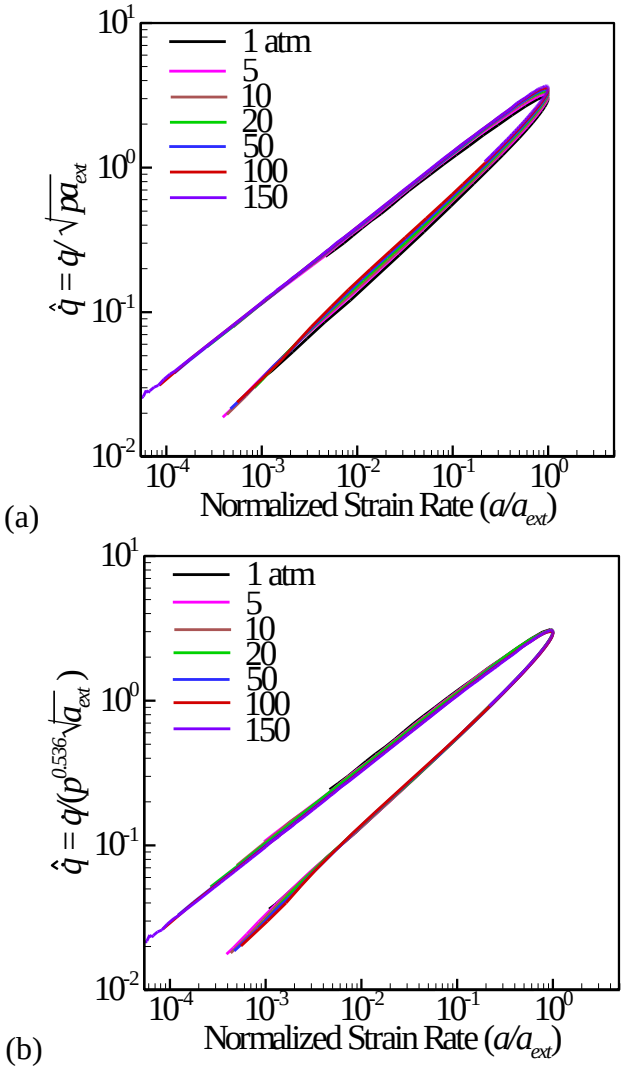

Figure 8.13: Scaled heat-release rate q as a function of normalized strain rate (a/a_{ext}). Oxygen/methane system with $T_{O_2} = T_{CH_4} = 300$ K. (a) $q = q/\sqrt{pa_{ext}}$; (b) $q = q/p^{0.536}\sqrt{a_{ext}}$.

To identify intrinsic flame similarities at different pressures, a scaled heat-release rate, defined by $\tilde{q} = q / \sqrt{p a_{ext}}$, is plotted as a function of a normalized strain rate, a/a_{ext}, as shown in Fig. 8.13a. The profiles very nearly collapse to a single curve. Huo et al. [121] developed a scaling analysis and found that to obtain a more accurate result, an additional pressure exponent accounting for the effect of pressure on the peak flame temperature should be included,

$$q \sim \frac{T_{eq}^{0.75}}{MW_{mix}^{0.25}} \sqrt{pa} \tag{8.1}$$

Substitution of the pressure dependence of the flame temperature, $T_{eq} \sim p^{0.0474}$, into the above equation gives the following correlation for the heat-release rate.

$$q \sim p^{0.536} \sqrt{a} \tag{8.2}$$

Figure 8.13b shows this new scaled heat-release rate,

$$\tilde{q} = q / p^{0.536} \sqrt{a_{ext}} \tag{8.3}$$

allows for the collapse of all the heat-release rate profiles to a single function of the normalized strain rate, a / a_{ext}. This flame similarity implies that the heat-release behaviors at high pressure can be obtained from their counterparts at low pressure through proper scaling analysis.

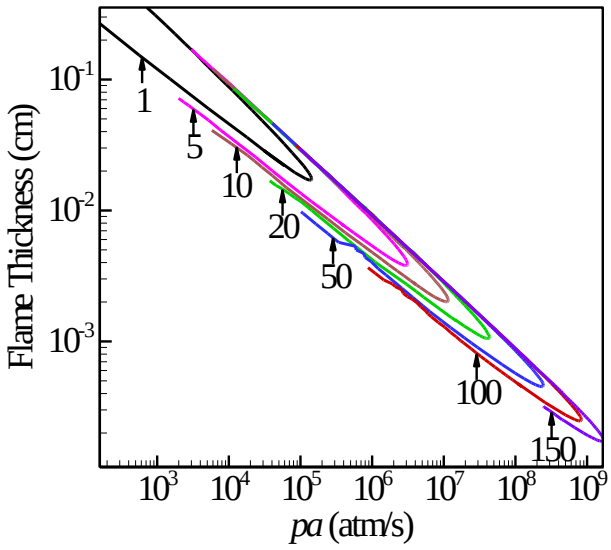

Figure 8.14: Flame thickness as a function of strain rate in the pressure range of 1-150 atm. Oxygen/methane system with $T_{O_2} = T_{CH_4} = 300$ K.

Like the heat-release rate, the flame thickness δ, defined as the full width at half maximum of the temperature distribution, correlates well with the product of pressure and flow strain rate, pa, as shown in Fig. 8.14. In the stable burning (upper) branch (except in the vicinity of the extinction point), the flame thickness exhibits the following trend,

$$\delta \sim 1/\sqrt{pa} \tag{8.4}$$

The strong flame similarity at various pressures can be further consolidated using a scaled flame thickness, $\hat{\delta} \equiv \delta\sqrt{pa_{ext}}$, and a normalized flow strain rate, a/a_{ext} [121]. Figure 8.15 shows the result. Similar correlations exist for major-species distributions, as elaborated by Huo et al. [121] for the oxygen/hydrogen system. The flame characteristics at high pressure can be predicted from the corresponding results at low pressure.

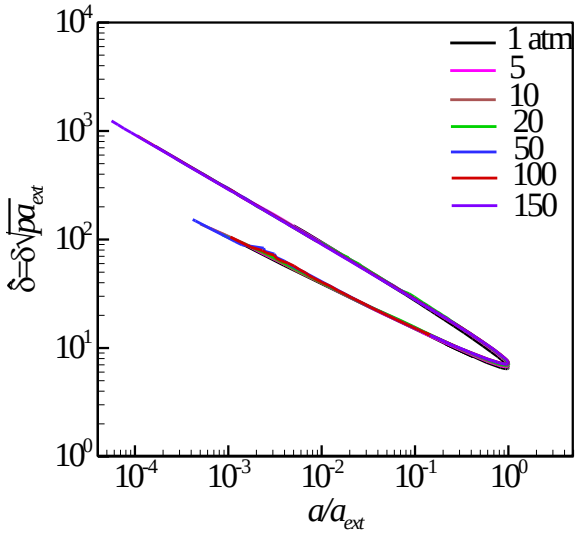

Figure 8.15: Scaled flame thickness $\hat{\delta}=\delta\sqrt{pa_{ext}}$ as a function of normalized strain rate (a/a_{ext}). Oxygen/methane system with $T_{O_2}=T_{CH_4}=300$ K.

8.2.2 Oxygen/n-Heptane System

N-Heptane, C_6H_{14}, is a primary reference fuel for the study of combustion in internal combustion engines, due to its zero octane rating. The detailed chemical mechanism developed by Curran et al. [66], including 560 species and 2538 reversible reactions, is employed in the present study, as listed in Table 8.2. This mechanism has been validated against experimental data obtained from flow reactors, shock tubes, and rapid compression machines over the pressure and temperature ranges of 3 to 50 atm and 650 to 1200 K, respectively. To avoid complexities associated with fuel vaporization, the inlet temperature remains at 600 K or above in the present study.

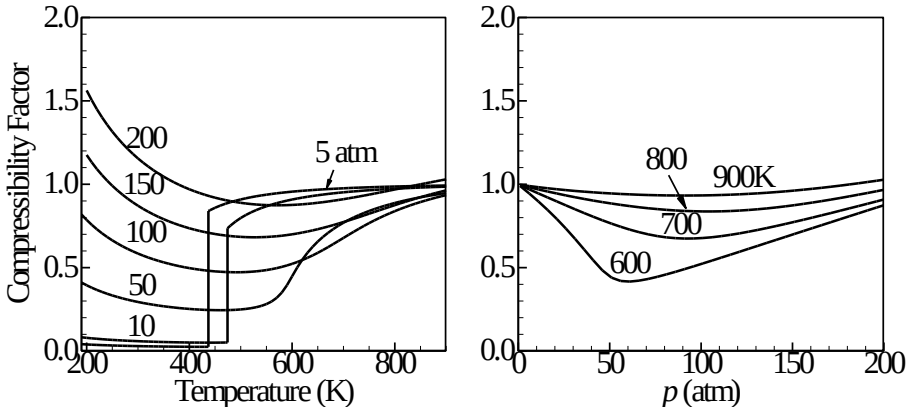

Figure 8.16: Compressibility factor of n-heptane at different pressures and temperatures.

Figure 8.16 shows the variation of the compressibility factor with pressure and temperature. At 600K, the compressibility factor reaches as small as 0.4 for p = 60 atm. It approaches unity when the temperature exceeds 900 K. As noted previously [59, 121], the real-fluid effect takes place only in the region close to a low-temperature, high-pressure inlet. The fluid essentially behaves like an ideal gas when it approaches the flame zone. In light of this, the real-fluid property evaluations are neglected here for simplicity. Figure 8.17 shows the distributions of the temperature and mass fractions of major species. n-Heptane first decomposes to intermediate species of C_2H_2 and C_2H_4, and then produces H_2 and CO on the fuel side. The maximum of H_2O and CO_2 mole fractions occurs close to the oxygen side.

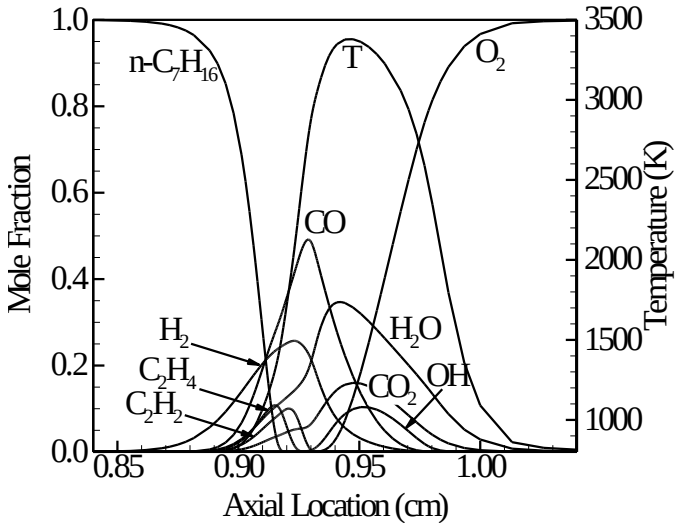

Figure 8.17: Distributions of temperature and mass fractions of major species. Oxygen/n-heptane system with *p*=10 atm, $T_{O_2} = T_{C_7H_{16}} = 800$ K, and *a* = 1000 s-1.

Figure 8.18 shows the effects of the inlet temperature on the flame properties, including the maximum flame temperature, flame thickness, and heat-release rate, at various pressures. The flow strain rate remains fixed at 1000 s^{-1}. As in the oxygen/methane system, the disparities of flame properties for different inlet temperatures appear to be quite modest at a given pressure, indicating the negligible influence of the inlet temperature on the flame response.

Figure 8.19 shows the variations of the heat-release rate and flame thickness as a function of strain rate over the pressure range of 1-200 atm. Only the results for the stable burning branch of the S-curve are presented. The flame behaviors near the extinction point and in the unstable burning branch can be captured following the same approach for the oxygen/methane system. The heat-release rate increases linearly with the strain rate, and the flame thickness decreases in a linear manner. As in the oxygen/methane system, the heat-release rate and flame thickness correlates well as, $q \sim \sqrt{pa}$ and $\delta \sim 1/\sqrt{pa}$. The former correlation can be further modified to account for the pressure dependence of the peak flame temperature, as described in the previous section.

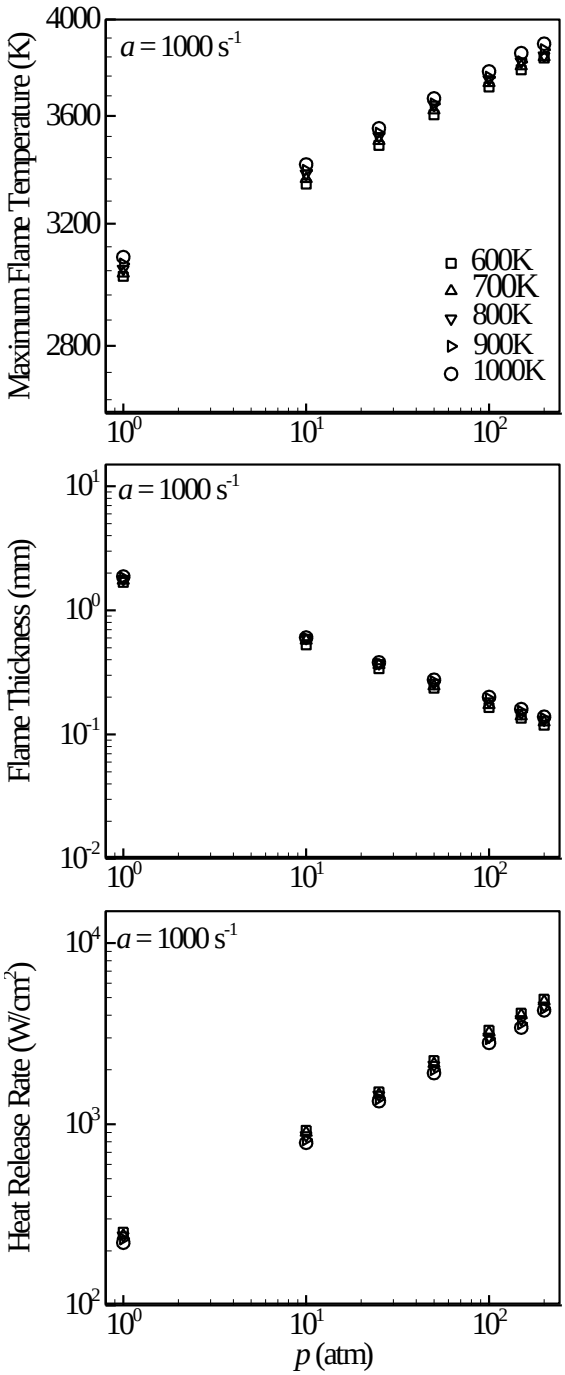

Figure 8.18: Effects of inlet temperature on flame maximum temperature, flame thickness, and heat-release rate at different pressures for oxygen/n-heptane system

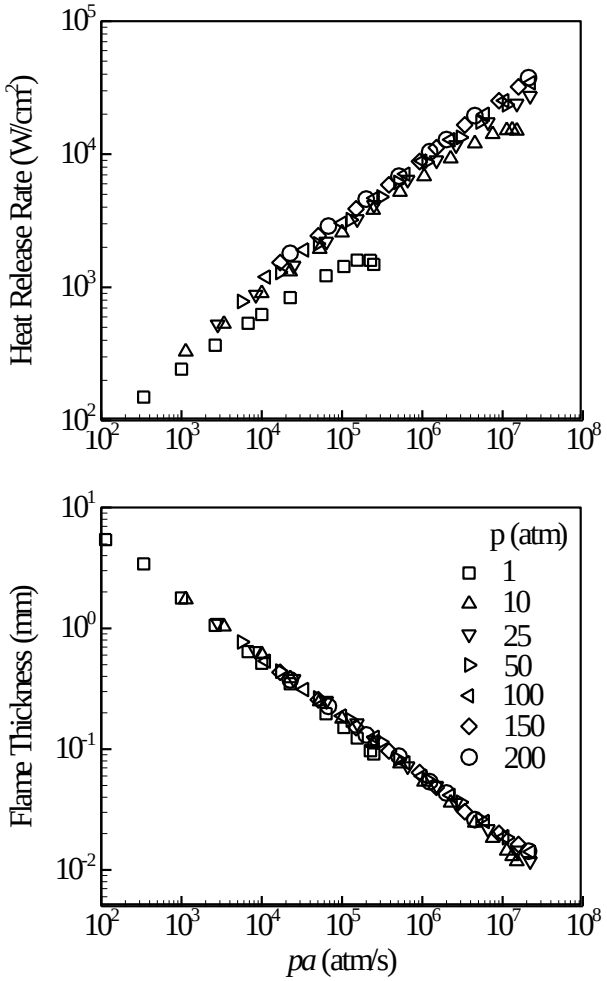

Figure 8.19 continued: Distributions of the heat-release rate and flame thickness as a function of strain rate in the pressure range of 1 to 200 atm. Oxygen/n-heptane system with $T_{O_2} = T_{C_7H_{16}} = 800$ K.

Substitution of the flame temperature-pressure relation obtained from Fig. 8.18a, $\bar{T}_{eq} \sim p^{0.045}$, into Eq. 8.1 gives the following correlation of the heat-release rate for the oxygen/n-heptane system,

$$q \sim p^{0.534}\sqrt{a} \tag{8.5}$$

The pressure exponent of 0.534 coincides with that of the oxygen/hydrogen system [121]. An identical scaling can thus be achieved for the flame thickness and heat-release rate using Eqs. 8.4 and 8.5, respectively, in the normalized strain rate space. The intrinsic

similarities of the flame response are obtained for the oxygen/n-heptane system in a broad range of pressures and strain rates.

8.2.3 Oxygen/ n-Alkane (CH_4-$C_{16}H_{34}$) Systems

The common features of oxygen/methane and oxygen/n-heptane flames suggest that the same kind of flame similarities may be applied to the entire n-alkane family (CH_4-$C_{16}H_{34}$). Table 8.2 lists the detailed chemical mechanisms of the n-alkanes employed in the present study. Figure 8.20 shows the compressibility factors for n-dodecane ($C_{12}H_{26}$) and n-hexadecane ($C_{16}H_{34}$) in the pressure-temperature space. The compressibility factor approaches unity when the temperature exceeds 800 K and the pressure is smaller than 100 atm. For simplicity, all the calculations are conducted at this inlet temperature, with the ideal-gas equation of state implemented for property evaluations.

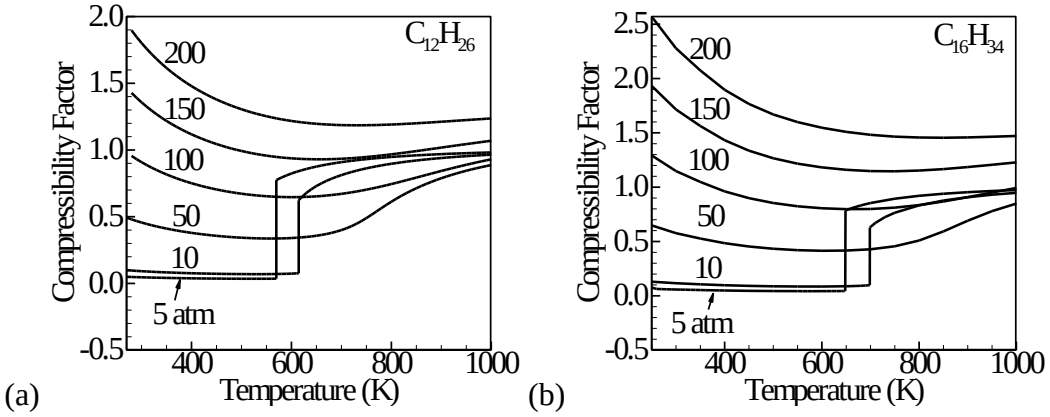

Figure 8.20: Compressibility factors of (a) $C_{12}H_{26}$ and (b) $C_{16}H_{34}$ at different pressures and temperatures.

Figure 8.21 shows the flame properties as a function of the number of carbons in the n-alkane fuel molecule. Also included is pure hydrogen. The strain rate is set to 1000 s^{-1} and the pressure to 10 atm. Hydrogen has a much higher maximum flame temperature and a wider flame zone, as well as greater heat release, than all members in the alkane

family. The flame thickness for the n-alkanes is nearly the same regardless of the number of carbons. The peak flame temperature increases slightly with increasing number of carbons from 3350 K for CH_4 and levels off at 3800 K when the carbon number exceeds 5. The heat-release rate experiences a sharp increase from methane to ethane, and then decreases gradually to saturate at n-pentane. The flame properties of heavy hydrocarbons (C_5-C_{16}) are nearly identical. Light hydrocarbons exhibit distinct flame behaviors, mainly due to the variation of the carbon-hydrogen mass ratio, which changes significantly when the number of carbons varies from 0 to 5. Although not shown here, the flame thickness and heat-release rate of all hydrocarbon fuels can be correlated with pressure and strain rate in a manner similar to those of methane and n-heptane. The flame properties at high pressure can be obtained from their counterpart at low pressure.

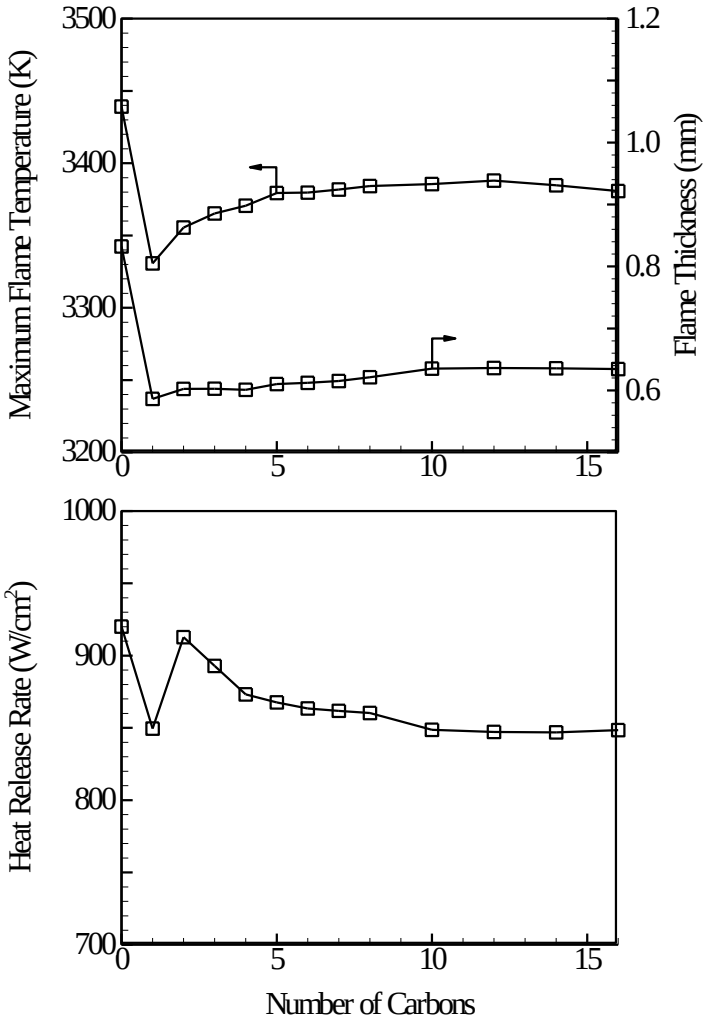

Figure 8.21: Maximum flame temperature, flame thickness, and heat-release rate as a function of number of carbons in the n-alkane fuel molecule. Oxygen/hydrogen and oxygen/n-alkanes systems with *p* = 10 atm, $T_{O_2} = T_{Fuel} = 800$ K, and *a* = 1000 s-1.

Figure 8.22 shows the scaled flame thickness ($C = \delta\sqrt{pa}$) as a function of the number of carbons in the n-alkane fuel molecule. The scaled flame thickness remains nearly constant for all hydrocarbons at the given pressure and strain rate. The flame properties of a given hydrocarbon fuel can be evaluated by those of another hydrocarbon fuel at the same flow conditions. The validity of scaling and similarity becomes even greater if the carbon numbers of the two hydrocarbons of concern are higher than 5. This finding can be effectively used to considerably improve computational efficiency for the modeling of oxygen/hydrocarbon turbulent flames using tabulated chemistry.

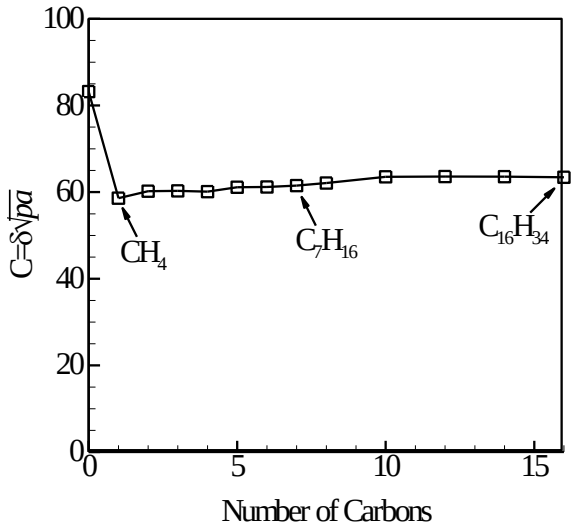

Figure 8.22: Flame thickness parameter ($C=\delta\sqrt{pa}$) as a function of number of carbons in the n-alkane fuel molecule. Oxygen/hydrogen and oxygen/n-alkanes systems with *p* = 10 atm, $T_{O_2}=T_{Fuel}=800$ K, and *a* = 1000 s-1.

8.3 Conclusion

A systematic investigation of counterflow diffusion flames of oxygen and n-alkanes (CH_4-$C_{16}H_{34}$) has been conducted. The numerical framework incorporates fundamental thermodynamics and transport theories for general fluids, detailed chemical mechanisms, and an improved flame-controlling continuation method. The flame response over the entire S-curve is explored under a broad range of pressures, flow strain rates, and inlet temperatures. The main conclusions are as follows:

(1) The inlet temperature yields insignificant effects on the flame structure; ideal-gas flame solutions can be used for fluids at supercritical conditions.

(2) For the oxygen/methane system, the flow strain rate at the extinction point increases linearly with pressure up to 50 atm, but the rate of increase decreases beyond this point. The extinction characteristics for other n-alkanes follow a similar trend.

(3) The flame thickness of all hydrocarbon fuels is inversely proportional to the square root of the product of pressure and strain rate, $\delta\sim\sqrt{pa}$, and all profiles of scaled

flame thickness collapse to a single curve in the normalized strain-rate space (a/a_{ext}). At a given pressure and strain rate, the scaled flame thickness ($C=\delta\sqrt{pa}$) of all hydrocarbon fuels has nearly identical value.

(4) The global heat-release rate is proportional to the square root of the pressure-weighted strain rate, $q\sim\sqrt{pa}$, or more precisely proportional to $p^{0.536}\sqrt{a}$ for methane and to $p^{0.534}\sqrt{a}$ for n-heptane, when the pressure effect on the peak flame temperature is taken into account. With this correlation, the profiles of the scaled heat-release rate for all pressures under consideration overlap completely as a function of the normalized strain rate, a/a_{ext}.

The similarities of flame properties among the n-alkane family suggest that the flame solutions of any n-alkane at a given pressure can be predicted from those of another n-alkane at another pressure provided that the value of *pa* is the same. This will significantly improve the computational efficiency of turbulent combustion modeling using tabulated chemistry.

CHAPTER 9

CONCLUSIONS

This dissertation established a unified theoretical and numerical framework, which is capable of studying supercritical fluid flows and combustion over the entire range of fluid thermodynamic states of concern. Turbulent closure is achieved using LES. A steady laminar flamelet approach is implemented to model turbulence/chemistry interactions. Thermodynamic properties, including density, enthalpy, and specific heat at constant pressure, are evaluated according to the modified Soave-Redlich-Kwong equation of state and fundamental thermodynamic theories. Transport properties, including thermal conductivity and dynamic viscosity, are estimated according to an extended corresponding-state principle. The numerical scheme is preconditioned along with a dual-time-step integration using finite-volume approach. Finally, a multi-block domain decomposition technique associated with the message passing interface of parallel computing is applied to facilitate computational speed.

The ensuing framework was first applied to study the three-dimensional flow dynamics of a liquid oxygen swirl injector at supercritical pressure. The complex flow structures are visualized and explored for the first time .Various fundamental instability mechanisms determining the flow dynamics were examined by implementing the spectral analysis and proper orthogonal decomposition technique. The interface, representing the phase change from dense liquid to light gas at subcritical conditions, disappears at supercritical pressures and is replaced by a transition region in which density varies smoothly and continuously with temperature. The hydrodynamic instability in the longitudinal direction is dominant across the injector, and the azimuthal wave at mode 3 resonates with acoustic wave at 4.8 kHz and amplifies itself significantly compared to other modes. A parametric study is made to examine the pressure and temperature effects on the injector design. The gaseous core decreases with the increasing pressure. The liquid film

thickness increases slightly with pressure and is consistent with the prediction by the inviscid theory. The axisymmetric study estimates a much smaller film thickness and larger spreading angle than the 3D studies due to the lack of flow dynamics in the azimuthal direction. The spreading angle defined by the maximum density gradient provides more physical interpretation of liquid spreading than the traditional definition by the ratio of axial and tangential velocity component. The spreading angle is nearly independent of the pressure.

The injection and mixing characteristics of the LOX/kerosene bi-swirl injectors were also investigated at supercritical conditions. The accuracy of numerical resolution was tested through the grid independence study. The flow similarities were observed for different levels of grid resolution. The finer vortical structures were obtained as the grid size decreases. The mixing characteristics and flow dynamics were discussed in depth. The recess region significantly improves the mixing efficiency by advancing the interaction of propellants. The spreading angle of the LOX film increases, as either the post thickness or the annulus width increases. The larger spreading angle enables the LOX film to intercept the kerosene film in a more effective way, therefore facilitating the mixing. Although the wider annulus requires a longer time to reach a fully-developed state in the annulus, it shifts the recirculation bubble upstream and recirculates the propellant mixture into the inner swirler, which could stabilize the combustion in the reacting flows. In the process of industrial design, these parameters must be selected carefully to achieve the desired injector performance.

Near-field flame dynamics under various injector geometries were systematically investigated. The flame is stabilized by two counter-rotating recirculation flows containing hot combustion products in the recess region, which plays a significant role in not only accomplishing efficient mixing and combustion but providing thermal protection of the injector faceplate. Decreasing the annulus width or post thickness might induce the initially lifted-off flame to detach from the injector post surface. Consistent with results of cold-

flow studies, the spreading angle increases as either the post thickness or the kerosene annulus width increases. But neither of them can sustain a completely thermal protection of the injector post surface. The larger annulus width produces the largest amplitude of pressure oscillations and introduces flame in the lower surface of the annulus, potentially leading to unstable combustion. In order to achieve the optimal combustion performance, further parametric studies have to be performed to determine values of the group of recess length, post thickness, and kerosene annulus width.

A general study was performed to explore the effect of strain rate on counterflow diffusion flames for real fluids over the entire thermodynamic regime. The species of interest covered oxygen/hydrogen mixtures and oxygen/n-Alkane Hydrocarbons (CH_4-$C_{16}H_{34}$). An improved two-point flame-controlling continuation method is employed to solve the singularity problem at the turning points on the flame-response curve (the S-curve). Intrinsic flame similarities were demonstrated for such properties as flame temperature, flame thickness, species concentrations, reaction rates, and heat release rate at different pressures. The correlation between the heat release rate and the product of pressure and strain rate was modified by including the pressure-dependence of flame temperature. The profiles of the scaled flame thickness and heat release rate collapse to a single curve in the normalized strain-rate space. Tabulation of pressure-dependent flame properties can be achieved by mapping the flame solution at a given pressure, according to the correlations in the normalized strain-rate space, even if the extinction strain rate is not available beforehand. This will significantly improve computational efficiency for combustion models using tabulated chemistry, such as the flamelet, FGM, and FPI models. Cryogenic inlet temperature appears to affect only the flame location, and has a negligible effect on the flame structure over the entire S-curve. Consequently, the ideal-gas flame solutions can be used for fluids at supercritical conditions.

APPENDIX A

PROPERTIES OF THE FAVRE AVERAGE

The Favre average is defined as,

$$\tilde{f} = \frac{\overline{\rho f}}{\bar{\rho}} \ . \tag{A.1}$$

Based on the definition, we have

$$\begin{aligned} \overline{\rho f} &= \overline{\rho(\tilde{f} + f'')} = \overline{\rho}\tilde{f} + \overline{\rho f''} \\ &= \overline{\rho}\overline{\rho\tilde{f}} / \overline{\rho} + \overline{\rho f''} = \overline{\rho}\overline{\rho f} / \overline{\rho} + \overline{\rho f''} \\ &= \overline{\rho f} + \overline{\rho f''} \end{aligned} \tag{A.2}$$

$$\overline{\rho f''} = 0 \, . \tag{A.3}$$

The relation between Favre averaged and Reynolds averaged variables is given by:

$$\tilde{f} = \frac{\overline{\rho f}}{\bar{\rho}} = \frac{\overline{(\bar{\rho} + \rho')(\tilde{f} + f'')}}{\bar{\rho}} = \frac{\overline{\bar{\rho}\tilde{f}} + \overline{\bar{\rho} f''} + \overline{\rho'\tilde{f}} + \overline{\rho' f''}}{\bar{\rho}} = \tilde{f} + \frac{\overline{\rho' f''}}{\bar{\rho}} \ . \tag{A.4}$$

We also have $\overline{\rho f} = \overline{\rho}\tilde{\tilde{f}} + \overline{\rho f''} = \overline{\rho}\tilde{f}$, then

$$\overline{\rho f} = \bar{\rho}\tilde{f} \ . \tag{A.5}$$

By definition, we have $\overline{\rho\tilde{f}} = \bar{\rho}\tilde{\tilde{f}} = \bar{\rho}\tilde{f}$, so

$$\tilde{\tilde{f}} = \tilde{f} \ . \tag{A.6}$$

Another important relation is given by:

$$\overline{\rho fg} = \overline{\rho(\tilde{f} + f'')(g + g'')} = \overline{\rho\tilde{f}g + \rho\tilde{f}g'' + \rho f''g + \rho f''g''} = \bar{\rho}\tilde{f}g + \overline{\rho f''g''} \ . \tag{A.7}$$

APPENDIX B

THERMODYNAMICS RELATIONSHIPS

The thermodynamic relations, such as those for evaluations of specific internal energy, specific enthalpy, and specific heat capacities, and those for evaluations of preconditioning and Jacobian matrices, are presented in this Appendix.

The partial density internal energy ($\tilde{e}_i$) of species i will be derived. We first need to find the expression for the internal energy (e). From the fundamental thermodynamic theory, we have

$$e(T,\rho)=e_0(T)+\int_0^{\rho}\left[\frac{P}{\rho^2}-\frac{T}{\rho^2}\left(\frac{\partial p}{\partial T}\right)_{\rho}\right]_T d\rho, \tag{B.1}$$

where the subscript 0 indicates a reference ideal state at a low pressure.

Utilizing the modified SRK equation of state and the partial derivative relation Eq. 2.38-2.40, Eq. B.1 is integrated, which leads to the following relationship

$$e(T,\rho)=e_0(T)+\frac{T^2}{bM_w}\left(\frac{\partial a\alpha/T}{\partial T}\right)_{\rho,Y_j}\ln\left(1+\frac{b\rho}{M_w}\right), \tag{B.2}$$

where the partial derivative $\dfrac{\partial a\alpha/T}{\partial T}$ is presented in Appendix C.

According to the definition for the partial-density property, the partial-density internal energy ($\tilde{e}_i$) can be expressed as

$$\begin{aligned}\tilde{e}_i = e_{i,0}+\frac{2}{bM_{wi}}\left[\sum_j x_j\left(T\frac{\partial}{\partial T}\left(a_{ij}\alpha_{ij}\right)-a_{ij}\alpha_{ij}\right)\right]\ln\left(1+\frac{b\rho}{M_w}\right)\\ +\frac{b_i}{bM_{wi}}\left[T\frac{\partial}{\partial T}(a\alpha)-a\alpha\right]\left[\frac{\rho}{M_w+b\rho}-\frac{1}{b}\ln\left(1+\frac{b\rho}{M_w}\right)\right].\end{aligned} \tag{B.3}$$

In addition, utilizing Eq. B.3, the internal energy of a mixture can be related to the partial-density internal energy as

$$e=\sum_i Y_i \bar{e}_i - \frac{1}{M_w}\left[T\frac{\partial}{\partial T}(a\alpha)-a\alpha\right]\frac{\rho}{M_w+b\rho} \ . \tag{B.4}$$

Based on the definition of enthalpy,

$$\rho h=\rho e+p \ . \tag{B.5}$$

Apply the partial-density derivative on both side of Eq. B.5,

$$\left(\frac{\partial \rho h}{\partial \rho_i}\right)_{T,\rho_{j\neq i}}=\left(\frac{\partial \rho e}{\partial \rho_i}\right)_{T,\rho_{j\neq i}}+\left(\frac{\partial p}{\partial \rho_i}\right)_{T,\rho_{j\neq i}} \ , \tag{B.6}$$

which is equivalent to Eq. B.7

$$\bar{h}_i=\bar{e}_i+\left(\frac{\partial p}{\partial \rho_i}\right)_{T,\rho_{j\neq i}} \ . \tag{B.7}$$

Substituting Eq. B.7 into Eq. 2.55, the following relation concerning the partial-mass enthalpy ($\bar{h}_i$) can be established

$$\bar{h}_i=\bar{e}_i+\frac{T}{\rho}\frac{\left(\frac{\partial p}{\partial T}\right)_{\rho_j}}{\left(\frac{\partial p}{\partial \rho}\right)_{T,Y_j}}\left(\frac{\partial p}{\partial \rho_i}\right)_{T,\rho_{j\neq i}} \ . \tag{B.8}$$

Next, we begin to find the expressions for the constant-volume and constant-pressure heat capacities based on the SRK equation of state.

The definition of constant volume heat capacity is

$$C_v=\left(\frac{\partial e}{\partial T}\right)_{\rho,Y_j} \ . \tag{B.9}$$

Utilizing Eq. B.2, it is straightforward to find

$$C_v = C_{v,0} + \frac{T}{bM_w}\frac{\partial^2}{\partial T^2}(a\alpha)\ln\left(1+\frac{b\rho}{M_w}\right). \tag{B.10}$$

Following fundamental thermodynamic relationships, the constant-pressure heat capacity can be expressed as

$$C_p = C_v + \frac{T}{\rho^2}\left(\frac{\partial p}{\partial T}\right)^2_{\rho_j} \Bigg/ \left(\frac{\partial p}{\partial \rho}\right)_{T,Y_j}. \tag{B.11}$$

In order to find the chemical potential, the partial-density and partial-mass entropy have to be derived first

$$s(T,\rho) = s_0(T,\rho_0) - \int_{\rho_0}^{\rho}\left[\frac{1}{\rho^2}\left(\frac{\partial p}{\partial T}\right)_{\rho}\right]_T d\rho. \tag{B.12}$$

Based on the definition of partial density entropy, it is found

$$\begin{aligned} S_i = {} & \int_{T_{ref}}^{T} C_{p_i,0}\frac{dT}{T} - \frac{R_u}{M_{wi}}\left(1+\ln x_i\right) - \frac{R_u}{M_{wi}}\ln\frac{\rho\frac{R_u}{M_w}T}{p_{ref}} \\ & + \frac{R_u}{M_{wi}}\ln\left(1-\frac{b\rho}{M_w}\right) - R_u\frac{b_i}{M_{wi}}\frac{\rho}{M_w - b\rho} + \frac{b_i}{M_{wi}}\frac{1}{b^2}\frac{\partial\, a\alpha}{\partial T}\left[\frac{b\rho}{M_w + b\rho}\right. \\ & \left. - \ln\left(1+\frac{b\rho}{M_w}\right)\right] + \frac{2}{bM_{wi}}\left[\sum_j x_j\frac{\partial}{\partial T}\left(a_{ij}\alpha_{ij}\right)\right]\ln\left(1+\frac{b\rho}{M_w}\right). \end{aligned} \tag{B.13}$$

The partial mass entropy can be further related to the partial density entropy as

$$\bar{S}_i = S_i + \left(\frac{\partial p}{\partial T}\right)_{\rho,Y_i}\bar{V}_i, \tag{B.14}$$

where the partial mass volume is

$$\bar{V}_i = \frac{1}{\rho}\left(\frac{\partial p}{\partial \rho_i}\right)_{T,\rho_{j\neq i}} \Bigg/ \left(\frac{\partial p}{\partial \rho}\right)_{T,Y_j}. \tag{B.15}$$

The chemical potential of species *i* can be calculated as

$$\mu_i = \bar{f}_i = \bar{e}_i - T\bar{s}_i \ . \tag{B.16}$$

The partial derivatives regarding chemical potential can be expressed as

$$\left(\frac{\partial \mu_i}{\partial p}\right)_{T,Y_j} = \bar{V}_i \ , \tag{B.17}$$

$$\left(\frac{\partial \mu_i}{\partial T}\right)_{T,Y_j} = -\bar{S}_i \ , \tag{B.18}$$

When the mixture fraction equation instead of the species equations is solved for chemistry closure, the derivative of any scalar ϕ with respect to the mixture fraction is evaluated based on the chain rule, shown as following.

$$\left(\frac{\partial \phi}{\partial f}\right)_{T,p} = \sum_{i=1}^{N-1}\left(\frac{\partial \phi}{\partial Y_i}\right)_{T,p,Y_{j\neq i}} \left(\frac{\partial Y_i}{\partial f}\right)_{T,p} , \tag{B.19}$$

where $\left(\partial Y_i / \partial f\right)_{T,p}$ is obtained from the flamelet library, that is, it is dependent on the local flame structures.

Next, we want to derive the partial derivatives needed in the calculation of the precondition and Jacobian matrices. First, a thermodynamic relationship correlating pressure as a function of temperature, density, and mass fractions is derived. According to thermodynamics, each intensive property will depend on $N+1$ other intensive variables in a mixture. We begin with the following relation

$$p = p(T, \rho_i), \tag{B.20}$$

where $i = 1, .., N$. Here we are interested in the differential form, it can be expressed as

$$dp = \left(\frac{\partial p}{\partial T}\right)_{\rho_i} dT + \sum_{i=1}^{N}\left(\frac{\partial p}{\partial \rho_i}\right)_{T,\rho_{j\neq i}} d\rho_i . \tag{B.21}$$

Rearrange it, we have

$$dp = \left(\frac{\partial p}{\partial T}\right)_{\rho_i} dT + \sum_{i=1}^{N-1} \left[\left(\frac{\partial p}{\partial \rho_i}\right)_{T,\rho_{j\neq i}} - \left(\frac{\partial p}{\partial \rho_N}\right)_{T,\rho_{j\neq N}}\right] d\rho_i + \left(\frac{\partial p}{\partial \rho_N}\right)_{T,\rho_{j\neq N}} d\rho. \tag{B.22}$$

Since $\rho_i = \rho Y_i$

$$d\rho_i = Y_i d\rho + \rho dY_i. \tag{B.23}$$

Substituting Eq. B. 9 into Eq. B. 8 leads to following expression

$$dp = A_T dT + A_{Y_i} dY_i + A_\rho d\rho, \tag{B.24}$$

where

$$A_T = \left(\frac{\partial p}{\partial T}\right)_{\rho_i}, \tag{B.25}$$

$$A_{Y_i} = \rho\left[\left(\frac{\partial p}{\partial \rho_i}\right)_{T,\rho_{j\neq i}} - \left(\frac{\partial p}{\partial \rho_N}\right)_{T,\rho_{j\neq N}}\right], \tag{B.26}$$

$$A_\rho = \left(\frac{\partial p}{\partial \rho}\right)_{T,Y_i}. \tag{B.27}$$

A very useful formulation can be derived from Eq. B. 10, which is

$$d\rho = \frac{dp - \left(\frac{\partial p}{\partial T}\right)_{\rho_i} dT + \sum_{i=1}^{N-1}\left[\left(\frac{\partial p}{\partial \rho_i}\right)_{T,\rho_{j\neq i}} - \left(\frac{\partial p}{\partial \rho_N}\right)_{T,\rho_{j\neq N}}\right] dY_i}{\left(\frac{\partial p}{\partial \rho}\right)_{T,Y_i}}. \tag{B.28}$$

Next, a thermodynamic relationship correlating internal energy as a function of pressure, density, and mass fractions is derived. We begin with the following one

$$\rho e = \rho e(T, \rho_i), \tag{B.29}$$

where $i = 1, \cdots, N$, and e is the internal energy per unit mass. Its differential form can be written as

$$d\rho e = \rho\left(\frac{\partial e}{\partial T}\right)_{\rho_i} dT + \sum_{i=1}^{N}\left(\frac{\partial \rho e}{\partial \rho_i}\right)_{T,\rho_{j\neq i}} d\rho_i. \tag{B.30}$$

Based on the definition of partial density properties, it is recognized

$$e_i = \left(\frac{\partial \rho e}{\partial \rho_i}\right)_{T,\rho_{j\neq i}}, \tag{B.31}$$

which is the partial density internal energy of species i in the mixture. The first derivative in Eq. B. 11 is the constant volume heat capacity C_v. Substituting the partial density internal energy of each species into Eq. B. 11 leads to the following expression

$$d\rho e = \rho C_v dT + \sum_{i=1}^{N} e_i d\rho_i. \tag{B.32}$$

Inserting Eq. B. 9 into Eq. B. 12,

$$d\rho e = \rho C_v dT + \sum_{i=1}^{N} e_i \rho dY_i + \sum_{i=1}^{N} e_i Y_i d\rho. \tag{B.33}$$

Since $d\rho e = \rho de + e d\rho$, the following expression is easily derived

$$de = C_v dT + \sum_{i=1}^{N-1} (e_i - e_N) dY_i + \frac{1}{\rho}\left(\sum_{i=1}^{N} Y e_i - e\right) d\rho. \tag{B.34}$$

Substituting Eq. B. 13 into Eq. B. 14, we can establish

$$de = B_T dT + B_p dp + \sum_{i=1}^{N-1} B_{Y_i} dY_i, \tag{B.35}$$

where

$$B_T = C_v - \frac{1}{\rho}\left(\sum_{i=1}^{N} Y_i e_i - e\right)\left(\frac{\partial \rho}{\partial p}\right)_{T,Y_i}\left(\frac{\partial p}{\partial T}\right)_{\rho_i}, \tag{B.36}$$

$$B_p = \frac{1}{\rho}\left(\sum_{i=1}^{N} Y_i e_i - e\right)\left(\frac{\partial \rho}{\partial p}\right)_{T,Y_i}, \tag{B.37}$$

$$B_{Y_i} = \left\{(e_i - e_N) - \left(\sum_{i=1}^{N} Y_i e_i - e\right) \cdot \left(\frac{\partial \rho}{\partial p}\right)_{T,Y_i} \cdot \left[\left(\frac{\partial p}{\partial \rho_i}\right)_{T,\rho_{j\neq i}} - \left(\frac{\partial p}{\partial \rho_N}\right)_{T,\rho_{j\neq N}}\right]\right\}. \tag{B.38}$$

Based on fundamental thermodynamic theories, the following relation can be obtained

$$dh = de + \frac{1}{\rho} dp - \frac{p}{\rho^2} d\rho. \tag{B.39}$$

Substituting Eq. B.15 into Eq. B.16, the following expression is derived after some straightforward manipulations

$$dh = D_T dT + D_p dp + \sum_{i=1}^{N-1} D_{Y_i} dY_i, \tag{B.40}$$

where

$$D_T = C_v - \frac{1}{\rho}\left(\frac{\partial p}{\partial T}\right)_{\rho_i}\left(\frac{\partial \rho}{\partial p}\right)_{T,Y_i}\left(\sum_{i=1}^{N} Y_i e_i - e - \frac{p}{\rho}\right), \tag{B.41}$$

$$D_p = \frac{1}{\rho} + \frac{1}{\rho}\left(\frac{\partial \rho}{\partial p}\right)_{T,Y_i}\left(\sum_{i=1}^{N} Y_i e_i - e - \frac{p}{\rho}\right), \tag{B.42}$$

$$D_{Y_i} = e_i - e_N - \left(\frac{\partial \rho}{\partial p}\right)_{T,Y_i}\left(\sum_{i=1}^{N} Y_i e_i - e - \frac{p}{\rho}\right)\left[\left(\frac{\partial p}{\partial \rho_i}\right)_{T,\rho_{j\neq i}} - \left(\frac{\partial p}{\partial \rho_N}\right)_{T,\rho_{j\neq N}}\right]. \tag{B.43}$$

According to the definition in thermodynamics, we recognize that the coefficient D_T equals to the constant pressure heat capacity C_p of a fluid mixture,

$$C_p = D_T = C_v - \frac{1}{\rho}\left(\frac{\partial p}{\partial T}\right)_{\rho_i}\left(\frac{\partial \rho}{\partial p}\right)_{T,Y_i}\left(\sum_{i=1}^{N} Y_i e_i - e - \frac{p}{\rho}\right). \tag{B.44}$$

Finally a relationship regarding the speed of sound in the mixture is derived. According to the definition of the speed of sound

$$a^2 = \left(\frac{\partial p}{\partial \rho}\right)_{s,Y_i}. \tag{B.45}$$

Based on the Eq. B.10, the following expression is obtained in a straightforward manner.

$$\left(\frac{\partial p}{\partial \rho}\right)_{s,Y_i} = \left(\frac{\partial p}{\partial T}\right)_{\rho_i}\left(\frac{\partial T}{\partial \rho}\right)_{s,Y_i} + \left(\frac{\partial p}{\partial \rho}\right)_{T,Y_i}. \tag{B.46}$$

Given

$$s = s(T, \rho, Y_i), \tag{B.47}$$

where $i = 1, \cdots N-1.$

After utilizing some fundamental thermodynamic relationships, the following differential form of Eq. B.19 can be obtained

$$ds = \frac{C_v}{T} dT - \frac{1}{\rho^2}\left(\frac{\partial p}{\partial T}\right)_{\rho_i} d\rho + \sum_{i=1}^{N-1}\left(\frac{\partial s}{\partial Y_i}\right)_{T,\rho,Y_{j\neq i}} dY_i. \tag{B.48}$$

Based on Eq. B.20, the following expression is further derived

$$\left(\frac{\partial T}{\partial \rho}\right)_{s,Y_i} = \frac{T}{\rho^2}\left(\frac{\partial p}{\partial T}\right)_{\rho_i} \Big/ C_v \ . \tag{B.49}$$

Substituting Eq. B.21 into Eq. B.18, an expression of the speed of sound in the general fluid mixture is established as

$$a^2 = \left(\frac{\partial p}{\partial \rho}\right)_{s,Y_i} = \frac{C_p}{C_v}\left(\frac{\partial p}{\partial \rho}\right)_{T,Y_i} \ . \tag{B.50}$$

Equations B.24, B.35, B.40, and B.50 are the important thermodynamic relationships required in evaluating the preconditioning and Jacobian matrices.

APPENDIX C

DERIVATIVE EXPRESSIONS IN SRK EOS

In SRK EOS, the terms $a\alpha$ and $\alpha_{ij}a_{ij}$ are a function of temperature. The derivative of $a\alpha$ with respect to temperature is given as

$$\frac{\partial a\alpha}{\partial T}=\sum_{i=1}^{N}\sum_{j=1}^{N}x_i x_j\sqrt{a_i a_j}\,\frac{\partial\sqrt{\alpha_i\alpha_j}}{\partial T}\,, \tag{C.1a}$$

where

$$\frac{\partial\sqrt{\alpha_i\alpha_j}}{\partial T}=\frac{1}{2}\left(\frac{\alpha_i}{\alpha_j}\right)^{\frac{1}{2}}\frac{\partial\alpha_j}{\partial T}+\frac{1}{2}\left(\frac{\alpha_j}{\alpha_i}\right)^{\frac{1}{2}}\frac{\partial\alpha_i}{\partial T}\,, \tag{C.1b}$$

$$\frac{\partial\alpha_i}{\partial T}=-\frac{S_i}{\sqrt{TT_{c,i}}}\left[1+S_i\left(1-\sqrt{\frac{T}{T_{c,i}}}\right)\right], \tag{C.1c}$$

$$\frac{\partial a_{ij}\alpha_{ij}}{\partial T}=\sqrt{a_i a_j}\,\frac{\partial\sqrt{\alpha_i\alpha_j}}{\partial T}\,. \tag{C.2}$$

The second derivative of parameter $a\alpha$ to temperature is

$$\frac{\partial^2 a\alpha}{\partial T^2}=\sum_{i=1}^{N}\sum_{j=1}^{N}x_i x_j\sqrt{a_i a_j}\,\frac{\partial^2\sqrt{\alpha_i\alpha_j}}{\partial T^2}\,, \tag{C.3a}$$

where

$$\begin{aligned}\frac{\partial^2\sqrt{\alpha_i\alpha_j}}{\partial T^2}=&\frac{1}{2}\left(\frac{1}{\alpha_i\alpha_j}\right)^{\frac{1}{2}}\frac{\partial\alpha_i}{\partial T}\frac{\partial\alpha_j}{\partial T}-\frac{1}{4}\left(\frac{\alpha_i}{\alpha_j^3}\right)^{\frac{1}{2}}\left(\frac{\partial\alpha_j}{\partial T}\right)^2\\&-\frac{1}{4}\left(\frac{\alpha_j}{\alpha_i^3}\right)^{\frac{1}{2}}\left(\frac{\partial\alpha_i}{\partial T}\right)^2+\frac{1}{2}\left(\frac{\alpha_i}{\alpha_j}\right)^{\frac{1}{2}}\frac{\partial^2\alpha_j}{\partial T^2}+\frac{1}{2}\left(\frac{\alpha_j}{\alpha_i}\right)^{\frac{1}{2}}\frac{\partial^2\alpha_i}{\partial T^2}\,,\end{aligned} \tag{C.3b}$$

$$\frac{\partial^2 \alpha_i}{\partial T^2} = \frac{1}{2}\frac{S_i^2}{T T_{c,i}} + \frac{1}{2}\frac{S_i}{\sqrt{T^3 T_{c,i}}}\left[1 + S_i\left(1 - \sqrt{\frac{T}{T_{c,i}}}\right)\right]. \qquad \text{(C.3c)}$$

The variable α_i for species H_2 (α_{H_2}), is treated differently since hydrogen is a quantum gas. The derivative of this variable is

$$\frac{\partial \alpha_{H_2}}{\partial T} = -\alpha_{H_2}\left[0.30228\frac{1}{T_{c,i}}\right], \qquad \text{(C.4)}$$

$$\frac{\partial^2 \alpha_{H_2}}{\partial T^2} = \alpha_{H_2}\left[0.30228\frac{1}{T_{c,i}}\right]^2. \qquad \text{(C.5)}$$

APPENDIX D

JACOBIAN MATRICES

The Jacobian matrices employed in Chapter 3 are defined as follows.

D.1 Jacobian of Primitive Variables

The Jacobian of primitive variables $T = \partial Q / \partial Z$ is given by

$$T = \begin{pmatrix} (\frac{\partial \rho}{\partial p})_{T,Y_i} & 0 & 0 & 0 & \rho_T & \rho_f \\ u(\frac{\partial \rho}{\partial p})_{T,Y_i} & \bar{\rho} & 0 & 0 & u\rho_T & u\rho_f \\ v(\frac{\partial \rho}{\partial p})_{T,Y_i} & 0 & \bar{\rho} & 0 & v\rho_T & v\rho_f \\ w(\frac{\partial \rho}{\partial p})_{T,Y_i} & 0 & 0 & \bar{\rho} & w\rho_T & w\rho_f \\ [\tilde{h}_t + (\sum_{i=1}^{N} Y_i e_i - e - \frac{p}{\rho})](\frac{\partial \rho}{\partial p})_{T,Y_i} & \bar{\rho}u & \bar{\rho}v & \bar{\rho}w & \bar{\rho}c_p + h_t\rho_T & \rho_f E + \bar{\rho}E_f \\ f(\frac{\partial \rho}{\partial p})_{T,Y_i} & 0 & 0 & 0 & \rho_T f & \bar{\rho} + f\rho_f \end{pmatrix}, \quad \text{(D.1)}$$

$$\rho_T = (\frac{\partial \rho}{\partial T})_{p,Y_i} = -\frac{A_T}{A_p}, \quad \text{(D.2)}$$

$$\rho_f = \left(\frac{\partial \rho}{\partial f}\right)_{T,p} = \sum_{i=1}^{N-1}\left[\left(\frac{\partial \rho}{\partial Y_i}\right)_{T,p,Y_{j\neq i}}\left(\frac{\partial Y_i}{\partial f}\right)_{T,p}\right] = -\sum_{i=1}^{N-1}\left[\left(\frac{A_{Y_i}}{A_p}\right)\left(\frac{\partial Y_i}{\partial f}\right)_{T,p}\right], \quad \text{(D.3)}$$

$$E_f = \left(\frac{\partial E}{\partial f}\right)_{T,p} = \sum_{i=1}^{N-1}\left[\left(\frac{\partial E}{\partial Y_i}\right)_{T,p,Y_{j\neq i}}\left(\frac{\partial Y_i}{\partial f}\right)_{T,p}\right], \quad \text{(D.4)}$$

$$\rho_f E + \rho E_f = \sum_{i=1}^{N-1}\left[\left(\frac{\partial Y_i}{\partial f}\right)_{T,p}\left(\frac{\partial \rho}{\partial Y_i}E + \rho B_{Y_i}\right)\right] = \sum_{i=1}^{N-1}\left\{\left(\frac{\partial Y_i}{\partial f}\right)_{T,p}\left[\rho_{Y_i}\tilde{h}_t + \rho\left(\tilde{h}_i - \tilde{h}_N\right)\right]\right\}, \quad \text{(D.5)}$$

where the coefficients A_p, A_T, A_{Y_i}, B_p, B_T, and B_{Y_i} are defined in the Appendix B. The terms e_t and h_t denote total energy and total enthalpy, respectively.

$$e_t = e + \frac{1}{2}(u^2 + v^2 + w^2), \tag{D.6}$$

$$h_t = e_t + \frac{p}{\rho}. \tag{D.7}$$

D.2 Convective Flux Jacobians

The Jacobian matrix $\mathbf{A} = \partial \mathbf{E} / \partial \mathbf{Z}$ is given by

$$\mathbf{A} = \begin{pmatrix} U\rho_p & \bar{\rho} l_x & \bar{\rho} l_y \\ l_x + uU\rho_p & \bar{\rho}(U + ul_x) & \bar{\rho} ul_y \\ l_y + vU\rho_p & \bar{\rho} vl_x & \bar{\rho}(U + vl_y) \\ l_z + wU\rho_p & \bar{\rho} wl_x & \bar{\rho} wl_y \\ (\rho_p \tilde{h}_t + \bar{\rho} h_p)U & \bar{\rho}(\tilde{h}_t l_x + uU) & \bar{\rho}(\tilde{h}_t l_y + vU) \\ \tilde{f} U\rho_p & \bar{\rho} \tilde{f} l_x & \bar{\rho} \tilde{f} l_y \end{pmatrix}$$
$$\begin{pmatrix} \bar{\rho} l_z & U\rho_T & U\rho_f \\ \bar{\rho} ul_z & uU\rho_T & uU\rho_f \\ \bar{\rho} vl_z & vU\rho_T & vU\rho_f \\ \bar{\rho}(U + wl_z) & wU\rho_T & wU\rho_f \\ \bar{\rho}(h_t l_z + wU) & (\rho_T h_t + \bar{\rho} h_T)U & (\rho_f h_t + \bar{\rho} h_f)U \\ \bar{\rho} \tilde{f} l_z & \tilde{f} U\rho_T & (\tilde{f}\rho_f + \bar{\rho})U \end{pmatrix}, \tag{D.8}$$

where l_x, l_y, and l_z represent the three scalars in the direction vector $\mathbf{l} = l_x\mathbf{i} + l_y\mathbf{j} + l_z\mathbf{k}$. If we replace $\mathbf{l}$ with any of the following vectors, we can get the Jacobian matrices $\mathbf{A} = \partial \mathbf{E} / \partial \mathbf{Z}, \mathbf{B} = \partial \mathbf{F} / \partial \mathbf{Z}, \text{ and } \mathbf{C} = \partial \mathbf{G} / \partial \mathbf{Z}$, respectively.

$$\begin{aligned}\boldsymbol{\xi} &= \xi_x \mathbf{i} + \xi_y \mathbf{j} + \xi_z \mathbf{k}\,, \\ \boldsymbol{\eta} &= \eta_x \mathbf{i} + \eta_y \mathbf{j} + \eta_z \mathbf{k}\,, \\ \boldsymbol{\zeta} &= \zeta_x \mathbf{i} + \zeta_y \mathbf{j} + \zeta_z \mathbf{k}\,. \end{aligned} \tag{D.9}$$

REFERENCES

[1] V. Yang, *Modeling of supercritical vaporization, mixing, and combustion processes in liquid-fueled propulsion systems.* Proceedings of the Combustion Institute, 2000. **28**: p. 925-942.

[2] J. Bellan, *Supercritical (and subcritical) fluid behavior and modeling: drops, streams, shear and mixing layers, jets and sprays.* Progress in Energy and Combustion Science, 2000. **26**(4-6): p. 329-366.

[3] F.E. Culick and V. Yang, *Overview of combustion instabilities in liquid-propellant rocket engines.* Liquid Rocket Engine Combustion Instability, 1995. **169**: p. 3-37.

[4] J.A. Newman and T. Brzustowski, *Behavior of a liquid jet near the thermodynamic critical region.* AIAA journal, 1971. **9**(8): p. 1595-1602.

[5] W. Mayer, A. Schik, M. Sch-aring, ffler, and H. Tamura, *Injection and mixing processes in high-pressure liquid oxygen/gaseous hydrogen rocket combustors.* Journal of Propulsion and Power, 2000. **16**(5): p. 823-828.

[6] B. Chehroudi, R. Cohn, and D. Talley, *Cryogenic shear layers: experiments and phenomenological modeling of the initial growth rate under subcritical and supercritical conditions.* International Journal of Heat and Fluid Flow, 2002. **23**(5): p. 554-563.

[7] R. Branam and W. Mayer, *Characterization of cryogenic injection at supercritical pressure.* Journal of Propulsion and power, 2003. **19**(3): p. 342-355.

[8] S. Candel, M. Juniper, G. Singla, P. Scouflaire, and C. Rolon, *Structure and dynamics of cryogenic flames at supercritical pressure.* Combustion Science and Technology, 2006. **178**(1-3): p. 161-192.

[9] J.C. Oefelein and V. Yang, *Modeling high-pressure mixing and combustion processes in liquid rocket engines.* Journal of Propulsion and Power, 1998. **14**(5): p. 843-857.

[10] N. Zong, H. Meng, S.-Y. Hsieh, and V. Yang, *A numerical study of cryogenic fluid injection and mixing under supercritical conditions.* Physics of fluids, 2004. **16**: p. 4248.

[11] J.C. Oefelein, *Thermophysical characteristics of shear-coaxial LOX-H-2 flames at supercritical pressure.* Proceedings of the Combustion Institute, 2005. **30**: p. 2929-2937.

[12] N. Zong and V. Yang, *Near-field flow and flame dynamics of LOX/methane shear-coaxial injector under supercritical conditions.* Proceedings of the Combustion Institute, 2007. **31**(2): p. 2309-2317.

[13] M. Juniper and S. Candel, *Edge diffusion flame stabilization behind a step over a liquid reactant.* Journal of Propulsion and Power, 2003. **19**(3): p. 332-341.

[14] M.P. Juniper and S.M. Candel, *The stability of ducted compound flows and consequences for the geometry of coaxial injectors.* Journal of Fluid Mechanics, 2003. **482**: p. 257-269.

[15] M. Masquelet, S. Menon, Y. Jin, and R. Friedrich, *Simulation of unsteady combustion in a LOX-GH(2) fueled rocket engine.* Aerospace Science and Technology, 2009. **13**(8): p. 466-474.

[16] M. Masquelet and S. Menon, *Large-eddy simulation of flame-turbulence interactions in a shear coaxial injector.* Journal of Propulsion and Power, 2010. **26**(5): p. 924-935.

[17] V.R. Rubinsky, ed. *Combustion instability in the RD-0110 engine*. Liquid Rocket Engine Combustion Instability, ed. V. Yang. Vol. 169. 1995, Progress in Astronautics and Aeronautics. 89-112.

[18] Y. Huang and V. Yang, *Effect of swirl on combustion dynamics in a lean-premixed swirl-stabilized combustor.* Proceedings of the Combustion Institute, 2005. **30**(2): p. 1775-1782.

[19] N. Syred and J. Beer, *Combustion in swirling flows: a review.* Combustion and Flame, 1974. **23**(2): p. 143-201.

[20] Y. Huang and V. Yang, *Dynamics and stability of lean-premixed swirl-stabilized combustion.* Progress in Energy and Combustion Science, 2009. **35**(4): p. 293-364.

[21] V.G. Bazarov and V. Yang, *Liquid-propellant rocket engine injector dynamics.* Journal of Propulsion and Power, 1998. **14**(5): p. 797-806.

[22] K. Ahn and H.-S. Choi, *Combustion dynamics of swirl coaxial injectors in fuel-rich combustion.* Journal of Propulsion and Power, 2012. **28**(6): p. 1359-1367.

[23] V. Bazarov, V. Yang, and P. Puri, *Design and dynamics of jet and swirl injectors*, in *Liquid Rocket Thrust Chambers: Aspects of Modeling, Analysis, and Design*, V. Yang, M. Habiballah, J. Hulka, and M. Popp, Editors. 2004, Progress in Astronautics and Aeronautics. p. 19-103.

[24] A. Datta and S. Som, *Numerical prediction of air core diameter, coefficient of discharge and spray cone angle of a swirl spray pressure nozzle.* International journal of heat and fluid flow, 2000. **21**(4): p. 412-419.

[25] D. Kim, J.-H. Im, H. Koh, and Y. Yoon, *Effect of ambient gas density on spray characteristics of swirling liquid sheets.* Journal of propulsion and power, 2007. **23**(3): p. 603-611.

[26] Q.-f. Fu, L.-j. Yang, and X.-d. Wang, *Theoretical and experimental study of the dynamics of a liquid swirl injector.* Journal of Propulsion and Power, 2010. **26**(1): p. 94-101.

[27] Q.-F. Fu, L.-J. Yang, W. Zhang, and K.-D. Cui, *Spray Characteristics of an Open-end Swirl Injector.* 2012. **22**(5): p. 431-445.

[28] R. Richardson, H. Park, J.V. Canino, and S.D. Heister, *Nonlinear Dynamic Response Modeling of a Swirl Injector*, in *AIAA Paper*2007.

[29] M. Ismailov and S.D. Heister, *Dynamic Response of Rocket Swirl Injectors, Part I: Wave Reflection and Resonance.* Journal of Propulsion and Power, 2011. **27**(2): p. 402-411.

[30] M. Ismailov and S.D. Heister, *Dynamic Response of Rocket Swirl Injectors, Part II: Nonlinear Dynamic Response.* Journal of Propulsion and Power, 2011. **27**(2): p. 412-421.

[31] S. Cho, G. Park, Y. Chung, Y. Yoon, and V.G. Bazarov, *Surface Instability on Cryogenic Swirl Flow at Sub-to Supercritical Conditions.* Journal of Propulsion and Power, 2014: p. 1-9.

[32] N. Zong and V. Yang, *Cryogenic fluid dynamics of pressure swirl injectors at supercritical conditions.* Physics of Fluids, 2008. **20**(5).

[33] H. Huo, N. Zong, and V. Yang, *Cryogenic fluid dynamic response of swirl injector to external forcing at supercritical conditions*, in *AIAA Paper*2009.

[34] H. Huo, X. Wang, and V. Yang, *Flow Dynamics of a Simplex Swirl Injector at Supercritical Conditions*, in *AIAA Paper*2014, AIAA Paper.

[35] M. Sasaki, H. Sakamoto, M. Takahashi, T. Tomita, and H. Tamura, in *AIAA Paper*. 1997.

[36] P.-G. Han, J. Seol, S. Hwang, and Y. Yoon, in *AIAA Paper*. 2003.

[37] T. Inamura, H. Tamura, and H. Sakamoto, *Characteristics of liquid film and spray injected from swirl coaxial injector.* Journal of propulsion and Power, 2003. **19**(4): p. 632-639.

[38] M. Soltani, K. Ghorbanian, M. Ashjaee, and M. Morad, *Spray characteristics of a liquid–liquid coaxial swirl atomizer at different mass flow rates.* Aerospace science and technology, 2005. **9**(7): p. 592-604.

[39] M.D. Lightfoot, S.A. Schumaker, L.A. Villasmil, and S.A. Danczyk, *The Effect of Swirl on Gas-Centered Swirl Coaxial Injector Sprays*, 2011, DTIC Document.

[40] J.-H. Im, S. Cho, Y. Yoon, and I. Moon, *Comparative study of spray characteristics of gas-centered and liquid-centered swirl coaxial injectors.* Journal of Propulsion and Power, 2010. **26**(6): p. 1196-1204.

[41] S.-H. Kim, Y.-M. Han, S. Seo, I.-Y. Moon, J.-K. Kim, and W.-S. Seol, in *AIAA Paper*. 2005.

[42] K. Ahn, Y.-M. Han, S. Seo, and H.-S. Choi, *Effects of injector recess and chamber pressure on combustion characteristics of liquid–liquid swirl coaxial injectors.* Combustion Science and Technology, 2010. **183**(3): p. 252-270.

[43] K. Ahn, Y.-M. Han, and H.-S. Choi, *Effects of Recess Length on Discharge Coefficients of Swirl Coaxial Injectors.* Combustion Science and Technology, 2012. **184**(3): p. 323-336.

[44] F.A. Williams, *Combustion Theory.* Addison-Wesley, Reading, MA, 1985.

[45] C.K. Law, *Combustion physics.* Cambridge University Press, 2006.

[46] C.K. Law, *Combustion physics*. 2006, Cambridge; New York: Cambridge University Press. 722.

[47] N. Peters, *Turbulent combustion*. 2000, Cambridge, England: Cambridge University Press. xvi, 304 p.

[48] V. Yang and W.E. Anderson, *Liquid rocket engine combustion instability*. Vol. 169. Vol 169, AIAA 1995, Washington, DC: Prog. Astro. Aero.

[49] T.C. Lieuwen and V. Yang, *Combustion instabilities in gas turbine engines: operational experience, fundamental mechanisms and modeling*. Progress in Astronautics and Aeronautics. Vol. 210. Vol 210, 2005, Reston, VA: Prog. Astro. Aero. xiv, 657 p.

[50] A. Linan, *The asymptotic structure of counterflow diffusion flames for large activation energies.* Acta Astronautica, 1974. **1**(7): p. 1007-1039.

[51] G. Dixon-Lewis, T. David, P. Gaskell, S. Fukutani, H. Jinno, J. Miller, R. Kee, M. Smooke, N. Peters, and E. Effelsberg, *Calculation of the structure and extinction limit of a methane-air counterflow diffusion flame in the forward stagnation region of a porous cylinder.* proceedings of the Combustion Institute, 1985. **20**: p. 1893-1904.

[52] R.J. Kee, J.A. Miller, G.H. Evans, and G. Dixon-Lewis, *A computational model of the structure and extinction of strained, opposed flow, premixed methane-air flames**. Proceedings of the Combustion Institute, 1989. **22**: p. 1479-1494.

[53] H. Chelliah, C. Law, T. Ueda, M. Smooke, and F. Williams, *An experimental and theoretical investigation of the dilution, pressure and flow-field effects on the extinction condition of methane-air-nitrogen diffusion flames.* proceedings of the Combustion Institute, 1991. **23**: p. 503-511.

[54] V. Giovangigli and M.D. Smooke, *Extinction of Strained Premixed Laminar Flames with Complex Chemistry.* Combustion Science and Technology, 1987. **53**(1): p. 23-49.

[55] H.B. Keller, in *Applications of Bifurcation Theory*, P.H. Rabinowitz, Editor. 1977, Academic Press: New York. p. 389.

[56] M. Nishioka, C.K. Law, and T. Takeno, *A flame-controlling continuation method for generating S-curve responses with detailed chemistry.* Combustion and Flame, 1996. **104**(3): p. 328-342.

[57] H. Pitsch. *FlameMaster, a C++ computer program for 0D combustion and 1D laminar flame calculations*. 1998; Available from: 1998; available from http://www.stanford.edu/~hpitsch/FlameMaster.html.

[58] R. Kee, R. Rupley, J. Miller, M. Coltrin, J. Grcar, E. Meeks, H. Moffat, A. Lutz, G. Dixon-Lewis, and M. Smooke, *CHEMKIN-PRO, Reaction Design.* Inc., San Diego, CA, 2008.

[59] G. Ribert, N. Zong, V. Yang, L. Pons, N. Darabiha, and S. Candel, *Counterflow diffusion flames of general fluids: Oxygen/hydrogen mixtures.* Combustion and Flame, 2008. **154**(3): p. 319-330.

[60] N. Darabiha, S.M. Candel, V. Giovangigli, and M.D. Smooke, *Extinction of Strained Premixed Propane-Air Flames with Complex Chemistry.* Combustion Science and Technology, 1988. **60**(4-6): p. 267-285.

[61] G. Lacaze and J.C. Oefelein, *A non-premixed combustion model based on flame structure analysis at supercritical pressures.* Combustion and Flame, 2012. **159**(6): p. 2087-2103.

[62] L. Pons, N. Darabiha, and S. Candel, *Pressure effects on nonpremixed strained flames.* Combustion and Flame, 2008. **152**(1-2): p. 218-229.

[63] L. Pons, N. Darabiha, S. Candel, G. Ribert, and V. Yang, *Mass transfer and combustion in transcritical non-premixed counterflows.* Combustion Theory and Modelling, 2009. **13**(1): p. 57-81.

[64] S. Li and F. Williams, *Counterflow heptane flame structure.* Proceedings of the Combustion Institute, 2000. **28**(1): p. 1031-1038.

[65] R. Seiser, H. Pitsch, K. Seshadri, W. Pitz, and H. Gurran, *Extinction and autoignition of n-heptane in counterflow configuration.* Proceedings of the Combustion Institute, 2000. **28**(2): p. 2029-2037.

[66] H. Curran, P. Gaffuri, W.J. Pitz, and C.K. Westbrook, *A comprehensive modeling study of n-heptane oxidation.* Combustion and flame, 1998. **114**(1-2): p. 149-177.

[67] C.K. Westbrook, W.J. Pitz, O. Herbinet, H.J. Curran, and E.J. Silke, *A comprehensive detailed chemical kinetic reaction mechanism for combustion of n-alkane hydrocarbons from n-octane to n-hexadecane.* Combustion and Flame, 2009. **156**(1): p. 181-199.

[68] H. Meng and V. Yang, *A unified treatment of general fluid thermodynamics and its application to a preconditioning scheme.* Journal of Computational Physics, 2003. **189**(1): p. 277-304.

[69] M. Benedict, G.B. Webb, and L.C. Rubin, *An Empirical Equation for Thermodynamic Properties of Light Hydrocarbons and Their Mixtures I. Methane, Ethane, Propane and n-Butane.* The Journal of Chemical Physics, 1940. **8**(4): p. 334-345.

[70] D.Y. Peng and D.B. Robinson, *A new two-constant equation of state.* Industrial & Engineering Chemistry Fundamentals, 1976. **15**(1): p. 59-64.

[71] G. Soave, *Equilibrium constants from a modified Redlich-Kwong equation of state.* Chemical Engineering Science, 1972. **27**(6): p. 1197-1203.

[72] J.A. Manrique and G.L. Borman, *Calculations of Steady State Droplet Vaporization at High Ambient Pressures.* International Journal of Heat and Mass Transfer, 1969. **12**(9): p. 1081-1095.

[73] K.C. Hsieh, J.S. Shuen, and V. Yang, *Droplet Vaporization in High-Pressure Environments .1. Near Critical Conditions.* Combustion Science and Technology, 1991. **76**(1-3): p. 111-132.

[74] P. Lafon, V. Yang, and M. Habiballah, in *AIAA, ASME, SAE, and ASEE, Joint Propulsion Conference and Exhibit, 31st, San Diego*. 1995. United States.

[75] H. Meng, *Liquid-fuel droplet vaporization and cluster behavior at supercritical conditions*, 2001, Pennsylvania State University, 2001. p. 196 leaves.

[76] V. Vesovic and W. Wakeham, *Transport Properties of Supercritical Fluids and Fluids Mixtures*, in *Supercritical fluid technology : reviews in modern theory and applications*, T.J. Bruno and J.F. Ely, Editors. 1991, CRC Press: Boca Raton. p. 593 p.

[77] B.E. Poling, J.M. Prausnitz, and J.P. O'Connell, *The properties of gases and liquids*. 5th ed. 2001, New York: McGraw-Hill. 1 v. (various pagings).

[78] J.F. Ely and H.J.M. Hanley, *Prediction of Transport-Properties .1. Viscosity of Fluids and Mixtures.* Industrial & Engineering Chemistry Fundamentals, 1981. **20**(4): p. 323-332.

[79] U. Piomelli, *Large-eddy simulation: achievements and challenges.* Progress in Aerospace Sciences, 1999. **35**(4): p. 335-362.

[80] P. Sagaut, *Large eddy simulation for incompressible flows : an introduction*. 2001, Berlin ; New York: Springer. xv, 319 p.

[81] P. Moin and K. Mahesh, *Direct numerical simulation: A tool in turbulence research.* Annual Review of Fluid Mechanics, 1998. **30**: p. 539-578.

[82] R.S. Miller, K.G. Harstad, and J. Bellan, *Direct numerical simulations of supercritical fluid mixing layers applied to heptane-nitrogen.* Journal of Fluid Mechanics, 2001. **436**: p. 1-39.

[83] N. Okong'o, K. Harstad, and J. Bellan, *Direct numerical simulations of O-2/H-2 temporal mixing layers under supercritical conditions.* AIAA journal, 2002. **40**(5): p. 914-926.

[84] L. Vervisch and T. Poinsot, *Direct numerical simulation of non-premixed turbulent flames.* Annual Review of Fluid Mechanics, 1998. **30**: p. 655-691.

[85] S.B. Pope, *Turbulent flows*. 2000, Cambridge ; New York: Cambridge University Press. xxxiv, 771 p.

[86] D.R. Chapman, in *American Institute of Aeronautics and Astronautics, Aerospace Sciences Meeting, 17th, New Orleans*. 1979. United States.

[87] W. Cabot, *Large-eddy simulations with wall models*, 1995.

[88] E. Balaras, C. Benocci, and U. Piomelli, *Two-layer approximate boundary conditions for large-eddy simulations.* AIAA Journal, 1996. **34**(6): p. 1111-1119.

[89] P.R. Spalart, *Detached-Eddy Simulation.* Annual Review of Fluid Mechanics, 2009. **41**: p. 181-202.

[90] A. Leonard, in *Turbulent diffusion in environmental pollution; Proceedings of the Second Symposium, Charlottesville*. 1974. Proceedings of the Second Symposium, Charlottesville, Va ; United States: New York, Academic Press, Inc.

[91] S. Ghosal and P. Moin, *The Basic Equations for the Large-Eddy Simulation of Turbulent Flows in Complex-Geometry.* Journal of Computational Physics, 1995. **118**(1): p. 24-37.

[92] H. Vanderven, *A Family of Large-Eddy Simulation (Les) Filters with Nonuniform Filter Widths.* Physics of Fluids, 1995. **7**(5): p. 1171-1172.

[93] C. Le Ribault, S. Sarkar, and S.A. Stanley, *Large eddy simulation of a plane jet.* Physics of Fluids, 1999. **11**(10): p. 3069-3083.

[94] P. Moin, *Progress in large eddy simulation of turbulent flows.* 1997.

[95] A. Favre, *Statistical equations of turbulent gases (Statistical equations for compressible gas, discussing turbulent quantities separated into fluctuating and macroscopic parts).* 1969.

[96] W.H. Calhoon, Jr. and S. Menon, in *AIAA, Aerospace Sciences Meeting and Exhibit, 34th, Reno*. 1996. United States.

[97] J. Smagorinsky, *General Circulation Experiments with the Primitive Equations. I-the Basic Experiment.* . Monthly Weather Review, 1963. **91**: p. 99-164.

[98] D.K. Lilly, *The representation of small scale turbulence in numerical simulation experiments.* 1967.

[99] G. Erlebacher, M.Y. Hussaini, C.G. Speziale, and T.A. Zang, *Toward the Large-Eddy Simulation of Compressible Turbulent Flows.* Journal of Fluid Mechanics, 1992. **238**: p. 155-185.

[100] P. Moin and J. Kim, *Numerical Investigation of Turbulent Channel Flow.* Journal of Fluid Mechanics, 1982. **118**(May): p. 341-377.

[101] M. Martin, U. Piomelli, and G. Candler, in *Proceedings of the 3rd ASME/JSME Joint Fluid Engineering Conference, .* 1999. San Francisco, California, USA.

[102] M. Germano, U. Piomelli, P. Moin, and W.H. Cabot, *A Dynamic Subgrid-Scale Eddy Viscosity Model.* Physics of Fluids a-Fluid Dynamics, 1991. **3**(7): p. 1760-1765.

[103] A. Juneja and J.G. Brasseur, *Characteristics of subgrid-resolved-scale dynamics in anisotropic turbulence, with application to rough-wall boundary layers.* Physics of Fluids, 1999. **11**(10): p. 3054-3068.

[104] M. Germano, *Turbulence - the Filtering Approach.* Journal of Fluid Mechanics, 1992. **238**: p. 325-336.

[105] D.K. Lilly, *A Proposed Modification of the Germano-Subgrid-Scale Closure Method.* Physics of Fluids a-Fluid Dynamics, 1992. **4**(3): p. 633-635.

[106] M. Masquelet and S. Menon, *Large Eddy Simulation of Flame-Turbulence Interactions in a Shear Coaxial Injector.* journal of Propulsion and Power, 2010.

[107] A. Klimenko, *Multicomponent diffusion of various admixtures in turbulent flow.* Fluid Dynamics, 1990. **25**(3): p. 327-334.

[108] R.W. Bilger, *Conditional Moment Closure for Turbulent Reacting Flow.* Physics of Fluids a-Fluid Dynamics, 1993. **5**(2): p. 436-444.

[109] A.R. Kerstein, *Linear-Eddy Modeling of Turbulent Transport .7. Finite-Rate Chemistry and Multistream Mixing.* Journal of Fluid Mechanics, 1992. **240**: p. 289-313.

[110] A.R. Kerstein, *Linear-Eddy Modeling of Turbulent Transport .4. Structure of Diffusion Flames.* Combustion Science and Technology, 1992. **81**(1-3): p. 75-96.

[111] P.A. Mcmurtry, S. Menon, and A.R. Kerstein, *Linear Eddy Modeling of Turbulent Combustion.* Energy & Fuels, 1993. **7**(6): p. 817-826.

[112] V. Sankaran and S. Menon, *Subgrid combustion modeling of 3-D premixed flames in the thin-reaction-zone regime.* Proceedings of the Combustion Institute, 2005. **30**: p. 575-582.

[113] J. Légier, T. Poinsot, and D. Veynante, in *Proceedings of the Summer Program*. 2000.

[114] P.E. DesJardin and S.H. Frankel, *Large eddy simulation of a nonpremixed reacting jet: Application and assessment of subgrid-scale combustion models.* Physics of Fluids, 1998. **10**(9): p. 2298-2314.

[115] A.W. Cook and J.J. Riley, *Subgrid-scale modeling for turbulent reacting flows.* Combustion and Flame, 1998. **112**(4): p. 593-606.

[116] S.S. Girimaji and Y. Zhou, *Analysis and modeling of subgrid scalar mixing using numerical data.* Physics of Fluids, 1996. **8**(5): p. 1224-1236.

[117] H. Pitsch, E. Riesmeier, and N. Peters, *Unsteady flamelet modeling of soot formation in turbulent diffusion flames.* Combustion Science and Technology, 2000. **158**: p. 389-406.

[118] H. Pitsch and N. Peters, *A consistent flamelet formulation for non-premixed combustion considering differential diffusion effects.* Combustion and Flame, 1998. **114**(1-2): p. 26-40.

[119] G. Ribert, N. Zone, V. Yang, L. Pons, N. Darabiha, and S. Candel, in *45th AIAA Aerospace Sciences Meeting and Exhibit*. 2007. Reno, NV: American Institute of Aeronautics and Astronautics, 1801 Alexander Bell Drive, Suite 500, Reston, VA, 20191-4344, USA, [URL:http://www.aiaa.org].

[120] T. Poinsot and D. Veynante, *Theoretical and numerical combustion*. 2nd ed. 2005, Philadelphia: Edwards. xiv, 522 p.

[121] H. Huo, X. Wang, and V. Yang, *A general study of counterflow diffusion flames at subcritical and supercritical conditions: Oxygen/hydrogen mixtures.* Combustion and Flame, 2014.

[122] X. Wang, H. Huo, and V. Yang, *Counterflow Diffusion Flames of Oxygen and N-Alkane Hydrocarbons (CH4-C16H34) at Subcritical and Supercritical Conditions.* Combustion Science and Technology, 2014. **187**(1-2): p. 60-82.

[123] C.D. Pierce and P. Moin, *Progress-variable approach for large-eddy simulation of non-premixed turbulent combustion.* Journal of Fluid Mechanics, 2004. **504**: p. 73-97.

[124] Y.H. Choi and C.L. Merkle, *The Application of Preconditioning in Viscous Flows.* Journal of Computational Physics, 1993. **105**(2): p. 207-223.

[125] J.S. Shuen, K.H. Chen, and Y.H. Choi, *A Coupled Implicit Method for Chemical Nonequilibrium Flows at All Speeds.* Journal of Computational Physics, 1993. **106**(2): p. 306-318.

[126] E. Turkel, *Review of Preconditioning Methods for Fluid-Dynamics.* Applied Numerical Mathematics, 1993. **12**(1-3): p. 257-284.

[127] S.Y. Hsieh and V. Yang, *A preconditioned flux-differencing scheme for chemically reacting flows at all Mach numbers.* International Journal of Computational Fluid Dynamics, 1997. **8**(1): p. 31-49.

[128] N. Zong and V. Yang, *An efficient preconditioning scheme for real-fluid mixtures using primitive pressure-temperature variables.* International Journal of Computational Fluid Dynamics, 2007. **21**(5-6): p. 217-230.

[129] N. Zong, *Modeling and simulation of cryogenic fluid injection and mixing dynamics under supercritical conditions*, 2005, Pennsylvania State University.

[130] P.E.O. Buelow, *Convergence enhancement of Euler and Navier-Stokes algorithms*, 1995, Pennsylvania State University. p. 247 leaves.

[131] S. Venkateswaran and C.L. Merkle, in *AIAA, Aerospace Sciences Meeting and Exhibit, 33rd, Reno*. 1995. United States.

[132] P.E.O. Buelow, S. Venkateswaran, and C.L. Merkle, *Effect of Grid Aspect Ratio on Convergence.* AIAA Journal, 1994. **32**(12): p. 2401-2408.

[133] K.A. Hoffmann and S.T. Chiang, *Computational fluid dynamics*. 3rd ed. 1998, Wichita, Kan.: Engineering Education System.

[134] W. Kordulla and M. Vinokur, *Efficient Computation of Volume in Flow Predictions.* Aiaa Journal, 1983. **21**(6): p. 917-918.

[135] M. Rai and S. Chakrvarthy, in *AIAA Computational Fluid Dynamics Conference, 11th, Orlando*. 1993. United States: Washington, American Institute of Aeronautics and Astronautics.

[136] A. Fosso, H. Deniau, F. Sicot, and P. Sagaut, *Curvilinear finite-volume schemes using high-order compact interpolation.* Journal of Computational Physics, 2010. **229**(13): p. 5090-5122.

[137] R.C. Swanson and E. Turkel, *On Central-Difference and Upwind Schemes.* Journal of Computational Physics, 1992. **101**(2): p. 292-306.

[138] P. Jorgenson and E. Turkel, *Central Difference Tvd Schemes for Time-Dependent and Steady-State Problems.* Journal of Computational Physics, 1993. **107**(2): p. 297-308.

[139] S. Apte and V. Yang, *Unsteady flow evolution in porous chamber with surface mass injection, part 1: Free oscillation.* AIAA Journal, 2001. **39**(8): p. 1577-1586.

[140] T.J. Poinsot and S.K. Lele, *Boundary-Conditions for Direct Simulations of Compressible Viscous Flows.* Journal of Computational Physics, 1992. **101**(1): p. 104-129.

[141] D.H. Rudy and J.C. Strikwerda, *A Nonreflecting Outflow Boundary-Condition for Subsonic Navier-Stokes Calculations.* Journal of Computational Physics, 1980. **36**(1): p. 55-70.

[142] M. Baum, T. Poinsot, and D. Thevenin, *Accurate Boundary-Conditions for Multicomponent Reactive Flows.* Journal of Computational Physics, 1995. **116**(2): p. 247-261.

[143] T.J. Poinsot, amp, and S. Lelef, *Boundary conditions for direct simulations of compressible viscous flows.* Journal of computational physics, 1992. **101**(1): p. 104-129.

[144] C.W. Rowley, T. Colonius, and R.M. Murray, *Model reduction for compressible flows using POD and Galerkin projection.* Physica D: Nonlinear Phenomena, 2004. **189**(1): p. 115-129.

[145] Y. Huang, S. Wang, and V. Yang, *Systematic analysis of lean-premixed swirl-stabilized combustion.* AIAA journal, 2006. **44**(4): p. 724-740.

[146] P. Dagaut, in *ASME Turbo Expo 2006: Power for Land, Sea, and Air*. 2006. American Society of Mechanical Engineers.

[147] P. Dagaut and M. Cathonnet, *The ignition, oxidation, and combustion of kerosene: A review of experimental and kinetic modeling.* Progress in energy and combustion science, 2006. **32**(1): p. 48-92.

[148] J.C. Hunt, A. Wray, and P. Moin, *Eddies, streams, and convergence zones in turbulent flows.* 1988.

[149] P. Dagaut, A. El Bakali, and A. Ristori, *The combustion of kerosene: Experimental results and kinetic modelling using 1-to 3-component surrogate model fuels.* Fuel, 2006. **85**(7-8): p. 944-956.

[150] Q.-D. Wang, Y.-M. Fang, F. Wang, and X.-Y. Li, *Skeletal mechanism generation for high-temperature oxidation of kerosene surrogates.* Combustion and Flame, 2012. **159**(1): p. 91-102.

[151] H. Yamashita, M. Shimada, and T. Takeno, *A numerical study on flame stability at the transition point of jet diffusion flames.* Symposium (International) on Combustion, 1996. **26**(1): p. 27-34.

[152] N. Zong and V. Yang, *Near-field flow and flame dynamics of LOX/methane shear-coaxial injector under supercritical conditions.* Proceedings of the Combustion Institute, 2007. **31**: p. 2309-2317.

[153] T.H. Chung, M. Ajlan, L.L. Lee, and K.E. Starling, *Generalized Multiparameter Correlation for Nonpolar and Polar Fluid Transport-Properties.* Industrial & Engineering Chemistry Research, 1988. **27**(4): p. 671-679.

[154] S. TAKAHASHI, *Preparation of a generalized chart for the diffusion coefficients of gases at high pressures.* Journal of Chemical Engineering of Japan, 1975. **7**(6): p. 417-420.

[155] H. Meng, G.C. Hsiao, V. Yang, and J.S. Shuen, *Transport and dynamics of liquid oxygen droplets in supercritical hydrogen streams.* Journal of Fluid Mechanics, 2005. **527**: p. 115-139.

[156] J. Li, Z.W. Zhao, A. Kazakov, and F.L. Dryer, *An updated comprehensive kinetic model of hydrogen combustion.* International Journal of Chemical Kinetics, 2004. **36**(10): p. 566-575.

[157] B.E. Poling, J.M. Prausnitz, and J.P. O'Connell, *The properties of gases and liquids*. 5th ed. 2001, New York: McGraw-Hill. 768.

[158] R.J. Kee, J.A. Miller, G.H. Evans, and G. Dixon-Lewis, *A computational model of the structure and extinction of strained, opposed flow, premixed methane-air flames.* Twenty-second Symposium (International) on Combustion, 1989. **22**(1): p. 1479-1494.

[159] E.L. Petersen, D.F. Davidson, and R.K. Hanson, *Kinetics modeling of shock-induced ignition in low-dilution CH4/O2 mixtures at high pressures and intermediate temperatures.* Combustion and Flame, 1999. **117**(1-2): p. 272-290.

[160] M. Ó Conaire, H.J. Curran, J.M. Simmie, W.J. Pitz, and C.K. Westbrook, *A comprehensive modeling study of hydrogen oxidation.* International journal of chemical kinetics, 2004. **36**(11): p. 603-622.

[161] N.M. Marinov, W.J. Pitz, C.K. Westbrook, A.M. Vincitore, M.J. Castaldi, S.M. Senkan, and C.F. Melius, *Aromatic and Polycyclic Aromatic Hydrocarbon Formation in a Laminar Premixed n-Butane Flame.* Combustion and Flame, 1998. **114**(1): p. 192-213.

[162] P.J. Linstrom and W.G. Mallard, eds. *NIST Chemistry WebBook, NIST Standard Reference Database Number 69*. 2014, National Institute of Standards and Technology: Gaithersburg MD, 20899.

[163] K. Seshadri and N. Peters, *Asymptotic structure and extinction of methane-air diffusion flames.* Combustion and Flame, 1988. **73**(1): p. 23-44.

[164] C.H. Sohn, S.H. Chung, S.R. Lee, and J.S. Kim, *Structure and acoustic-pressure response of hydrogen-oxygen diffusion flames at high pressure.* Combustion and Flame, 1998. **115**(3): p. 299-312.

VITA

XINGJIAN WANG

Xingjian Wang was born in Bozhou, Anhui, China on Oct. 13, 1987. He received his Bachelor of Engineering in Thermal Science and Energy Engineering from University of Science and Technology of China (Hefei, Anhui) in 2010 and his Master of Science Degree in Aerospace Engineering from Georgia Institute of Technology (Atlanta, GA) in 2013.